IN-FLIGHT GAS PHASE PASSIVATION OF SILICON NANOCRYSTALS FOR NOVEL INORGANIC-SILICON NANOCRYSTAL BASED ELECTROLUMINESCENT DEVICES

A DISSERTATION
SUBMITTED TO THE FACULTY OF THE GRADUATE SCHOOL
OF THE UNIVERSITY OF MINNESOTA
BY

Richard William Liptak

IN PARTIAL FULFILLMENT OF THE REQUIREMENTS
FOR THE DEGREE OF
DOCTOR OF PHILOSOPHY

Stephen A. Campbell and Uwe Kortshagen, Advisors

October 2009

Acknowledgements

I would first like to express my sincerest gratitude to those who have made this thesis a reality.

First, I would like to thank my advisors Prof. Stephen A. Campbell and Prof. Uwe Kortshagen for their guidance, support, and encouragement during the past five years. Thank you for giving me an opportunity to work in a cutting edge field of technology, which will no doubt help me in my future endeavors. It was always a great time discussing the failure that is Cleveland sports with Prof. Campbell after another disappointing Browns or Indians game.

I would also like to thank Prof. Joey Talghader and Prof. Bethanie J. H. Stadler, for being my committee members and reviewing this dissertation.

I would also like to express my gratitude to Dr. John Thomas III. Over the years, he has provided a free education on surface science. I have been able to gain invaluable knowledge from working with John, and his career advice is second to one. Get well soon.

I am thankful for my fellow group members Maryam Jalali, Sang Ho Song, Min Woo Jang, Dan Yu, Gagan Aggarwal, Brijesh Kumar, Kush Nagaich, Dr. An-Jen Cheng, and Dr. Rebekah Ligman. Their assistance with the project, insightful discussions, and friendships have made these past 5 years wonderful. I am especially grateful to Dr. An-Jen Cheng for his help on the inorganic-NC based devices.

I am also thankful for my fellow Kortshagen group members Dr. Lorenzo Mangolini, Dr. Xiaodong Pi, Dr. Curtis Anderson, Rebecca Anthony, Chin-Yi Liu, Federico Galli, Dave Rowe, Zak Holman, and Ryan Gresbeck for their help and assistance for the past few years. I am especially grateful to Dr. Xiaodong Pi for his assistance on the CF_4 passivation project and to Dr. Lorenzo Mangolini for teaching me the finer points of the non-thermal plasma synthesis of Silicon Nanocrystals

I am also grateful to Greg Cibuzar, Gary Olin, Rich Macy, Terry Brough, Lage Matzke, Tony Whipple, Mark Fisher, Kevin Roberts, Mike King, and Bruce Pannkuk of the NFC for their assistance, guidance and friendship over the past few years. I was great to turn to the staff for any fabrication and vacuum science/gas line questions that I had. I am also grateful to the CHARFAC staff. Without their help, I would not have been able to perform the characterization needed to complete this work.

I would like to acknowledge my funding sources: the NSF MRSEC program under awards DMR-0212302 and DMR-0819885, the NSF IGERT program under award DGE-0114372, and SPAWAR through NSF grant DMI-0556163. I would also like the Center for Nanostructured Applications for their support as well.

Finally, I would like to thank my parents, Richard and Linda, my brother Bob, and my sister Sarah for their love, support and encouragement during these past few years.

Abstract

Silicon nanocrystals (SiNCs) have become a heavily researched material over the past several years. Researchers envision that this material can be used in many diverse applications such as electronic devices, non-toxic biological tags, optical devices such as LEDs, lasers or displays, thermoelectrics, and photovoltaic (PV) applications. For many of these proposed applications one needs to properly control the NC size and the surface chemistry via passivation. Current passivation techniques allow for the creation of highly efficient SiNC optical emitters, however the emission of these NCs are fixed in the red-NIR range. To resolve this issue several novel in-flight passivation techniques were investigated.

A novel dual-plasma setup which allows for the in-flight passivation of SiNCs through a thermal or LPCVD based nitridation process was developed first. FTIR and XPS analysis were used to study the surface chemistry on of the nitride passivated NCs while TEM was used to investigate whether or not a "shell" was grown on the surface. PL measurements and thermal stability tests were performed on the nitride passivated NCs to gain a further understanding of the stability (in both air as well as other ambients) of the NCs and their surface chemistry.

Tunable full color emission from SiNCs was developed for the dual-plasma reactor utilizing CF_4 as both an etching and passivating source. F radicals generated in the etching plasma remove Si from the surface of the NC, while at the same time CF_2 radicals lead to the formation of a fluorocarbon passivation layer on the NC surface. By controlling the parameters of the reactor (CF_4 flow rate, power), the NC size and thus its color can be controlled. Red to green luminescence was observed from SiNCs and is believed to be due to the quantum confinement effect. The blue emission observed from the NCs is appears to be related to oxide related surface states. Despite the defects, high QY was observed from these CF_4-etched NCs.

The fluorocarbon passivation layer, although stable, prevents further functionalization of the NCs. To counteract this problem another silicon-based dry etch chemistry, SF_6 was investigated. Full-color emission was observed from SF_6 etched NCs, with QY 2X higher than that of CF_4-etched NCs. A maximum QY of nearly 55% at

700 nm was observed after several weeks in air, comparable to that observed with alkyl passivation. The native oxidation of the bare oxidized and SF_6-etched NCs were also studied. Results show that the NC oxidation follows the Cabrera-Mott mechanism for low temperature oxidation.

Inorganic-NC based LED structures were then investigated. Fabrication processes for the inorganic hole and electron transport layers were developed by RF sputtering and atomic layer deposition (ALD). Thorough characterization was performed on the metal-oxide films (ZnO, TiO_2, NiO) to verify their stoichiometry as well as study their optical and electrical properties. Novel inorganic-NC device structures were fabricated. Inorganic NC devices which use a metal-oxide HTL but no ETL, emit light, however their emission is so weak. The addition of an ETL increases the light output by a factor of 4, but the device reproducibility is poor. To improve efficiency two insulating matrix layers were investigated. In both cases, the film deposited on the top of the NC is rough, porous, discontinuous, and potentially full of traps – certainly not the ideal film for a device. Therefore, more work is needed, specifically on the NC layer to improve the structure of the as-deposited NC film, but efficient device structures appear to be possible.

Table of Contents

List of Tables

Chapter 4

Chapter 5

List of Figures

Chapter 1

Chapter 2

Chapter 3

Chapter 4

Chapter 5

Chapter 1

Introduction

1.1.1 Semiconductor Nanocrystals / Quantum Dot Intro

Semiconductor nanocrystals (also known as quantum dots or artificial atoms) are inorganic semiconductors on the order of 10 nm or less whose material properties (electrical, optical, etc.) deviate from the bulk material (of the same type) due to size-related effects. This deviation occurs once the size of the NC approaches that of the Bohr radius of the bulk material (For silicon this occurs around 2.5 nm). Thus, as the size of the NC decreases, the energy levels of the NC become more separated (or discrete), leading to an effective increase in the bandgap. This effect, known as quantum confinement, has spurred interested in this area, because it is possible to synthesize a material which has the same composition and crystal structure can have different properties based solely on its physical size.

The first report of NCs may have actually occurred in the 1930's. H. P. Rocksby observed that the color change observed in some silicate glasses was the result of CdS or CdSe inclusions. [1-3] The cause of this color change in the silicate glass would not be answered for another 50 years, when quantum confinement was demonstrated in CdS and CdSe nanocrystals. [4-8] This demonstration of quantum confinement in II-VI quantum dots as well as the realization that the quantum dots had optical properties far better than that observed with quantum wells or wires leads to the technological revolution that we

observe today. [9-10] Shortly after the demonstration of quantum confinement in II-VI NCs researchers began developing liquid-phase synthesis procedures. These simple fabrication techniques [11-14] yielded high quality NCs which were extensively characterized. Because of the simple deposition techniques, the II-VI NC system is the most widely studied.

Following the demonstration of simple fabrication methods for II-VI NCs, researchers began to investigate techniques which could produce monodisperse NCs (because the physical properties, especially the optical properties are size-dependent). [15] Since II-VI NCs have a direct bandgap, both radiative recombination and absorption (light) will occur without phonon assistance. Phonons are needed in indirect bandgap materials in order to conserve energy and momentum. Because of this II-VI NCs have sharp absorption and emission features, high quantum yields (since most if not all recombination events will be radiative), and short radiative lifetimes. The direct bandgap properties make II-VI NCs attractive for several devices such as lasers, LEDs, or PVs.

The surface of NC is often covered with dangling bonds which typically act as trap states. In addition to trapping charge, these states often behavior as nonradiative recombination centers. To improve the efficiency of the NC, researchers typically passivate or cap the dangling bonds at the surface. This surface passivation leads to an increase in the overall efficiency of the device by reducing the non-radiative states at the surface. This is typically done in II-VI NCs by fabricating core-shell NCs. [16, 17] The inorganic shell suppresses interface defects and can lead to an increase in the PL QY of the NCs. Furthermore, the shell prevents the NC core from oxidation. It is also possible

to tailor both the shell and the core in order to tune the emission from the II-VI NCs. [18] For a concise review of the liquid-phase synthesis and passivation of compound semiconductors we encourage the reader to consult Reiss. [18] Despite the attractiveness of the core-shell system, no comparable technique has been demonstrated for silicon.

1.1.2 Drawbacks to II-VI NCs

Despite the obvious potential applications for II-VI NCs, there are still some serious drawbacks that may hinder their acceptance in the commercial market. One of the biggest concerns with II-VI NCs is that most of the materials are toxic. Cd, Se, Pb, and Te are all toxic materials. [19] Although a core-shell approach [20] may be able to reduce exposure, it would safer to work with a non-toxic material such as silicon. Furthermore, the II-VI NC processing is not compatible with current microelectronic processing.

CdSe NCs have been typically used in NC based EL devices because of ease of fabricating a stable shell (ZnS). During the synthesis Trictylphosphine Oxide (TOPO, ($[CH_3(CH_2)_7]_3PO$)) is typically applied to the surface of the core-shell NC to prevent agglomeration. [21] However, work by Greenham *et al*. [22] has shown that TOPO prevents charge transfer from organic materials to the NCs. This may be the reason why a low EL efficiency is observed with TOPO capped II-VI NC LEDs: one of the highest reported device efficiencies is 1.1% [23] (for materials with a PL of QY 50% [24]). Thus low efficiency and toxicity concerns of the materials may prevent the commercialization of the device presented in [23].

1.2 Luminescence From Silicon

Until Canham's report in 1990 [25], no one would believe that silicon could be used as an efficient light emitting material. The luminescence observed was attributed to quantum confinement. Shortly after this publication, novel synthesis processes surfaced leading to the production of red emitting NCs. [26, 27] This was exciting because an efficient Si light emitter would be cheap, stable, and could be integrated in existing microelectronic architectures such as optical interconnects. As a result, theoretical studies were performed to gain a better understanding of the light emission mechanism in SiNCs. Figure 1.1 provides a plot one of theoretical studies performed by Zunger and Wang. In Figure 1.1 the predicted light emission (and energy) from quantum confined SiNC is plotted as function of particle size. [28, 29]

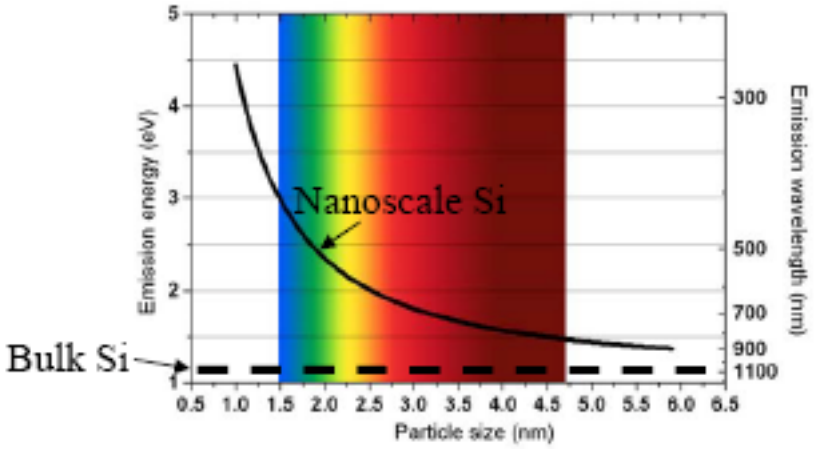

Figure 1.1: Predicted light emission wavelength and emission energy as a function of NC size. From Zunger and Wang [28-29].

Unfortunately, experimental results [30] did not follow the model predictions. Work published by Wolkin [31] and Ramos [32] presented to a solution to why a deviation existed between the experimental and theoretical results. Figure 1.2(a) presents a plot of

the electron states in SiNCs as a function of both size and surface passivation while Figure 1.2(b) predicts the light emission from NC with an oxide passivation layer.

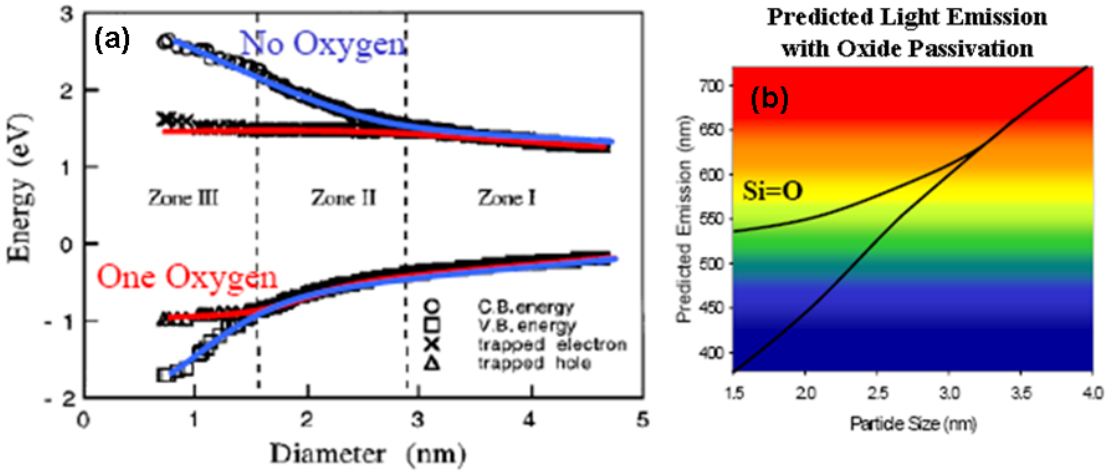

Figure 1.2: (a) Electronic states of from oxidized SiNCs as a function of size. Reproduced from [31]. (b) Predicted Light Emission from Oxidized SiNCs as a function of NC size.

Examining Figure 1.2(a) it is clear that once the NC reach a certain size (≈ 2.5 nm) oxide related traps become an important factor in determining the bandgap. It is also probable that recombination events will occur through this trap state, limiting the PL to that trap energy. Eventually, another trap state becomes an allowed transition around 1.5 nm. Although oxide passivation allows for the synthesis of efficient red emitting NCs, other passivation approaches are needed in order to achieve short-wavelength emission from SiNCs.

1.3 Alternative Passivation Schemes for EL and PL Applications

In order to fabricate efficient electroluminescent (EL) and photoluminescent (PL) NC devices, a stable and robust passivation layer is needed. Unpassivated SiNCs have

dangling Si bonds at the surface. When exposed to air, a native oxide forms on the surface of NC, effectively passivating the dangling Si bonds. However, this type of passivation is not suitable for EL devices. Silicon oxide is highly resistive and its band gap is not suitable for charge injection. Furthermore, the native oxidation process yields SiNCs that PL in the red-orange (see Figure 1.2). According to this theory, the formation of a silicon oxygen double bond (or backbonded oxygen bonds) at the surface of the SiNCs pins the PL in the red (due to trap states in bandgap). Besides pinning the PL in the red-orange, oxidized SiNCs have a QY of 10% or less. This makes it very difficult to fabricate intense and efficient SiNCs with an oxidized surface. Thus, native oxidation is a poor passivation technique for a SiNC device.

Since silicon oxide is an insufficient passivation layer, researchers have investigated several alternative passivation approaches. The approaches can be summarized into four basic categories: solution (or wet chemistry)-based techniques, mixed-phase films, gas phase techniques, and polymer / organic encapsulation.

Solution-based techniques is a general term that describes the three basic liquid-phase passivation approaches: acid etching, hydrosilylation, and halide solutions. Acid etching for SiNCs is a technique introduced by Swihart. [33-35] In this technique SiNCs are immersed in a hydrofluoric (HF) and nitric (HNO_3) acid solutions. After the acid etched the SiNCs are placed into an organic solvent, usually methanol, and the PL characteristics are studied. By controlling the etch chemistries the particles can be passivated by either hydrogen or oxygen. Another benefit of this technique is the fact that shortwave PL can be achieved by this method. Orange, yellow, and green PL NCs

have been observed. Despite the exciting optical characteristics of these SiNCs there are few drawbacks to the acid etching passivation technique. First of all, a secondary technique is needed to create the SiNCs. In this study, CO_2 laser-driven pyrolysis of silane (SiH_4) was utilized to fabricate the SiNCs, but other techniques exist. Secondly, the passivation layer that forms on the SiNC during the acid treatment is unstable. Hydrogen passivated surfaces will oxidize over time and particles may agglomerate in some organic solutions. [36, 37] Oxygen passivated surfaces suffer from a similar fate. The optical characteristics of the oxidized SiNC degrade as well. The intensity weakens over time while the PL spectrum blue shifts. The worst case is the green light emitting SiNC produced by the acid etch method. Swihart reports that SiNCs emitting at a wavelength of 600 nm or above are stable. The SiNCs blue shift about 12 nm and decrease in intensity by a factor of 2.5 over a period of about six days. The SiNCs which emit in the green part of the visible spectra also demonstrated some interesting characteristics. The intensity of the PL spectrum decreases rapidly in less than an hour and the PL spectrum red shifts. This suggests that the trap states discussed above are beginning to form in these dots. The efficiency of these NCs are unknown. Swihart contends that they were able to measure a QY of 0.5 % – 1 %, but he questions their measurement technique. If these particles are subject to native oxidation, their QY is probably 10% or less due to the oxygen formation on the surface of the SiNCs.

The acid etch technique provides an avenue to shortwave luminescent SiNCs; however the QE and intensity are extremely low. Their stability in air is also poor. Furthermore, an additional technique is needed to synthesize the NCs. With respect to

EL devices, the acid-based etching techniques do not provide the passivation or efficiencies that are needed.

In an attempt to improve the QY as well as the passivation, many researchers turn to the chemical process known as hydrosilylation. During this process a hydrogen terminated surface is reacted with an alkene (H_2C=C-R), such as octadecene. The Si-H bond at the surface of the SiNC is replaced by a Si-C bond. The Si-C bonds prevent a native oxide layer from forming on the surface of the NC. The NCs are now carbon terminated.

Exciting results on hydrosilylation have been published by both Swihart [38-40] and Mangolini. [41] Recent published work from Mangolini [41] demonstrated hydrosilylated SiNCs with a QY of ≈ 60%. Many believe that this is a stable passivation technique, meaning that no blue shift is observed in the PL spectrum once the hydrosilylated particles are exposed to air. However, results published by Mangolini [41] show that even a hydrosilylated surface can be oxidized (visible blue shifts in the PL spectrum) thus reducing the QY. It is believed that the blue shift observed in red light emitting SiNCs is due to the formation of silicon oxide on the surface of the NC, which leads to a reduction of the crystalline core of the SiNC. [42] The drastic loss in QY is also most likely due the oxidation of the SiNC surface.

Another problem exists with hydrosilylation; it may make efficient EL devices problematic. Calculations performed by Reboredo and Galli suggest that Si-C bonds actually reduce the electron affinity of the SiNCs. [43] This effect is shown in Figure 1.3 This does not affect the bandgap of the NC, but does complicate charge injection

(specifically electron injection). Couple this with the fact that two fabrication steps (SiNC fabrication, H-Termination) are often carried out before hydrosilylation occurs makes this a difficult and tedious process.

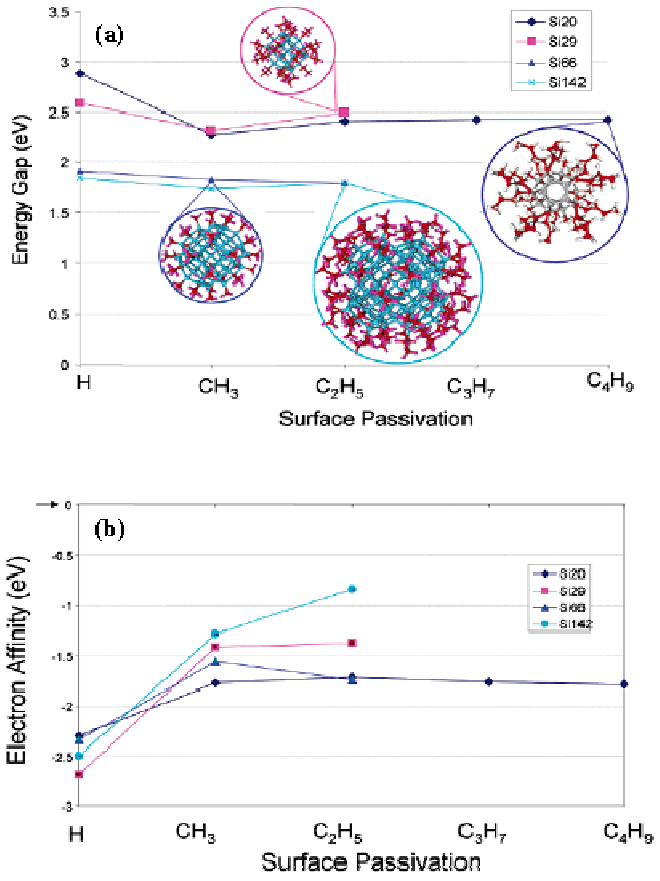

Figure 1.3: Band energy gap of SiNCs for specified sizes as a function of the alkyl surface passivation. (b) Electron affinity of SiNCs for specified sizes as a function of the alkyl surface passivation. Reproduced From [43].

A third liquid phase technique that is currently under investigation is surface passivation using halides. Halides have been successful in passivating bulk silicon films [44] and as a result researchers [45, 46] have been studying iodine (I_2) and chlorine (Cl)

as possible passivation materials. In this approach, SiNCs must first be manufactured ex-situ. As stated before, several methods can be used. After fabrication, the NCs are dipped in HF acid, however agglomeration is a concern as described above.

Following the HF dip the particles were immediately immersed 7 X 10^{-4} M solution of iodine in methanol. [45] Results published by Seraphin [45] and his research group provide some interesting possibilities. They performed XPS on oxidized, HF treated, and halide treated SiNCs. The results are provided in Figure 1.4(a). Examining the top figure, one notices two distinctive peaks at 103 eV and 99 eV. The peak at a binding energy of 103 eV corresponds to SiO_2 (indicates that some SiNCs are oxidized) while the peak at 99 eV represents a Si-Si bond. The XPS spectra shown in the middle of the figure is a little different. In this case, Seraphin placed oxidized SiNCs into a HF acid bath and then performed the XPS analysis.

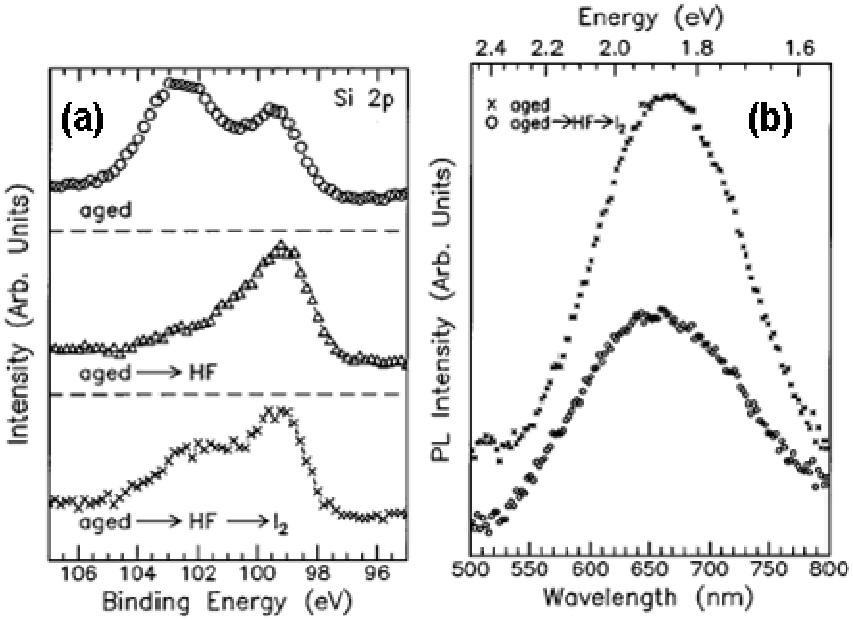

Figure 1.4: (a) Si 2p XPS spectra of aged, HF treated, and iodine (I_2) treated films. (b) PL spectra of aged and iodine treated silicon SiNC thin films. Reproduced from [45].

The peak corresponding to the oxide layer is no longer present. This is because the surface is hydrogen terminated and had not yet been exposed to air. However, if the particles were exposed to air the XPS spectra in the middle of the figure would slowly begin resemble the top XPS spectra. Finally, the third XPS spectrum (bottom plot on Figure 1.4(a) shows the XPS results from SiNCs that have been oxidized, HF dipped, and then halide treated. The interesting feature of this spectrum is the fact that the peak for the unoxidized Si is stronger than the peak for the oxidized Si. There still appears to be a significant amount of oxidized Si, but the iodide treatment seems to provide another approach that can be used to passivate the surface of SiNCs. Figure 1.4(b) shows the PL spectrum of oxidized and iodide-treated SiNCs. No significant differences are seen in the two spectra except that the intensity of the iodide treated SiNCs are significantly lower. Seraphin explains that the intensity of the PL peak is dependent on the number of non-radiative states at the surface, and thus can be used a measure of surface passivation. [45] Therefore, by this statement one can conclude that iodide does not passivate the surface completely.

There are drawbacks to this process. Similar to the other wet chemistry techniques, another method is needed to fabricate SiNCs. Furthermore, several additional steps are needed to passivate the surface. The intensity of the PL does not improve with this technique and it is difficult to image this process being adapted as a commercial fabrication approach.

Liquid phase techniques are not the only methods employed to passivate the surface of SiNCs. SiNCs can be embedded into films, often referred to as mixed-phase

films. The two most common are SiNCs embedded into silicon oxide (SiO_2) or silicon nitride (Si_3N_4). The fabrication processes used for these films typically require high-vacuum conditions. The first step in the creation of these NC films is the film deposition on the substrate (usually Si). Several processes can be used for the deposition for the SiO_2 or Si_3N_4 layer. They include ion-beam sputter deposition, co-sputtering, ion implantation and PECVD. [47-50] The salient feature of these processes is that they can be run far from chemical equilibrium, producing a silicon-rich film. After the film deposition, high-temperature anneals are used to induce phase separation between the dielectric medium and the Si which leads to the nucleation and growth of SiNCs. [50-54] The intensity and peak position of the PL is dependent on the Si content in the films and on the annealing temperature that is applied to the film after fabrication. Figure 1.5 presents results obtained by Iacona [50] and his group on silicon-rich silicon oxide (SRSO) films. Figure 1.5(a) shows the PL of a SRSO film at three different annealing temperatures. As the temperature increases (or decreases), the PL peak position shifts significantly. Furthermore, examining Figure 1.5(b) one notices that at a specific temperature the PL peak position can differ depending on the concentration of Si in the film. Therefore, sensitive control over the fabrication process is needed to control the PL.

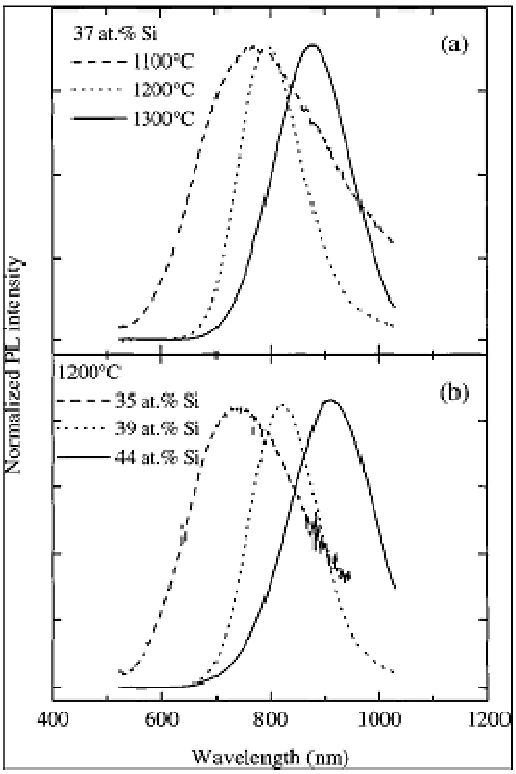

Figure 1.5: Normalized room temperature PL of (a) SiO_x film with a Silicon concentration of 37% after anneals at 1100ºC, 1200ºC, and 1300ºC for 1 hour. (b) SiO_x films with Si concentrations of 35%, 39%, and 44% after a 1 hour thermal anneal at 1200ºC. Reproduced from [50].

These in-situ growth techniques provide a stable oxide or nitride passivation for SiNCs by passivating the dangling bonds (thus reducing non-radiative recombination pathways) at the SiNC/matrix interface. Furthermore, the fabrication process also minimized particle aggregation that can result in the formation of pin holes in the device which can create specific current pathways in the device causing heating and eventually burn out. Despite the advantages of the passivation discussed above, there are several issues with this passivation technique. First of all, one technique passivates the NC with oxygen. As stated before, trap states with oxide passivation limit the emission from the NCs to the red-NIR range. Secondly, the control over the size and the shape of the NCs

grown in the dielectric matrix was extremely poor leading to large size distributions with unstable PL (of NCs) in the films. [50, 55-56] Thirdly, high temperature anneals required to form SiNCs would most likely damage any polymer, organic material that may be used in the device. They also make these devices incompatible with CMOS. Finally, these NC embedded devices have poor EL which is caused by the insulating host. [51, 55, 57-60]

As a result, silicon-rich silicon nitride (SRSN) or SRSO films are not a good choice for NC passivation. For instance, the SiNCs are embedded into the film, thus no additional processing of the SiNCs can occur unless the film is etched away. Once this has occurred, the SiNCs would then be subject to oxidation. Similar to the liquid phase approaches, this passivation technique also requires several steps to fabricate and passivate the SiNCs.

In terms of EL devices, SRSN and SRSO are wide bandgap insulators, so it is difficult to pass current through an EL device. SRSN has a smaller band gap than SRSO and may be more suitable for charge injection. But the same problem arises. Once the SiNCs are fabricated no additional processing of the SiNCs can occur. This puts a restriction on the type and structure of the device that can be built.

Gas-phase passivation is another process currently under investigation. Unfortunately, little or no gas phase techniques exist today to passivate SiNCs entirely in the gas phase. Dinh [61] reports on one gas phase technique used to terminate the surface of SiNCs with hydrogen or oxygen. In this particular setup, the SiNCs are created using a thermal vaporization technique [62, 63] which resembles the technique used in thin-film fabrication industry. An inert gas, usually argon is pumped into an ultra-high vacuum

system to set a specific chamber pressure. Premelted and outgassed Si lying inside a carbon boat is then affixed to a tungsten wire mesh. Using resistive heating to heat the samples past its melting point and monitoring the temperature with standard sensors, Dinh was able to evaporate SiNCs onto several different substrates. After the SiNC deposition the passivation process was initialized. In order to passivate the surface with hydrogen, Dinh exposed atomic hydrogen to the SiNCs by passing molecular hydrogen through the tungsten mesh at a temperature of 2000ºC and a pressure of 2×10^{-6} torr. [64, 65] A similar technique was used to O-passivate the surface except molecular oxygen was flowed through the tungsten mesh at a room temperature and a pressure of 300 mtorr.

Dinh was able to fabricate SiNCs with specific diameters which PL using the technique referenced above. In terms of fabricating an EL device, this approach has several drawbacks. First of all, SiO_2 passivation can not be used. This was discussed earlier. Secondly, the processing temperatures would destroy any polymer or organic material that is built into the device. Finally, this is another multi-step process which is difficult, which may increase the total fabrication time and cost.

Roberts and coworkers have published results describing a novel gas phase process that successfully grafts both inorganic materials [66-67] and organic solvents onto the surface of SiNC inflight. [68] Although the effectiveness of this functionalization was studied (via FTIR), no information was provided with regard to the PL spectrum, its stability in air, or the quantum efficiency of these SiNCs. Nevertheless, this paper introduces another possible avenue of passivation.

The most promising gas-phase passivation technique was developed within the past two years building off of earlier published results. The experimental setup developed by Mangolini *et al*. [69] is shown in Figure 1.6.

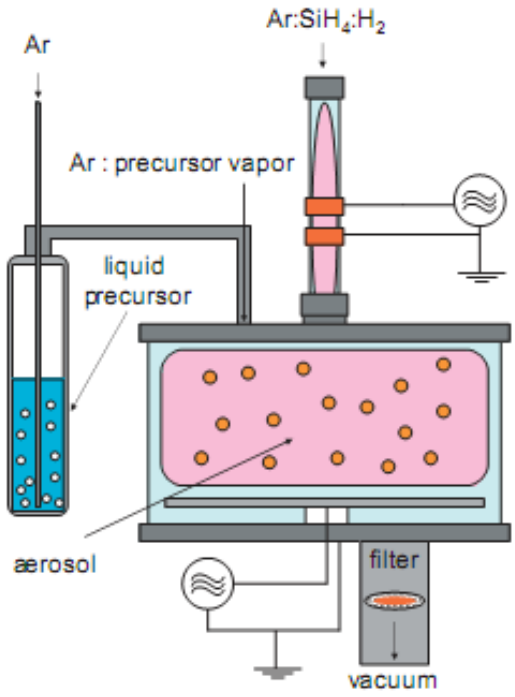

Figure 1.6: Novel two-stage plasma reactor used for the synthesis and in-flight passivation of SiNC. Reproduced from [69].

The SiNCs are synthesized in a SiH_4/He, Ar, and H_2 non-thermal plasma. [70] Following the synthesis, the NCs are pushed into the second reactor where they are combined with a vaporized liquid precursor which was carried into the reactor by inert Ar gas. According to Mangolini [69], reactive radicals of the organic ligands are formed through electron impact dissociation, which enable the reaction of the organic ligands with the surface of the silicon nanocrystals. NCs can be passivated by a variety of different organic

precursors using this process. However, unlike its liquid-phase counterpart, the QY of these in-flight hydrosilylated NCs are only 10%. [69]

Polymers can also be used to passivate the surface of SiNC. Work has been performed on several polymer materials including: polyaniline (PANI), poly (N-vinylcarbazole, PVK), poly(phenylene-vinylene, PPV), and poly(methyl methacrylate, PMMA). Swihart and coworkers have demonstrated that polymer coatings on SiNCs are feasible. [71] These processes often include complicated wet chemistry procedures. It is believed that the polymers will be able to encapsulate and shield the SiNC thus avoiding the PL degradation and blue shift that is seen when SiNCs are dispersed in organic solvents and oxidized.

Polymer processes used to passivate SiNCs appear to suffer from the same problems discussed in other passivation schemes. SiNCs first need to be fabricated from another process. Following the SiNC fabrication several complicated wet chemistry steps follow to prepare the surface of the SiNC for polymerization. However, some polymers will not work with an EL device. For example, PMMA is an insulator and therefore it will be difficult to inject charge. SiNC coated or embedded in PMMA have interesting PL characteristics, but the fact that PMMA is an insulator may negate its use in an EL device. Similarly, researchers have discovered that the PL spectrum of bare SiNCs embedded in PVK and other amines is severely quenched. [36-37, 72-73] The third problem with polymers concerns their stability in microelectronic processing. The addition of a polymer passivation may just be the next step in the construction of an EL device. Even at room temperature, most polymers are highly transmissive to water vapor.

Furthermore, the chosen polymer material must be able to withstand high temperature processes such as rapid thermal annealing, sputtering, evaporation, plasma deposition, etc. As a result a greater emphasis must be placed in the design, of both the structure as well as the fabrication process, of SiNC EL devices incorporating a polymer passivation layer. Despite the obvious problems with polymer passivation it provides another viable technique to passivate SiNCs.

1.4 Si-Based Electroluminescent Devices

For the most part most research in SiNC has been focused on the development of novel synthesis techniques and the characterization of the NCs. Little work has been done in the area SiNC based EL devices. Most SiNC based EL device are based on SiNC embedded in a dielectric matrix such as SiN_x, SiO_x, or a-Si, since the only additional step is the formation of the upper charge injection electrode. As discussed earlier, the embedded NCs have an improved efficiency due to the passivation of dangling bonds. However, these devices suffer from a poor control over the size and the shape of the embedded NCs (which could lead to unstable emission). The most efficient device demonstrated by an embedded SiNC was reported to be 1.6% [51], however the method used by these authors to calculate this efficiency is not clear. No follow-up on this work has been published by this group.

Another approach to produced efficient SiNC devices is based upon hybrid devices demonstrated in the II-VI NC system. Ligman [74] demonstrated SiNC EL from NCs dispersed into PVK. Figure 1.7 shows the device architecture, PL and EL of the

device. Figure 1.7(a) shows the device design. It is a simple sandwich based architecture where ITO and Ag/Mg act as the hole and electron injection electrodes. Figure 1.7(b) shows the PL and EL spectra from the device. Both PL and EL are observed from the NC embedded in the PVK. Interestingly, the PVK also emits light.

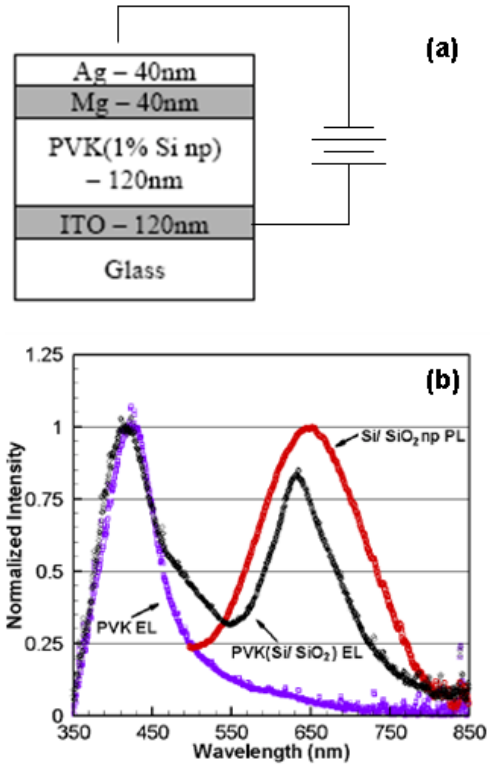

Figure 1.7: (a) Device schematic and (b) EL and PL spectra from SiNCs dispersed in PVK. Reproduced from [74].

This device is cheap and simple to fabricate. However, it does have a few problems. First of all, oxidized NCs are used as the emissive material. As discussed earlier, this will pin the emission in the red due to trap states in the bandgap. Secondly, the oxide shell on the NCs may make charge injection difficult. The stability of the soft material (PVK) is another issue. Nevertheless it presents a unique approach to generate efficient EL from SiNCs.

Although efficient devices [23, 75] have been demonstrated utilizing organic materials, researchers are concerned about the lifetime of these organic materials. It has been shown that metal contacts on organic materials are unstable and degrade when exposed to air [76-77]. As a result the II-VI community has been actively pursing inorganic materials to replace organic layers in hybrid-NC devices. Recent results using metal-oxide layers are promising [78-79] and provide another possible approach to creating an efficient EL SiNC based device.

1.5 Scope of the Thesis

The lack of passivation techniques which allows for air stable full-visible spectrum emission from silicon prevents silicon from becoming a competition in the LED field. In order to overcome this shortcoming, alternative passivation techniques need to be developed which allow for short-wavelength emission from silicon despite oxidation. In order to solve this issue, three novel in-flight passivation process were developed. Chapter 2 presents a novel gas-phase nitridation passivation process which allows for a in-flight nitride film (Thermal or LPCVD) to be grown on the SiNCs. Chapter 3 presents work done on CF_4 etching of SiNCs. Not only does this process provide a stable passivation layer (fluorocarbon) it allows for tunable emission from SiNCs. Chapter 4 discusses a second passivation/etching process utilizing SF_6 which allows for the creation of both full-visible spectrum emission and high QY (55%) from the SiNCs. Finally, chapter 5 discusses device integration. The fabrication and characterization of metal-oxide transport layers for an inorganic-SiNC based LED are discussed. Device

fabrication and early results are presented. Chapter 6 summarizes the work and provides recommendations on future direction.

Chapter 2

Early Passivation Approaches

2.1 Chapter Overview

This chapter discusses early gas-phase passivation approaches for plasma synthesized silicon nanocrystals (SiNCs). Utilizing a novel two-stage plasma reactor, the SiNCs are synthesized in stage 1 using the process developed by Mangolini *et al*. [1] and subsequently passivated with a nitride layer in stage 2. Both a thermal based (LCPVD) and a plasma based (PECVD) approach was investigated for the passivation step. The surface of the passivated NCs was investigated with XPS and FTIR to determine what effect the nitride passivation had on the NCs. The optical properties of the NCs were also studied. Initially, no PL was observed from the NCs. After nearly a week in air a weak red emission was observed, possibly due to oxidation of the passivation layer. Finally, the last section of the chapter discusses some simple thermal stability measurements performed on as-produced (oxide passivated) and nitride passivated NCs. This simple yet necessary experiment was needed in order to determine at what temperature SiNC begin to show signs of degradation, specifically loss in PL intensity. This information is vital especially if NCs are to be used in device structures in which high-temperature processing (such as rapid thermal annealing) is needed.

2.2 Silicon Nanocrystal Synthesis

Mangolini *et al*. [70] is responsible for the creation of a novel plasma synthesis reactor which can make large amounts of crystalline SiNC in a few hours. By controlling certain experimental parameters of the reactor the user can control the size and the structure (amorphous or crystalline) of the NCs. The basic schematic of this reactor is shown in Figure 2.1.

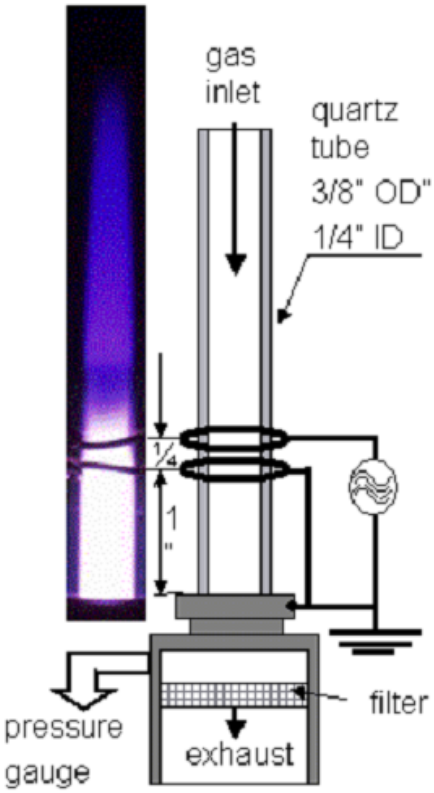

Figure 2.1: Novel low-pressure SiNC synthesis system. Reproduced from [70].

The dual-plasma reactor (DPR) used to create and passivate NCs in the gas phase is based upon the system shown in Figure 2.1. The DPR is broken down into two sections, first a NC synthesis section based upon [70] and a gas-phase passivation section. The following paragraphs describe the DPR in greater detail.

As mentioned above, the synthesis of the NCs occurs in a reactor similar to that shown in Figure 2.1, with a few notable changes. In order to synthesize NCs with the DPR the following standard conditions were utilized. 5% silane (SiH_4) in helium (He), argon (Ar), and hydrogen (H_2) are flowed through a 3/8" outer diameter quartz tube. An RF voltage at 13.56 MHz was applied to the reaction tube creating a plasma with a pressure near 3 torr, which disassociated the precursors. This disassociation of the Si-H bonds in SiH_4 yields SiNCs whose size and crystal structure depend on the residence time, gas flow rates and system pressure in the quartz reaction tube. The pressure in the reaction tube was fixed by an orifice. The orifice is simply a copper gasket with a hole drilled through the middle which creates a pressure drop between the synthesis and passivation regions, giving the NCs the energy to traverse the entire passivation section and reach the fine stainless steel mesh grid where the NC are captured (via impaction). A 2.5 mm hole along with normal gas flow rates (50 sccm Ar, 10 sccm SiH_4/He, 3.5 sccm H_2) yields crystalline SiNCs with a diameter between 4 and 7 nm. Figure 2.2 displays a TEM bright field image of SiNCs fabricated by this process. The scale bar on the figure is 5 nm.

Crystalline facets can be identified on the figure. Coupled with the diffraction pattern (not shown) this proves the SiNCs are indeed crystalline. NC sizes on the order of 4-7 nm in diameter can be identified in the figure. It is important to make the following statement. We do not make one specific size of SiNCs in the synthesis plasma; rather we create a variety of sizes. This is one reason the PL spectrum of the SiNCs are so broad. In order to collect one specific size of SiNCs, particle sizing equipment such as

a differential mobility analyzer would need to be added to the system. Processing times would also increase because more SiNCs would be needed in order to see PL. H_2 is added into the precursors for one simple reason. Once the silane is disassociated, SiNCs are created. However, the NCs tend to agglomerate very quickly.

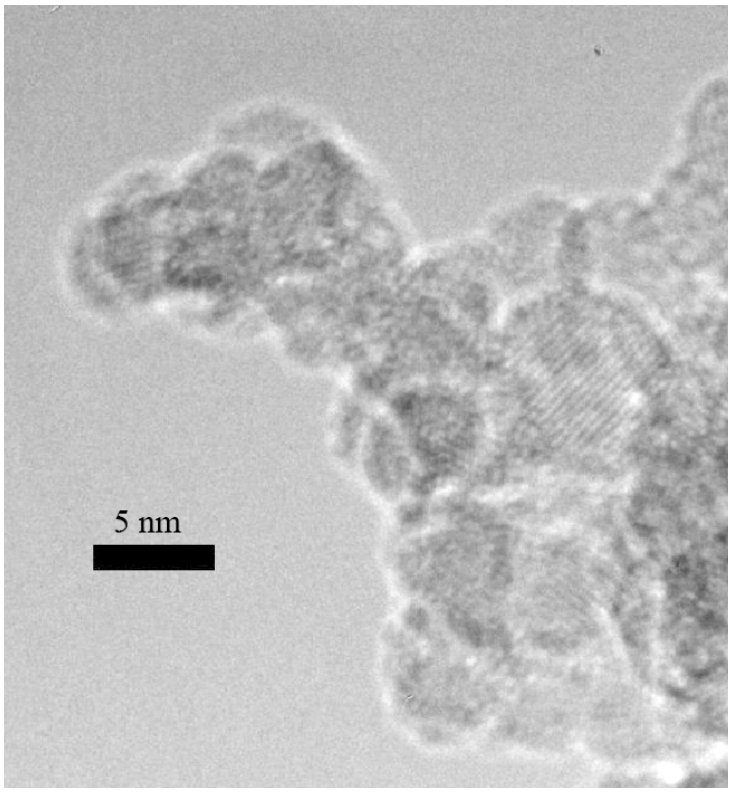

Figure 2.2: TEM bright field image of SiNCs created in the synthesis plasma (no in-flight passivation). The scale bar is 5 nm.

Since particles with sizes around 5 nm are believed to PL [31, 42, 70, 80-88], we would like to prevent the NC from growing larger. Therefore, we add the additional H_2 into the plasma to H-passivate the SiNC, reduce dangling bonds (or surface states) and reduce the rate of agglomeration.

SiNCs can be collected in a variety of locations throughout the system. Figure 2.3 presents the basic system schematic. The two most common deposition locations are indicated on the figure. The first collection point occurs directly after the SiNCs leave the first chamber. Only untreated (meaning they did not undergo in-flight passivation) SiNCs are collected here. The second collection point lies at the entrance to chamber two. Both untreated and treated SiNCs can be collected here. SiNCs are normally collected on stainless steel mesh, Si wafers, glass slides, or TEM grids. The selected characterization technique dictates the type of substrate used in a specific experiment.

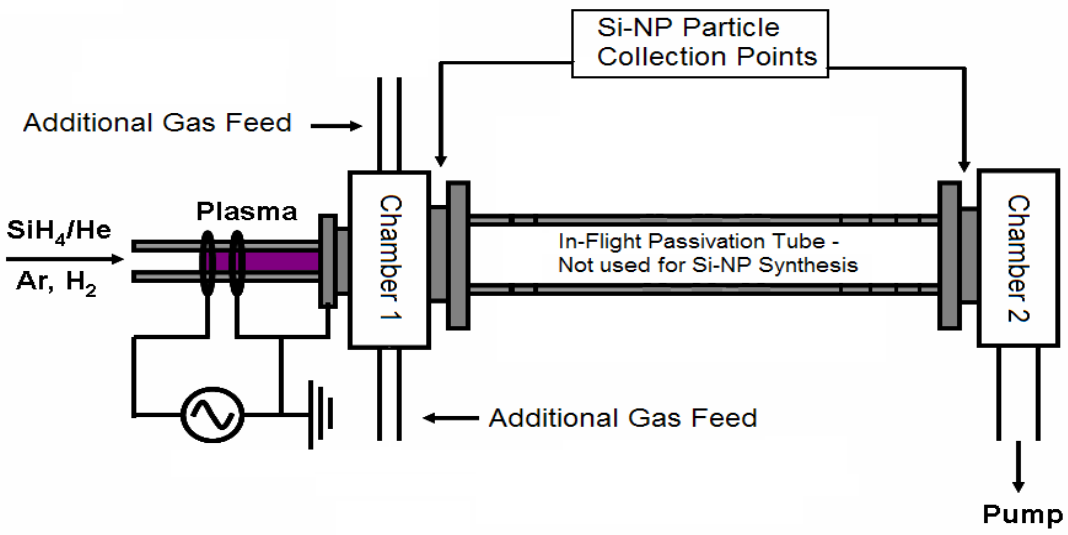

Figure 2.3: Basic system schematic and experimental setup of the SiNC in-flight passivation system. This setup is used to fabricate untreated or bare SiNCs.

2.3 Gas-Phase Thermal Nitridation

2.3.1 Experimental Setup

In-Flight Thermal Nitridation is one of the novel gas-phase passivation techniques which can be performed with this system. Figure 2.4 displays the basic experimental

setup for this process. The first part of this setup is exactly the same as the configuration used to make SiNCs. The only changes in this system are the addition of a Lindberg/Blue M tube furnace and a 5% ammonia (NH_3) in N_2 gas line. The SiNCs are collected after they pass through the tube furnace.

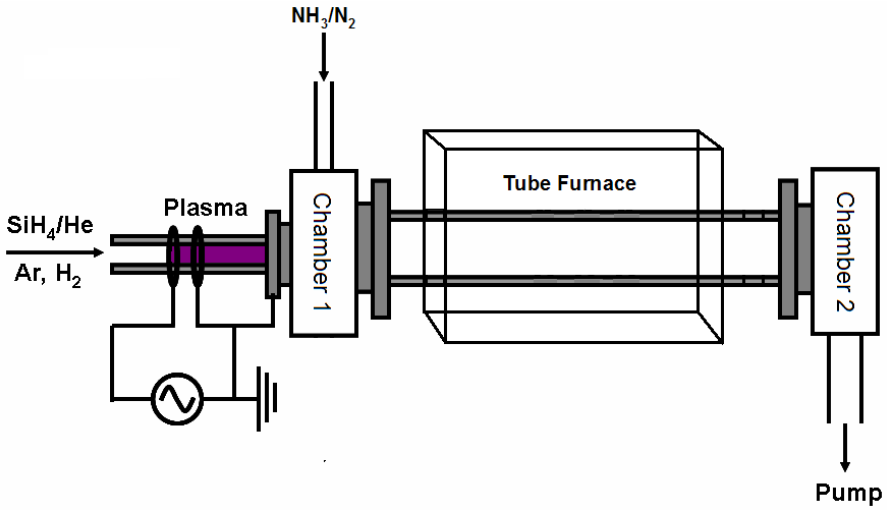

Figure 2.4: System schematic of the SiNC in-flight passivation system when a thermal nitridation process will be used to passivate the SiNCs.

The operation of this experimental setup is straightforward. The SiNCs are first created in the procedure described in section 2.2. After the SiNCs leave the first plasma, they cross the orifice which accelerates them into the second tube (quartz, 25 mm OD). Experiments have shown that without the orifice in the system no particles are collected. More importantly, the added acceleration of the SiNCs due to the pressure drop between the synthesis plasma (≈ 3 torr) and the rest of the system (≈ 300 mtorr) is crucial in this setup because many NCs can be lost to the chamber walls and the gas flow.

The thermal nitridiation process is operated at a temperature of approximately 800 ^{o}C, the point at which ammonia decomposes. [89] Since a pure ammonia source is not

used in the experiment (rather 5% NH_3 in N_2 is used), several different flow rates were investigated in order to determine how much ammonia was needed for this process.

Once ammonia decomposes, free nitrogen atoms can react with dangling Si bonds at the surface of the SiNCs forming a silicon nitride passivation layer on the surface.

2.3.2 Results and Discussion

In order to verify if a passivation layer was formed on the surface, several types of characterization was performed on the NCs. Figure 2.5 provides the TEM bright field image of thermal nitrided SiNC, while the inset shows the corresponding diffraction pattern.

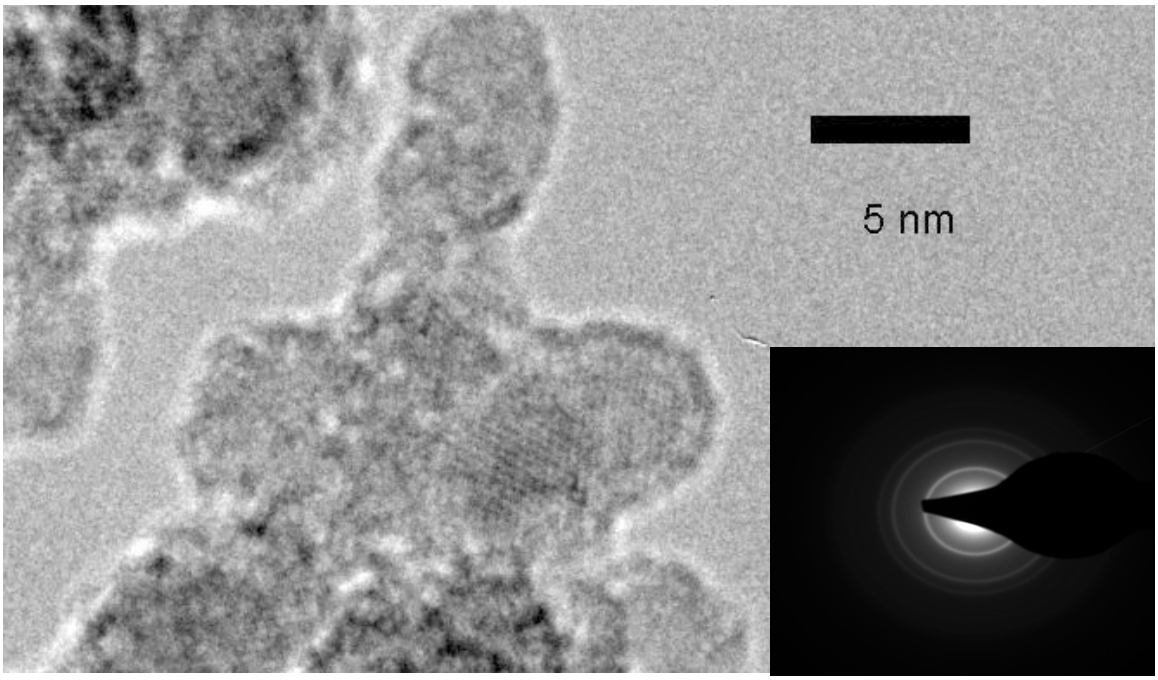

Figure 2.5: (a) TEM bright field image of thermal nitrided SiNCs. The scale bar is 5 nm. Inset: Thermal Nitrided SiNC diffraction pattern.

Studying Figure 2.5 one notices several interesting features. First of all, it appears that NCs still exist after the nitridation process. Crystalline facets can be seen in the TEM image. Secondly, it appears that there is a shell around the SiNCs. It is difficult from this image to conclude that this shell is the result of the nitridation process, or a result of oxygen exposure. Other characterization methods need to be used in order to validate that a nitride passivation process worked as designed. Examining the inset of Figure 2.5, we observe rings in the diffraction pattern which indicates that both crystalline and polycrystalline NCs are generated.

FTIR was utilized to better understand the surface chemistry of these NCs. Figure 2.6 displays an FTIR spectrum (taken from a Nicolet Magna-IR 750 FTIR Spectrometer) from untreated SiNCs and thermal nitrided SiNCs. Examining the three FTIR spectra one notices several differences and similarities. First of all, the two spectrums related to nitrided NCs have large peaks near 1070 cm^{-1}. These are peaks are due to the stretching mode of Si-O-Si [90], indicating that in both cases the NCs were exposed to oxygen. The bare SiNCs (which were collected in a glove bag) exhibit a weak peak at ≈ 1070 cm^{-1} indicating little oxide growth on the NC surface. Further evidence of oxidation from the nitride passivated NCs can be seen in the emergence of oxidized hydride peaks (O_2SiH_2 ≈ 2175 cm^{-1}, O_3SiH ≈ 2250 cm^{-1}), O-related peak at ≈ 980 cm^{-1} and the broad stretch that spans from 3500 cm^{-1} to 3000 cm^{-1}. [91-95] This stretch, which is observed in both spectrums from the nitrided NCs, is most likely due to N-H, O-H, or Si-OH stretches. [96] The presence of O in the nitrided NC samples is not surprising, because the

NCs were not collected in a glove bag and several hours elapsed before they were transported to the FTIR for analysis.

Both the bare SiNCs and nitrided NCs also exhibit SiH_x stretches. This is not surprising given the synthesis method in a SiH_4 plasma. With respect to the bare SiNCs, the band near ≈ 2110 cm^{-1}, associated with Si-H stretching in SiH_2, is the most intense peak in the spectra followed by bands attributed to SiH_3 (≈ 2136 cm^{-1}) and SiH (2095 cm^{-1}). [92, 97] The SiH_x stretch of the nitrided NCs is reduced in intensity. This may be due to the nitride passivation process.

As stated above there are also some notable differences between the two FTIR spectra. First of all, the bare SiNC exhibit strong doublet peaks between 850 and 900 cm^{-1}. These peaks are attributed to the bend-wag deformation modes of SiH_2 and SiH_3. [92, 97]

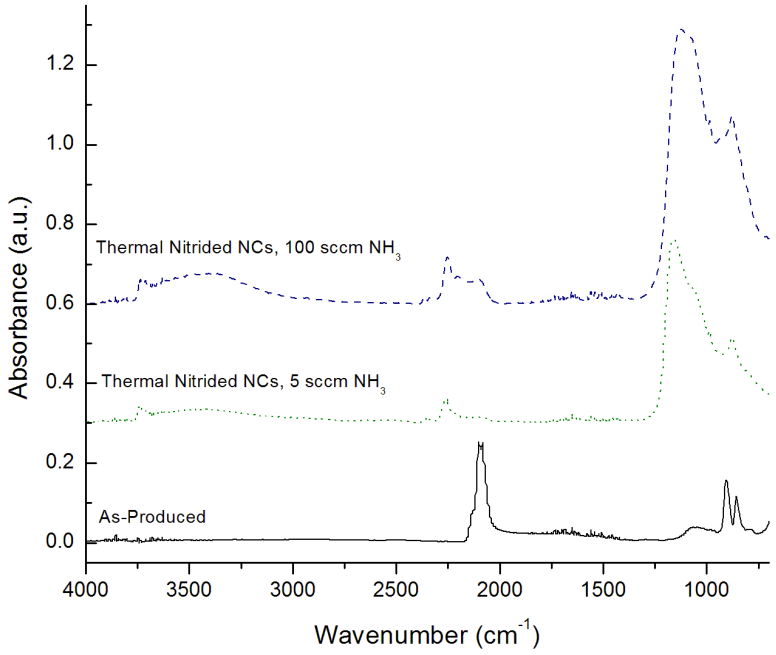

Figure 2.6: FTIR of as-produced and thermal nitrided SiNCs.

Similarly, the nitrided SiNC FTIR spectrum has peaks that do not appear in that of the untreated SiNCs. As stated before, both samples have a Si-O-Si stretch ($\approx$ 1070 cm^{-1}). Peaks at wavenumbers of $\approx$ 1140 cm^{-1}, $\approx$ 865 cm^{-1}, and $\approx$ 912 cm^{-1} appear to be unique to the nitride process. The three absorption peaks that appear in the thermal nitride FTIR spectrum are difficult to identify. The peak at 865 cm^{-1} may be due to oxidized hydrides [92], Si-N stretch in Si_3N_4 [99] or to a Si-N stretch in Si-N with H incorporated [100] in the NC structure. However, from the discussion above, we know that SiH_x deformation occurs in this region as well. As a result, it is difficult to identify this peak. The absorption peak near 912 cm^{-1} could be the result of Si-N stretches in SiO_xN_y. [101-103] The absorption peak at 1140 cm^{-1} is even more difficult to identify. This peak could be related to Si-O in Si_3N_4 [101], Si-O in SiO_xN_y [101], Si-O [100], or N-H bending in Si_3N_4 [99, 100, 103-105].

The variation that is observed in the two FTIR spectra indicate that the structure (i.e. molecular components, compounds, functional groups) of the bare and thermal nitrided NCs are different. However, FTIR does not give us any conclusive information about what is exactly happening at the surface of the SiNC. In order to determine whether or not a passivation layer is being formed on the SiNC, surface characterization must be used.

Surface characterization was carried out on the bare and nitrided SiNC using a Physical Electronics Model 550 X-Ray Photoelectron Spectrometer. Figure 2.7 provides a typical XPS spectrum of untreated SiNCs. Four peaks are readily identifiable. These correspond to the Si 2s and 2p, C 1s, and O 1s states. Figure 2.8 displays an XPS survey

spectrum from thermal nitrided SiNCs. Peaks due to Si 2s and 2p, N 1s, C 1s, and O 1s are observed. The most significant difference between the two spectra is the strength of the carbon peak. In the untreated SiNC sample, a large carbon peak is observed. This is most likely due to contamination (pump oil, air exposure) at the surface. [106] However, the carbon peak of the nitrided SiNCs is much weaker.

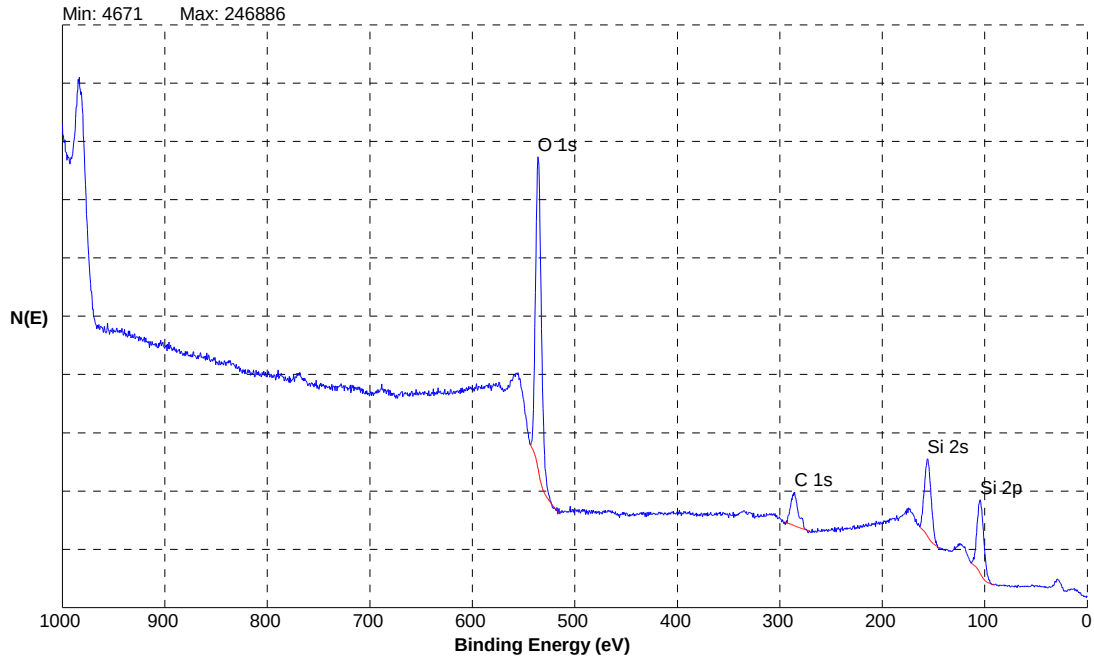

Figure 2.7: XPS Survey Spectrum from Untreated (Bare) Silicon Nanocrystals.

There is also an identifiable nitrogen peak in the spectrum. It is possible that due to the fact that a passivation layer was grown on the surface. If that explanation is accepted, then the formed Si-N bonds must be more resistant to carbon insertion from various air-borne contaminants than the Si-H bonds present on unpassivated particles. However, this may also be due to how the samples were handled. It is difficult to make a definitive conclusion on why carbon peak in the nitrided SiNC signal is reduced. However, the presence of nitrogen indicates that a Si-N passivation layer may have formed at the

surface. This should not be taken at face value. HR scans and atomic concentration calculations suggest that there is a trace amount of nitrogen at the surface. As a result, we may not be growing a thick "enough" passivation layer to protect the SiNCs from oxidation. Again, this is not surprising. Even stoichiometric silicon nitride is known to form a thin native oxide when exposed to air. [107] In this case however, it appears that the nitride layer is so thin that the entire layer is oxidized during the process.

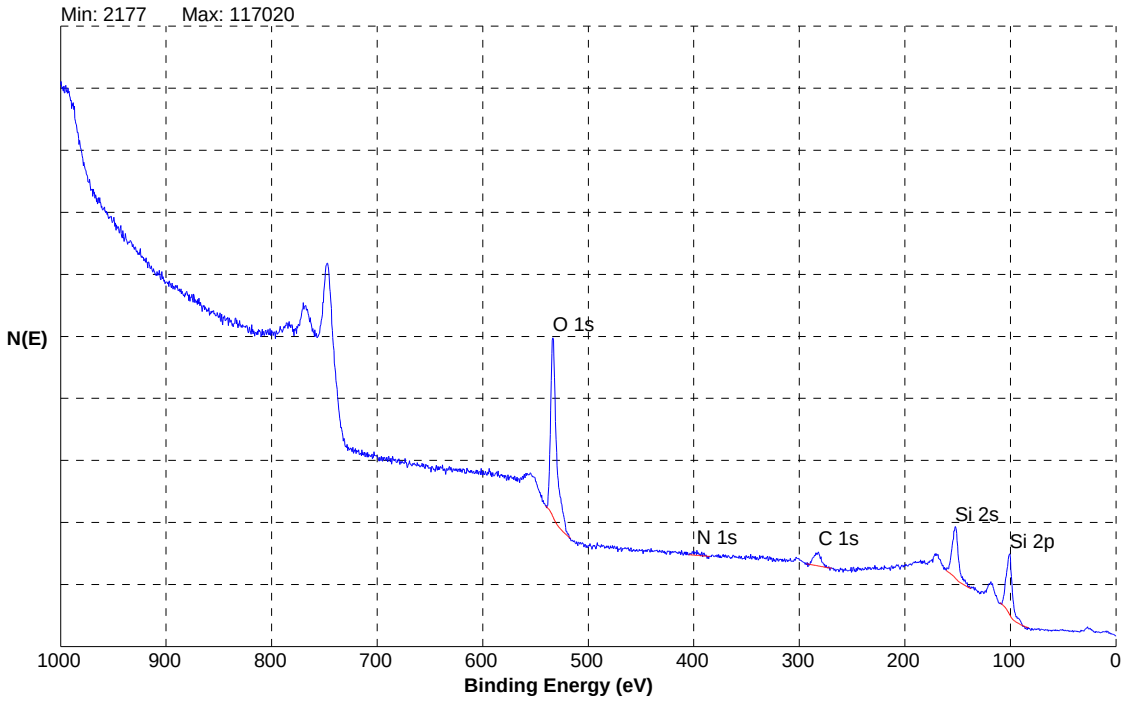

Figure 2.8: XPS Survey Spectrum from Thermally Nitrided SiNCs.

The thermal stability of the untreated and nitrided SiNCs was investigated. It was observed that once SiNCs were heated to a temperature of approximately 250ºC, the PL ceased. In order to verify this claim, this experiment was carried out in four different apparatuses. First, this experiment was performed in air on a hot plate. While the sample was heated the sample a UV lamp (365 nm emission wavelength) was used to irradiate

the sample causing PL. As previously observed, the PL of both the untreated and nitrided SiNCs ceased at about 250ºC. Similar results were seen when the particles were heated in air in a furnace. In order to verify if air was the cause of this problem, this experiment was performed in the Plasma Therm 340 Plasma Enhanced Chemical Vapor Deposition System (PECVD) and the XPS. The PECVD was chosen because it had the capability of heating the samples under a nitrogen (or vacuum) atmosphere at a low pressure, 300 mtorr – 1.20 torr. Even at these lower pressures, the same trend was observed; the PL of both the untreated and nitrided particles ceased at approximately 250ºC. The same experiment was run on the XPS. Due to the nature of the XPS, both the PL and the surface of the SiNCs were investigated simultaneously. Unfortunately, only untreated SiNCs were investigated due to equipment problems with the XPS. However, the same trend was observed again at pressures of 10^{-8} torr. The PL was quenched at 250ºC and the only changes seen in the XPS spectrum was an increase in the oxygen signal and a decrease in the carbon signal. Heating the sample appears to provide a cleaner SiNC surface, because of the removal of surface contamination. The loss of PL is generally associated with the creation of nonradiative recombination pathways. Since the only difference in the XPS spectrum was the reduction of carbon, it is tempting to correlate the two observations. One might suppose, for example, that chemically absorbed carbon is released, perhaps through a reaction with H or O, and leaves behind an unsatisfied bond. The fact that the process is independent of ambient suggests that it does not depend on the arrival of gas molecules. It is likely that the SiNC has a significant amount of H incorporated, both on the surface and in the "bulk". Of course, they also have oxygen on

the surface once they are exposed to air. More work will be needed to definitively establish the mechanism.

The optical properties of the thermally nitrided SiNC were also investigated. PL measurements were taken on the SiNC once they PL. This is important. Normally, with untreated SiNC it takes roughly a day for them to PL. It is believed that all of the dangling bonds and non-radiative states at the particle surface must be passivated in order for the particles to PL. However, this is drastically different with the thermal nitrided SiNC. After 5-7 days in air, the nitrided SiNCs PL in the red. This result indicates that the particles are passivated with silicon nitride, but since they eventually luminesce, oxidation still occurs. Therefore, the thermal nitride process passivates the SiNCs, but only to a degree. Perhaps there some dangling bonds still exist at the surface from which oxygen can bond. The formation of the surface oxide is retarded by the nitride, but eventually reaches the silicon surface to allow the PL.

2.4 LPCVD Gas Phase Nitridation

2.4.1 Experimental Setup

This setup is very similar to the in-flight thermal nitridation process except for one major difference. In the synthesis plasma, silane is completely exhausted. Therefore, SiH_4 does not exist anywhere else in the system. In order to run a LPCVD process, which is the standard microelectronic film growth process for silicon nitride, an additional silane gas feed is needed. The LPCVD setup is illustrated in Figure 2.9. This setup resembles the two previous setups. The only difference in this setup is that a

second SiH_4 gas line is fed into the system after the NC synthesis stage. The ratio of NH_3 to SiH_4 in the furnace determines the stoichiometry and therefore the stress of the deposited film. It is important to note that two different SiH_4 mass flow controllers and lines were used in this process. We needed to create the SiNCs under the standard conditions while adding more SiH_4 into the system for the LPCVD. LPCVD processing usually occurs at temperatures between 800ºC – 900ºC and low pressures (< 20 mtorr). [108-110] We mimicked the gas flow ratios of NH_3 to SiH_4 used in standard microelectronic processing during our experiments.

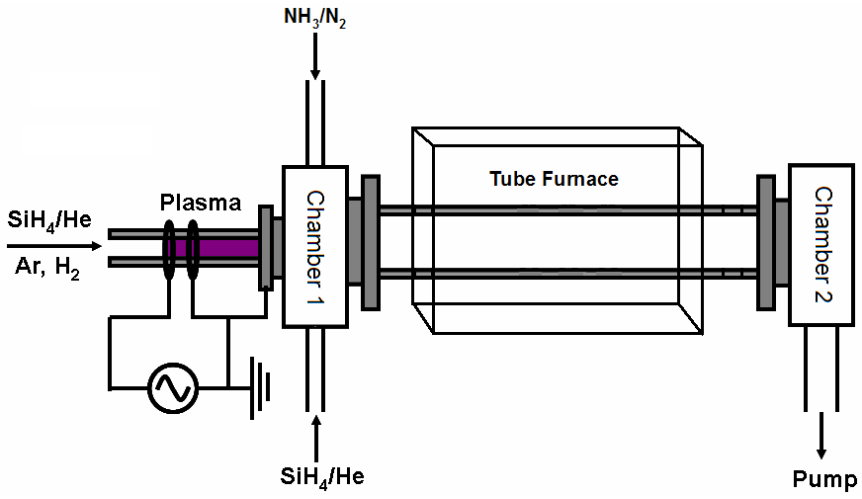

Figure 2.9: System schematic of the SiNC in-flight passivation system when LPCVD nitridation is used to passivate the SiNCs.

Typically dichlorosilane (DCS) SiH_2Cl_2, is used as the silicon precursor for LPCVD processing. Due to the fact that the experiment is not in a clean room environment with an extensive control system which handles the neutralization of the effluent from chlorine containing precursors, SiH_4, not DCS, was used.

2.4.2 Results and Discussion

Despite the differences in the experimental setup, similar results were observed. Figure 2.10 presents three FTIR spectra: 2 LPCVD and 1 thermal nitride. The difference in the two LPCVD experiments was the ratio of SiH_4 to NH_3 in the reaction tube. Trace A presents the FTIR spectrum of a LPCVD run with a 1 SiH_4 to 6 NH_3 ratio, where as trace B is the FTIR spectrum of a LPCVD run with a 1 SiH_4 to 4 NH_3 ratio. Trace C provides an FTIR spectrum from the thermal nitrided SiNCs. Examining Figure 2.10 one notices that while the FTIR plots of all three experiments are similar, there are some differences.

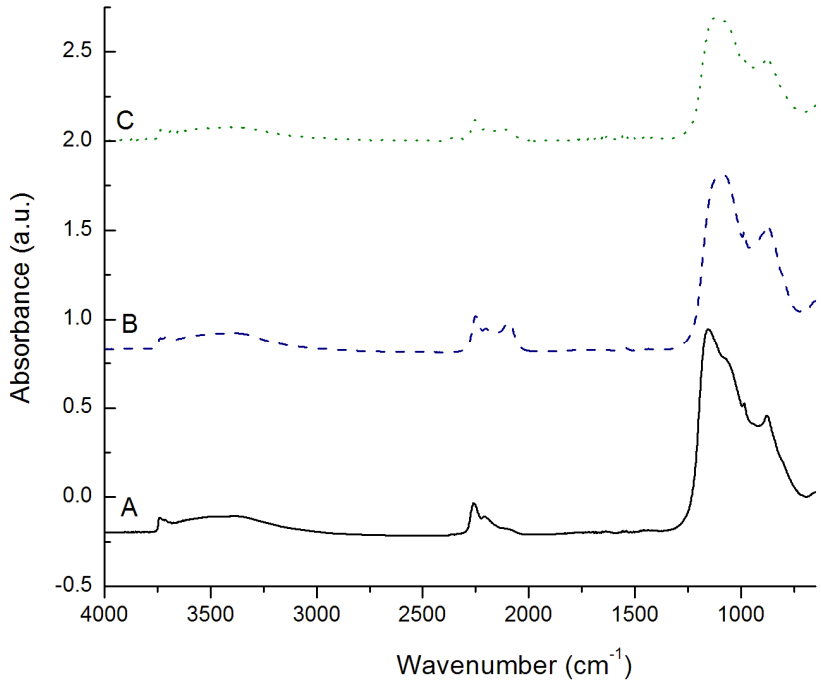

Figure 2.10: FTIR spectra of (A) thermal nitrided and (B-C) LPCVD nitrided SiNCs

For example, the SiH_x absorbance peak at 2100 cm^{-1} is much stronger for traces B and C. The peak at 2100 cm^{-1} is almost non-existent in trace A. Another significant difference

can be seen in the Si-O-Si stretching region of the FTIR spectra. Investigating the data one notices that the FTIR plots are almost identical, except for the peak at 1160 cm^{-1} that occurs in trace A. Examining the literature, this peak seems to correspond to N-H bending in Si_3N_4. [101] Since there is more nitrogen available when the SiH_4 to NH_3 ratio is 1:6 this may cause the observed peak shift. However, it is difficult to make this conclusion without other evidence. Nevertheless, the FTIR spectra presented in Figure 2.10 indicates that the structure of the LPCVD and thermal nitrided SiNCs are different than untreated SiNCs.

TEM and XPS results on the LPCVD treated SiNCs mirror the results obtained from the thermally nitrided SiNCs. TEM images of LPCVD treated SiNCs reveal a shell-like structure surrounding the crystalline SiNCs. Diffraction experiments also prove that the LPCVD treated SiNCs are a mixture of crystalline and polycrystalline material. XPS results show a trend that resembles that of the thermal nitrided SiNCs. Peaks due to Si 2s and 2p, O 1s, N 1s, and C 1s are observed in XPS spectrum. Furthermore, a weaker carbon peak (compared to that of untreated SiNCs) is observed. This is consistent with the thermal nitridation results.

Thermal stability tests, similar to the ones previously discussed, were carried out on these NCs as well. Similar results were observed. Once the temperature reached 250ºC, the PL of the LPCVD nitrided NCs ceased. This was observed on three of the four testing apparatuses. Thermal stability tests were not able to be carried out in the XPS system due to equipment issues, but the results from the PECVD setup (300 mtorr) indicate that the same trend, no PL after 250ºC, will be seen in the XPS. It appears that

pressure or air does not play a role in the quenching of the PL at temperatures greater than 250ºC.

2.5 Conclusions

In this chapter two processes for gas-phase silicon nanocrystal passivation utilizing nitride passivation was introduced. Both thermal and LPCVD passivation schemes were discussed. FTIR characterization was performed on as-produced NC, and NCs passivated using thermal and LPCVD nitridation processes. The bare SiNCs exhibit a similar surface structure to that of nitride passivated NCs with a few notable differences. The bare SiNCs have distinct SiH_x stretches where the nitride passivated NCs have significantly reduced SiH_x peaks. Furthermore, the nitride passivated NCs have peaks that relate to Si-N bonds. XPS analysis validates the information obtained by the FTIR, but the N atomic concentration is extremely low, indicating only a small amount of the atoms at the surface of the NCs actually are bonded to N. Further study on the PL and thermal stability of the NCs provide insight into NC properties. NCs passivated by either O (bare NCs) or N lose their PL when heated in N_2, air, or vacuum to 250°C. N passivated NCs PL in the red after 7 days. Although a "shell" is observed on the TEM, it appears further air exposure leads to O incorporation in the N passivation layer, leading to the PL observed from the NCs.

Chapter 3

Gas Phase Passivation and Etching with CF_4

3.1 Chapter Overview

This section of the thesis focuses on the gas-phase passivation and in-flight etching of plasma-synthesized silicon nanocrystals (SiNCs) using a standard silicon etchant, carbon tetrafluoride (CF_4). The chapter will discuss the process used to etch the SiNC as well as the apparatus utilized. A significant amount of characterization was performed on these etched NCs and this will also be described in section. In particular, we will discuss the optical properties, tunability and lifetime (of generated carriers) of the CF_4-etched NCs. The surface (or passivation) structure of the NCs will also be discussed, specifically FTIR and XPS results. The crystallinity of the NCs both before and after the CF_4 passivation was studied by HRTEM and associated diffraction. The majority of this work presented in this chapter has been published elsewhere [111, 112].

3.2 Experimental Setup

The in-flight CF_4 Silicon Dry Etching/Passivation process is drastically different than the two nitridation processes discussed in chapter 2. In this configuration, no tube furnace is used. Rather, a dual capactively-coupled plasma arrangement is used. The first plasma is used to synthesize the SiNCs, where as the second plasma is used to etch

the SiNCs to smaller sizes in-flight while passivating the surface with a fluorocarbon film. As with the other two setups, all of this processing is performed in the gas phase while the NCs are in-flight from the synthesis tube to the collection point which occurs after the second plasma for this experiment.

Figure 3.1 provides the basic system setup of the CF_4 passivation approach. The first plasma is operated with the same precursors that were used in the nitride passivation. Typically the gas flow rates in the synthesis plasma are: 50 sccm Ar, 2-10 sccm of SiH_4/He, and 1-4 sccm H_2. These flow rates keep the pressure in the first plasma reactor between 3-4 torr which yields approximately 4-7 nm SiNCs. After the SiNCs leave the synthesis reactor they enter the second plasma reactor. In this reactor the SiNCs are etched to a smaller size (via the removal of volatile SiF_2 or SiF_4) and passivated with a fluorocarbon or Teflon "like" coating.

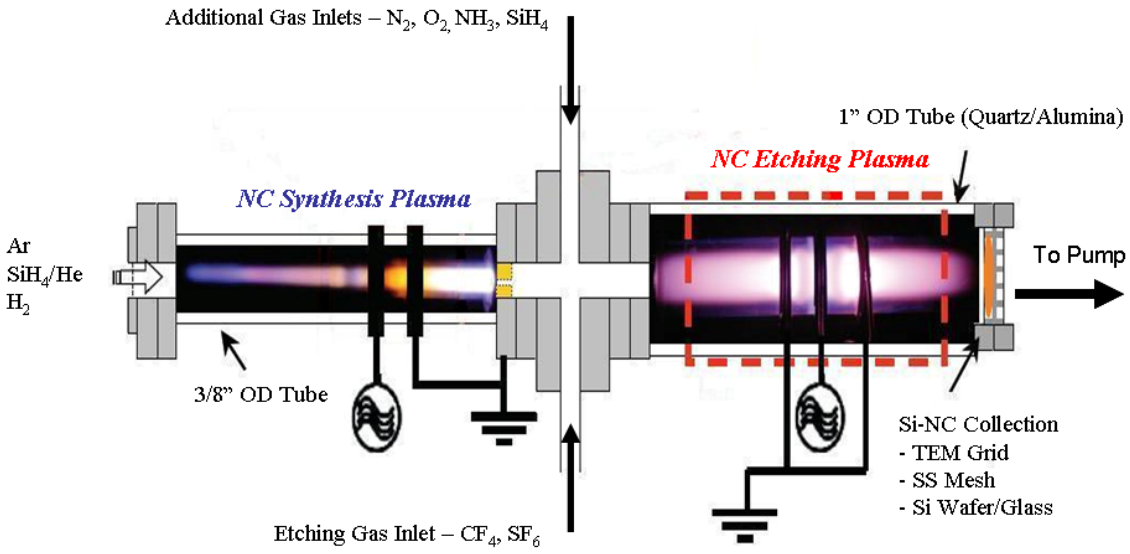

Figure 3.1: Novel dual plasma reactor used for gas-phase SiNC Synthesis and in-flight passivation/etching with CF_4.

The etching process, which was adapted from standard silicon dry etch processes, utilizes two additional gases fed into the system after the synthesis stage. CF_4 and H_2 are used to etch and passivate the SiNCs. These two gases are disassociated in the second plasma creating hydrogen, carbon, and fluorine radicals and other species. The fluorine radicals are known to etch silicon. Therefore, the larger the concentration of available fluorine radicals in the second plasma, the greater the etch rate. However, there is a limit on the etch rate. During etching with CF_4, a fluorocarbon forms on the surface of the SiNC. The fluorocarbon is generated by the CF_2 radicals from the CF_4 plasma. [113, 114] Once the thickness of this fluorocarbon reaches approximately 25Å the etching ceases. [113-119] One way to counteract the formation of the fluorocarbon is to feed O_2 rather than H_2 into the etching plasma. Adding in O_2 into the plasma leads to the formation of volatile products CO and CO_2 causing an increase in the etch rate. [120, 121] Since the O scavenges the C, this inhibits the growth of the fluorocarbon on the surface. This approach was set up on the experiment illustrated in Figure 3.1. Although NCs were produced, no visible PL was observed from these samples. As a result, we decided to use H_2 to control the etch rate and use the fluorocarbon as a passivation layer.

The etch rate of the SiNCs can be controlled by the addition or subtraction of H_2. [113] This is not the H_2 source that is used in the first plasma to H-passivate the NC surface to prevent agglomeration. Rather a second H_2 gas line with a separate mass flow controller unit is used. By increasing the amount of H_2 in the second plasma, the etch rate is decreased because the fluorine radicals in the second plasma will bond with the free hydrogen (forming gaseous HF). Thus as the H_2 flow rate is increased, more

gaseous HF is formed, reducing the amount of free fluorine radicals left to etch the SiNCs. Figure 3.2 shows the dependence of the silicon etch rate on the mixture of CF_4 and H_2 in the etching of silicon substrates. Examining the figure one realizes that as the amount of H_2 is increased, the etch rates falls drastically. This trend is also observed in the dual plasma setup. As the H_2 concentration is increased, the PL of the SiNCs red shift. This is expected because less etching will occur due to the increased concentration of H_2 in the etch plasma. Therefore, by carefully controlling the CF_4/H_2 ratio, SiNCs that PL in the entire visible spectrum can be synthesized.

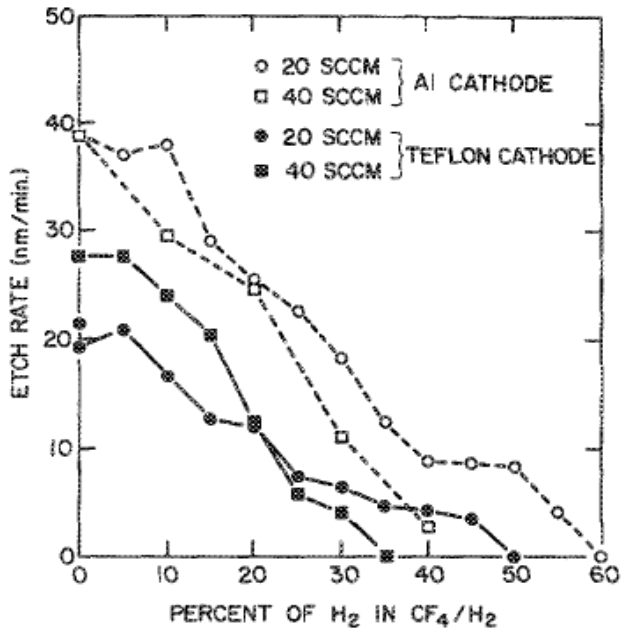

Figure 3.2: CF_4 Etch Rate of Planar Silicon as a function of added H_2 in a CF_4/H_2 discharge. Reproduced from [113].

The process run times for the CF_4 in-flight passivation depend on the size of the NCs that needs to be fabricated. For example, the system makes approximately 10 mg/hour of material when only making bare SiNCs (no in-flight passivation) under

standard conditions – 50 sccm Ar, 7 sccm SiH_4/He, and 1-4 sccm H_2. Once the etch process begins this figure drops to about 3 mg/hour. For extremely small SiNCs (< 2.5 nm diameter) run times of up to 4 hours may be needed to collect enough material to see visible PL. NCs may be lost to the reactor tube walls, to thermophoresis, or they may simply follow the gas flow streams into the exhaust. Because of these long process times and loss of SiNCs, additional collection schemes such as electro-assisted deposition may be needed to help increase the system production yield if commercial use of the SiNCs is considered.

After the synthesis and etching process is completed, the SiNCs can be left on the deposition substrate (typically a SS Mesh or Si Wafer) or placed in an ultrasonic bath to dislodge the SiNCs off of the substrate. The SiNCs then can be transferred into an organic solvent (methanol, etc.) for characterization. Whether the material is simply analyzed in powder form or is placed into a solvent depends on the type of characterization that will be performed. For example, the SiNCs are suspended in an organic solvent when using ATR-FTIR (Attenuated Total Reflection – Fourier Transform Infrared Spectrometry). However, when performing XPS measurements the SiNCs are drop coated onto a silicon substrate which has been processed with an Au/Cr top layer and an Al back contact to minimize charging effects which arise from the insulating fluorocarbon coating on the surface of the NCs.

3.3 Etching Mechanism

Flamm in *Plasma Etching: an Introduction* [122] provides a simple yet through model of silicon etching by F atoms. Although this particular model might not be the most accurate for the CF_4 etching of NCs, due to the fact that C, O, and H are present in the etching plasma, it does provide a simple explanation of the etching process on Si substrates. Figure 3.3 provides a schematic of the etching process as described by Flamm and Manos.

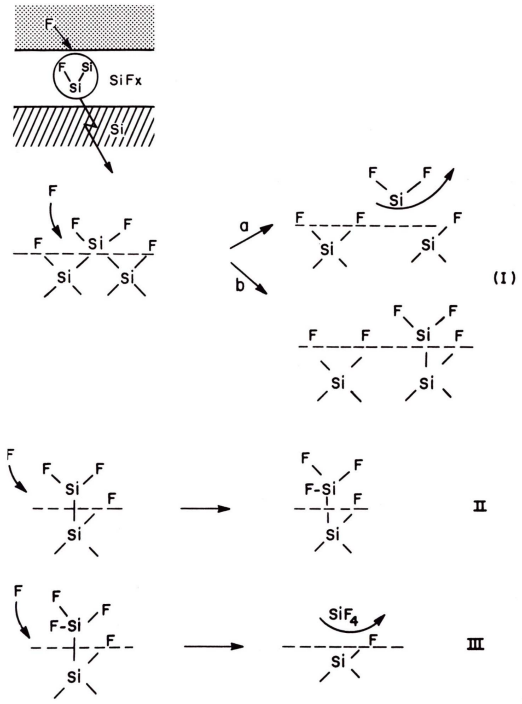

Figure 3.3: Proposed silicon etching mechanism of Si by formation of SiF_x and subsequent removal via volatile SiF_2 and SiF_4. Reproduced from [122].

Upon initial exposure to atomic F, a SiF_x layer is formed on the silicon substrate. Further F exposure leads to process (I) shown in Figure 3.3. If (a) occurs, the F atom breaks the Si-Si bond (near the interface between the Si substrate and SiF_x layer) and leads to the

release of volatile SiF_2. However, (b) can occur as well, were F breaks the Si-Si bond, but does not create a volatile product. Rather the broken bond is then passivated by another F atom. Etching can also be carried out through the combination of processes (II) and (III). First, in process (II) a stable SiF_3 group (bonded to another Si atom) is formed when a Si-Si bond is broken and F passivates the dangling bond. Following this step, in process (III), another F atom severs the final Si-Si bond and the broken bond is passivated by F, leading to the formation of the volatile product SiF_4. It is possible that this is the primary etching mechanism in the CF_4 passivation plasma. However, many chemistries can be generated in the NC etching plasma making it difficult to definitively identify the dominant etching mechanism. Therefore, this mechanism is presented as one possibility.

3.4 Characterization of CF_4-Etched NCs

3.4.1 HRTEM

Before initiating a thorough investigation of the etched NCs, High Resolution Transmission Electron Microscopy (HRTEM, FEI Tecnai G2 30) was used to determine whether or not the SiNCs remained crystalline after passing through the CF_4 plasma. Figure 3.4 presents HRTEM images of NCs deposited on a TEM grid (a) before passivation (as-produced NCs) and (b) after passivation.

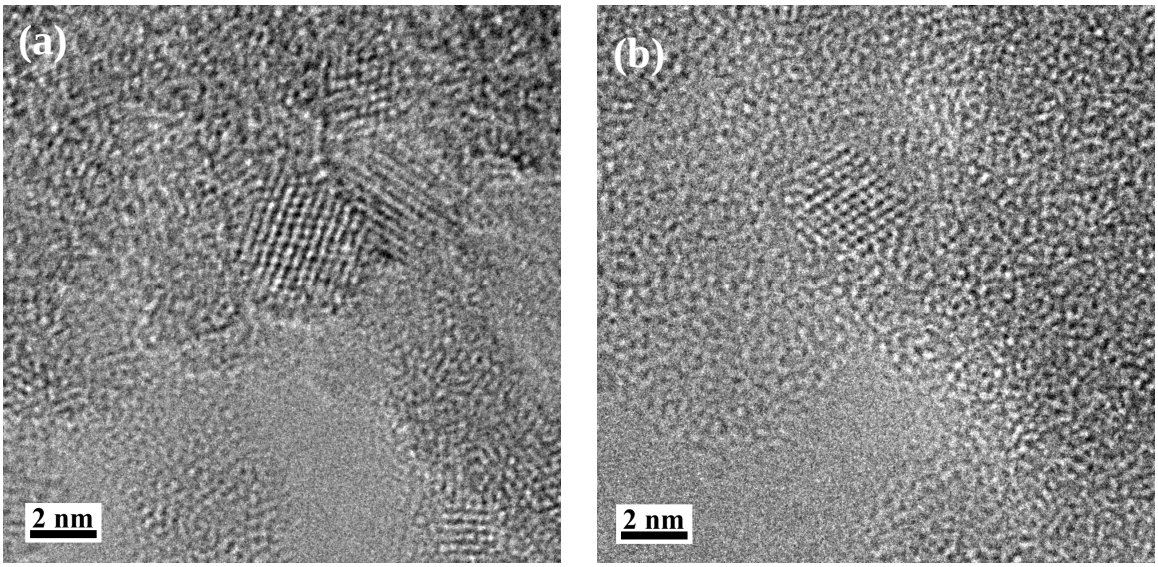

Figure 3.4: HRTEM images of (a) as-produced and (b) CF_4-etched SiNCs synthesized by the dual plasma reactor.

Lattice fringes with a spacing of 0.31 nm indicative of Si {111} are observable in both TEM images. This indicates that crystalline material exists after the CF_4 passivation process. It is important to point out, however, that the existence of crystallinity in some particles should not be taken as proof that all of the crystalline particles that enter the second plasma remain crystalline, nor that the remaining crystalline particles are undamaged. Indeed, it is not only possible but likely that ion impingement on the SiNCs in the etch plasma leads to some level of defect creation.

3.4.2 Surface Characterization

3.4.2.1 XPS Results

A physical electronics model PHI 555 X-ray photoelectron spectrometer (XPS) was used to study the surface chemistry of the CF_4-etched NCs deposited on SS Mesh.

Since the resolution of XPS is only on the order of 4-5 nm, we only observe the surface and a small portion of the bulk material. XPS does not detect H. For this reason, FTIR was also performed and will be discussed in the next section. The first step in performing an XPS analysis is to initialize a survey scan. A survey scan (using MgKα X-rays) sweeps over a range of energies at a low resolution. This survey provides the user with elemental identification and atomic concentration, but not chemical shift information. Chemical shifts, which are observed in high resolution (HR) scans, provide insight into the bonding arrangement at the surface of the NCs. Both of these techniques were utilized to study the etched NCs. XPS peaks assignments were determined with the help of two online databases: Lasurface [123] and the NIST XPS database [124].

Figure 3.5 displays a XPS survey spectrum from (a) as-produced and (b) CF_4-etched NCs.

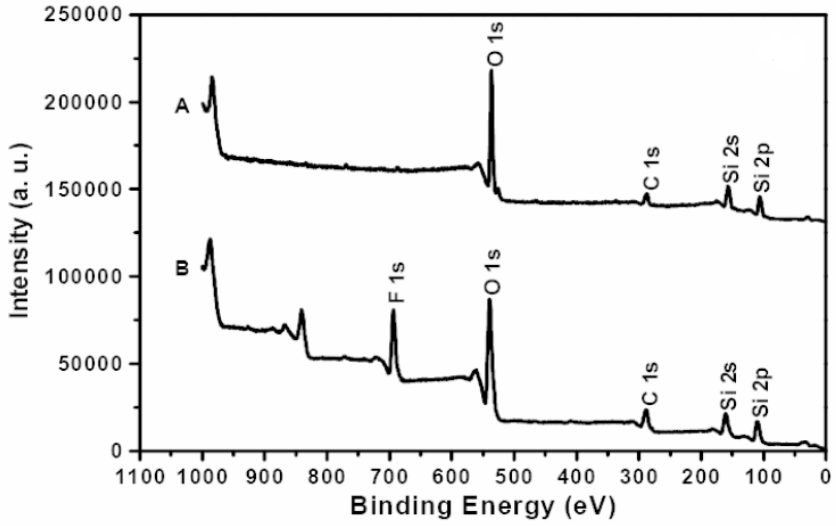

Figure 3.5: XPS survey spectra from (A) as-produced and (B) CF_4-etched SiNCs synthesized by the dual plasma reactor.

Figure 3.5 does not shed any light on the surface structure of either the bare or etched NCs. Rather, as stated above, it simply provides a fingerprint of what elements are present on the surface. Examining trace A (bare SiNC) one notices peaks related to Si, O, and C. The peaks related to Si and O should be present since we have SiNCs with an oxide shell formed upon exposure to air. The C peak is most likely due to contamination – either pump oil (from the system) or from air. C contamination is always observed in samples which have been exposed to air. The unlabeled peak near 1000 eV is an O KLL Auger peak. Auger transitions can be observed in XPS, but they are typically not used in analysis. Comparing the survey spectra of the bare NC to the etched NCs one notices three major differences: a F 1s signal near 690 eV, two F Auger peaks near 850 eV, and a increase in the C 1s signal. Since the etching process uses CF_4, it is not surprising that an increased C and F signal are observed. Based on [113-119], it is likely that a fluorocarbon film is deposited on the surface of the NCs and this leads to the increase in the C signal. The F signal is most likely due to the incorporation of F on the surface of the NC and as a part of the fluorocarbon. O is also still present on the surface of the CF_4-treated SiNCs. Oxygen is generated when the F radicals attack reaction tube leading to a release of O (We performed an experiment to validate this effect. The results of this experiment are presented in the chapter 4 of this thesis). This occurs because oxygen may easily diffuse through the fluorocarbon films and oxidize the underlying SiNCs in air at room temperature (inside of the vacuum system) even if there is a considerable fluorocarbon-film coating. [125]

Figure 3.6 provides XPS HR spectra of the Si 2p region for (a) as-produced and (b) CF_4-etched NCs.

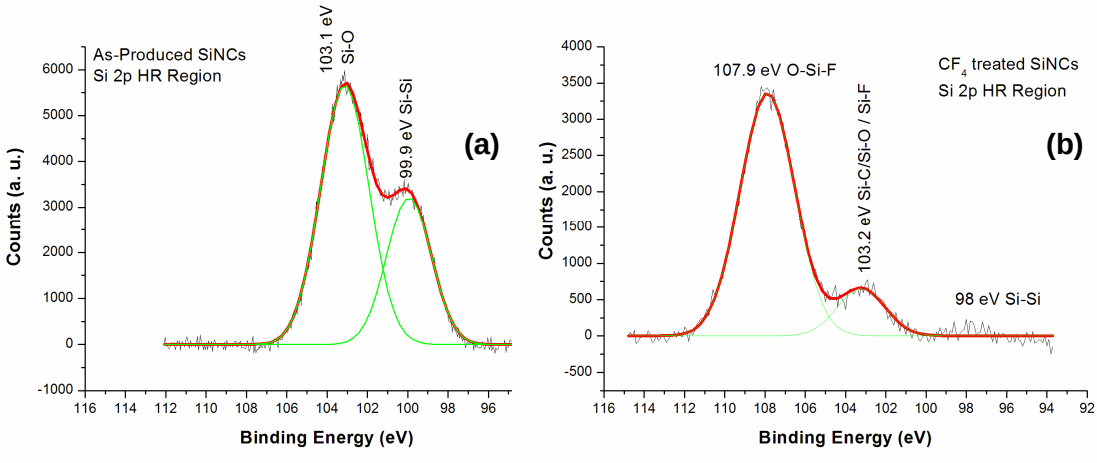

Figure 3.6: XPS HR scans from the Si 2p region for (a) as-produced and (b) CF_4-etched SiNCs. The solid lines are a Gaussian fit to the raw data.

Figure 3.6(a) is a typical HR scan for bare oxidized silicon. Two identifiable peaks related to Si-Si [126, 127] and Si-O [128] appear in the spectrum. From Figure 3.4(a) it appears that the SiNCs have oxidized quite a bit since the Si-O peak is much larger than the elemental Si-Si peak. A clean Si substrate would have a large elemental Si peak and a weak Si-O peak. The HR spectrum of the CF_4-treated NCs is significantly different. This is not surprising. The peak that appears near 108 eV is related to oxidized Si-F groups. A weak peak related to elemental Si is observed near 98 eV. Finally, a third peak at approximately 103 eV is more difficult to identify. This peak may be related to Si-O, Si-C, or Si-F. All three of these bonds may form at the surface of the NCs during the CF_4 process.

Figure 3.7 displays the O 1s HR survey scans of both (a) as-produced and (b) CF_4-etched NCs.

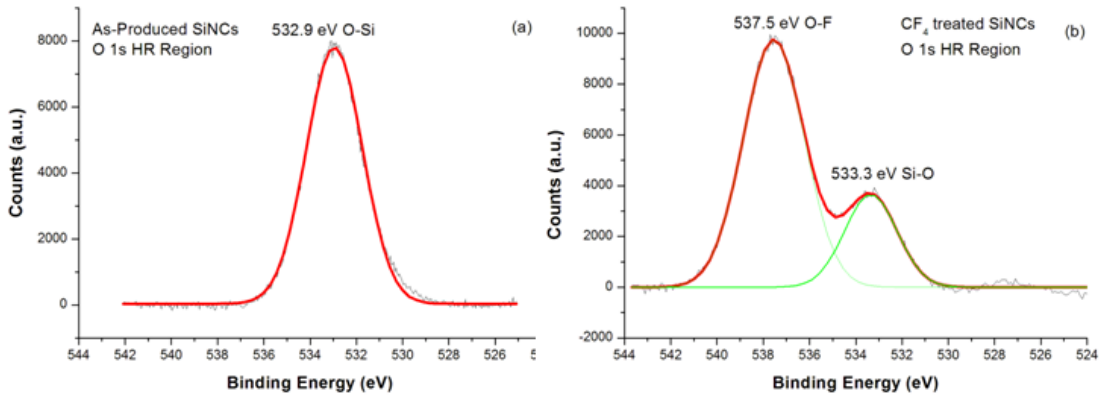

Figure 3.7: XPS HR Scans from the O 1s region of (a) as-produced and (b) CF_4-etched SiNCs. The solid lines are a Gaussian fit to the raw data.

Figure 3.7(a) displays the XPS spectrum from the O 1s HR region for bare oxidized SiNC. As expected, only 1 curve is observed. This curve is related to Si-O. In Figure 3.7(b) peaks corresponding to Si-O (similar to Figure 3.7(a)) and O-F are identified. The area under the O-F peak is much larger than that of the Si-O peak, indicating that there is a larger amount of O-F bonds at the surface of the etched NCs. However, since the Si-O peak is still present, some Si-O bonds exist as well. The origin of the Si-O peak could result from either air exposure where surface reorganization allows O to bond to Si atoms or due to O atoms which are released from the quartz reaction tube and may passivate Si dangling bonds inside the plasma system.

The C 1s spectrum of the etched NCs is provided in Figure 3.8:

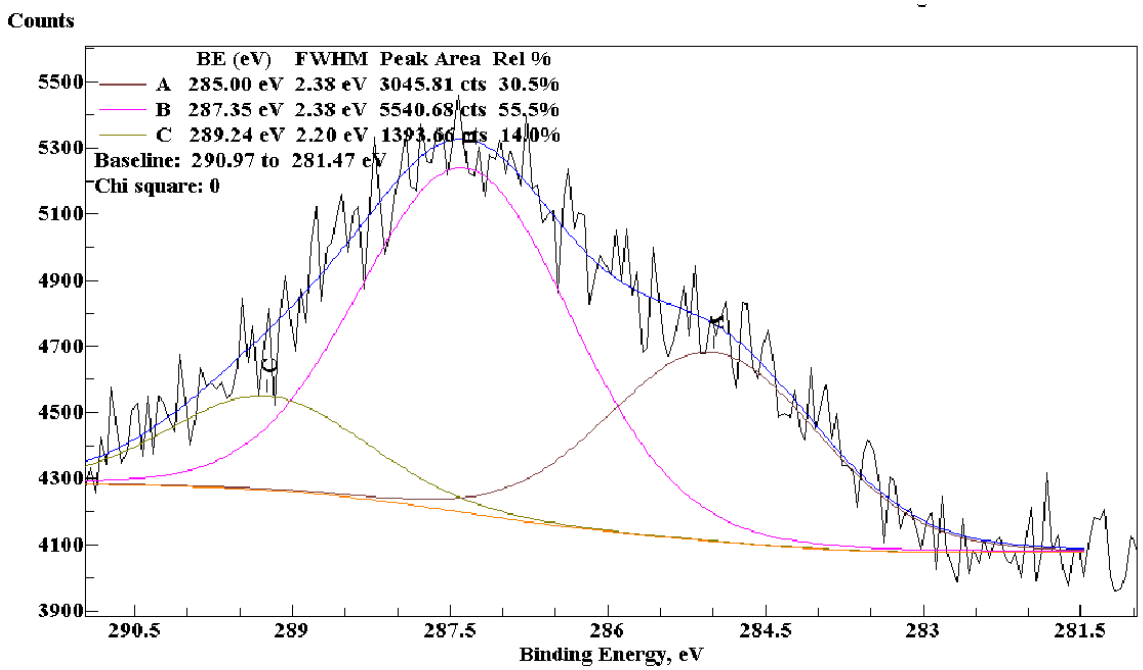

Figure 3.8: XPS HR Scans from the C 1s region from of CF_4-etched NCs. The solid lines are a Gaussian fit to the raw data.

These three peaks derived from the curve fit provide further insight into the surface structure of the etched NCs. The peak near 284.5 eV is C-C. [113, 129] This peak is always observed in C contaminated samples. However, since CF_4 is used as an etching source, it is impossible to rule out the idea that this peak may also be due to C from the CF_4 disassociation. Figure 3.9 displays peak assignments related to CF bonding groups. Examining Figure 3.9 and applying this to the data shown in Figure 3.8 the following assignments can be made. The peak at 287.3 eV may be associated with –CF bonding while the peak near 290 eV may be related to CF-CF_X bonding. [113, 129] It is important to note that also in this region peaks related to CO and COOH also appear. Once again, it is difficult to ascertain the exact surface chemistry of the NCs. Additional information is needed.

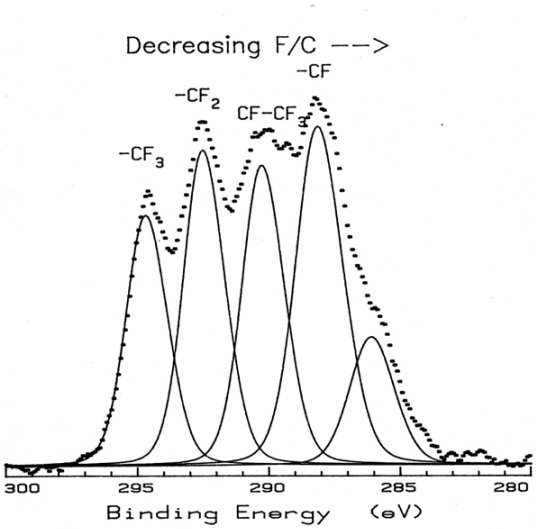

Figure 3.9: Fluorocarbon related bonding groups as a function of XPS binding energy. C 1s HR spectrum is shown. Image courtesy of Dr. John Thomas III.

Figure 3.10 provides the HR spectrum from the F 1s region:

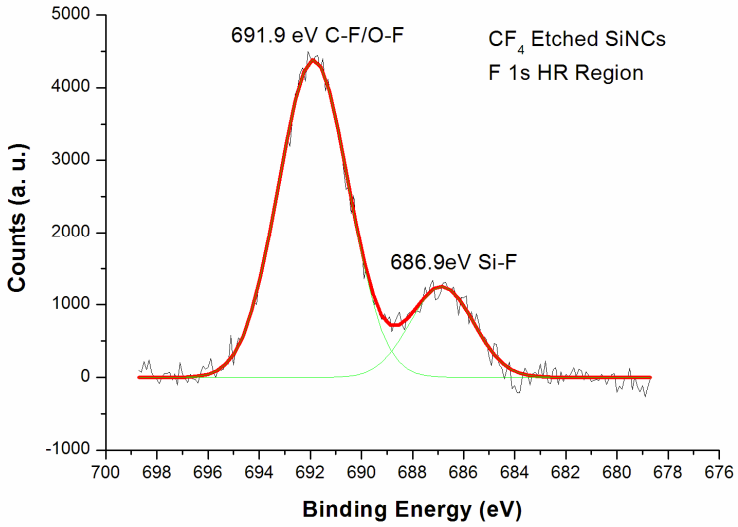

Figure 3.10: XPS HR scan from the F 1s HR region from CF_4-etched NCs. The solid lines are a Gaussian fit to the raw data.

Two peaks are readily identifiable from this scan. The first peak centered near 687 eV is believed to be related to Si-F bonds. [129] If the etching process occurs in the manner described by Flamm and Manos, then it is not surprising that Si-F is observed. Furthermore, F forms an extremely stable bond with Si; therefore if any dangling bonds are passivated with F they will be hard to be remove and thus will appear on an XPS scan. The other peak could be related to either O-F or C-F bonds [129]; however it is impossible to determine the correct assignment simply from this data. It is possible that either bonding arrangement could exist at the surface.

From the XPS analysis it appears that the surface of the CF_4-etched NCs is most likely comprised of an oxidized fluorocarbon. However, before making any further conclusions, we need to understand what is happening with the H at the NC surface and in the etching plasma.

3.4.2.2 FTIR

ATR-FTIR was utilized in order to further study the structure of the CF_4-etched NCs. Figure 3.11(a) shows the FTIR spectra of bare SiNC (A) and CF_4-etched NCs (B). The FTIR scans shown in Figure 3.11(a) are scaled to the region of interest. Peaks associated to SiH_x, CH_x and SiOH stretching also appear, but this information is of less interest. Therefore, the FTIR scans are scaled between 1600 and 800 cm^{-1}. The FTIR spectrum from the bare SiNCs, trace A in Figure 3.11(a), is nearly identical to the one presented in chapter 2. An Si-O-Si stretch is observed near 1070 cm^{-1} [90] and oxidized SiH_x deformation modes appear between 800 and 900 cm^{-1}. [91, 130, 131] Comparing

these spectra to that of the CF_4-etched NCs, trace B in Figure 3.11(a), one notices several differences.

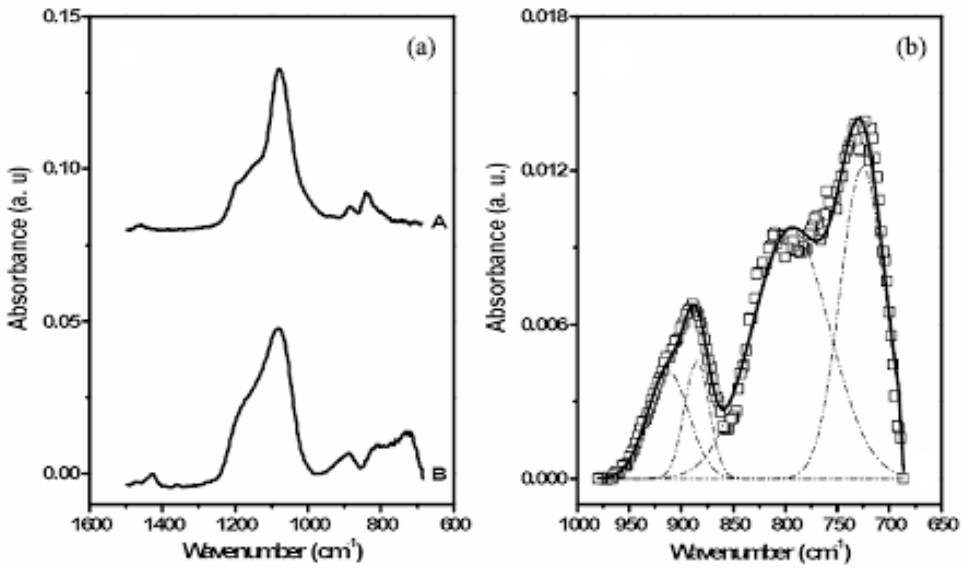

Figure 3.11: (a) FTIR spectra from as-produced and CF_4-etched NCs in the range from 600 to 1600 cm^{-1}. A: As-produced SiNCs. B: CF_4-etched SiNCs. Deconvolusion of spectrum B in the range of 600 to 1000 cm^{-1} is provided in figure (b).

New peaks emerge between 700 and 900 cm^{-1} and there is a distinct change in the shape of the Si-O-Si peak. In order to better understand the new peaks observed in the FTIR scan of the CF_4-etched NCs, the spectrum was rescaled between 700 and 1000 cm-1 and deconvoluted. This is shown in Figure 3.11(b). Examining Figure 3.11(b) one notices 4 peaks centered at 726, 795, 885, and 913 cm^{-1}. The peak at 726 cm^{-1} is related to the bending mode of CF_2. [132] while the peak centered at 795 cm^{-1} [133] is believed to be related to Si-C stretching. The peak near 885 cm^{-1} is most likely due to oxidized Si-H groups. [91, 130, 131] An Si-F stretch is also observed in this region at 913 cm^{-1}. [134] Absorption modes due to fluorocarbon films also cause the broadening observed in the Si-O-Si stretch. [114, 128] From the appearance of these new FTIR modes it is clear that

a fluorocarbon film forms on the surface of the etched NCs. However, H is still present on the surface. From the information gathered by the XPS and the FTIR it is clear that the surface of the CF_4-etched NCs is mostly covered with an oxidized fluorocarbon but still retains a small amount of oxidized Si hydrides.

From the XPS and FTIR measurements we can conclude that the CF_4-treated SiNC are passivated by O, H, C and F in contrast to only O and H for those oxidized SiNC. The effect of C and F on the effective bandgap of SiNC is much weaker than that of O. [43, 135] Because of this fact it is possible that C and F may play a role in preventing the formation of oxygen-related intra-bandgap energy levels, which prevent short wavelength light emission from SiNCs and so allow short wavelength emission. [31, 135]

3.4.3 Routes to Full-Visible Spectrum Emission from SiNCs

Achieving air-stable full-visible spectrum emission from SiNCs has been very difficult. Near IR and red emission has been demonstrated from oxidized SiNCs [136], but methods to synthesize NC with shortwave PL [33, 38, 91, 137] has remained elusive. Tunable emission from a-Si in oxide or nitride matrices have been reported [53, 138], however the efficiency of these structures are low [53, 139] which makes them nearly impossible to use in a useful device structure. One approach to solve this problem is to utilize a two-step process. Researchers have demonstrated that full-visible emission can be achieved from porous Si [31, 140] or SiNC [33, 38, 137] synthesized in the gas phase followed by a wet etching setup intended to remove the SiO_2 shell and etch the Si.

Although the shortwave PL was observed from these etched NCs, their stability was limited once the NCs were exposed to air. [33, 38, 137] The authors tried to prevent oxidation by using an alkyl passivation, but this added step did completely resolve the shortwave PL problems once the NCs were exposed to air.

Utilizing CF_4 allows for the creation of full-visible spectrum emission from SiNCs which are air stable. Tuning the emission of the NCs is straightforward using the reactor discussed in Figure 3.1. Controlling simple parameters of the system (such as flow rate and power) allows the user to tune the NC size. The synthesis and etching occurs all in one step (where as the liquid-phase typically is a three stage process), produces a large amount of material, and is compatible with existing Si fabrication techniques. This makes the CF_4 etching of NCs the best option for creating shortwavelength PL. The next section discusses methods to fabricated etched SiNC whose PL spans the visible.

3.4.3.1 Tunability of the NC Emission by varying CF_4 Plasma Power

One method to adjust NC size is to adjust the RF power applied to the etching plasma. In this particular setup, the synthesis plasma conditions and (45 sccm Ar, 9 sccm SiH_4/He @ 80W) CF_4 flow rate (3 sccm CF_4) are fixed. The power applied to the etching plasma is varied between 15 and 75 W. Following synthesis, the SiNC PL is measured (within 30 min) by a Spex Fluorolog-2 Spectrofluormeter. A 385 nm long-pass filter was used in front of the input slit of the detection monochromator in all the PL measurements. Figure 3.12 presents the PL taken from this study.

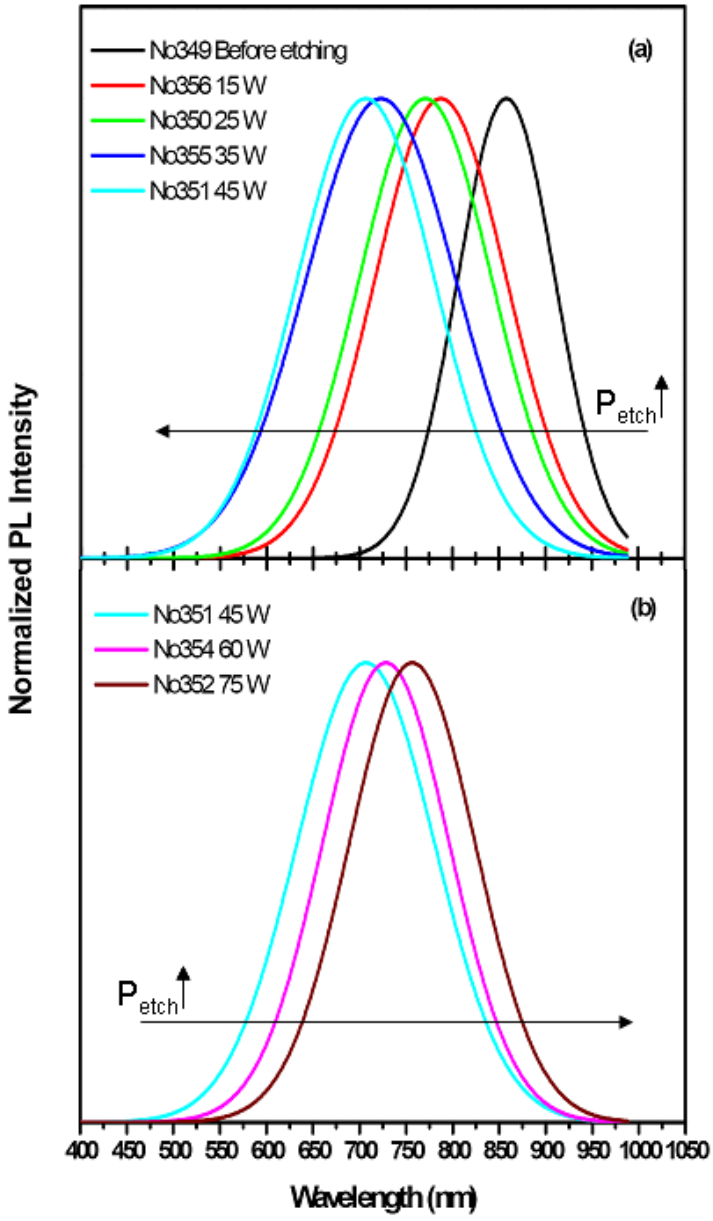

Figure 3.12: Normalized PL data from a series of CF_4-etched NC samples were the CF_4 etching power was adjusted from 15-75W with all other parameters constant. (a) PL spectra from NCs which were etched between 15-45W. (b) PL spectra from NCs etched between 45-75W. The PL curve with a peak at 850 nm in (a) is a as-produced sample. In (a) the PL peak blueshifts from 850 (far right curve) to 700 nm as the etch power is increased from 0 to 45 W. In (b) the PL peak position redshifts from 700 nm (far left curve) to 750 nm as the etch power is increased from 45 to 75W.

The PL from the unetched (or controlled) NCs emits near 860 nm. As the etching power is increased from 15 to 45W the peak PL position of the NCs blueshift. This observed blueshift indicates that the NCs are indeed being etched to a smaller size since in the quantum confinement model the bandgap of the NCs increases with the decrease in NC size. The etching continues up to 45W and then a redshift occurs with a further increase in power. This redshift indicates that at higher etching powers the etch rates are decreased. This phenomenon can be explained by the following argument.

It has been shown in the literature that an increase in power will lead to an increase in both F and CF_2 radicals. [141] At low etching powers is it generally believed that the rate of nonvolatile film deposition is less than the rate at which it is removed by physical ion bombardment. However, at increased powers with a larger concentration of fluorocarbon forming radicals, the film that forms on the surface of the NC accumulates and becomes thick enough to inhibit the etching process. This mechanism may cause the redshift that occurs at high etch power.

Figure 3.13 presents the raw data that was presented in Figure 3.12. Typically, the PL spectra which are obtained are normalized to the intensity of the excitation source. However, plotting the raw data provides further insight into the surface of the NCs.

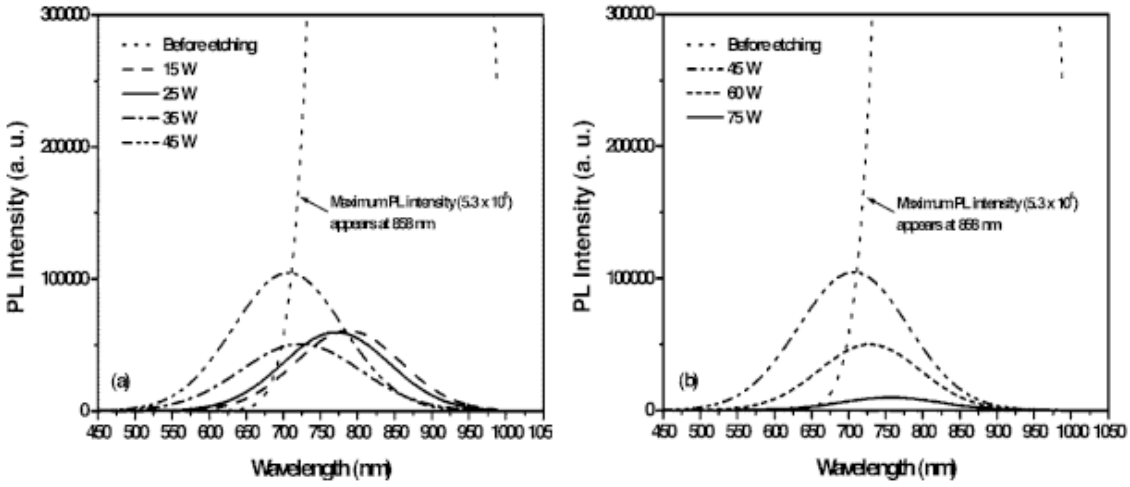

Figure 3.13: Raw PL data from the etched power series which was introduced in Figure 3.12. (a) Etch power tuned between 15-45W. (b) Etch power varied between 45-75W. The as-produced sample is provided to show how the intensity of the as-produced NCs compares with the etched NCs.

Examining both (a) and (b) one notices that the intensity of the CF_4-etched NCs has been significant reduced after exposure to the CF_4 plasma. It is possible that this loss in intensity is the result of damage induced by ion-bombardment when the NCs pass through the etching plasma or while they are collected on the substrate. [120, 141] Furthermore, as the power is increased, the PL intensity of the NCs decreases. This effect is demonstrated in Figure 3.13(b). The PL intensity drops significantly as the power is increased from 50 to 75W. The higher power in the etching plasma not only generates more CF_2 and F radicals, but may also lead to the formation of higher energy ions which may cause damage to the NC surface leading to the formation of non-radiative recombination states which can reduce the etched NC PL.

3.4.3.2 Tunability of the NC Emission by Varying CF_4 Flow Rates

Varying the CF_4 flow rate in the etching plasma is another method which can be used to adjust (or select) the size of the NCs. With the increase of the CF_4 flow rate into the etch plasma, more CF_2 and F radicals will be present leading to an increase in the etch rate via the process described by Flamm. [122] Figure 3.15 presents PL data from CF_4-etched NCs in which the emission of the NCs is controlled by the CF_4 flow rate. In this study the synthesis conditions of the NC growth plasma were held constant (45 sccm Ar, 12 sccm SiH_4/He @ 100W) as was the applied RF power to the etching plasma (25W). Samples were deposited for 20 minutes and then PL measurements were performed.

The as-produced SiNCs emit near 885 nm. When the CF_4 plasma is used, PL blueshifts are observed. At a CF_4 flow rate of 1.5 sccm the PL peak position shifts to 787 nm. This blueshift indicates that the NCs are infact being etched to smaller sizes. When the CF_4 flow rate is increased to high flows (3 and 6 sccm) the PL peak position of these NCs are blueshifted from the as-produced sample, but are redshifted with respect to the NCs which have been etched with 1.5 sccm CF_4. As with the power study, it appears that large CF_4 flow rates may lead to a thicker fluorocarbon film on the NC surface which may inhibit further etching.

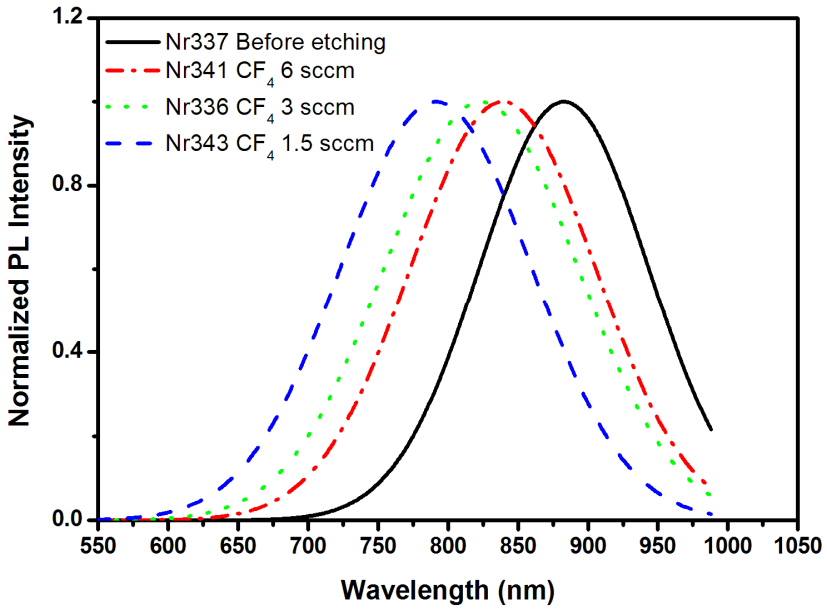

Figure 3.14: Change in the PL peak position for CF_4-etched NCs as a function of the CF_4 flow rate (all other parameters constant). PL excitation is fixed at 325 nm.

The results from Figure 3.14 originate from large SiNCs. As a result, the PL of these SiNC is limited in the red-orange range of the visible spectrum. In order to synthesize shortwavelength emission, the SiH_4/He flow rate was reduced, leading to the formation of smaller NCs. These smaller NCs were then passed through the CF_4 plasma to be etched to a smaller size. Figure 3.15 displays PL data from a second study in which the CF_4 flow rate was altered while keeping the rest of the experimental parameters constant. The NC synthesis conditions were fixed at 50 sccm Ar, 3 SiH_4, and 3.5 sccm H_2. The additional H_2 fed into the etching plasma was fixed at 6 sccm. The power was coupled into the synthesis and etching plasmas were 100 and 25W respectively. NCs were collected for 1 hour.

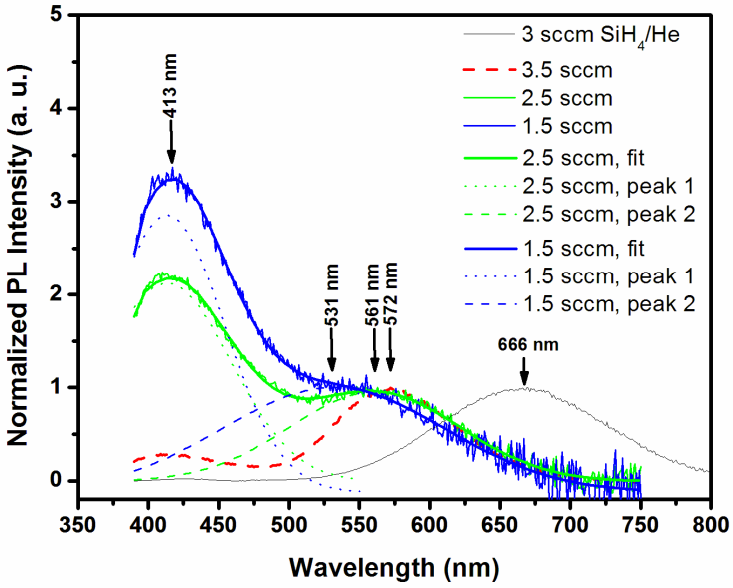

Figure 3.15: Normalized PL data from CF_4-etched NCs synthesized with a variable CF_4 flow rate set between 1.5 and 3.5 sccm (all other parameters constant). Two peaks are observed: 1 peak at 410 nm which is believed to be a defect state, and the longer wavelength peak associated with quantum confinement. The normalized PL spectra from an as-produced sample (growth conditions same as the etched NCs, no etch plasma) is added to show the PL blueshift an indicator for etching.

The as-produced SiNCs emit near 666 nm. Similar to what was observed with the larger NCs, as CF_4 is added, a PL blueshift is observed. However, there is a significant difference. Two distinct peaks are observed in the PL spectra of the etched NCs. One peak is fixed at 413 nm for all three CF_4 flow rates, while the second peak changes slightly (from 531 nm for 1.5 sccm CF_4 to 572 nm for 3 sccm CF_4.). The peak at 413 nm will be discussed in detail later in this section. Once again a redshift is observed when the CF_4 flow rate is increased. As the CF_4 flow rate is increased, the production of CF_2 radicals (precursor to fluorocarbon films) increases leading to a thicker fluorocarbon film on the surface of the NCs and thus less etching. The results shown from Figures 3.12

through 3.15 illustrate that full visible wavelength emission is possible from SiNCs. By controlling the parameters of both the NC synthesis and etching plasmas, the PL can be tuned between 530 and 900 nm.

3.4.3.3 Tunability of the NC Emission by varying SiH_4 Flow Rates

There is a third approach which can be used to tune the NC size. Previous work [70] has shown that the NC size in a plasma-based reactor can be adjusted by the partial pressure (of SiH_4) and the residence time of the processing gases inside of the synthesis (or growth) zone. Therefore by adjusting the SiH_4/He flow rate, the NC size can be tailored to bigger or smaller sizes before entering the etching plasma. This effect is illustrated by Figure 3.16.

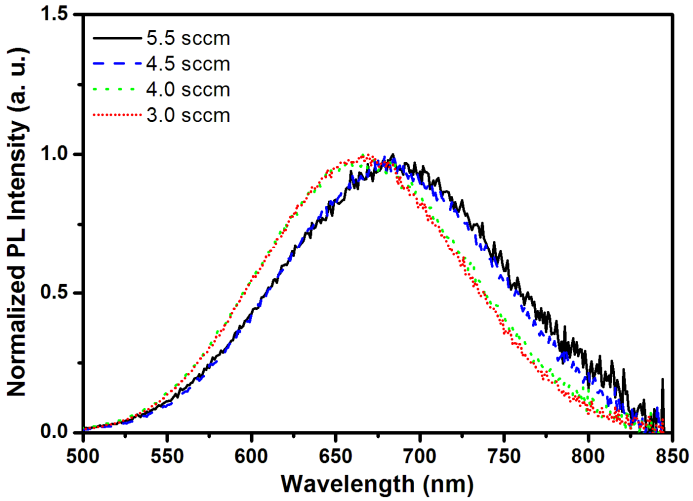

Figure 3.16: Normalized PL data from as-produced SiNCs where the SiH_4/He flow rate is varied in the synthesis plasma. No etching plasma is utilized. A small blueshift is observed from the 5.5 sccm (PL peak position ≈ 680 nm) to 3 sccm (PL peak position ≈ 660 nm) case demonstrating that the NC size can be tuned by the SiH_4 flow rate (or partial pressure).

Although the NC size is tuned somewhat by changing the SiH_4/He flow rate the NC emission is observed in the red-orange range. In order to achieve shortwavelength emission utilizing this process, the CF_4 plasma needs to be used as well. A simple experiment was designed to demonstrate that shortwavelength PL could be produced in the dual-plasma system by only changing the SiH_4/He flow rate. For this experiment, several parameters are fixed. The Ar (45 sccm) and H_2 (3.5 sccm) flow rates in the synthesis plasma is fixed while the CF_4 (1.5 sccm) and the H_2 (6 sccm) flow rate in the etching plasma are fixed. The power coupled into the growth plasma and etching plasmas were fixed at 100 and 25W respectively. NCs were collected for 1 hour. Following deposition the NCs were transferred to the Spex-2 for PL measurements.

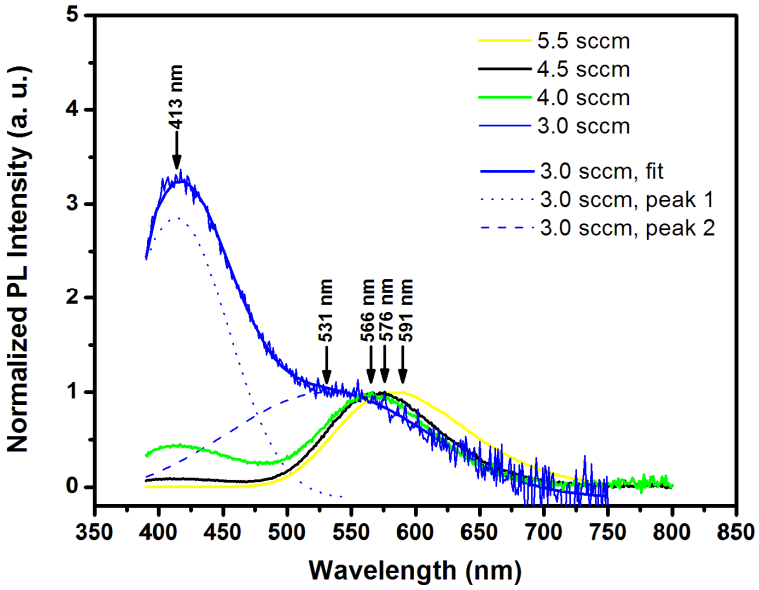

Figure 3.17: Normalized PL data from CF_4-etched NCs synthesized with a variable SiH_4/He flow rate set between 3 and 5 sccm, (all other parameters constant). Two peaks are observed: 1 peak at 410 nm which is believed to be a defect state, and the longer wavelength peak associated with quantum confinement.

Figure 3.17 demonstrates that changing the SiH_4 flow rate can lead to shortwave PL. As the SiH_4 flow rate is decreased, the PL blueshifts. With the CF_4 flow rate fixed in the etching plasma, the concentration of CF_2 and F radicals should remain approximately constant throughout each sample run. Therefore, the etching that occurs at the NC surface should also be constant for the sample set in Figure 3.19. Therefore the PL blueshift is related to the size of the NCs from the synthesis plasma. Figure 3.16 demonstrated that the size of the NCs can be adjusted by the SiH_4 flow rate and this is what causes the blueshift in observed from the samples in Figure 3.17. The decrease in SiH_4 flow rate leads to a decrease in initial NC size and with the etching constant over the same period of time, the smallest synthesized NC should remain the smallest after etching.

Using a modified equation [42, 142] for the relationship between the PL energy ($E = 1240/\lambda$, where E is the photon energy in eV and λ is the wavelength in nm) and SiNC size, we calculate the sizes of SiNCs to be 3.57 nm and 3.40 nm for the PL peaks at 686 nm and 666 nm (Figure 3.16). The partial pressure of SiH_4 in the synthesis plasma decreases with the decrease of SiH_4/He flow rate. Published work by Mangolini [39] has shown that SiNC size is proportional to the partial pressure of SiH_4, which is what is observed in Figures 3.16 and 3.17. Performing some simple calculations we note that for the PL peaks at 591 nm, 576 nm, 566 nm, and 531 nm we can calculate the sizes of Si-NPs to be 2.86 nm, 2.76 nm, 2.70 nm, and 2.48 nm, respectively. Comparing these numbers with those of the red light emitting SiNCs depicted in Figure 3.18, these short-wavelength light-emitting SiNCs are about 0.82 nm smaller.

3.4.3.4 Tunability of the NC Emission by varying H_2 flow rate

As mentioned in the experimental section, additional H_2 is mixed into the etching plasma to help control the etching rate. Figure 3.2 illustrates the fact that as the H_2 concentration in the CF_4 plasma is increased the etch rate is decreased significantly. This provides yet another controllable experimental parameter which can be used to tailor SiNC PL in the dual plasma setup. Figure 3.18 demonstrates this capability.

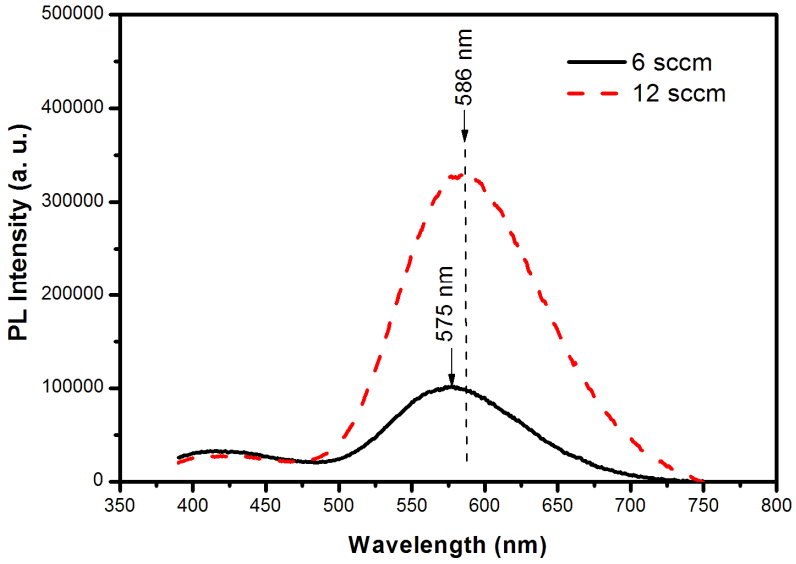

Figure 3.18: Normalized PL data from CF_4-etched NCs in which the H_2 flow rate in the etching plasma is varied.

For the data presented in Figure 3.18, the synthesis plasma conditions (50 sccm Ar, 4 sccm SiH_4 and 3.5 sccm H_2 @ 100W) CF_4 flow rate (1.5 sccm) and etch power (25W) are fixed. Only the additional H_2 flow rate is varied. In Figure 3.20, the H_2 flow rate is varied between 6 and 12 sccm. Consistent with the data published by Oehrlein (reproduced in Figure 3.2) larger flow rates of H_2 lead to a decrease in the etch rate. [113] This is mostly likely due to the fact that the additional H will scavenge available F in the

etch plasma forming HF and reducing the concentration of F radicals which are crucial to the etching process.

3.4.3.5 H_2 Etching

H_2 plasma etching of SiNCs is another possible route to full visible spectrum emission. Etch rates of bulk Si in a H_2 discharge confined in a quartz tube can be as high as 500Å/min at an RF power of 400W. [143] To test what effect H_2 etching would have on bare SiNCs we performed a simple experiment using the dual-plasma reactor. SiNCs were first synthesized (45 sccm Ar, 9 sccm SiH_4/He @ 100W for 10 min). Then the NCs were sent through a CF_4 plasma (3 sccm CF_4 @ 45W) or simply an Ar/H_2 (@ 45 W) plasma where the H source originates from the SiH_4. Three plots are shown on Figure 3.19. The black curve near 860 nm is PL emission from bare SiNCs while the red trace is from a CF_4-etched NC sample. When the NCs are exposed to only an Ar/H_2 plasma, etching still occurs. However, the PL intensity observed from these NCs is approximately 2X less than that of CF_4-etched NCs. Furthermore, the NCs treated by only an Ar/H_2 plasma are etched less (PL peak is redshifted with respect to CF_4-treated NCs) than those of CF_4-etched NCs. The drop in intensity could be related to increased surface damage caused by Ar ions or H. However, more work is needed to understand this process. Specifically, we need to add more H_2 into the etching plasma and investigate if we observe a drastic change in either PL intensity or peak position with respect to CF_4-etched NCs. Nevertheless, this approach may provide another method to full visible emission. It is attractive because there is no fluorocarbon on the surface,

rather the surface should be composed of most H and O bound to Si. This surface chemistry could be functionalized to further improve the optical properties of the NCs.

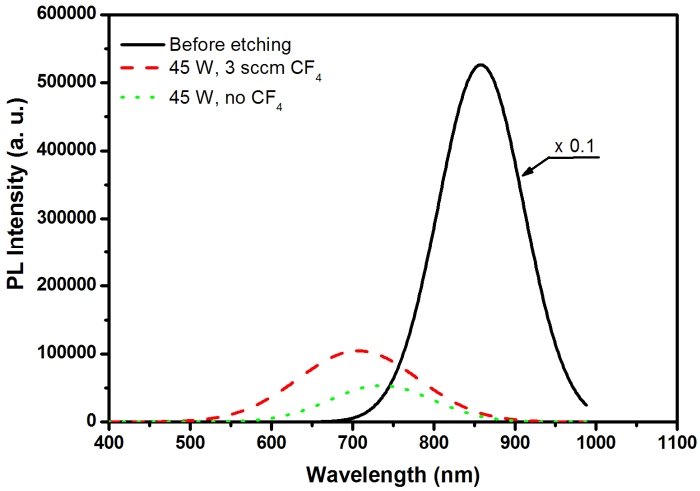

Figure 3.19: Raw PL data from SiNCs. The black curve is from as-produced NCs. The red and green curves correspond to NCs which have been etched by CF_4 (red) and Ar/H_2 (green).

3.4.3.6 Changes in PL Peak Position and Intensity Upon Air Exposure

Although liquid-phase etching has been demonstrated to produce short wavelength PL from SiNCs, the stability of the NCs in air was a serious limitation. [33, 38, 137] Within a few hours the PL from the NCs was quenched. In order to determine whether or not the CF_4-etched NCs suffered from the same problem, the NCs were exposed to air and the PL peak position and intensity was tracked over a period of several days. Figure 3.20(a-d) displays the change in peak position and intensity for different etched NC samples.

The red and the blue curves in Figure 3.20(a) are unetched NCs while the black and green curves are from etched NCs. It is clear from Figure 3.20(a) that the PL from all four samples blueshift with increasing air exposure time (at room temperature). This

indicates that we are observing oxidation-induced size reduction of SiNCs. [42, 91] After about 100 h in air, the blueshift begins to slow and eventually saturates. This is consistent with self-limiting oxidation of nanocrystalline Si. [91, 144, 145]

Not only does the peak position of the NCs change with oxidation time, so does the PL intensity. Figure 3.20(b) plots the ratio of PL intensity over the initial PL intensity. What is interesting about this plot is the fact that the etched NC PL intensity increases by nearly a factor of 10X greater than that of the unetched NCs. It is possible that the etched NC/oxide surface is passivated while inside the plasma system by fluorocarbon film. This fluorocarbon film passivates dangling bonds or trap states which can lead to a reduction in the optical properties of NCs. On the other hand, the as-produced NCs have no means of in-situ passivation; therefore there may be many surface states which reduce PL intensity prior to air exposure. Nevertheless, an increase in PL intensity is observed for both unetched and etched NCs. This is exactly opposite to the trend observed with SiNCs which have been treated with solvents or etched in the liquid phase. [33, 38, 91, 137]

The significant increase in the PL intensity of the etched NCs may be the result of the structure of the etched NC surface. During etching surface damage may lead to the formation of dangling bonds or weakened Si-Si bonds [120] which are both reactive and easily removable. It is likely that these types of bonds which are not passivated by the fluorocarbon film will oxidize more readily (or faster) in air than Si-H bonds on the surface of the unetched NCs. Although the PL intensity of the etched NCs increases by a factor of about 10X more than unetched NCs, the actual PL intensity is still low. A prime

example of this can be observed in Figure 3.14 where the raw PL data for a CF_4 power series study is shown. Examining that plot one observes that the PL from the as-produced NCs is significantly larger than that of the etched NCs. Although the PL intensity is increased by oxidation, it appears that the induced surface damage is not completely remedied by either the fluorocarbon film or native oxidation.

Figure 3.20(c) shows the evolution of PL spectra from shortwavelegth NCs. Similar to Figures 3.15 and 3.17 there are two peaks. The peak on near 410 nm is the blue band emission. The peak position does not change as the NCs oxidize, but the PL intensity increases significantly. The other peak which is initially centered near 578 nm blueshifts nearly 10 nm over the span of about 230 h. This effect is similar to that observed in Figure 3.20(a-b), where oxidation causes a reduction in the size of SiNCs and therefore this emission follows the quantum confinement model. Figure 3.21(d) provides a study of the position of PL intensity and peak position of CF_4-etched NCs initially emitting near 580 nm. Looking at the intensity of the blue band, one notices that it encounters the same effect as observed in Figure 3.20(c). As the NCs oxidize, the blue band emission increases. The green band (or longer wavelength) position blueshifts while the NCs oxidize. However, the PL intensity of the green band decreases significantly while the NCs are oxidized. This is significantly different from what was observed from larger sized etched SiNCs. As the SiNCs become smaller the bandgap of the NCs increases (via quantum confinement).

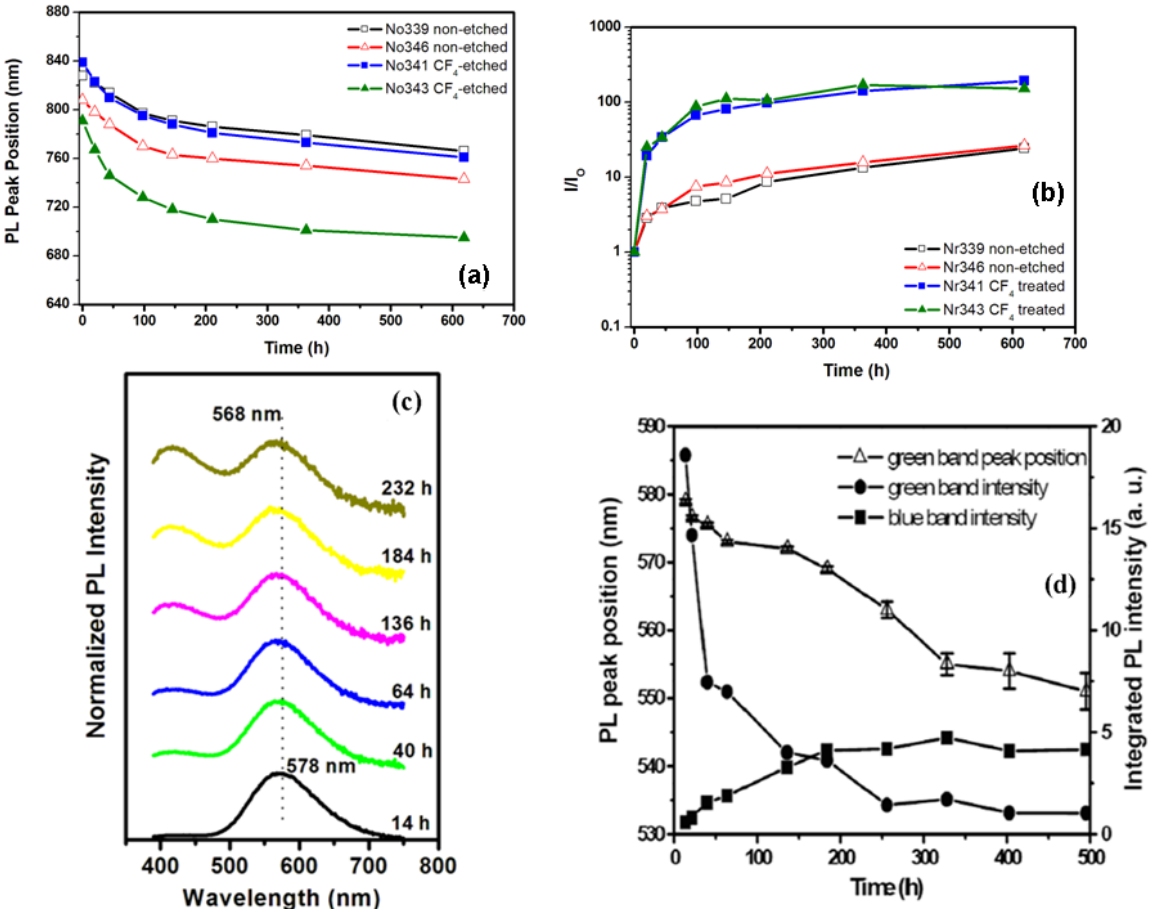

Figure 3.20: Four curves are presented. (a) Change in PL peak position and (b) intensity for both etched and unetched NCs as a function of air exposure. The red and black traces are from unetched NCs while the green and blue traces are from etched NCs. (c) PL spectra from CF_4-etched NC sample. The PL spectra are tracked over time. The longer wavelength peak shift about 10 nm in 230 hours, while the blue band peaks remains constant. (d) Change in PL peak position and intensity of the green emission and intensity of the blue emission as a function of air exposure.

From Figure 3.20(d) it appears that near 200 h a transition occurs where the emission from the blue band dominates the emission from the green band. It is possible at this point, the bandgap of the NCs is wide enough that recombination via surface states is a more favorable transition than a recombination event through exciton formation and annihilation from the NCs VB and CB. Thus with increased oxidation more trap states

will be come available and recombination will occur at these sites leading to the increase in the blue band PL and decrease in the PL from quantum confinement. More evidence of this surface state as well as what type it may be will be discussed in the section covering the blue-band.

3.4.3.7 Quantum Yield, PL Lifetimes and the Blue Band

In Figure 3.21 we show digital pictures of CF_4-etched NCs dispersed in methanol which emit in the deep red (740 nm), red-orange (675 nm), yellow (592 nm), green (572 nm) and blue (441 nm) when excited by a UV source (365 nm). All of the samples are more than 12 days old.

The optical properties of the CF_4-etched SiNC have been investigated by measuring the quantum yield (QY) and PL decay. A basic discussion on how the QY measurements were performed will follow, however, for a more through discussion on how the quantum yield is measured; we encourage the reader to consult [41, 146].

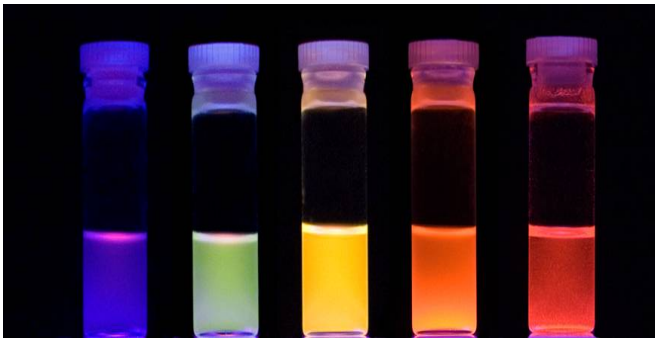

Figure 3.21: A photo of the red (675 nm), yellow (592 nm), green (572 nm) and blue (441 nm) light emissions from Si-NPs under the illumination of an UV lamp (excitation wavelength 365 nm). A 385 nm short-pass filter was placed between the UV lamp and each sample to remove any stray non UV light.

The quantum yields of the etched NCs were measured using an “absolute method”. [41, 146] In this approach the both the emission and the absorption of the NCs (suspended in a solution) were investigated by an integrating sphere (Labsphere) which was connected to an Ocean Optics 2000 USB Spectrometer (usable range 350-1000 nm) via a fiber optic cable. The spectral response of the spectrometer was calibrated by a NIST traceable source. The NCs were excited by a UV LED with peak emission near 395 nm. First, a baseline or reference measurement was performed. In this measurement, the intensity of the excitation source was measured with only a cuvette filled with a solvent (same solvent in which the NCs will be suspended) inside the integrating sphere. Three reference measurements were taken and stored. Following the reference scans, the etched NCs were suspended in solution (same as the reference sample) inside of an identical cuvette and placed in the sphere. Three scans were also performed. The PL signal as well as the absorption signal (which is derived from the change observed in the LED excitation) was acquired simultaneously [41, 146]. Taking the ratio of the integrated PL and absorption spectrum provides a measure of the quantum efficiency of the NCs [41, 146]. However, we are interested in the QY of the sample. The quantum yield which is defined as:

$$QY = \frac{\#of\ emitted\ photons}{\#of\ absorbed\ photons}$$

can be calculated by multiplying the PL and absorption signals by their respective wavelengths and reintegrating the processed data. The accuracy of this method has been tested thoroughly by utilizing calibration standards such as Coumarin 6 and comparing the measured QY with previously published data [41].

QY measurements were performed on the CF_4-etched NCs once the PL blueshift ceased. This occurred typically after 15 days. The CF_4-etched samples were placed in methanol and then measured in the setup described above. Figure 3.22 shows the quantum yield data from air stable etched NCs. When the PL shifts from red to green emission the QY measured from the NCs drop from 16% to 2% respectively. This drop in QY has been observed in SiNCs which emit at higher wavelengths (> 650 nm), but the reasons behind this effect are still unclear.

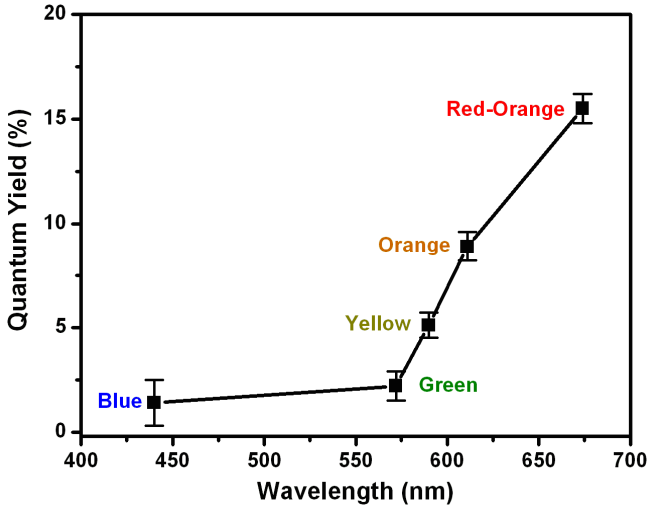

Figure 3.22: Quantum yields of oxidized CF_4-etched Si nanocrystals. The excitation is from the 392 nm line of a UV LED. The PL from SiNC was collected in an integrating sphere and analyzed with an Ocean Optics spectrometer. All the Si nanocrystals were measured more than 15 days after synthesis. The blue QY is estimated to 1%.

The QY for the blue emitting NCs are estimated because the QY setup discussed above can not provide an accurate measurement. The NC emission and the LED excitation are too close to each other and thus the PL and the absorption peaks overlap one another making it impossible to directly measure the QY. This could remedied by changing the

excitation source to 325 nm. However, we would also have to change the spectrometer since the USB2000 only has a workable wavelength range of 350-1000 nm.

The QY of the etched NCs is low compared to other passivated SiNCs. Alkyl-passivated SiNCs synthesized by the same process have been shown to have QY as high 60% [41, 146-148], the highest QY reported for free standing silicon NCs. Nevertheless, QY as high as 15% after 15 days in air are observed. This QY are on par with previous published results. [42] The major challenge in improving the QY of the CF_4-etched NCs is the removal or modification of the fluorocarbon surface. Although stable, it is nearly impossible to remove without damaging the NC cores. More research is needed to determine whether or not the QY can be improved with this surface chemistry.

PL decay measurements were also performed on the CF_4-etched NCs. The PL lifetimes for NCs emitting from red to green were measured while under excitation from a 392 nm UV LED driven by a function generator (Textronix AFG320). The PL was detected by a photomultiplier tube (PMT, Hamamatsu) which was connected to an oscilloscope (Textronix TDS 460A) which sampled the PL decay. The system response time was ≈ 150 μs. Pulses from the function generator were set to be 10X shorter than the longest measured PL lifetimes. The blue PL decay was measured by means of a time-correlated PL lifetime setup with a response time of ≈ 1.5 ns, where the excitation was fixed at 375 nm from a pulse laser diode (pulse width ≈ 300 ps). The response of both systems was taken into account while analyzing the PL lifetime data. Figure 3.23(a-b) provides lifetime data from CF_4-etched NCs. Figure 3.23(a) presents PL lifetime data from orange-red (654 nm), yellow (590 nm) and green (569 nm) etched NCs.

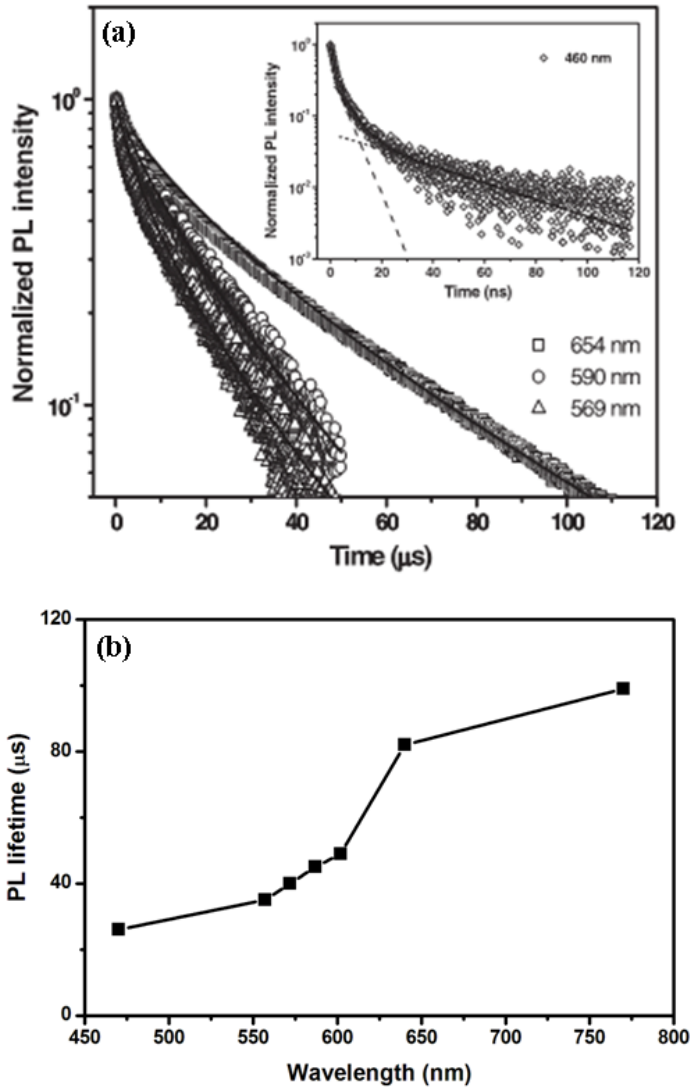

Figure 3.23: Decay of the PL from CF_4-etched NCs emitting from the red to blue range. NCs with peak emission centered at 654, 590, and 569 were excited at 392 nm. Each solid line results from a stretched exponential fit with a dispersion factor of approximately 0.7. The insert of (a) presents PL decay from blue emitting NCs with a peak wavelength centered at 460 nm. The solid line is from a bi-exponential fit. The dashed lines on the figure illustrate the two components from the blue PL decay. (b) Presents the PL lifetime of etched NCs as a function of wavelength.

Each of the PL lifetime traces are fitted to an stretched exponential decay function with a dispersion factor of ≈ 0.7, which was described in [146, 149]. The PL lifetimes were calculated at 23, 14 and 9 μs for the red-orange, yellow and green etched NCs. It appears

that the PL lifetimes decrease as the NC size increases. This trend is consistent with previous observations in quantum-confined Si. [149, 150] However, the PL lifetime from the blue emission, shown in the insert of Figure 3.23(a) exhibits a different trend. The PL decay of the blue emitting NCs (excited at 375 nm) shows two components, a fast decay at 5 ns and a slower decay of 37 ns.

Theoretical work [150] predicts that the blue lifetimes should be much longer than what was observed in this experiment. Rather, these lifetimes are closer to what was seen with oxidized porous Si. [151] For this reason, we suspect that the blue emission observed from CF_4-etched NCs is the result of defect states at the surface of the NCs.

Further evidence to the origin of the blue emission can be seen in Figure 3.24. In this figure, the excitation energy of the blue emitting NCs is varied, while taking a PL scan. The peak position of the blue band changes with excitation energy. The peak PL position shifts from 411 nm (325 nm excitation) to 441 nm (365 nm excitation) as the excitation energy is varied. This change does not occur with the etched NCs which emit from the red through the green (those which follow quantum confinement). This PL wavelength redshifts with respect to the excitation energy indicates that the trap states may have several different available energy levels from which an electron and hole may be captured. This effect is has also been observed in silica due to the change in defect states. [152]

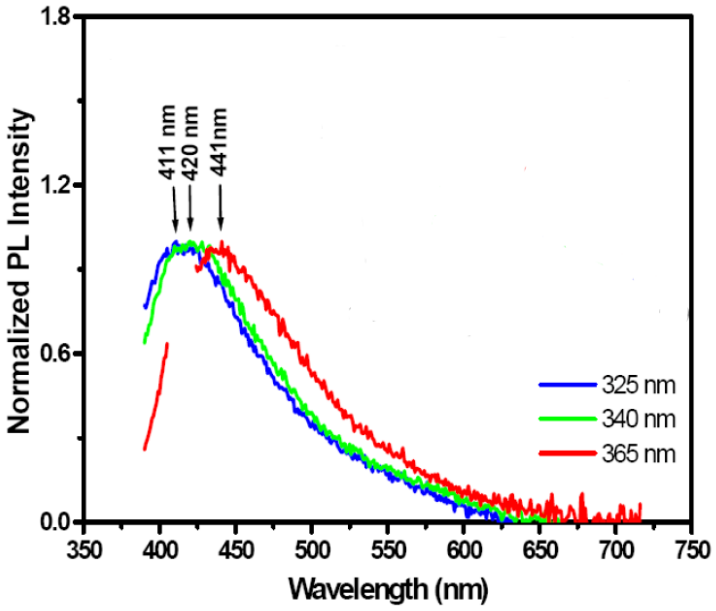

Figure 3.24: Change in the peak position of the blue band as a function of excitation wavelength. The peak position of the blue band changes from 411 nm at 325 nm excitation to 441 nm at 365 nm.

The blue band emission is present in larger NCs as well. Figure 3.25 shows the PL data from a SiNC sample which emits near 675 nm. The blue band PL is also measured from this sample although its intensity is 200X less than that of the peak associated with quantum confinement. It is possible that as the NCs become smaller and the bandgap is widened, more trap states become accessible providing more radiative pathways for electrons and holes inside the NC. Other groups have attributed this blue emission to a direct bandgap transition. [87, 88] Further study is needed in order to better understand the origin of the emission from the blue band as well as to determine how the surface passivation affects this phenomenon.

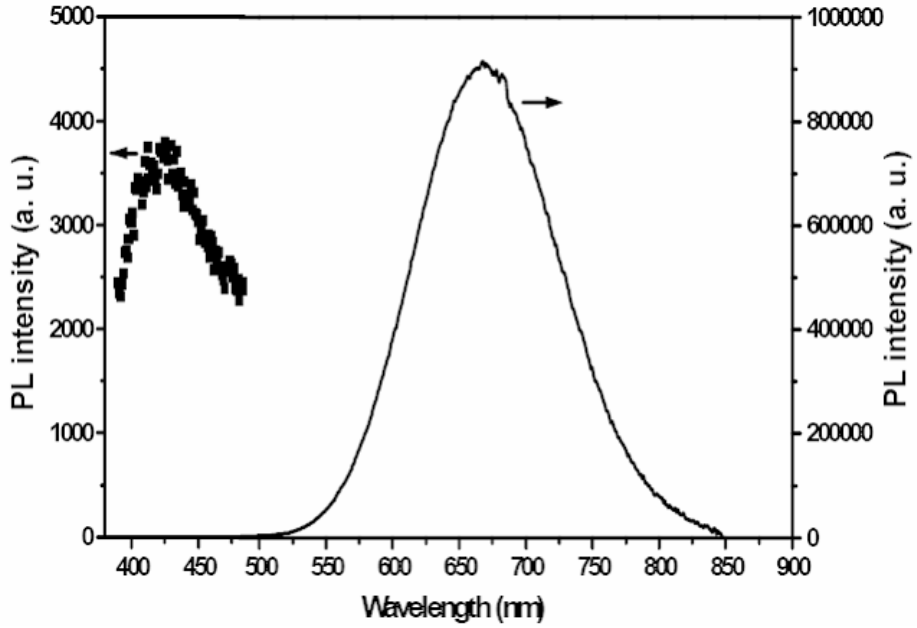

Figure 3.25: Raw PL data from a CF_4-etched NC sample. 2 peaks are observed. The longer wavelength peak is related to PL resulting from quantum confinement while the shorter wavelength peak, which is 200 X less intense, is due to blue band emission.

Several important aspects of the CF_4 process still need to be mentioned. First, the SiNCs PL immediately after being removed from the plasma reactor. This supports the idea that some surface passivation occurs in the chamber. Secondly, blueshifts of the yellow and orange SiNC are negligible. They shift approximately 0.05 eV in 12 days. Therefore, we can state that the yellow and orange light emitting SiNCs are stable in air. Finally, the emission of the green and blue SiNC last for several weeks, much longer than the times reported by those working on liquid phase techniques. [33, 38, 137]

3.5 Conclusions

In conclusion we have demonstrated that tunable, full-visible wavelength emission from SiNCs is possible by the use of a novel two stage plasma reactor. By controlling different parameters of the experimental setup, a particular NC size can be fabricated. The NCs which are etched by this process are passivated with a fluorocarbon film which results from the generation of CF_2 radicals in the etching plasma. Although this later provides an adequate passivation layer, it is difficult to remove and prevents further processing of the NCs. Optical measurements indicate that the emission from red to green emitting NCs follow the quantum confinement model, but the blue NC emission does not. The blue emission is believed to result from oxide related surface states and is observed even in large NCs. A transition point occurs at $\approx$ 540 nm, (or core NC size of approximately 2.3 nm) the emission from the blue band begins to dominate that from quantum confinement since the widening of the NC bandgap has caused more surface states to become radiative recombination pathways. Nevertheless, air-stable QY as high as 20% have been observed for CF_4-etched NCs.

Chapter 4

Alternative SiNC Etching/Passivation with SF_6

4.1 Chapter Overview

This section of the thesis presents an alternative gas-phase passivation approach to CF_4 using another standard silicon (plasma-based) etchant, sulfur hexafluoride (SF_6). The chapter will discuss the experimental setup of the process as well as discuss characterization results performed on these NCs. Surface characterization techniques such as FTIR and XPS were used to examine the surface of the NCs before and after etching. HRTEM was used to investigate the crystallinity of the SF_6-etched NCs. Photoluminescence and quantum yield measurements were also performed on the etched NCs to study the change in the NC size due to the plasma etching. The effect of air exposure on the surface chemistry and the optical properties was investigated thoroughly and will be discussed in this chapter. Finally, the effect of SF_6 plasma etching on NiO thin films (which are used for hole transport layers in our NCs devices – see Chapter 5) will be investigated. The majority of the work presented in this chapter has been published. [153, 154]

4.2 The need for alternative gas-phase passivation/schemes

Chapter 3 provided data which showed that the CF_4 etching process is capable of producing full-visible spectrum light from silicon nanocrystals which have relatively high quantum yields and are air-stable. The system can be controlled with relative ease by simply changing experimental parameters such as RF etching power, CF_4 flow rate, and SiH_4/He flow rate. Although the CF_4 process performs exactly how it was designed, it suffers from one major flaw, the formation of CF_2 radicals in the etching plasma leads to the growth of a fluorocarbon film on the surface of the NCs. The fluorocarbon film is a stable passivation layer, but further functionalization or device integration may be problematic since the fluorocarbon layer is insulating and it will be difficult to inject and transport charge to and from the NCs. The fluorocarbon film is difficult to remove. There are no known wet chemical methods to remove this layer. We also tried alkyl passivation to produce a colloidal NC solution in hopes that heat would remove this layer and replace it with an alkyl chain, but this attempt failed as well. O_2 plasma etching on drop coated CF_4-etched NCs on flat Si wafers did remove the fluorocarbon layer but also destroyed the NCs as well. Therefore, in order to create light emitting devices with SiNCs as the emissive layer, CF_4-etched NCs may not be the best option. The most obvious question would be to ask what could be used. There are several other silicon based dry etched chemistries which may be good alternative to CF_4. These chemistries are displayed in Figure 4.1:

Si	CF_4/O_2, CF_2Cl_2, CF_3Cl, $SF_6/O_2/Cl_2$, $Cl_2/H_2/C_2F_6/CCl_4$, C_2ClF_5/O_2, Br_2, SiF_4/O_2, NF_3, ClF_3, CCl_4, CCl_3F_5, C_2ClF_5/SF_6, C_2F_6/CF_3Cl, CF_3Cl/Br_2
SiO_2	CF_4/H_2, C_2F_6, C_3F_8, CHF_3/O_2
Si_3N_4	$CF_4/O_2/H_2$, C_2F_6, C_3F_8, CHF_3
Organics	O_2, CF_4/O_2, SF_6/O_2
Al	BCl_3, BCl_3/Cl_2,$CCl_4/Cl_2/BCl_3$, $SiCl_4/Cl_2$
Silicides	CF_4/O_2, NF_3, SF_6/Cl_2, CF_4/Cl_2
Refractories	CF_4/O_2, NF_3/H_2, SF_6/O_2
GaAs	BCl_3/Ar, $Cl_2/O_2/H_2$, $CCl_2F_2/O_2/Ar/He$, H_2, CH_4/H_2, $CClH_3/H_2$
InP	CH_4/H_2, C_2H_6/H_2, Cl_2/Ar
Au	$C_2Cl_2F_4$, Cl_2, $CClF_3$

Figure 4.1: Common Silicon Dry Etch Chemistries. Reproduced from [120, 155].

There are many etch chemistries shown in Figure 4.1 that could be a viable option. First of all, we decided to dismiss any chemistries which would lead to the formation of CF_2 radicals. CF_4/O_2 where O_2 can remove C leading to volatile CO or CO_2 has been tried, but no PL was observed after treating the NCs in this setup. Toxic precursors such as Br_2 or F_2 were also not viable due to the fact that a proper toxic gas exhaust system is not installed in the lab. Therefore, we decided to simply use sulfur hexafluoride (SF_6) as a replacement for CF_4, although many other chemistries displayed in Figure 4.1 could conceivably work as well.

SF_6, like CF_4 is an inert gas at room temperature and is non-toxic. It is does not form any fluorocarbon precursors, and it is known to produce high concentrations of free fluorine radicals which have been shown to etch planar silicon at 10-15X that of CF_4 under similar conditions [156]. Figure 4.2 (a-b) shows the etch rate of planar silicon in a parallel-plate reactor when exposed to CF_4 and SF_6 etching plasmas under similar conditions.

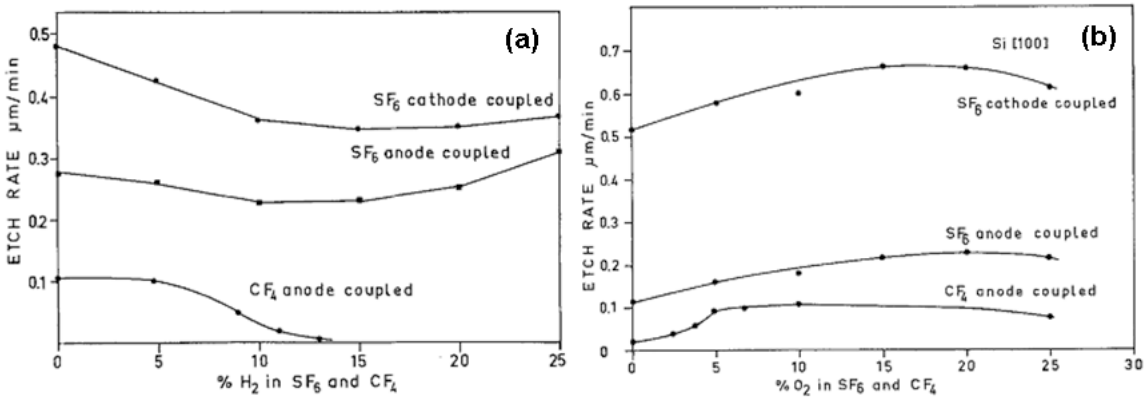

Figure 4.2: CF_4 and SF_6 etch rates of planar Silicon as a function of (a) H_2 concentration or (b) O_2 concentration. The parallel plate reactor used for the SF_6 plasma discharge was coupled to either the anode or cathode. All plasma parameters were held constant except for the flow rates of H_2 or O_2. Reproduced from [156].

Figure 4.2(a) displays the SF_6 and CF_4 etch rate of planar silicon as a function of the addition of H_2 into the plasma. At low concentrations of H_2, both SF_6 configurations have an etch rate which are 3-5X higher than that of CF_4. At high concentrations of H_2, the CF_4 rate tails off as observed in Figure 4.2 as well as in [113], while the SF_6 rate remains fairly constant. The drop in etch rate observed with added H_2 in the CF_4 plasma is due to the fact that the plasma chemistry is beginning to switch selectivity from Si to SiO_2 [156]. When O_2 is adjusted in the etching plasma as shown in Figure 4.2(b), the SF_6 etch rate (in both configurations) rises slowly, while the CF_4 flow rate increases drastically. The rise in the CF_4 flow rate can be attributed to the formation of CO and CO_2 volatile products and resulting reduction in fluorocarbon film precursors. [120, 121, 156] The data presented in Figure 4.2(a-b) illustrate that SF_6 etch rate has little dependence on H_2 or O_2 additions. Figure 4.3 shows the planar silicon etch rate as a function of the SF_6 in an SF_6/Ar plasma where the Ar flow rate, RF power and pressure are fixed. [156]

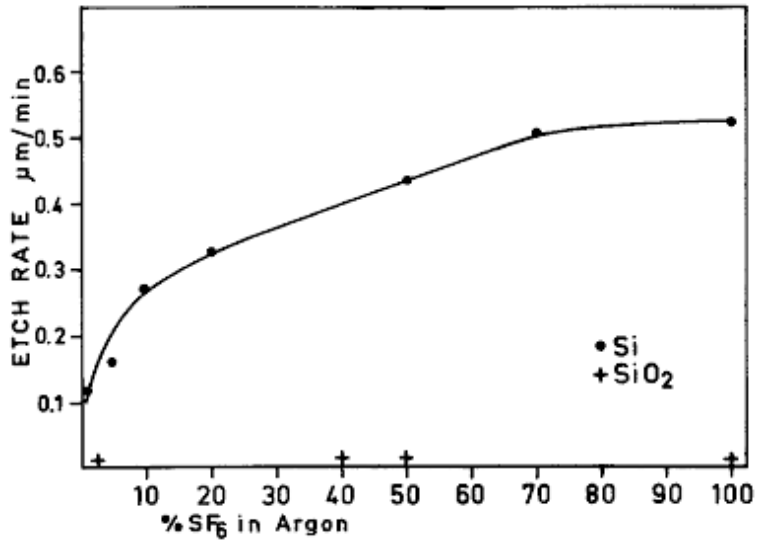

Figure 4.3: Planar Si Etch Rate as a function of SF_6 concentration in SF_6/Ar plasma. The circles correspond to the Si etch rate, while the crosses refer to the SiO_2 etch rate. Reproduced from [156].

Since there is no process inhibiting etching, the trend shown in Figure 4.3 is expected. The more SF_6 added into the plasma, the more etching occurs. Furthermore, from Figure 4.3 we can see that the SiO_2 etch rate is extremely low at high SF_6 concentrations. This could have either a positive or negative effect. On the one hand, if no O_2 is being released by F attacking the quartz tube, then it is possible that a significant amount of S deposition could occur on the surface because the low O flow rate is not producing enough S-related volatile products (SO_2 or SO). However, if S does not deposit on the surface, then the NCs will have a surface chemistry which is a combination of H and F bonds. This may allow for further functionalization of the NCs. Eisele shows evidence that S does not deposit on the surface of planar silicon. The XPS survey analysis performed by Eisele [156] and reproduced in Figure 4.4 shows peaks related to Si, C, O, and weak peaks near 400 eV and 680 eV related to N 1s and F 1s respectively. The inset

of Figure 4.4 provides further evidence of the lack of sulfur after etching. The inset shows the HR XPS spectrum from the S 2p line. As evident from the figure there is little or no S signal indicating no S is incorporated into the surface during etching.

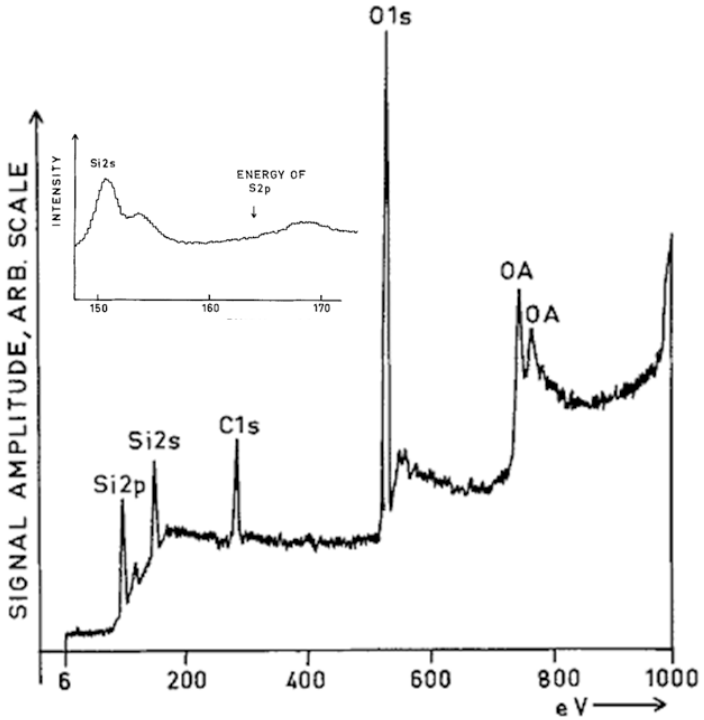

Figure 4.4: XPS survey spectrum from SF_6 etched Si substrates. Peaks corresponding to Si, O, C, and F are present on the scan. Inset: S 2p HR scan from the same sample. No S is present on the substrate. Reproduced from [156].

Although no S is deposited on the surface of the planar silicon samples, this does not ensure that the same would happen to the NCs. The surface of the NCs contains many dangling bonds which could be passivated by S. XPS was performed to determine what effect S plays in SF_6 etching of SiNCs. These results will be discussed later in this chapter. Because of the high rate of Si etching without additives (O_2 or H_2) and the fact that no fluorocarbon film is formed during the etching process we decided to use SF_6 as an alternative to CF_4.

4.3 Experimental Setup

The experimental setup use to synthesize SF_6 etched NC was adapted from the system utilized to etch CF_4-etched NCs. The setup utilizes two plasma (dual-plasma) in which the first plasma is responsible for the creation [41, 70] and H-passivation of the NCs and the second plasma etches in the NCs in flight. [111, 112] Figure 4.5 provides a basic schematic of the in-flight passivation/SF_6 etching reactor. The system illustrated in Figure 4.5(a-d) is similar to the CF_4 etching system with some notable changes. First of all, SF_6 replaced CF_4 as the etching source (including an SF_6 specific mass flow controller). Secondly, two reaction tubes were used when etching with CF_4: a quartz tube (similar to what was used in the CF_4 etching studies) and an alumina tube. Finally, a controllable throttle valve assembly, which allows for a more precise control of the system pressure, was installed at the inlet of the mechanical pump.

For air-free experiments a glove bag was installed on the system. Before using the glove bag, it was purged with dry N_2 for at least an hour. While in use the glove bag was maintained under positive pressure with respect to the environment. Following NC collection, the samples were removed from the reactor, placed in the glove bag, and then sealed inside of two KF flanges for transport to additional processing or characterization.

Operating parameters of the reactor varied depending upon what aspect of the etching/passivation process was being studied. Typically, the Ar flow rate was set between 50-55 sccm, the flow rate of the SiH_4/He varied between 5-10 sccm while the power coupled into the synthesis plasma was fixed at 100W. Following the synthesis the NCs were sent into the etching plasma where both the SF_6 flow rate (1-5.5 sccm) and

powers (5-50W) were adjusted. The pressure in the system was maintained near 3 torr and 300 mtorr for the synthesis and etching plasma respectively. The substrates used were dictated by the type of characterization technique that was to be performed on the samples. For the most part, samples were collected on SS Mesh or Au/Cr/Si.

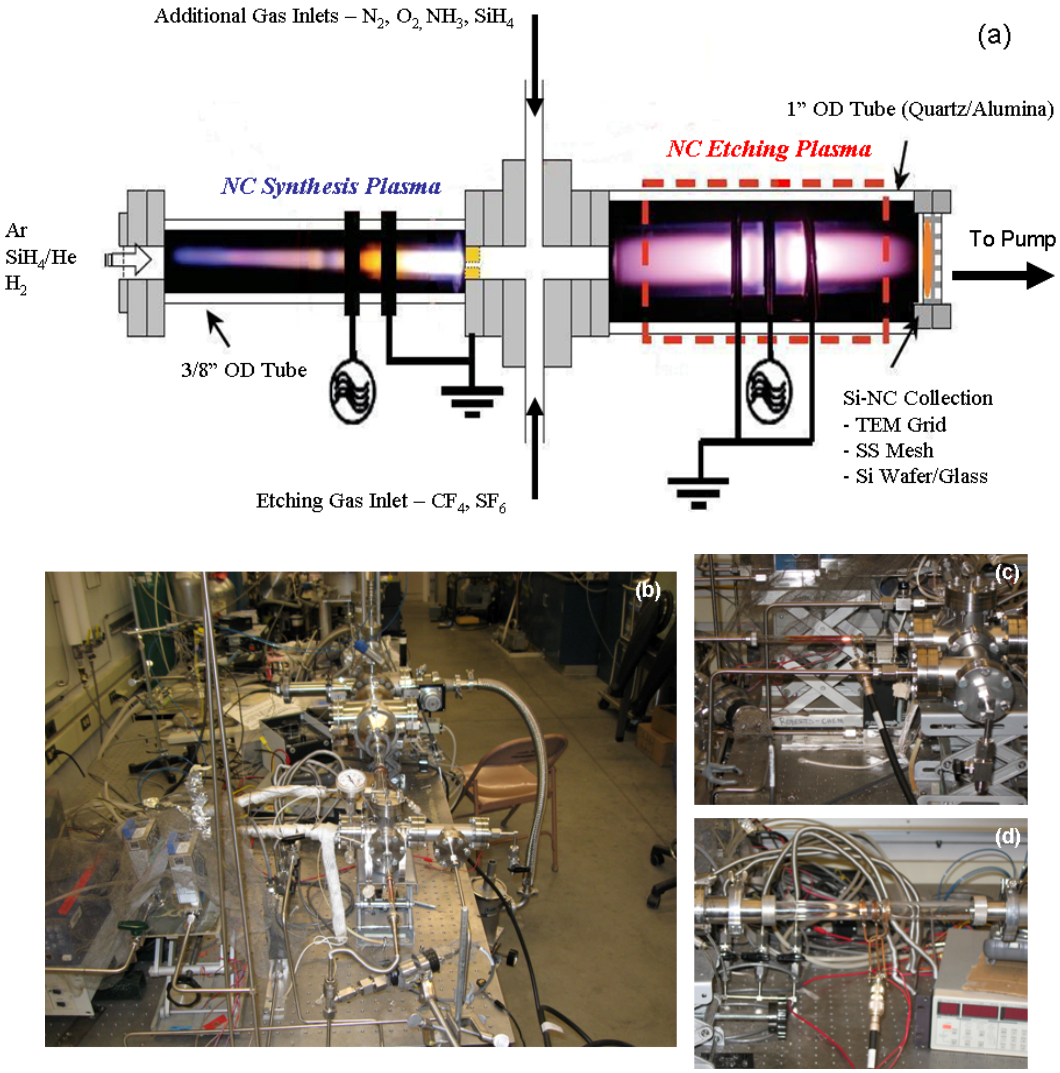

Figure 4.5: (a) Experimental setup used to synthesize and etch (in-flight) full-visible spectrum emitting silicon nanocrystals. SF_6 is utilized as the etching source for this experiment. Figures 4.5(b-d) provide pictures of the NC reactor. (b) is an overhead view. (c) and (d) shows a close-up of the synthesis and etching reactors the NC synthesis reactor while Figure 4.5(d) presents a close-up of the NC etching reactor.

4.4 Characterization of SF_6-Etched NCs

4.4.1 HRTEM

In order to study the crystallinity of the SF_6 etched NCs, HRTEM was performed. Lacy carbon TEM grids were placed either on the SS Mesh or mounting on carbon tape on the end of push-pull rod. The NCs were collected after the etching plasma in-flight and immediately taken over to the HRTEM for analysis to limit the oxidation of the SF_6 etched NCs. Figure 4.6 displays HRTEM images from (a) unetched and (b) SF_6 etched NCs.

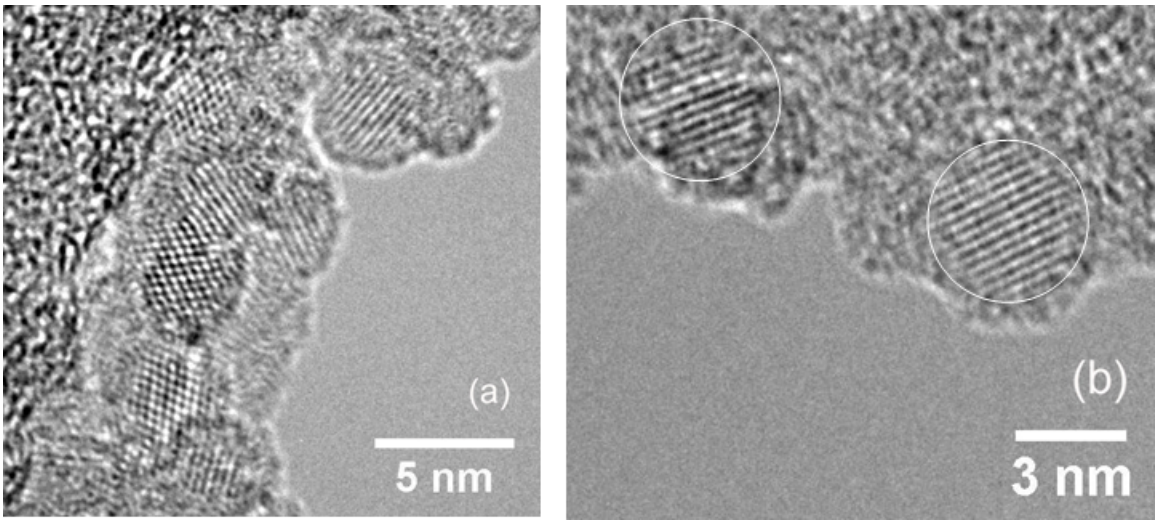

Figure 4.6: HRTEM images from (a) unetched and (b) SF_6 etched SiNCs. Both images show lattice fringes which are indicative of Si (111) are present. The scale bar in each image is (a) 5 nm and (b) 3 nm respectively.

In both images lattice fringes can be clearly identified. In Figure 4.6(a) it appears that most if not all of the as-deposited NCs deposited on the TEM grid are crystalline. After etching, there is still is evidence of crystalline material, but certainly much less than that what was observed in the as-produced case. Similar to the CF_4 etching, we may be losing

some material to the gas flow (since smaller NCs tend to follow the gas flow) or other processes in the etching plasma. Nevertheless, since we are etching we expect to have less material deposited on the grid than when as-produced NCs are deposited since there is no process which inhibits etching when using CF_4.

4.4.2 Surface Characterization – XPS

In order to study the surface chemistry of the SiNCs after they were exposed to the SF_6 plasma, XPS characterization was performed. A Surface Science Industries SSX-100 XPS was used for these experiments. Similar to the XPS performed on the CF_4 etched NCs both a survey (for elemental ID) and HR scan in order to determine surface bonding information (via chemical shifts). XPS scans were performed on the etched samples within a day of synthesis. Figure 4.7 presents XPS survey spectra from both as-produced and SF_6-etched SiNCs.

For the unetched NC sample shown in (A) the surface is mostly oxidized and is coated with a small amount of surface contamination. However, a different result is observed with the SF_6-etched NCs (B). A F 1s signal is observed. This is not unexpected since we are etching with SF_6 and F could conceivably attach to dangling bonds on the surface of the NCs. Furthermore, an extremely clean surface is observed, virtually free of carbon contamination. This is unusual because C contamination is common for samples which have been exposed to air. We also investigated the surface of freshly produced SF_6-etched NCs which were collected using the glove bag to keep them air free. Initially, the surface of the etched NCs contained a small amount of sulfur along with the other

elements shown in Figure 4.7 (B). However, the sulfur was simply removed by exposure to AlKα x-rays or to a low energy (< 1eV) electron source typically used to prevent surface charging. This indicates that the S on the surface is either weakly bonded or volatile. Since the S signal from the XPS disappears when the etched NCs are exposed to air it is likely that the S is being removed over time via the formation of volatile compounds such as SO and SO_2. [157]

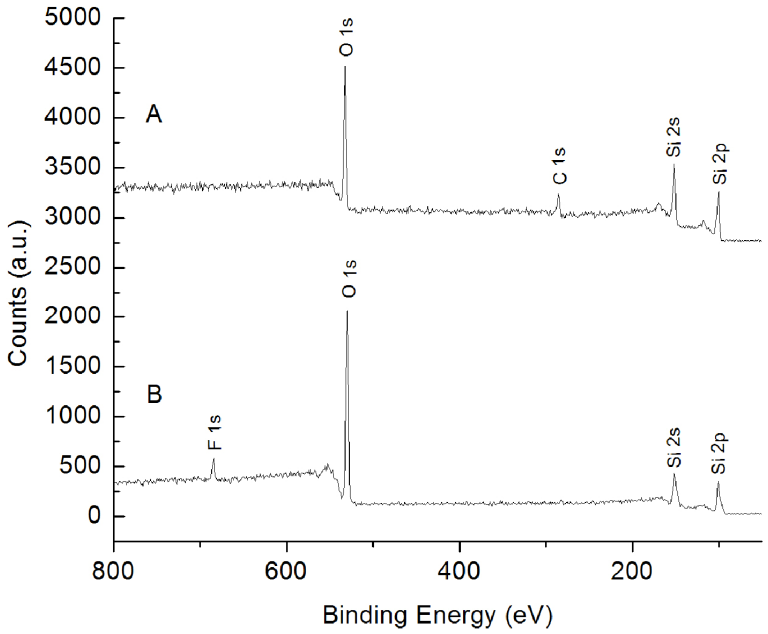

Figure 4.7: XPS survey spectra from (A) as-produced and (B) SF_6-etched SiNCs.

HR XPS was also performed on the SF_6-etched NCs (which were exposed to air for a few hours) to better understand the surface chemistry and bonding arrangement. The XPS system was operated at a pass energy of 150 eV for survey spectra and a 50 eV pass energy to obtain high resolution spectra. XPS data were excited using a monochromated aluminum K_α x-ray source operated at 200W onto an elliptical spot of

approximately 800 x 200 micrometers. Data were taken at a take-off angle of 55° relative to the sample normal. The vacuum during operation was maintained below 2 x 10^{-9} Torr. Typically, the C 1s peak which is related to contamination is used as a reference signal, to account for the effects of surface charging. However, since little or no carbon signal was observed on the XPS, this makes it difficult to account for surface charging. The solution to this problem would be to deposit the sample on Cr/Au/Si substrates. However, the XPS samples which were deposited were thick enough that the X-rays could not penetrate down to the substrate. Therefore, we will reference the peak assignments to the Si 2p line.

Figure 4.8 shows the XPS HR spectrum from the Si 2p region. Two peaks are identifiable on the spectrum and are related to Si-Si and Si-O bonds at the surface of the NCs.

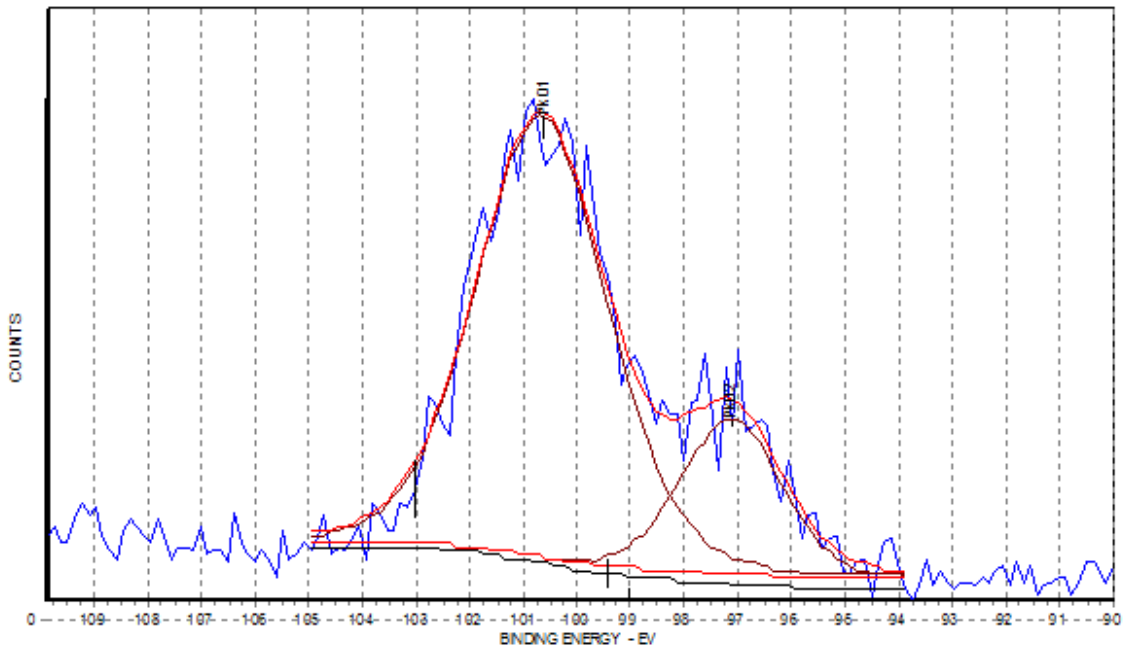

Figure 4.8: Si 2p HR spectrum from SF_6-etched NCs. A Shirley background is used for the Gaussian curve fit. 2 peaks are present related to Si-Si and Si-O or Si-F bonding.

The peak position of the Si-Si bond should be near 99 eV. [126, 127] Since our Si-Si peak is centered near 97eV, it is likely that the locations of our peaks have shifted by 2 eV. If we take this is into account with respect to the larger peak in the Si 2p spectrum, the peak position would shift near 103 eV which corresponds to SiO or SiF as shown in similar HR XPS peaks of CF_4 treated NCs. [128, 129] Since there is no peak near 108 eV, it is probable that no O-Si-F peaks exist on the surface. [129]

The O 1s HR spectrum, shown in Figure 4.9 only shows one peak. When the position is corrected, the position falls at 532.3 eV. This peak is associated with O-Si bonds on the surface of the NCs. [128] What is interesting from this plot is that there is no peak related to O-F on the spectrum. That peak would appear near 537 eV, and it is clear from Figure 4.9 that no such peak exists. This is fundamentally different than what was observed with CF_4 etched NCs. The NC surface of CF_4 etched NCs contained more O-F than O-Si bonds (Figure 3.7).

Figure 4.10 shows the HR spectrum from the F 1s HR region. The corrected peak position would be centered at 686.5 eV. Examining the literature and the HR spectra from the CF_4-etched NCs the peak at 686.5 eV is related to Si-F bonds [129]. Once again the F 1s HR spectrum of SF_6-etched NCs differs from that of CF_4-etched NCs. There is no O-F peak on the HR spectrum (near 692 eV). The differences in both the C 1s, O 1s, Si 2p, and F 1s demonstrate that the surface of the SF_6-etched NCs are significantly different than that of CF_4-etched NCs. Specifically, there is no fluorocarbon film (as expected) or carbon related contamination, and thus the surface of the SF_6-etched NCs is

composed of mostly O-Si, Si-F, and Si-Si after one day in air. However, XPS doesn't provide all information related to the surface chemistry. We need to consult FTIR to further investigate the surface structure of the SF_6-etched NCs.

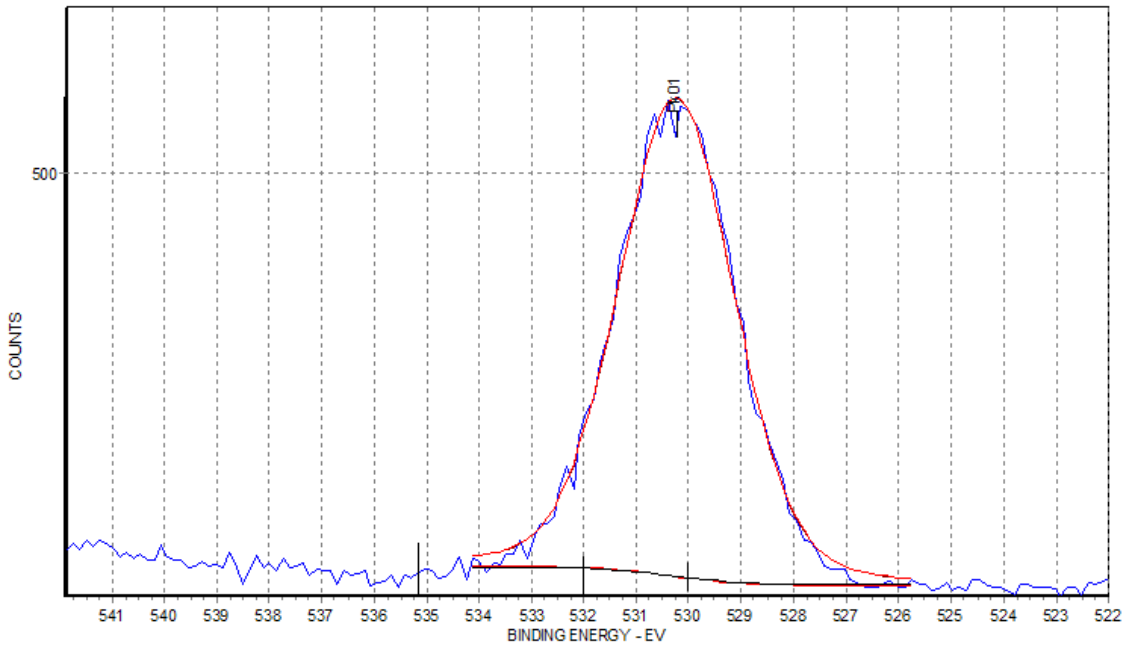

Figure 4.9: O 1s HR spectrum from SF_6-etched NCs. A Shirley background is used for the Gaussian curve fit. One peak is present and it is related to O-Si bonding.

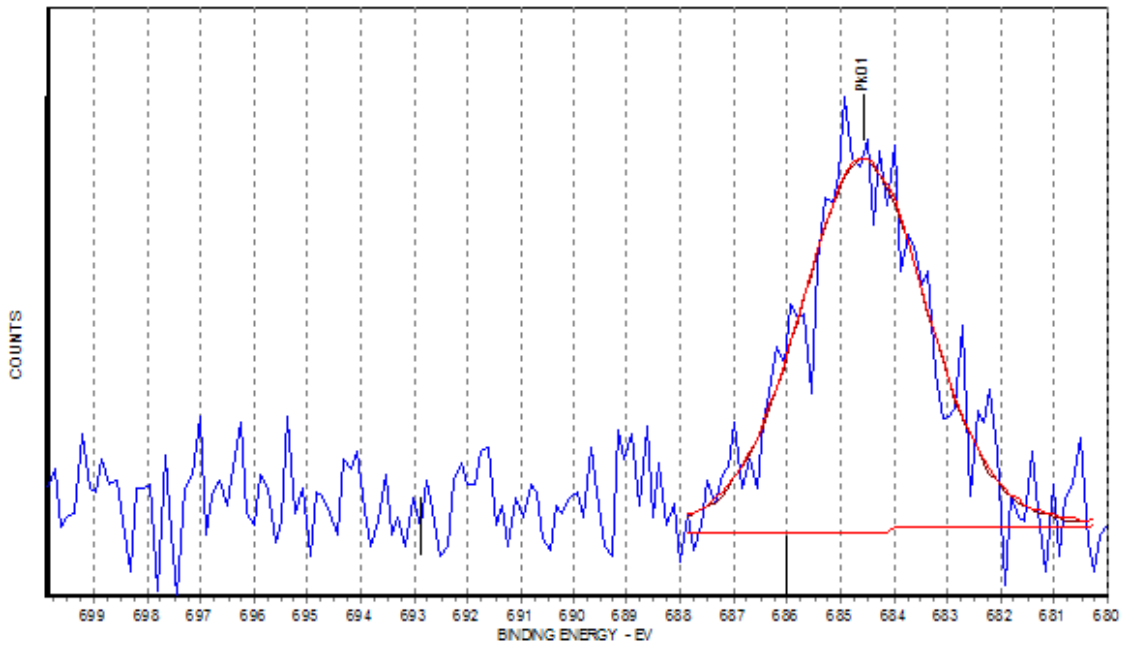

Figure 4.10: F 1s spectrum from SF_6-etched NCs. A Shirley background is used for the Gaussian curve fit. One peak is present in the spectrum and it is related to Si-F bonding.

4.4.3 FTIR

The FTIR spectrum from both unetched and SF_6-etched NCs was studied intensively. Specifically, FTIR spectra from both types of NCs were taken over a period of time and changes to the surface chemistry was tracked simultaneously.

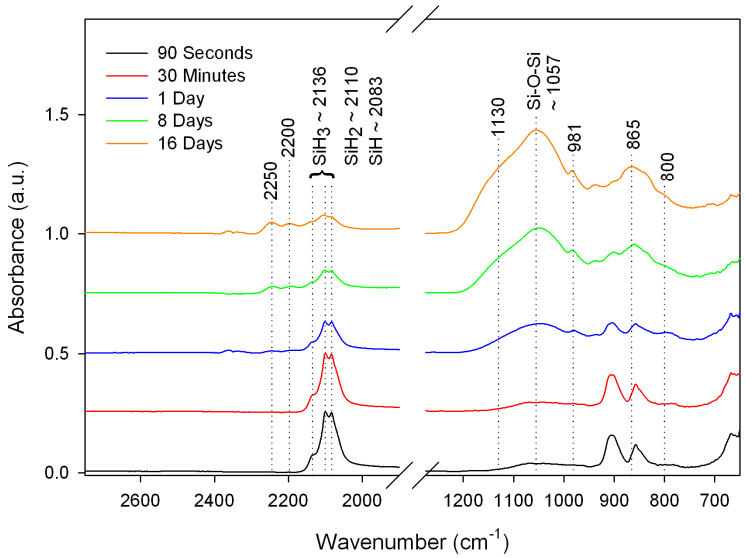

Figure 4.11: FTIR spectra of as-produced SiNCs as a function of air-exposure time. Curves correspond to measurement times with vary from 90 seconds (bottom curve) and 16 days (top curve). Lines have been added to the figure to highlight the most important peaks.

Figure 4.11 presents FTIR spectra from as-produced SiNCs. These NC were collected with the help of a glove bag. Examining Figure 4.11 it is clear that the NCs which were not treated by the SF_6 plasma are not initially oxidized because of the lack of an SiO-H stretch at ≈ 3650 cm^{-1} (not shown in the Figure 4.11) and a weak Si-O-Si peak at ≈ 1070 cm^{-1}. [90] Rather, the surface of as-produced NCs, is comprised mostly of SiH_x bonds (x=1, 2 and 3). This is not surprising given the synthesis method in a SiH_4 plasma. The band at ≈ 2110 cm^{-1}, associated with Si-H stretching in SiH_2, is the most intense peak in

the spectra followed by bands attributed to SiH_3 (≈ 2136 cm^{-1}) and SiH (≈ 2095 cm^{-1}). [92, 97] The doublet peaks located between 850 and 900 cm^{-1} are related to the bend-wag deformation modes of SiH_2 and SiH_3 species. [92, 97] As the NCs begin to oxidize over a period of several days, the surface structure begins to change. After a day in air, the Si-O-Si peak has increased with respect to the SiH_x peaks and an SiO-H peak is visible on the spectra (not shown). The NCs are fully oxidized after a week in air which can be observed in Figure 4.11. The appearance of a broad Si-O-Si peak, oxidized hydride peaks at ≈ 2175 cm^{-1} (O_2SiH_2), ≈ 2270 cm^{-1} (O_3SiH), 790 cm^{-1}, and 865 cm^{-1} (deformation of O_3SiH), and several other peaks (980 cm^{-1}, ≈ 1130 cm^{-1}) indicate a fully oxidized surface. [91-95]

Figure 4.12 displays the FTIR spectra from SF_6-etched NCs which like the as-produced SiNCs, were studied over a period of several weeks. Looking at the first FTIR scan (150 seconds) from the etched NCs, it is clear that the surface chemistry is fundamentally different that that of as-produced SiNCs (Figure 4.14). First of all, S is observed bonded to H [158] on the initial trace. However, after a day in air, the S signal has disappeared, indicating that the sulfur was removed from the surface. This effect was also observed in the XPS and we believe that S is most likely removed from the NCs via the formation of SO or SO_2 volatile compounds. There are also indications of oxidized hydrides and oxidized Si-F groups between 830 and 1000 cm^{-1} on the surface of the NC which appears on the initial FTIR scan. [92, 159, 160] Unlike the bare NCs, the FTIR spectra taken after 7 days in air (Figure 4.12) closely resemble that of the initial scan, suggesting significant fluorine incorporation in the native oxide. This can be seen as

peaks corresponding to $O_2Si\text{-}F_2$ stretches at approximately 920 cm^{-1} (as) and 985 cm^{-1} (ss) and $O_3Si\text{-}F$ at approximately 940 cm^{-1}. [159] Other minor OSi-F and Si-F peaks are lost in the major Si-O-Si and OSiH peaks. [161-164]

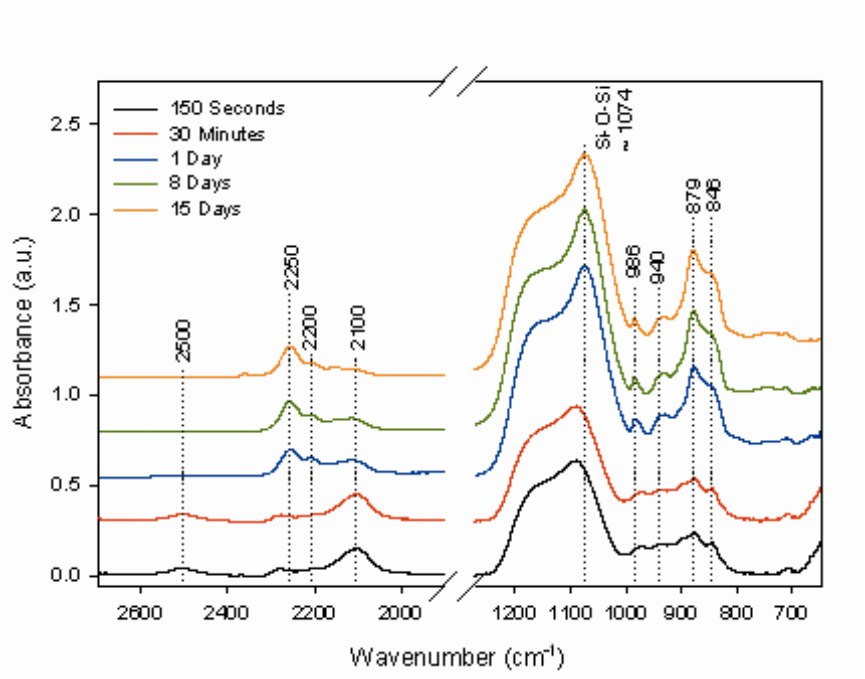

Figure 4.12: FTIR spectra of SF_6-etched SiNCs as a function of air-exposure time. These NCs were etched in a quartz reactor. Curves correspond to measurement times with vary from 150 seconds (bottom curve) and 15 days (top curve). Lines have been added to the figure to highlight the most important peaks.

The most prominent features of the spectra relate to oxidation. This is not surprising since it has been shown that quartz (which is the reaction tube where etching takes place) can be etched by F containing plasma if exposed to energetic radiation. [165-168] It is possible that ions are generated in the etching plasma and attack the quartz, releasing oxygen. Comparing these spectra to those of the unetched NCs it is clear that the etched NCs undergo oxidation prior to the measurement. A large Si-O-Si peak (≈ 1092 cm^{-1}), oxidized hydrides (≈ 2270 cm^{-1}) and an SiO-H peak near 3650 cm^{-1} (not

shown) are clearly visible on the first FTIR scan. The initial peak position of the Si-O-Si stretch is blueshifted with respect to the peak observed with bare Si NC (≈ 1060 cm^{-1}). This shift has been observed in fluorinated SiO_2 and is believed to be attributed to bond angle relaxation due to the incorporation of Si-F bonds in the Si-O-Si network. [159, 160] Following oxidation the NC surface is complex containing Si, O, F, C, H, and possibly S. The shift in the peak position of the Si-O-Si peak (from ≈ 1092 cm^{-1} to ≈ 1074 cm^{-1}) corresponds to a dilution in the F concentration due to oxidation. [159, 160]

The SiH_x band (≈ 2113 cm^{-1}), which is a prominent feature of the as-produced NC, is also significantly reduced, further indicating an oxidized surface. After 1 day in air the intensity of the peak related to the SiH_x band has decreased further, while peaks corresponding to O_2SiH_2 (≈ 2175 cm^{-1}) and O_3SiH (≈ 2270 cm^{-1}) are distinguishable. It is possible that the F radicals which are generated by the SF_6 plasma are attacking the quartz tube of the NC formation reactor and releasing oxygenated species which attach to dangling bonds at the surface of the etched NC. It is also possible that the surface of the etched NCs is extremely reactive and so oxidizes more rapidly than the measurement can be done.

In an effort to resolve this point, the SF_6 etching experiment was repeated with the fused silica tube replaced by a ceramic alumina tube. When a fluorine plasma is struck inside of an alumina tube, stable AlF_3 is formed which prevents the release of O. Under those conditions the initial FTIR measurements showed only very weak peaks as seen in Figure 4.13. After 10 minutes of air exposure a peak related to SiH_x stretching is

observed near 2110 cm^{-1} and a weak Si-O-Si peak appears near 1080 cm^{-1}. There is also evidence of SiH_x deformation peaks between 800-900 cm^{-1}.

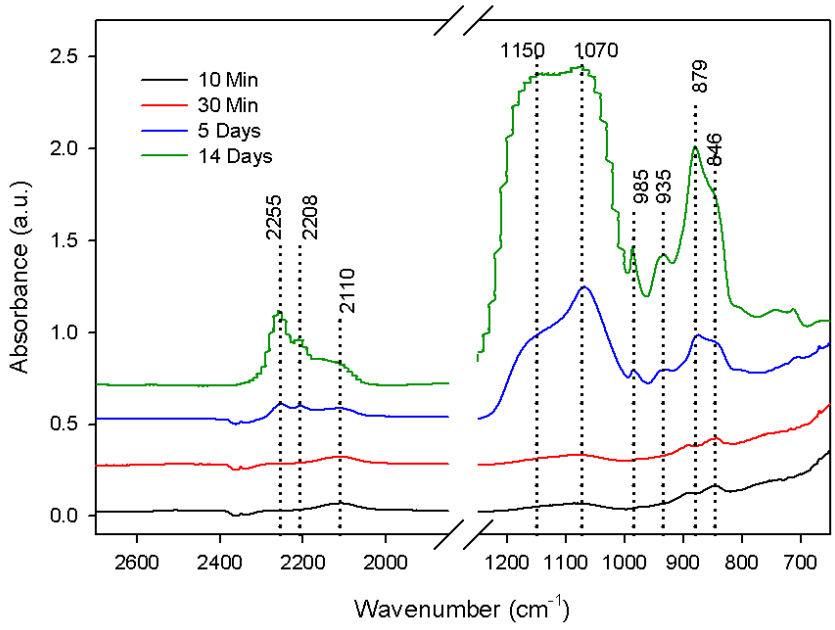

Figure 4.13: FTIR spectra of SF_6-etched SiNCs as a function of air-exposure time. These NCs were etched in an alumina reactor. Curves correspond to measurement times with vary from 10 minutes (bottom curve) and 14 days (top curve). Lines have been added to the figure to highlight the most important peaks.

After 5 days in air, the surface of the etched NCs appears to be completely oxidized. The SiH_x stretch at 2110 cm^{-1} has disappeared and replaced by two peaks related to oxidized hydrides at at ≈ 2175 cm^{-1} (O_2SiH_2), ≈ 2270 cm^{-1} (O_3SiH). A peak near 980 cm^{-1} also appears and this peak is also related to oxidation. The intensity of the Si-O-Si peak increases drastically and redshifts. The redshift is believed to be caused by dilution in the F concentration due to oxidation [159, 160], which was also observed in the NCs etched in the quartz tube. There are also peaks corresponding to oxidized hydrides and oxidized Si-F groups between 830 and 1000 cm^{-1} on the surface of the NC

which appear once the NCs have undergone significant air exposure. [92, 159, 160] Although the initial trace is quite different that the SF_6 samples processed in a fused silica tube, the final trace, taken after 15 days is nearly identical and the optical emission from these NCs are comparable.

The motivation behind this experiment was to determine the source of the fast oxidation from the SF_6-etched NCs etching in the quartz reaction tube. It is clear from the FTIR results of the etched NCs produced in the alumina tube that many of the initial oxide bonds are in fact formed *in-situ* during the etching process by a chemical attack of the fused silica tube.

4.5 Tuning the PL of SiNCs via SF_6 Etching

As mentioned in chapter 3, it has been difficult to demonstrate air-stable full-visible spectrum emission from SiNCs. The experimental setup described in chapter 3 demonstrated that it is possible to tune the PL of the SiNCs by simply changing a few experimental conditions of the reactor. Although tunable emission was demonstrated, one major problem existed, namely the creation of a fluorocarbon surface layer. This layer effectively passivates the surface, but leaves an insulating layer which cannot be remove safely or functionalized. For this reason, SF_6 was investigated as a potential replacement. The next two sections will describe the PL tunability from SF_6-etched NCs.

4.5.1 PL Peak Position dependence on RF Power coupled into the Etching Plasma or the SF_6 flow rate

The NC size can be adjusted by simply tuning the experimental parameters of the reactor used to synthesize etched NCs. This was demonstrated in chapter 3 with the CF_4 etching process. This simple approach also works with SF_6. In this particular setup, the synthesis plasma conditions were fixed (50 sccm Ar, 7 sccm SiH_4/He @ 100W) while the etching parameters, the SF_6 flow rate (0-10 sccm) or power (0-50W) were adjusted. Both the pressure in the growth and etching plasma were also held constant at ≈ 2.7 and 0.26 torr. Following synthesis the NCs were dispersed into toluene (C_7H_8) and their optical properties were studied using an Ocean Optics USB2000 spectrometer. The results of the study are shown in Figure 4.14(a-d).

The freshly produced (or unetched) SiNCs (black curve in Figure 4.14(a) and (c)) emits near in the red to infrared region at ≈ 816 nm, which suggests that the initial NC size is greater than 3nm [31, 42] which agrees with the HRTEM results shown in Figure 4.6(a). Furthermore, previous work has demonstrated that the effects of surface chemistry on the bandgap of SiNC is negligible for NCs larger than 3 nm, thus the size of the NCs can be reliably correlated to their PL energy via the quantum confinement model. [31, 42, 43, 135] The PL peak position of the NCs peaks near 816 nm before they are treated in the etching plasma, and blueshifts after undergoing treatment in the etch plasma as the RF power or SF_6 flow rate is increased. This blueshift can be attributed to the increase in the concentration of free F radicals as the RF power or SF_6 flow rate is increased, resulting in larger Si etch rates. This behavior is different than what was

observed with CF_4 etching. As seen in chapter 3, the increase of either the RF power or CF_4 flow rate leads to the increase in CF_x radicals, causing an increase in the growth of the fluorocarbon surface layer which prevents the removal of volatile SiF_x species which inhibits the etching process. [113, 119] This reduction in etch rates is not observed in SF_6 etching, as the PL continues to blueshift with an increase in the free fluorine radical concentration. Since there appears to be no etch inhibiting process when SF_6 is used, the simple process governed by Flamm likely governs the etching process in this study, where F radicals in an SF_6 plasma react readily to create volatile species such as SiF_2 or SiF_4, which results in the etching of Si. [122, 169, 170] The observed blueshift of the PL peak position with an increase in RF power or CF_4 flow rate suggests that the SiNCs are being etched, since the SiNCs bandgap increases (or PL energy blueshifts) with the decrease in NC size (via quantum confinement).

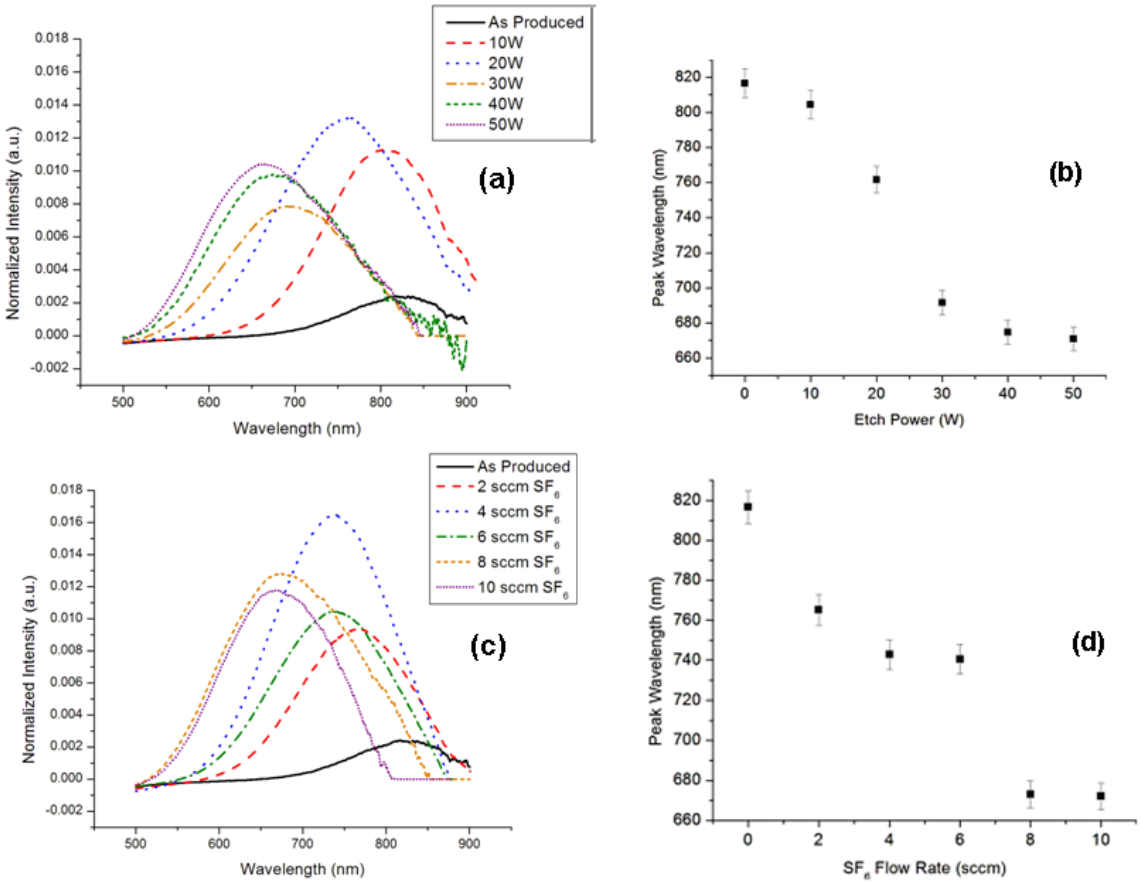

Figure 4.14: Peak PL Wavelength as a function of reactor parameters. (a) PL spectra from SF_6-etched NCs as the RF power coupled into the etching plasma is altered. (b) Change in the PL peak position of SF_6-etched NCs as a function of RF Power (simplified version of Figure 4.14(a)). (c) PL spectra from SF_6-etched NCs as the SF_6 flow rate added into the etching plasma is altered. (d) Change in the PL peak position of SF_6 etched NCs as a function of SF_6-flow rate (simplified version of Figure 4.14(c)).

4.5.2 Tunability via the change in SiH_4

Examining the PL data from Figure 4.14(a-d) one can see that the PL peak position is tunable by changing either the SF_6 flow rate or the RF power. However, the peak position of the NCs generated from this study was limited between 650 and 850 nm. In order to generate short wavelength light from SF_6-etched NCs, other experimental parameters need to be tuned, specifically the SiH_4 flow rate. As demonstrated in chapter 3 and in Figure 4.15, the peak PL position of the untreated NCs can be tuned by simply tuning the SiH_4/He flow rate.

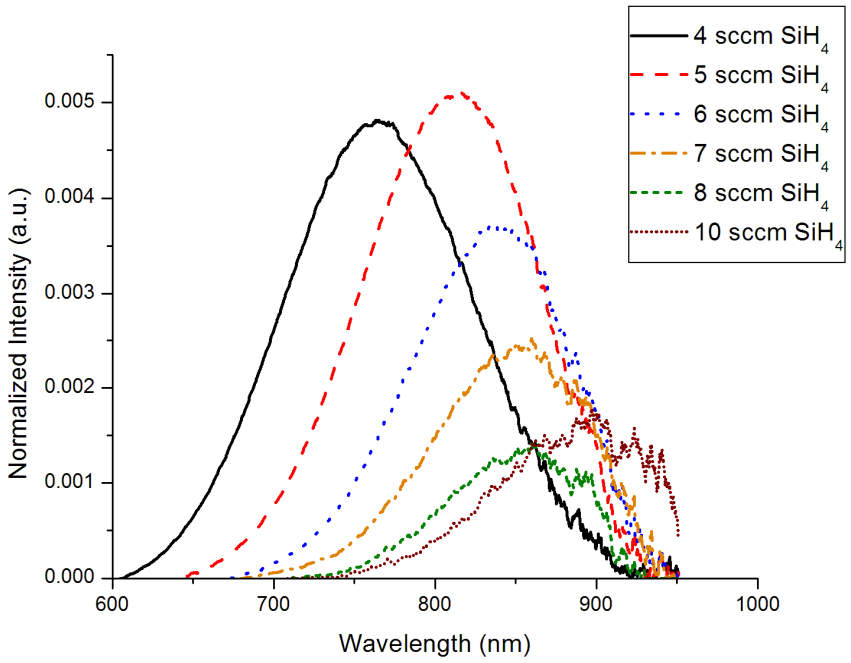

Figure 4.15: Peak PL Change in the PL peak position as the function of the SiH_4/He flow rate. The NCs are unetched. The SiH_4/He flow rate is varied between 4 and 10 sccm.

Thus by tuning both the SiH_4/He flow rate and varying the etch parameters one can achieve shortwave emission from SF_6-etched NCs.

4.6 Optical Properties

4.6.1 Changes in PL Peak Position Upon Air Exposure

We also investigated the oxidation-induced change in the PL of both as-produced and SF_6-etched NCs as illustrated in Figure 4.16. Samples A and B are unetched while

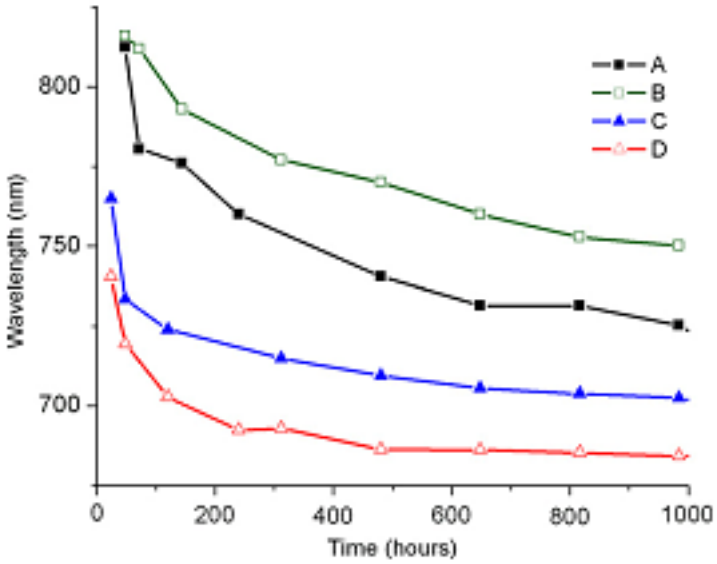

Figure 4.16: Changes in the PL peak position for both unetched and SF_6-etched NCs with the increase in air exposure time. The PL from samples A, B, C, and D originally peak at 812, 816, 724, and 719.5 nm.

samples C and D are SF_6-etched NCs. Samples A and B were initially measured ≈ 48 h after production because no visible PL was observed. This could due to the fact that the NCs initially emitted far into the infrared (which is outside the range of the spectrometer) or it took this amount of time to passivate non-radiative surface states via native oxide growth. The etched samples were measured within 24 h of production. Initially, the PL peak position from samples A, B, C, and D peak at 812, 816, 765, and 740 nm respectively. It is clear from Figure 4.16 that the NCs blueshift with continued exposure

to air at room temperature. This trend is indicative of oxidation-induced size reduction of SiNCs [42, 136] and was also observed with CF_4-etched NCs. After 500 h the rate of oxidation slows significantly for both the unetched and etched NCs as evidenced by small changes in the PL peak position. This observation is consistent to what has been previously observed for self-limiting oxidation of Si. [136, 144]

4.6.2 QY & QY Changes due to Oxidation

The quantum yield of SF_6-etched NCs was studied using the setup which was described in detail in section 3.4.3.7.

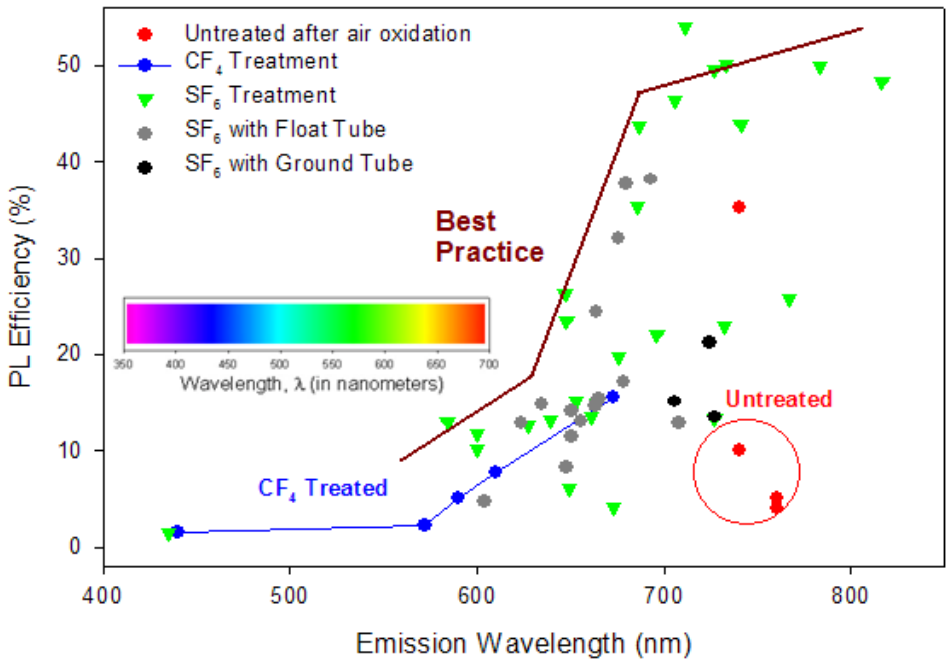

Figure 4.17: Quantum Yields from unetched and etched SiNCs synthesized with various etching configurations.

Figure 4.17 presents QY results from several different studies where the material of the etching tube was varied. All QY data presented in Figure 4.17 were measured after 15

days in air to ensure that the optical properties of the NCs have stabilized. The QY study from the CF_4-etched NCs shown in Figure 3.22 is replotted in Figure 4.17 to compare the efficiencies of the CF_4 and SF_6-etched NCs. From Figure 4.17 it is clear that the QY of the SF_6-etched NCs are significantly higher than those of CF_4-etched NCs at comparable wavelengths. For example at ≈ 590 nm, the QY of CF_4-etched NCs is approximately 5% while the SF_6 etched NCs have a QY of approximately 12%. The QY of SF_6-etched NCs is even higher than that of as-produced NCs at longer wavelengths. The highest QY that was observed for unetched NCs was approximately 30%. This is shown in Figure 4.17. SF_6-etched NCs emitting at a similar wavelength have QY which lie between 40 and 50%. Two other studies were also performed and the results are published in Figure 4.17. In this study a fine SS Mesh was placed inside of a hollowed out SS tube and centered inside of the quartz etching tube. We believed that the SS Mesh could capture the high energy particles which release O or damage the surface of the NCs causing a reduction in the QY. The polarity of the tube was either floated or fixed at ground. The hope was that this approach would improve QY past that of SF_6-etched NCs in the quartz tube. However, it is clear that the experiment did not work as planned. The QY of the SF_6-etched NCs synthesized with a grounded tube inside of the quartz tube has QY which are 2X less than that of the standard SF_6-etched NCs. A similar trend is observed when the floating tube is placed inside of the quartz reactor. The QY from several of these NCs are comparable but there are also several points that fall below that of CF_4-etched or as-produced NCs. This drop in QY may be the result of NC contamination from the incorporation of Fe, Ni, or Cr from the mesh removed during the etching process.

Further study is needed to develop a baseline in order to determine if the additional of a mesh inside of the etching plasma produces a positive effect.

Figure 4.18 provides a plot of the oxidation-induced change of the QY as a function of air exposure time. The unetched NCs, samples A and B exhibit little or no QY after 48h in air. After about 500 h in air, the QY of the unetched NCs has increases drastically and has stabilized near 30%. The behavior of the SF_6-treated NCs is quite different. After 48 h the QY of the etched samples C and D are ≈ 30%. As they continue to oxidize their QY approaches ≈ 40% after 500 h. This is very surprising for oxidized NCs. We have only observed efficiencies greater than 30% with NCs that have undergone alkyl passivation in a wet chemistry process. [41, 147, 148] Peak wavelengths from these NCs were limited to the red-infrared range. It is unusual for SiNCs to emit below 700 nm and be quite stable and efficient even after 1000 h in air.

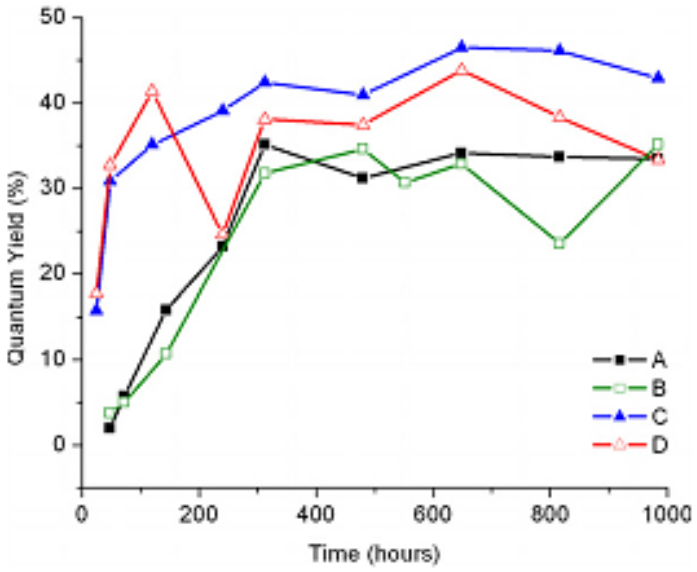

Figure 4.18: Changes in the QY for both unetched and SF_6-etched NCs with the increase in air exposure time. The QY from samples A, B, C, and D originally peak at 1.97%, 3.75%, 15.70%, and 17.74%.

From Figure 4.17 and 4.18 it is evident that the SF_6-etched NCs are much more efficient that that of as-produced or CF_4-etched NCs. Currently, we have no proven theory about why SF_6-etched NCs are so efficient. F incorporation in the oxide may play a role in the improved efficiencies by softening the oxide and improving the Si/SiOF interface. Also, the reduced plasma power in SF_6 plasmas compared to CF_4 plasmas may limit ion damage but more study is needed in order to develop a theory behind the enhanced PL and QY of SF_6-etched NCs.

4.7 Oxide Shell Calculations

The oxide shell thickness (or oxide growth rate) of both unetched and SF_6-etched NCs as a function of time was then estimated. In order to calculate the growth rate of the oxide (and its thickness), an approximation of the NC size was needed. This is a controversial topic at present and multiple models exist. Since were not interested absolute accuracy as much as the shift in the oxide thickness with exposure time to air, we adopted a relatively simple model constructed by Zunger and Wang. [28, 29] According to that analysis, the exciton energy (E_X) is defined as:

$$E_X = E_G - \frac{1.786}{E_C R} - 0.248 E_R$$

where E_G is the energy gap, given in eV by:

$$E_G = 1.167 + \frac{88.34}{(2R)^{1.37}}$$

and E_C is the coulomb energy which is given by:

$$E_C = 1 + \frac{(\sigma_{Si} - 1)}{1 + \left(\frac{0.69nm}{R}\right)^{1.37}}$$

where σ_{Si} is the bulk dielectric constant of Si (11.8) and R is the radius of the NC. The final term is the correlation energy. According to Zunger [29] E_R can be set to 8.18 meV. Thus, with the E_X measured by photoluminescence measurements, one can calculate R using the first and second terms on the right side of the equation. Finally, assuming a reasonably monodisperse NC size (from the synthesis plasma) and no initial oxide layer, the oxide thickness can be calculated by simply examining the change in the NC radius over time. This calculation must take into account that silicon oxidation consumes the bulk (≈ 44% of the oxide thickness) and that for a nonreentrant closed surface; the diameter of an oxidized NC includes two layers of shell oxide. The PL data was acquired by the USB2000 spectrometer.

Figure 4.19 provides the estimated oxidation data for several samples. One sample is an unetched NC sample, while the other three samples are SF_6-etched NCs. The SF_6 flow rate is varied in each of the three samples. From Figure 4.19 it is clear that the SF_6-etched samples oxidize much faster than the as-produced NC sample. The oxidation rate slows dramatically with increasing oxide thickness, achieving saturation at ≈ 2.3 nm. The results are in good agreement with the ellipsometry measurements by Raider *et al*. on flat silicon wafers. [171] It is interesting that the saturation value of oxide thickness is independent of surface treatment. Since this technique is actually measuring the change in oxide thickness rather than the thickness itself, this suggests that either the

NCs treated in the SF_6 plasma grow a much thicker oxide shell than the unetched NCs or that the initial oxide layer on the SF_6-treated NCs is extremely thin (<0.3 nm).

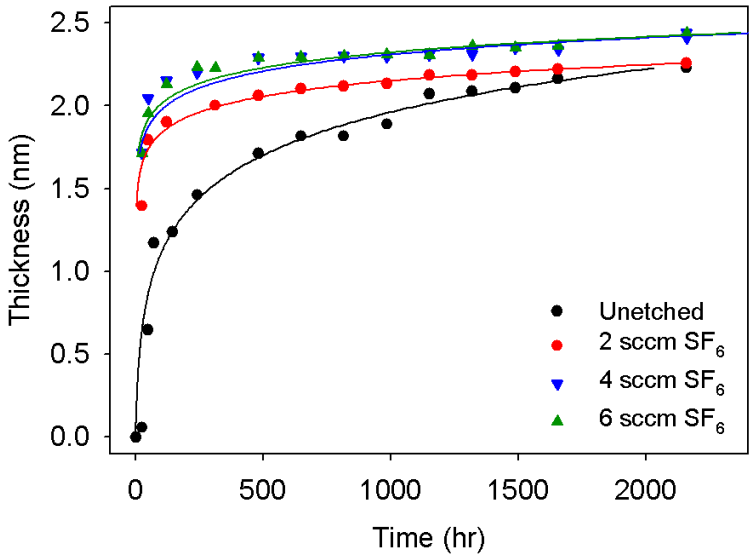

Figure 4.19: Oxide growth rate as a function of time for the unetched and SF_6-etched SiNCs with variable flow rates. The solid lines show 2 parameter fits to the Elovich equation.

The thermal oxidation of silicon has been heavily studied; however, most often these studies have been done at high temperature where the Deal-Grove mechanism, involving the diffusion of the oxidant through the growing oxide, is dominant. Near room temperature the diffusion coefficient of any potential oxidant in SiO_2 is far too small to support this oxidation mechanism. Instead, thermal oxidation follows the Cabrera-Mott mechanism. [172, 173] In this process, an electron from the silicon tunnels through the growing oxide and is captured by adsorbed oxidants such as O_2 and H_2O, due to their large electronegativity. This charged surface species creates an image charge in the silicon. The resultant dipole creates an electrostatic force that causes the oxidizing

species to drift through the growing oxide to the interface. The process is limited by the decaying exponential dependence of the tunneling probability on the oxide thickness.

The Cabrera-Mott mechanism is described by the Elovich [174] equation:

$$t_{OX} = r_O t_m * \ln\left(1 + \frac{t}{t_m}\right)$$

where r_o is the monolayer growth rate and t_m is a characteristic growth time. This equation was fit to the oxidation data, resulting in the solid lines shown in Figure 4.19. The Elovich equation provides an excellent fit to the data for the unetched sample and the 2 sccm SF_6 sample, but the fit is slightly less accurate for higher flow rates of SF_6. This may relate to the point raised previously, that a very thin initial oxide may be present in the films exposed to a larger free flux of fluorine radicals. It may also be the case that the oxidation rate slows with thickness as the surface fluorine is incorporated in the growing oxide and diluted by the oxidation process. Never the less, the fit is certainly adequate to provide useful information about the process.

The fit results are summarized in Figure 4.20. The initial monolayer growth rate increases sharply with the addition of SF_6 from 0.07 nm/hr for the unetched NCs to 915 nm/hr for the lowest SF_6 flow rate. Similarly, the characteristic growth time also drops by three to four orders of magnitude from 5.5 hours with the addition of F. Thus, it is clear that both the presence of fluorine and the absence of H on the surface of the NCs play important roles in the subsequent room temperature oxidation process. The lack of hydrogen termination leads to a much more rapid growth of the initial monolayer, while the incorporation of fluorine may lead to faster growth beyond the initial monolayer.

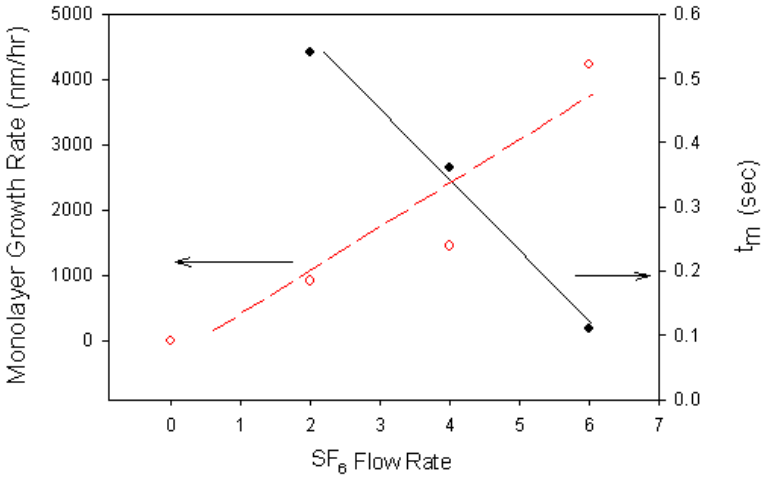

Figure 4.20: Elovich fit parameters as a function of the SF_6 flow rate. The left axis refers to the open circles, while the right refers to closed circles. The lines on the figure are only placed there as a guide.

Cerofolini *et al.* have looked at the dependence of the low temperature oxidation of planar silicon surfaces. [175] They demonstrated that the initial growth depends on both the surface chemistry and on the surface roughness. Unfortunately, little definitive experimental data exists for the situation present here: oxidation on rough, chemically treated (H or F) surfaces. Although they did not carry out a comprehensive study, Morita, *et al.* [176] found that a smooth hydrogen terminated (HF-treated) silicon surface had a monolayer coverage time of about 4 hours, comparable to our unetched value. For a rough but unpassivated surface Mende *et al.* found a t_m of 5 minutes and an initial growth rate of 0.84 nm/min. [177] Interestingly, Mende showed that the room temperature oxidation of unpassivated silicon is strongly affected by doping with N^+ doped silicon oxidizing much more rapidly than lightly doped material. Recalling that the Cabrera-Mott mechanism depends on the tunneling of electrons, this result is not too surprising. Fluorine is strongly electronegative. It would be reasonable to assume that F attaches to

the surface of the NC as F^- and so may change the effective doping of the NC. Finally, it is worth noting that NC size may play a role in the oxidation rate.

4.8 Effects of SF_6 plasma etching on NiO

The fabrication of novel materials is an interesting research topic. However, most researchers are not satisfied with the material itself. Most would like to try to integrate these materials into novel device architectures. The same can be said about the etched NCs. There optical properties are amazing and make them perfect choices for optoelectronic devices.

Recently, novel LED architectures have been developed by Bulovic and Bawendi at MIT for II-VI NCs utilizing both organic and inorganic transport layers. [21, 23, 78, 79] The device architectures introduced in [21, 23, 78, 79] is a starting point and or an initial architecture for SiNC based EL devices. Typically, TPD, which is a hole transporting small molecule material, is vapor-deposited on ITO/Glass and serves as the hole transport layer in the II-VI devices. [21, 23] However, organic materials do not survive exposure to F-based plasma. As a result, any hole transport layer must be able withstand the plasma chemistries generated in SF_6 plasma. Recently, Caruge *et al*. [78, 79] have demonstrated that it possible to use inorganic metal oxides as an alternative to organic materials. We are specifically interested in NiO because its E_C (-1.8 eV) and E_V (-5.5 eV) make it an ideal hole conducting material. [79] However, before we begin to integrate NiO with etched NCs in a novel device architecture we first need to determine what effects the SF_6 plasma will have on an NiO thin film. In order to resolve this we

performed a thorough XPS investigation of the surface of the NiO when it was exposed to common etching chemistries.

4.8.1 Deposition of NiO thin films

Nickel Oxide (NiO) thin films were deposited by sputtering from a NiO target (nominally 99.995% pure) in a mixture of Ar and O_2 on 4" silicon substrates using an ATC-2000 AJA custom sputtering system. The system was evacuated to a pressure below $9*10^{-7}$ Torr by a cryopump before beginning deposition. To minimize the amount of contamination on the samples, a 5 minute pre-sputter step was used. During this step, the plasma was lit inside of the chimney while the shutter remained closed. This allows the removal of any unwanted impurities (from the chimney walls) and at the same time coats the chimney with a NiO film. After this step, the shutter was opened allowing NiO to be deposited on the substrates. In this study, the Ar flow rate was set at 18 sccm and the O_2 flow rate was fixed at 2 sccm (controlled via mass flow controllers). The chamber pressure was held at 3 mTorr. The applied RF power was set at 200W. During sputtering the substrates were heated to 350C to minimize surface roughness.

Following deposition the sputtered NiO films, the samples were cut into several pieces and transferred to a custom silicon NC synthesis and passivation system which has been discussed in detail in both chapter 3 and the experimental setup in section 4.3. [111, 112, 153]. To avoid ion bombardment for this study and restrict the results to chemical effects only, the NiO films were placed downstream of two different plasma mixtures: SF_6/Ar and SF_6/Ar/H_2 The flow rate of Ar and SF_6 were held constant at 50 and 4 sccm in

both cases, while H_2 was fixed at 3 sccm. The power delivered to the RF capacitively coupled electrode was set at 10W at a pressure of approximately ≈ 300 mTorr. A NiO area of approximately the inner diameter of the tube (0.875 inches) was exposed to the down stream plasma for 30 minutes. Typical exposure times for the devices of interest will typically be less than 5 minutes.

4.8.2 Characterization Setup

After exposing the NiO films on silicon wafers to the fluorinated plasma, the samples were transferred to the x-ray photoelectron spectrometer (located remotely from the plasma system). As a consequence, the surfaces were air exposed. Surface measurements were then performed on the deposited NiO films. The XPS system was operated at a pass energy of 150 eV for survey spectra and a 50 eV pass energy to obtain high resolution spectra. XPS data were excited using a monochromated aluminum K_α x-ray source operated at 200W onto an elliptical spot of approximately 800 x 200 micrometers. Data were taken at a take-off angle of 55° relative to the sample normal. The vacuum during operation was maintained below 2×10^{-9} Torr.

Air exposure typically results in some carbon contamination and in the formation of a surface oxide on NiO. Analyses were performed from the survey spectra and from high resolution spectra taken of the C 1s, O 1s, F 1s and Ni 2p spectral regions. Curve fitting was performed using XPS International's Spectral Data Processor v4.3 and is based on a standard Gaussian-Lorentzian model. Peak background was approximated

using a Shirley background to determine peak amplitudes and to obtain curve fitting parameters to the high resolution spectra.

In general, the surface produced by sputter deposition is nearly stoichiometric NiO on silicon. For reference, an Auger electron spectroscopic depth profile obtained using a PHI 545 electron spectrometer was obtained for a typical "control" sample. The profile is shown in Figure 4.21 where Ni and O track over the depth of the film and show NiO. Therefore, it is adequate to discuss the surface composition as a function of post treatment with fluorine and hydrogen containing plasmas to obtain an overview of the chemistry.

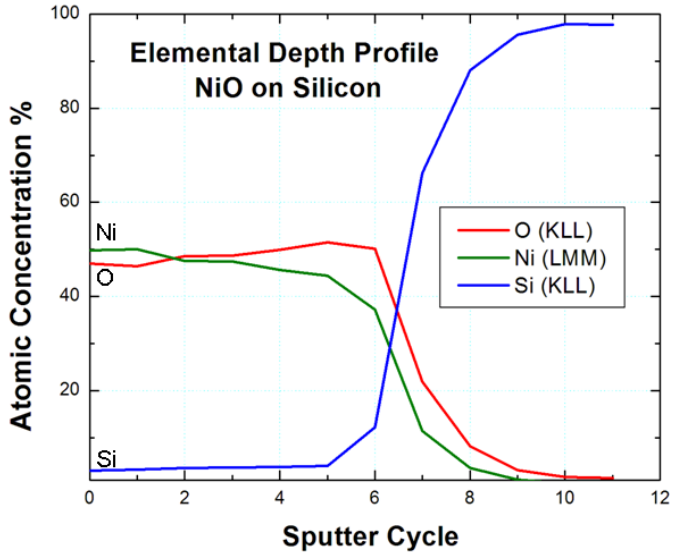

Figure 4.21. Auger Electron Spectroscopy (AES) elemental depth profile of as-deposited (control sample) NiO on Silicon.

4.8.3 XPS Characterization

Although a number of deposition conditions were employed to deposit the NiO films and the down stream plasma treatments were varied in a matrix, this has been reduced to the control sample, as reference, the sample treated in SF_6/Ar and the sample

treated in $SF_6/H_2/Ar$ as described above. Survey spectra were obtained of these 3 samples.

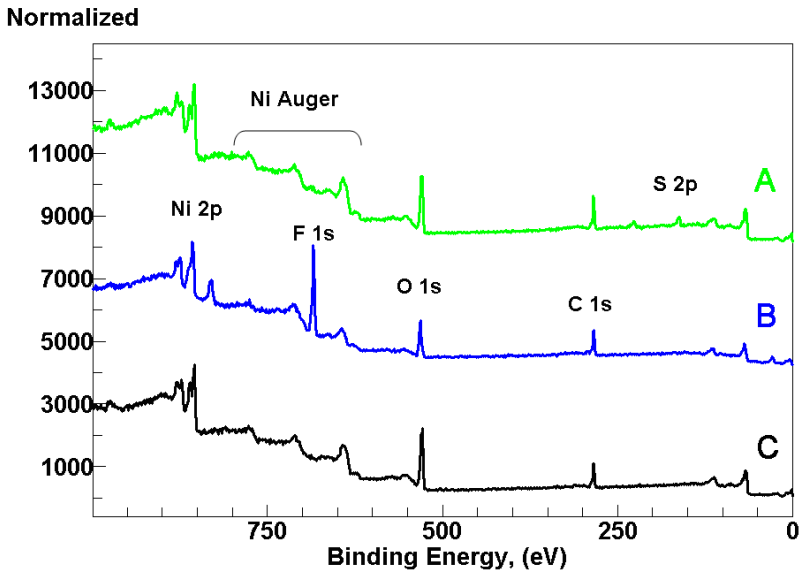

Figure 4.22. XPS survey overlays of $Ar/SF_6/H_2$ treated NiO on Si (A); Ar/SF_6 treated NiO on Si (B) and "as-deposited NiO on Si (C).

Figure 4.22 shows an overlay of the survey spectra from the NiO samples as a function of post treatments in the fluorine rich and hydrogen rich plasmas. The "as-deposited" survey spectrum shows, as expected, carbon, oxygen and nickel (their associated photo-electron and Auger peaks). Quantitative analysis from the survey spectra shows the surface to be carbon contaminated. However, quantitative analysis is not accurate. The Ni $2p_{3/2}$ was not used due to difficulties in approximating the background [178-182]. Table 4.1 shows the results of this semi-quantitative analysis from the survey spectral data.

After treating the sample in the Ar/SF_6 plasma, the surface becomes fluorinated. F 1s peak is observed at ≈ 680 eV (with an atomic concentration of 36%) and the composition of Ni, O and C is changed significantly relative to the untreated surface.

Element	As-Deposited	Ar/SF_6	$Ar/SF_6/H_2$
Ni	34%	19%	27%
C	32%	29%	37%
O	34%	19%	29%
F	-----	36%	<1%
S	-----	-----	6.5%

Table 4.1. Semi-quantitative analysis of the NiO treated surface from the survey spectra shown in Figure 4.21.

After exposure in the $Ar/SF_6/H_2$ plasma, most of the fluorine is removed resulting in a further modified surface composition. The NiO surface becomes fluorinated when exposed to the fluorinated plasma, but fluorine is mostly removed after hydrogen plasma treatment along with most of the NiO layer exposing some of the substrate and some sulfur contamination. It is well known that atomic hydrogen will rapidly reduce NiO to Ni [183, 184]. However, the mechanism involved in forming the fluorinated surface and removing it has not been studied.

The untreated NiO sample was used as a control to study the surface chemistry of the NiO deposition on silicon prior to surface treatment. Curve fitting the Ni $2p_{3/2}$ peak using the usual Gaussian/Lorentzian model is shown in Figure 4.23. The main peak is due to the Ni $2p_{3/2}$ photoelectron peak and is resolved into component peaks at 853.7 eV, 855.4 eV, and 857 eV and are due to NiO, $Ni(OH)_2$ and NiO_x ($x \approx 1.5$) using Barr's

scheme [185]. The peak components around 861 eV are due to shake-up phenomenon and will not be discussed here [178-182]. The peak positions are in good agreement with literature references [178-182, 186-189] observed for NiO. These data form the reference for the remainder of the analysis for post deposition plasma treatments.

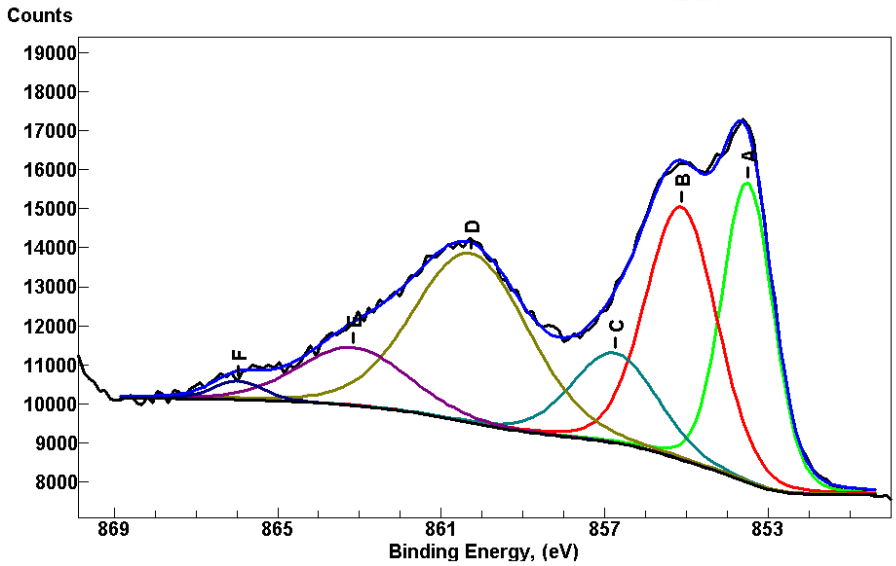

Figure 4.23. As deposited NiO on Si - Nickel 2p3/2 peak curve fitted. The main peaks (A, B, & C) are due to NiO, $Ni(OH)_2$ and $\approx NiO_x$ (where $x > 1$), respectively.

Semi-quantitative analysis of these data show a ratio of Ni (peak A):O (peak A) of 30:70 which is clearly not consistent with stoichiometric NiO. Using sensitivity factors and peak component areas to define the material does not appear to be a useful approach as shown in refs [178-182]. Using the Ni 3p or 3s peaks provides reasonable quantization of the surfaces but these peaks were not obtained as high resolution spectra. However, peak binding energies are consistent with published information for NiO. In the following discussion, all the peak component binding energies are summarized in table 4.2.

Assignment	As Deposited		Ar/SF_6		$Ar/SF_6/H_2$	
	BE (eV)	Rel. Area	BE (eV)	Rel. Area	BE (eV)	Rel. Area
Nickel $2p_{3/2}$						
NiO	853.5	22.6%	856.89	57.5%	853.71	30.0%
Ni-OH	855.13	26.6%	859.46	11.8%	855.39	21.8%
Ni_2O_3	856.75	11.3%	853.67	1.1%	856.85	11.0%
Shake-up	860.27	28.7%	-	-	860.56	31.5%
Shake-up	863.15	9.4%	862.75	26.1%	863.68	4.5%
Shake-up	865.96	1.4%	866	3.5%	866.04	1.2%
Shake-up Sum		39.5%		29.6%		37.2%
Oxygen 1s						
O_{ads} or OF_x	532.97	6.6%	532.26[a]	91.6%	532.99	9.2%
OH	531.11	51.6%			531.34	44.1%
O in NiO	529.14	41.7%	528.98	8.4%	529.34	46.7%
Fluorine 1s						
F-ONi	-	-	684.49	84.2%	683.65	<1%
curve fit			686.54	10.0%		
C-F Bond			688.28	5.8%		

[a)]The peak at 532.26 eV for O 1s is likely due to O-F bond formation

Table 4.2. The Ni 2p3/2, O 1s, and F 1s peak component relative areas (functional composition) are shown as a function of plasma treatment. C 1s is at 284.6 eV.

Peak components of the O 1s spectrum as shown in Figure 4.24 are observed at 532.85 eV, 530.95 eV, and 529.1 eV. Using Barr's [185] scheme for surface oxidation the peak at 532.85 eV is due to mostly adsorbed O, at 530.95 eV, it is due to hydroxide or a dissociated O species and 529.1 eV is due to stoichiometric NiO [178-182, 185]. This peak is observed to change with plasma treatment and will be described in more detail below.

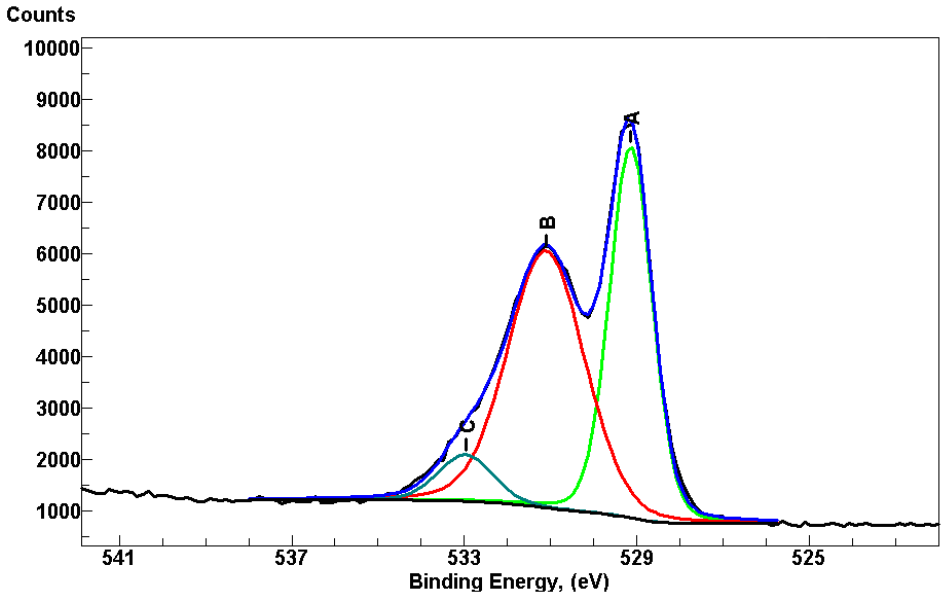

Figure 4.24. Oxygen 1s spectral region for the as deposited NiO on Si. Peak components are identified as (A) O-Ni bonded, (B) OH-/dissociated O/O-C and (C) adsorbed O.

Figure 4.25 shows the curve fitted Ni $2p_{3/2}$ and O 1s peaks after exposure to the Ar/SF_6 plasma. The Ni peak components are broadened as compared with the untreated sample and may not be well resolved. A small peak is observed at 853.6 eV and is likely due to residual NiO at the near surface. Although the Ni $2p_{3/2}$ shows that NiO is still observable, a large amount of fluorine is has been incorporated at the surface as shown from the survey spectrum in Figure 4.22. The large peak "A" is likely due to OF_x bonding [190]. It is interesting to note that the O 1s peak components are significantly changed as a result of this treatment. Figure 4.24 shows that the main peak (A) is observed at ≈ 532.3 eV. This is consistent with the formation of OF_x bonds. Both the Ni $2p_{3/2}$ and O 1s components are consistent with the formation of a layer of OF_x at the surface of the NiO deposited layer on silicon. The O 1s peak component "C" at ≈ 529 eV is due to O bound to Ni as NiO. This is consistent with the Ni $2p_{3/2}$ data

interpretation. The smaller O 1s component peak is not readily identified and may be a curve fitting artifact.

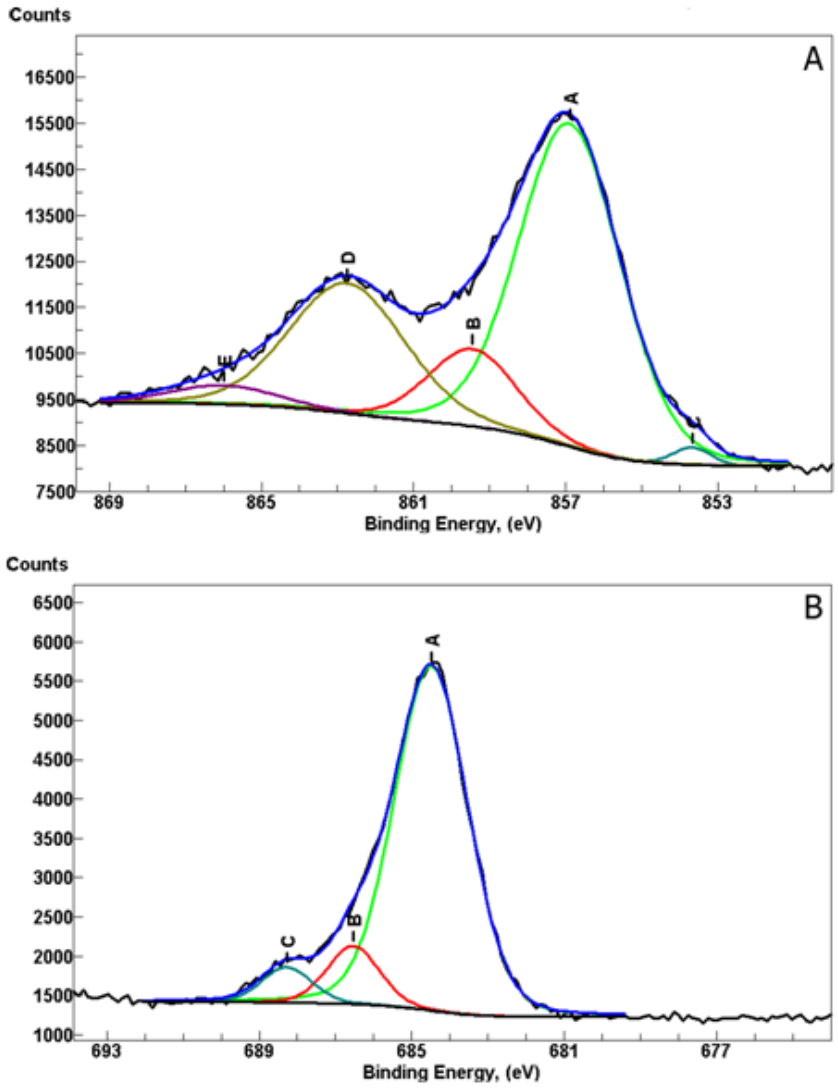

Figure 4.25. Ar/SF_6 treated NiO on Silicon. Curve-fitted components for the Ni $2p_{3/2}$ (A) and O 1s (B) peaks are shown.

Spectral data for C 1s (A) and F 1s (B) are shown in Figure 4.26. Four components were identified through curve fitting. First, in Figure 4.26(B) the main component "D" is due to C-C/H bonds. The smaller component "A" at ≈ 292.5 eV is due

-CF_3 bonded carbon showing that the SF_6 had a strong effect on the residual carbon chemistry at the surface. The other two components, “B” and “C” are likely due to -O/OH bonded and/or -CHF groups bonded to carbon. The F 1s peak (Figure 4.29(A)) consists of three components where the most intense peak component “A” at 684.5 eV is associated with F in $NiOF_x$ functionality as described in reference 72. The other two peaks are difficult to identify but may be, in part, due to curve fitting anomalies. The higher binding energy peak “C” appears to be real and from the literature it is identified as -F_3C pendant groups.

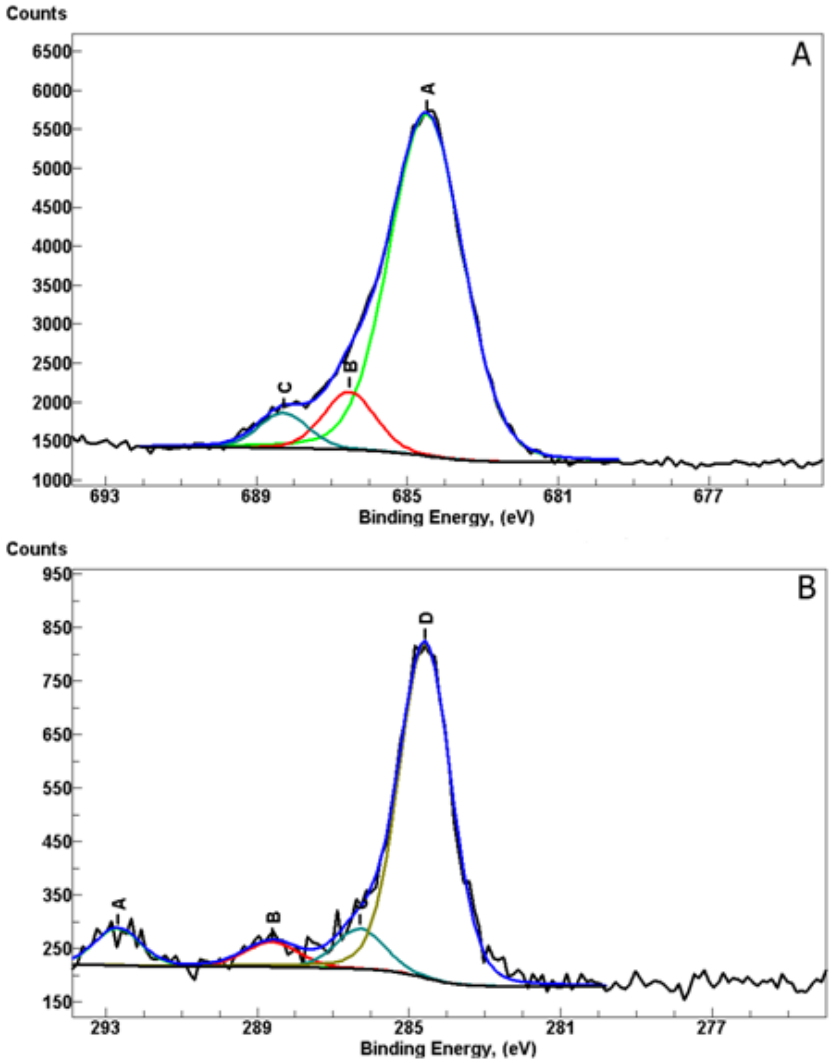

Figure 4.26. Ar/SF_6 treated NiO on Silicon. Curve fitted components for the (A) F 1s and (B) C 1s peaks are shown.

Figure 4.27 shows the Ni $2p_{3/2}$ and O 1s peaks and their curve fitted components after $Ar/SF_6/H_2$ plasma treatment of NiO. As shown in Figure 4.22, after $Ar/SF_6/H_2$ plasma treatment, the surface of the NiO deposit is returned mostly to its original state. This again shows that the Ar/SF_6 treatment does result in the formation of a thin layer that can be readily removed in the hydrogen rich plasma.

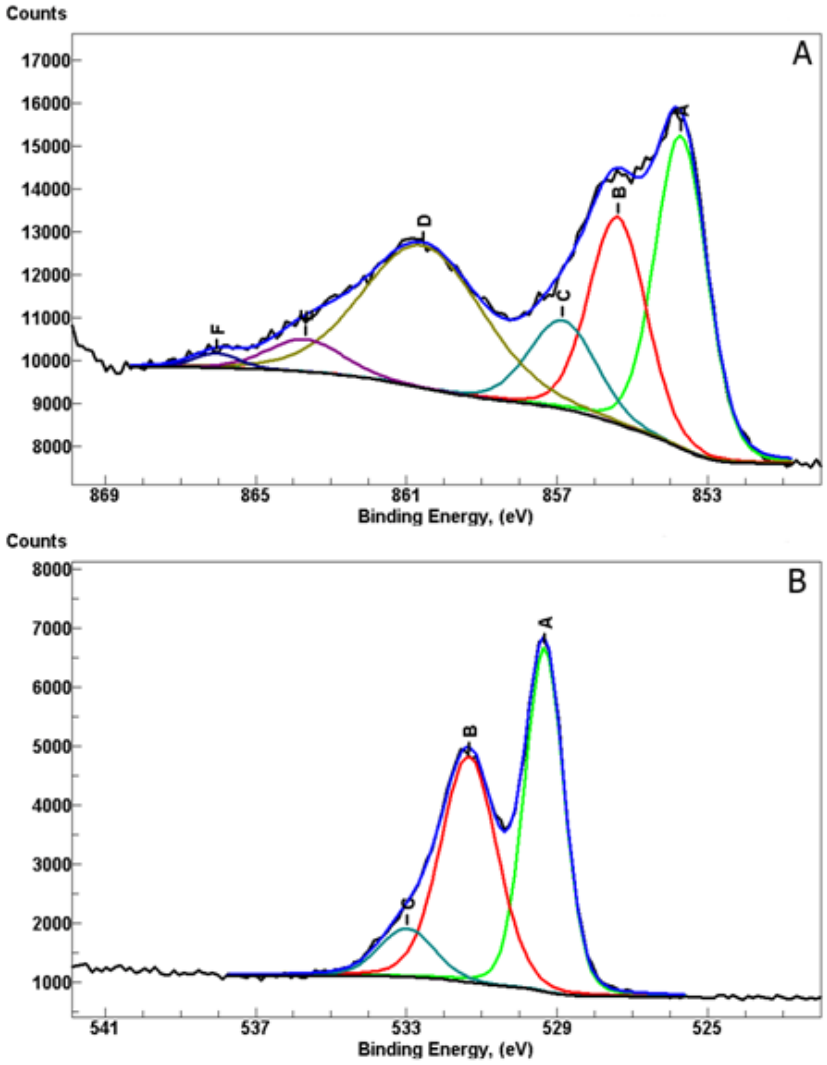

Figure 4.27. $Ar/SF_6/H_2$ treated NiO on Silicon. Curve fitted components for the (A) Ni $2p_{3/2}$ and (B) O 1s peaks are shown.

The Ni $2p_{3/2}$ main difference appears to be in the relative area (see table 2) of component "B" of the Ni $2p_{3/2}$ peak and component "B" of the O 1s peak. The ratio of the "A" component of the Ni $2p_{3/2}$ and O 1s peaks are similar to the NiO "standard." This surface is cleaned by exposure to the hydrogen containing plasma leaving a small amount of sulfur contamination (from table 4.1 around 7%.)

It is well known that hydrogen is effective in the reduction of many materials and in specific interest is the reduction of NiO to elemental Ni [183, 184, 191]. Therefore, it is reasonable to state that hydrogen reactively removed the fluorine bonded components at the surface of the NiO exposed to the Ar/SF_6 plasma.

Exposing NiO thin films, the chosen substrate material for subsequent device fabrication, to the low density capacitively coupled RF excited discharge results in a significantly modified surface layer. In the Ar/SF_6 plasma environment, the NiO surface becomes fluorinated similar to that observed for exposure to CF_4 plasma. The NiO surface is fluorinated as $NiOF_x$. After exposing the surface to the $Ar/SF_6/H_2$ plasma, the fluorinated species is mostly removed leaving a reasonably clean NiO surface. Analysis of the surface layer from the peak component binding energies show that the surface is contaminated with a small amount of sulfur is also observed on the NiO surface and is probably due to a reaction of a component of SF_6 formed in the plasma. Since the NiO surfaces are not subjected to high energy bombardment, physical sputtering is unlikely. No thickness change was observed from the NiO samples exposed to either Ar/SF_6 or $Ar/SF_6/H_2$ indicating that no etching of the bulk film occurred. Therefore, the species formed and removed appear to be limited to the immediate surface of NiO.

4.9 Conclusions

In conclusion we have demonstrated that SF_6 etching of SiNC is a viable alternative to CF_4 etching. Unlike the CF_4 process, there is no mechanism which inhibits etching. Therefore an increase in the RF power or the SF_6 flow rate yields smaller NCs. Measured QY of SF_6-etched NCs are at least 2X that of CF_4-etched NCs at comparable wavelengths. A maximum QY of 55% (at 710 nm) was measured for SF_6-etched NCs after 15 days of exposure air. This high QY has only been observed in alkyl passivated SiNCs. The origin of the improved optical properties is under investigation, but F may play a crucial role. The native oxidation of both unetched and SF_6-etched NCs follows the Cabrera-Mott mechanism where the oxide thickness saturates near 2.3 nm regardless of surface chemistry.

Ar/SF_6 and $Ar/SF_6/H_2$ plasmas were exposed to RF sputtered NiO thin films to determine what kind of an effect the NC synthesis and etching plasma would have on the NiO thin films. No physical etching was observed, but depending on the etch chemistry the surface either resembles that of clean NiO ($Ar/SF_6/H_2$) or fluorinated NiO (Ar/H_2). More work is needed to determine what kind of an effect the surface will have on the electrical properties of the NiO thin films.

Chapter 5

Fabrication and Characterization of Metal-Oxide Transport Layers and their Integration into Novel Inorganic-Silicon nanocrystal based Electroluminescent Devices

5.1 Chapter Overview

This chapter is divided into three sections. The first section will cover the fabrication of metal-oxide thin films which will be used as transport layers for the inorganic-NC based electroluminescent devices. Specifically, the fabrication techniques used to deposit (RF Sputtering and Atomic Layer Deposition) nickel oxide (NiO), titanium dioxide (TiO_2) and zinc oxide will be discussed. The optimal fabrication conditions will be discussed. The second part of this chapter will focus on the characterization of these thin films. Several different techniques were used to study the surface chemistry, surface topology, electrical, and optical properties of NiO, TiO_2, and ZnO. Finally, I will discuss the integration of these films into novel device architectures. The device design will be discussed and the fabrication procedure used to synthesize these devices will be introduced. Early results based on a simplified device design will be discussed. Finally, an improved device structure which requires some additional processing will be introduced.

5.2 Fabrication of Metal-Oxide Thin Films

This section will discuss the two techniques used to deposit the metal-oxide transport layers used for inorganic-NC EL devices. Before discussing the fabrication in greater detail, the following section will provide a basic review of the principles of both sputtering and atomic layer deposition. For a more through review on these fabrication techniques we encourage the reader to consult [192].

5.2.1 Atomic Layer Deposition – A Simple Overview

Atomic Layer Deposition (ALD) is an offshoot of chemical vapor deposition which was pioneered by Tuomo Suntola in the 1970's while developing electroluminescent flat panel displays. [193-197] Like CVD, gaseous precursors are introduced into the reactor which contains the substrate which will be coated. According to Campbell [192] the ALD process relies on sequential introduction into the reactor of two gases which have the following properties: (1) at least one of the precursors (in this case one of the gases) will saturate once a monolayer has formed on the sample's surface (thus preventing any further growth) and (2) the other precursors will react with the as-deposited precursor, forming a few atomic layers on the substrate. To avoid gas-phase reactions between the two thin film precursors, the ALD system typically is purged between cycles. However, newer industrial-based systems like the Savannah (Cambridge Nanotech) do not utilize this technique, rather nitrogen (standard purge gas) is passed through the chamber at all times helping to remove the unreacted precursor materials. The common ALD deposition sequence is as follows:

I. Pulse in precursor material A

II. Purge ALD chamber with N_2

III. Pulse in precursor material B

IV. Purge ALD chamber with N_2

V. Repeat Steps I-IV as needed

Figure 5.1 provides a visual representation of the ALD process.

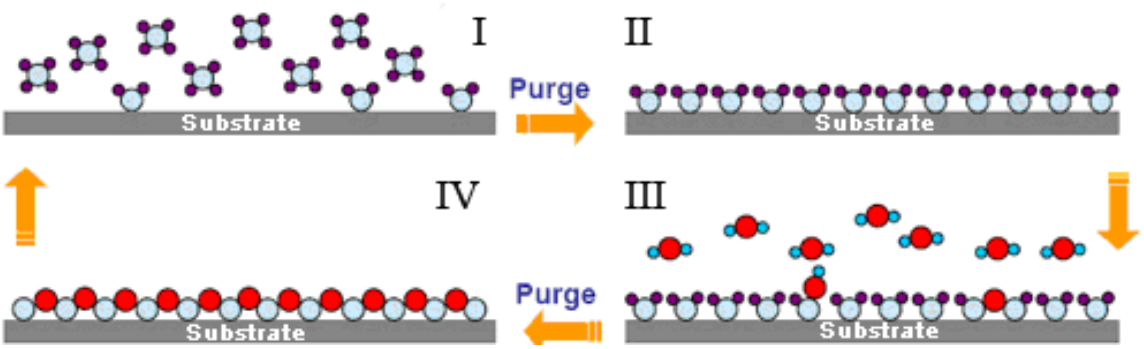

Figure 5.1: Visual representation of the ALD growth process. Reproduced from http://gcep.stanford.edu/research/factsheets/atomic_layer_deposition.html. One growth cycle is presented.

The ALD growth rate not only depends on the number of deposition cycles but also the growth temperature. Kim [198] notes that there is a growth window for ALD deposition. Figure 5.2 illustrates the growth window for ALD.

For low temperatures (Kim denotes 150°C – 300°C as low temperatures) the growth rate increases as the temperature increases. Further increase in the temperature generally leads to the so-called process window where the growth rate remains constant over a range of temperatures. At high temperatures, thermal decomposition of the precursors can lead to a further increase in the growth rate. This is essentially chemical vapor deposition. Desorption of some materials from the substrate may actually lead to a

decrease in the growth rate at high temperature. [198] The trend shown in Figure 5.2 should be treated as a guideline on ALD growth. The growth window will depend heavily on the chemistry of a particular process. In certain cases, there is no process window.

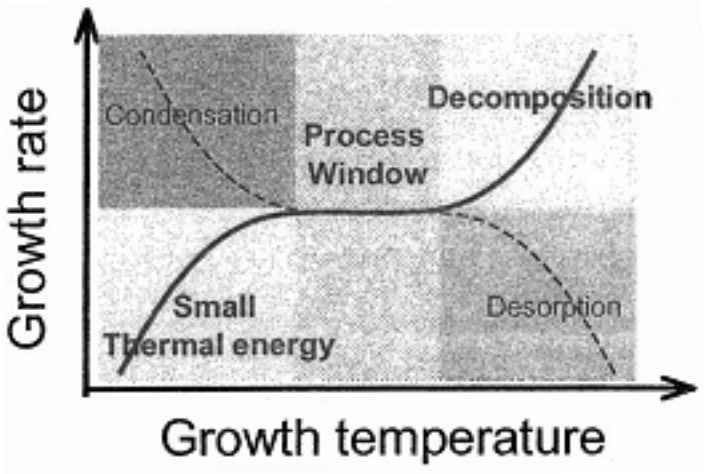

Figure 5.2: ALD growth rate as a function of growth temperature. The process window is the ideal region for ALD growth. Reproduced from [192, 198].

The ALD process has many advantages over similar fabrication processes (like CVD). The advantages of ALD are summed up below. First of all, the film thickness depends solely on the number of cycles (in the growth window) which allows for simple deposition process with an accurate thickness control. ALD has the capability of depositing a wide variety of high-quality materials (see Figure 5.3) that are free from impurities. pin-holes and are relatively smooth (compared to similar processes). Furthermore, low growth temperatures allow for the deposition of ALD films on materials which would not survive standard CVD or sputtering, such as polymers or small molecule materials which are extremely sensitive to temperature.

Elemental Metals	Cu, Ru, Ir, Pt, Pd, Co, Fe, Ni, Mo
Diffusion barriers	WN, TiN, NgN, MoN, TaN, Al_2O_3
Gate insulators	Al_2O_3, ZrO_2, HfO_2, $HfAlO_2$, Ta_2O_5, La_2O_3, PrAlO, TiO_2, $HfSiO_2$, HfSiON, laminates
Sensors and piezoelectrics	SnO_2, Ta_2O_5, ZnO, AlN, ZnS
Optical applications	AlTiO, SnO_2, ZnO, SrS:Cu, ZnS:Mn, ZnS:Tb, SrS:Ce, Al_2O_3, SnO_2, ZnS, Ta_2O_5, Ta_3N_5, TiO_2
Transparent conductors	ZnO:Al, InSnO

Figure 5.3: Materials which have been deposited by ALD. Reproduced from [192].

Despite the advantages of ALD, there are still several limitations to the process which may hinder widespread use of the technology. The major problem with ALD is the deposition time. The process is extremely slow. For example, the ALD NiO process that we use to deposit for HTL layers deposits only 0.4Å/cycle where 1 cycle takes 1 minute to complete. Therefore, to deposit 40 nm (a typical thickness for a transport layer); one would have to deposit for 1000 minutes (≈ 17 hours). Another major concern is the incorporation of impurities (or contamination) into the deposited film from unwanted or incomplete reactions which occur during the ALD process. A third issue with the ALD process is the low material consumption. The precursor materials which are pulsed into the reactor are not totally consumed during the process. As a result, a significant amount of precursor material is wasted. This problem is magnified when an expensive precursor is used during a long deposition run.

5.2.2 Sputtering – A Simple Overview

Sputtering is a common fabrication process which can be used for the deposition of both metals and oxide materials. Sputtering has been known to the scientific community since the 1850's [192, 199], but was not utilized for thin films until the

1920's. [192, 200] Figure 5.4 provides a simple schematic of a sputtering system. In order for sputtering to occur, the geometry of the chamber must be oriented to allow the generated ions to impact upon the target material. Thus the target is typically placed on the electrode which receives the largest ion flux. [192] In order to collect as many sputtered atoms as possible the working distance between the target and substrate electrode is small (≈ 10 cm [192]). An inert gas, typically Ar is fed into the chamber. A plasma is then struck, which generates different chemical species, including Ar ions which are used to sputter the target. The pressure in sputtering systems is usually in the mTorr range to ensure that the sputtered atoms can reach the substrate (creating a large mean free path) [192].

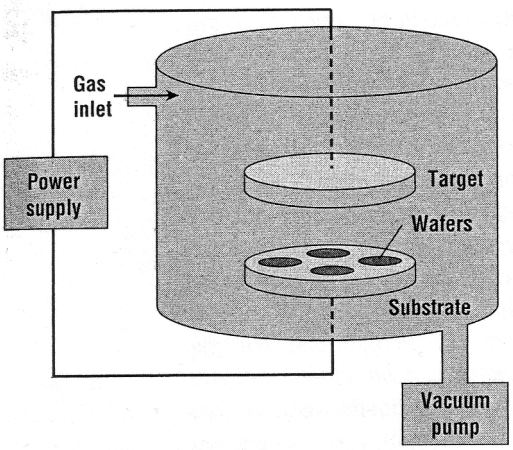

Figure 5.4: Simple Sputtering System Schematic. Reproduced from [192].

Sputtering systems are typically operated with a DC (for metals) or RF (insulating materials) plasma. [201] For a more thorough discussion on plasmas we encourage the reader to consult Lieberman and Lichtenberg. [202]

When a material is sputtered there are four possible outcomes. These outcomes are shown in Figure 5.5.

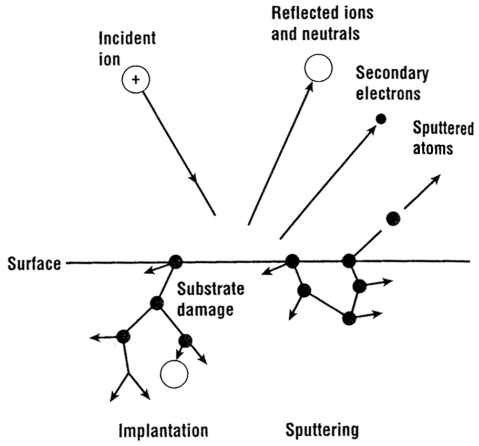

Figure 5.5: Outcomes when an incident ion hits the surface during the sputtering process. Four events typically occur: ions can bounce of the surface, adsorb to the surface, sputter off an atom, or be implanted. Reproduced from [192].

When an ion hits the surface of the target material with a low energy, the ion may simply bounce of the surface. At 10 eV the ions can absorb to the surface, transferring its energy to phonons. [192] Ions with extremely high energies (> 10 keV) are typically injected into the material (this is also known as ion implantation). When the energy of the ion falls between 10 eV and 10 keV both processes occur. Some ions simply absorb and heat is transferred to the substrate. However, physical rearrangement of the substrate can also occur, leading to the ejection of the target material.

The deposition rate of a particular material from a sputtering system depends on several factors which include: ion flux to the target, probability that the impact of an incident ion will eject a target atom and the transport of the sputtered material across the plasma to the substrate. [192] Examining the sputter yield of a particular material gives an indication of the deposition rate of that material. Materials with high sputter yields

will have high sputter deposition rates. Figure 5.6 presents the sputter yield of different metals at various ion energies.

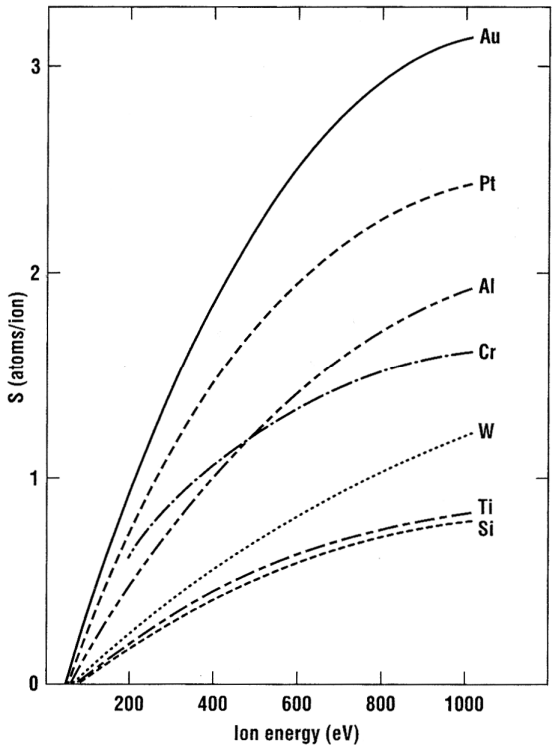

Figure 5.6: Sputter yields of a several elements as a function of Ar ion energy. Reproduced from [192].

This section only presents a basic review of the sputtering process. For more information on the sputtering process, glow discharges and ALD we encourage the reader to consult [192, 202, 203].

5.2.3 Sputter Deposition of Metal-Oxide Thin Films

The sputter deposition of both TiO_2 and NiO was carried out in a ATC-2000 AJA custom sputtering system which utilizes 4 sputtering guns (2 RF, 2 DC) and has precise

control over the system pressure (through a computer controlled throttling valve), gas flow rates, applied power, and substrate temperature. The next two sections describe the basic setup to deposit both NiO and TiO_2 thin films.

5.2.3.1 RF Sputtering of Nickel Oxide (NiO)

Although many deposition techniques exist for NiO [204-209], RF sputtering was chosen for two reasons. First of all, hybrid inorganic (or organic) – II-VI NC device architectures using RF sputtered NiO as a HTL had been demonstrated proving not only that NiO can act like a semiconductor [210], but also that RF sputtering was a viable deposition technique. [78, 79] Secondly, the AJA sputtering system in the NFC is similar to the system used in [78, 79] and thus we believed that it would be possible to obtain high quality, smooth NiO thin films that could be used as transport layers.

Early attempts at depositing NiO were a struggle. Initially, we tried to mimic the deposition parameters discussed in [78, 79], but the results were not encouraging. After this we decided to simply alter the deposition parameters until we arrived at the conditions which would yield a more ideal NiO film (Stoichiometric NiO, with a thickness of about 50-60 nm). The characterization of the sputtered NiO films will be discussed in detail in the section 5.3. Eventually, we were able to deposit stoichiometric NiO with the appropriate thickness by using a process which was developed by another graduate student in the research group. The deposition conditions are summarized below.

The Nickel Oxide (NiO) thin films were deposited by sputtering from a NiO target (nominally 99.995% pure) in a mixture of Ar and O_2 on 4" silicon substrates using

an ATC-2000 AJA custom sputtering system. Interestingly, most literature on sputtering NiO utilizes a pure O_2 [211-213] or Ar/O_2 plasma [78, 79, 210] as the sputtering source. We were unable to investigate NiO thin films sputtered in a pure O_2 plasma because of plasma stability problems in the sputtering system. Sputtering NiO in a pure O_2 discharge would be another worthwhile experiment, however we first need to determine why a pure O_2 plasma can not be maintained in the sputtering system.

The system was evacuated to a pressure below $9*10^{-7}$ Torr by a cryopump before beginning deposition. To minimize the amount of contamination on the samples, a 5 minute pre-sputter step was used. During this step, the plasma was lit inside of the chimney while the shutter remained closed. This allows for the removal of any unwanted impurities (from the chimney walls) and at the same time coats the chimney with a NiO film trapping any remaining impurities. After this step, the shutter was opened allowing NiO to be deposited on the substrates. The Ar flow rate was set at 18 sccm and the O_2 flow rate was fixed at 2 sccm (controlled via mass flow controllers). The chamber pressure was held at 3 mTorr by a throttle valve. The applied RF power was set at 200 W. During sputtering the substrates were heated to 250°C to minimize surface roughness and rotated to ensure thickness uniformity over the entire substrate. The deposition conditions above led to a NiO thickness of approximately 45 nm in a 2 hour deposition, yielding a deposition rate of approximately 23 nm/hr. The thickness of the NiO thin films were tested immediately after synthesis by ellipsometry and profilometry.

5.2.3.2 RF Sputtering of TiO_2

Similar to NiO, the sputter deposition of titanium dioxide has been investigated thoroughly. [214-225] For this study, TiO_2 thin films were deposited in the same sputtering system as the NiO thin films. In this particular setup, a TiO_2 target (nominally 99.998% pure) was sputtered in an Ar/O_2 atmosphere. To obtain stoichiometric TiO_2, the following conditions were used. The Ar and O_2 flow rates were set to 4 and 24 sccm respectively. The applied RF power was set to 175W and the substrate was heated to 200°C. The pressure in the system was maintained at 2 mTorr. Total sputtering time for these films was 5 hours. The major issue with sputtering TiO_2 is the deposition rate. Figure 5.7(a-b) displays the TiO_2 film thickness as a function of sputtering time and pressure. After 2 hours of sputtering only ≈ 10.5 nm of TiO_2 has deposited on the substrate. This figure increases to ≈ 17 nm after 4 hours of sputtering for a deposition rate of 4 to 5 nm/hr. This rate is about 4X less than that of NiO. As expected, as the system pressure is decreased, the film thickness increases (Figure 5.7(b)). This is the result of an increase in the ion mean free path as the pressure of the system is lowered. The greater the mean free path, the greater the average incident ion energy and so the higher the sputter yield. At very low pressures, the reduction in the number of ions becomes important and the sputter rate falls off with reducing pressure.

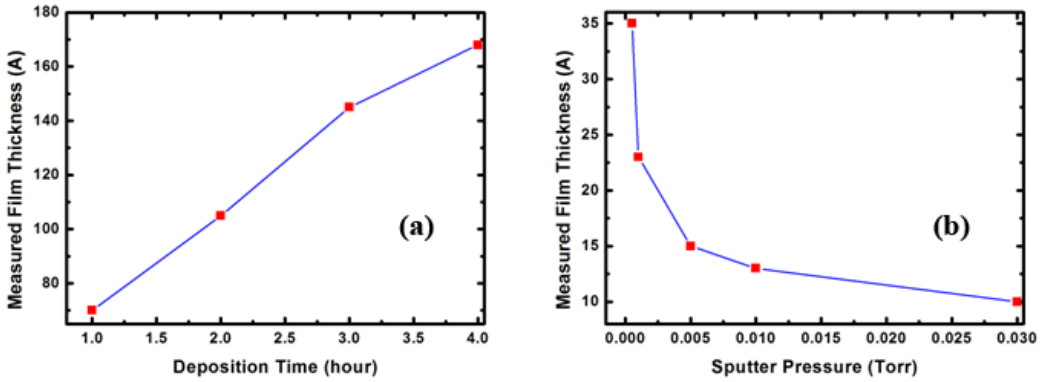

Figure 5.7: TiO_2 (a) Film thickness as a function of deposition time and (b) sputter system pressure.

Although we were able to successfully deposit thin films of TiO_2, the extremely low deposition rates of RF Sputtered TiO_2 process forced an investigation into alternative deposition techniques including ALD.

5.2.4 Atomic Layer Deposition of Metal-Oxide Thin Films

Atomic Layer Deposition (ALD) was utilized to deposit NiO, TiO_2 and ZnO thin films for use in inorganic-NC hybrid devices. The basics of the ALD process were presented in section 5.2.1. The following sections will discuss the ALD fabrication process for each material. For a thorough review of the ALD of oxide-based materials we suggest the reader to consult the review article by Niinistö *et al.* [226].

5.2.4.1 NiO ALD

ALD deposition of Nickel Oxide is a relatively new process which has gained more attention as the novel properties of NiO have become better understood. The ALD

process was carried out in the Savannah ALD system (Cambridge Nanotech) in the NFC. The ALD process setup in the Savannah system was provided by Cambridge Nanotech and based on work published by Kumagai *et al*. in 1996. [227] In this process alternate pulses of bis-methylcyclopentadienyl nickel ($Ni(CH_3C_5H_4)_2$) and hydrogen peroxide H_2O_2 (or H_2O) were sent into the ALD reactor. Figure 5.8 provides a visual representation of the process.

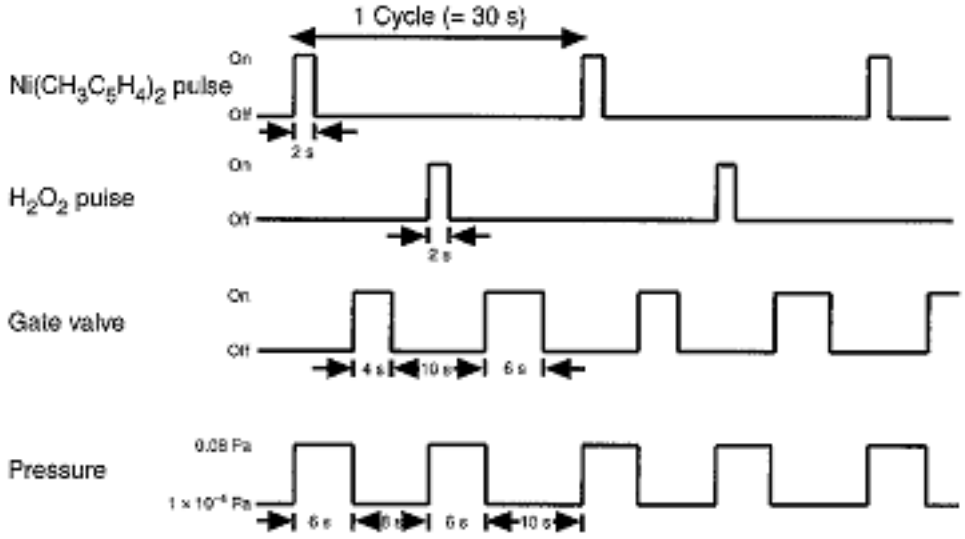

Figure 5.8: Visual representation of the NiO ALD Process used in the Savannah ALD Reactor. Reproduced from [227].

The Savannah ALD system was setup with the same conditions as those described in [227] with one notable difference. The Savannah ALD system purges in N_2 at all times, rather than just pulsing in the purge gas after each precursor cycle. This change should not significantly alter the deposition process, but more study is needed to determine what effect this change has on the deposition rates. Kumagai reported a growth rate of 0.14 nm/cycle where 1 cycle takes 30 seconds to complete. This corresponds to a deposition rate of about 0.28 nm/min. For 120 cycles, they obtain a thickness of nearly ≈ 17 nm.

[227] We tried to mimic this process in the Savannah ALD system and observed no NiO deposition. At 400°C, the temperature that is used in [227], the o-ring seal on the ALD reactor is destroyed. Lowering the growth temperature below 400°C shows no deposition as well. Furthermore, we changed the oxygen-containing precursor to H_2O from H_2O_2 and similar to early attempts no NiO was deposited. Because of the lack of progress with this precursor and the Savannah system we have abandoned our attempts of depositing NiO using the ALD in the NFC.

However, there are still many reports of successful ALD deposition using alternative NiO precursors. [228-230] Currently, we are investigating these other precursors in a custom NiO ALD system which allows for the use of O_3. O_3 is much more reactive than H_2O_2 or H_2O, so we hope that the O_3 will readily react with the Nickel precursor to form NiO and help to prevent contamination of the film by removing carbon by forming volatile CO or CO_2 compounds. The maximum deposition rate achieved so far has been 0.05 nm/cycle where 1 cycle is 30 sec. This gives a deposition rate of 6 nm/hr. Thus for a 40 nm thick film we would need to run this process for nearly 7 hours.

Although the deposition rates are slow, ALD is preferred over RF sputtering because it produces smooth, uniform thin films which conform to the substrate. The sputtered samples that are synthesized in the AJA have thicknesses that vary across the substrate and significant surface roughness. Furthermore, since many materials are sputtered in the system (multi-user) it is possible that some of those materials could be incorporated into the NiO sputtered film. However, until the deposition rate of the ALD

process is improved, RF sputtering will be the preferred method of deposition for the hybrid devices.

5.2.4.2 TiO_2 ALD

Within the past few months we have also started exploring the possibility of depositing TiO_2 with ALD. There are two typical titanium precursors used for TiO_2 ALD, titanium tetrachloride ($TiCl_4$) [231-234] or titanium isopropoxide (TTIP, $Ti(OCH(CH_3)_2)_4$) [234-238]. Other precursors exist such as tetrakis-dimethyl-amido titanium (TDMAT, $Ti(N(CH_3)_2)_4$)) [238] and titanium ethoxide (TEOTi, $C_8H_{20}O_4Ti$). [239] TTIP has been the most widely studied TiO_2 precursor using either H_2O or H_2O_2 as the oxide precursor. [235] For the Savannah system we attempted to deposit TiO_2 through alternating pulses of TTIP and H_2O.

Figure 5.9 shows the TiO_2 film thickness as a function of the ALD chamber temperature. The blue and pink data points on Figure 5.9 refer to measurements taken on an ellipsometer (diamonds) and nanospec film measurement system (squares). In any case, with 400 cycles (approximately 2.5 hour deposition) we are not obtaining a significant growth rate. A similar trend is observed when the substrate temperature is held constant while the temperature of the precursor material is increased. From the data in Figure 5.9 it is clear that we can deposit TiO_2 by ALD, but the process is very long, similar to the NiO ALD process. Further process development work is needed to improve the deposition rate of the TiO_2.

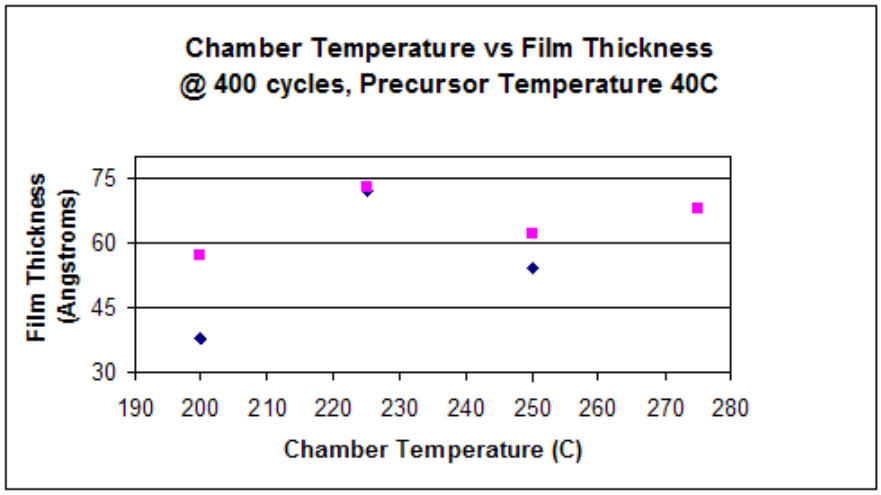

Figure 5.9: TiO_2 film thickness as a function of chamber temperature. The squares represent thickness measurements from a nanospec film measurement system, while the diamonds represent measurements from an ellipsometer. Image courtesy of Ryan Davis.

5.2.4.3 ZnO ALD

The ALD deposition of ZnO has also been investigated extensively over the past 10 years. [240-250] Out of the three ALD processes described in this section, the ZnO ALD process worked the best with some minor modifications. The basic ZnO ALD process (provided by Cambridge Nanotech) consists of alternating pulses of diethylzinc (DEZ, $(C_2H_5)_2Zn$) and H_2O. Figure 5.10 presents results from a growth study of ZnO films in the Savannah ALD Reactor. In this study the following ALD process was used:

Step 1. Set N_2 flow rate to 50 sccm

Step 2. Wait 60 seconds

Step 3. Pulse H_2O for 0.018 seconds

Step 4. Wait 5 seconds

Step 5. Pulse DEZ for 0.02 seconds

Step 6. Wait 10 seconds

Step 7. Repeat Loop 300 times (cycles) starting at step 2

300 cycles of the process shown above were run at different substrate temperatures to obtain the plot shown in Figure 5.10. The error bars show a 5% deviation from the measured value to account for possible error from the ellipsometer. In any case we see that the growth rate of the ZnO films is significantly higher than that of the NiO or TiO_2 ALD deposited films. The deposition rate is ≈ 0.17 nm/cycle for the "stock" ZnO process. Each cycle takes about 15 seconds and therefore 300 cycles takes just over 75 minutes to complete.

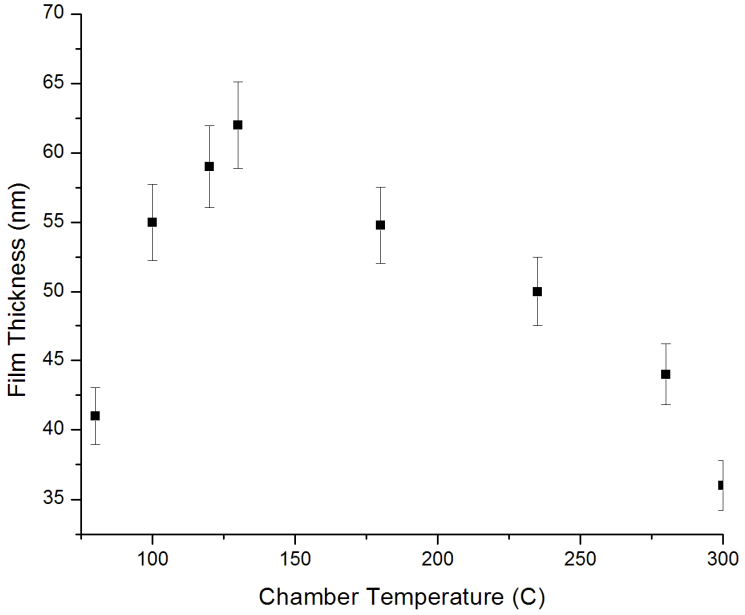

Figure 5.10: ZnO film thickness as a function of chamber temperature.

The one major change to the process discussed above was the addition of a final H_2O double pulse after the main deposition process (Step 2 – Step 7). We were concerned that a Zinc terminated surface may present some difficulties when integrated into a complex device structure. Specifically, we feared that the films would exhibit short circuit behavior. The double pulse ensures that the top layer of the ALD film is ZnO and not metallic Zn (with a small native oxide).

With respect to the fabrication of NiO, TiO_2, and ZnO we were only concerned about synthesizing a smooth, amorphous, stoichiometric, transmissive, and conductive thin films which can be integrated into the hybrid inorganic-NC based devices. We did not perform thorough studies on specific deposition parameters/conditions on each material system. This project would be a thesis on its own. Rather we limited our study to the reliable production of thin films of NiO, ZnO, and TiO_2 with the properties listed above.

5.3 Characterization of Metal-Oxide Thin Films

The next section will discuss the characterization of the thin films which were fabricated by the processes described in sections 5.1 and 5.2. The characterization will focus on the fabricated films which will be incorporated into the inorganic-NC devices. Several different characterization techniques were used to study the chemical, optical, mechanical and electrical properties of NiO, ZnO, and TiO_2. For each technique, results from all three material systems will be discussed. Since problems still exist with ALD deposited NiO and TiO_2 and they have yet to be integrated into a device structure we will not present any characterization results from these films.

5.3.1 Surface Characterization of Metal Oxide Thin Films.

The surface chemistry of NiO, TiO_2, and ZnO was studied by Auger Electron Spectroscopy (AES), X-ray Photoelectron Spectroscopy (XPS), and Rutherford Backscattering Spectrometry (RBS). We will not go into detail on the workings of each

characterization technique; rather we will present and discuss the results. For those interested in more information on the characterization techniques used in this chapter we encourage the reader to consult Schroder's work [251].

5.3.1.1 Auger Electron Spectroscopy and Depth Profiling of NiO Films

Figure 5.11 presents an AES survey scan, taken from a Physical Electronics Inc. (PHI) 545 Auger Electron Spectrometer, from an RF Sputtered NiO film which was fabricated using standard conditions (Flow Rates – 18 sccm Ar, 2 sccm O_2, Pressure – 3 mTorr, Power – 200W, and Substrate Temperature 350°C). AES characterization was performed within 1 day of synthesis to avoid significant contamination due to air exposure.

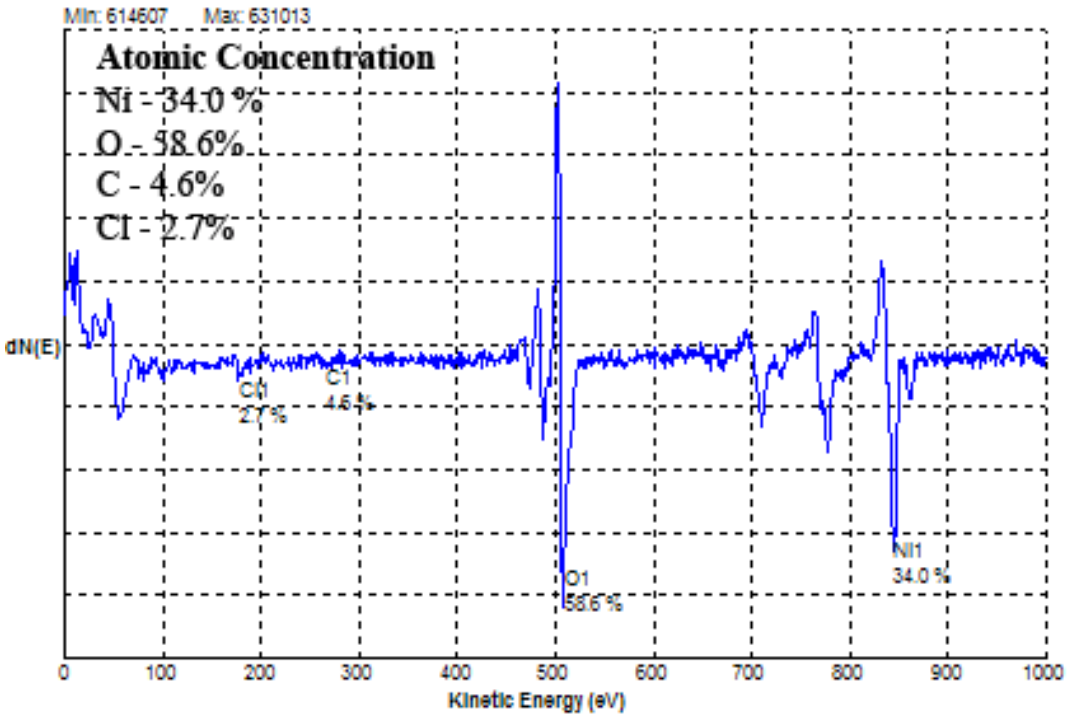

Figure 5.11: AES Survey Spectrum from RF Sputtered NiO thin film. Peaks related to Ni, O, C and Cl are observed.

From the AES survey spectrum we observe Ni, O, C, and Cl. Two additional Ni peaks can be near 710 and 780 eV, but in order to properly calculate the atomic concentration (at the surface) only one Ni peak is needed. The Augerscan 3 software (RBD Analysis) which is used to collect the data in real time also has a function which allows the user to easily calculate the atomic concentration once the related Auger peaks have been identified. For the standard deposition condition, we observe a NiO film which is Nickel deficient (Ni ≈ 34%, O ≈ 58%) with some contamination which is expected. We are unsure of the origin of the Cl contamination peak. Since there is no gas or sputtering target which utilizes Cl, it is possible that the peak may be due to contamination in the Auger system. However, since the main chamber is typically at 10^{-10} Torr, it is difficult to imagine Cl existing in that atmosphere. It could also be an artifact. We have not been able to perform AES in several months due to issues with the system. Therefore, once the system is operational once again, it would be advantageous to examine the stoichiometry of the RF sputtered NiO.

Like a survey spectra from XPS, an AES survey only provides a fingerprint or an identification of what is on the surface of a particular material. In order to understand the make-up of the bulk of the film, an AES depth profile must be performed. During this process, Ar ions are exposed to the film, sputtering off atoms and providing the user with insight into the stoichiometry of the film below the surface. To generate the profile an AES HR scan (similar to an XPS HR scan) is taken initially. The sample is then sputtered (for these samples the sputtering time is between 5 to 15 seconds) and following this process another HR scan is taken. This is one complete sputtering cycle.

This process is repeated until the substrate is reached. The provided software tracks the loss in peak area from element and generates a depth profile. The depth profile from the NiO sample shown in Figure 5.11 is provided below in Figure 5.12.

The depth profile is a plot of the atomic concentration as a function of the number of sputtering cycles. The initial surface chemistry of the film is shown left of cycle 0. As the material is sputtered, we observe a gradual decrease of O and increase of Ni and Si. This increase is attributed to the formation of a Ni-Si film at the interface of the Si substrate and NiO RF sputtered film. After 5 cycles we have sputtered down into the Si substrate. We observe a significant increase in the Si signal and a dramatic dropoff of the Ni and O signals.

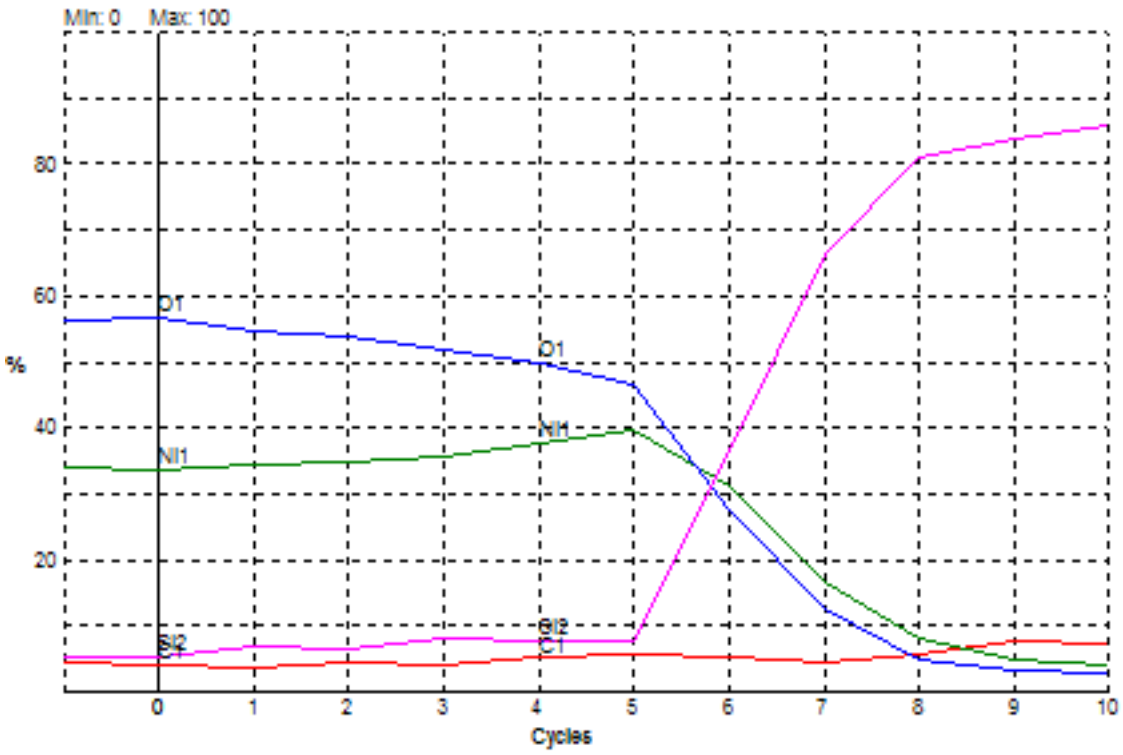

Figure 5.12: AES depth profile from an RF Sputtered NiO thin film.

It is important to note that the C signal remains more or less constant through the sputtering process, even into the single crystal silicon substrate, indicating that the C is not incorporated into the film but rather is an artifact of the measurement process.

5.3.1.2 XPS of RF Sputtered NiO

XPS survey and HR scan were performed on the sputtered NiO thin films in order to determine the atomic concentration at the surface of the NiO as well as the bonding arrangement (via HR XPS). The following figures present both a survey spectrum and HR spectrum from RF sputtered NiO (using similar deposition conditions as was used to collect the Auger data). Figure 5.13 presents a survey spectrum from the sputtered NiO.

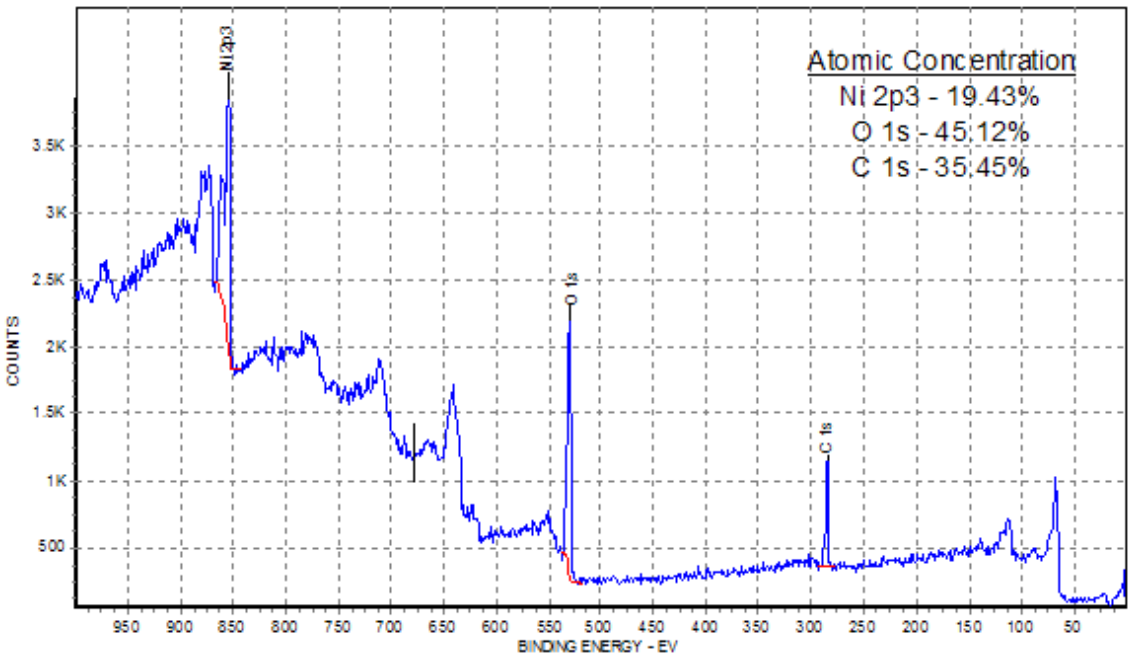

Figure 5.13: XPS Survey Spectrum from a Sputtered NiO thin film. Peaks related to Ni, O, and C are observed on the spectrum.

The survey and HR scan were performed within a few days of synthesis. On the survey spectrum there are several peaks. Most peaks are Ni related, either XPS or Auger peaks. The crucial peaks appear near 860 eV (Ni 2p3), 530 eV (O 1s), and 284.5 eV (C 1s). The spectrum is corrected to the position of the C peak. Similar to the Auger software package, the XPS data collection and analysis software automatically calculates the atomic concentration once a proper background is added to the peak. From the survey scan it appears that the surface is mostly comprised of C and O. The C signal originates from contamination. From this data it is difficult to make an accurate assessment of the stoichiometry due to the large surface contamination. We need to examine the HR XPS to gain a better understanding of the both the stoichiometry and surface chemistry.

Figure 5.14 depicts the HR XPS from the Ni 2p3 region.

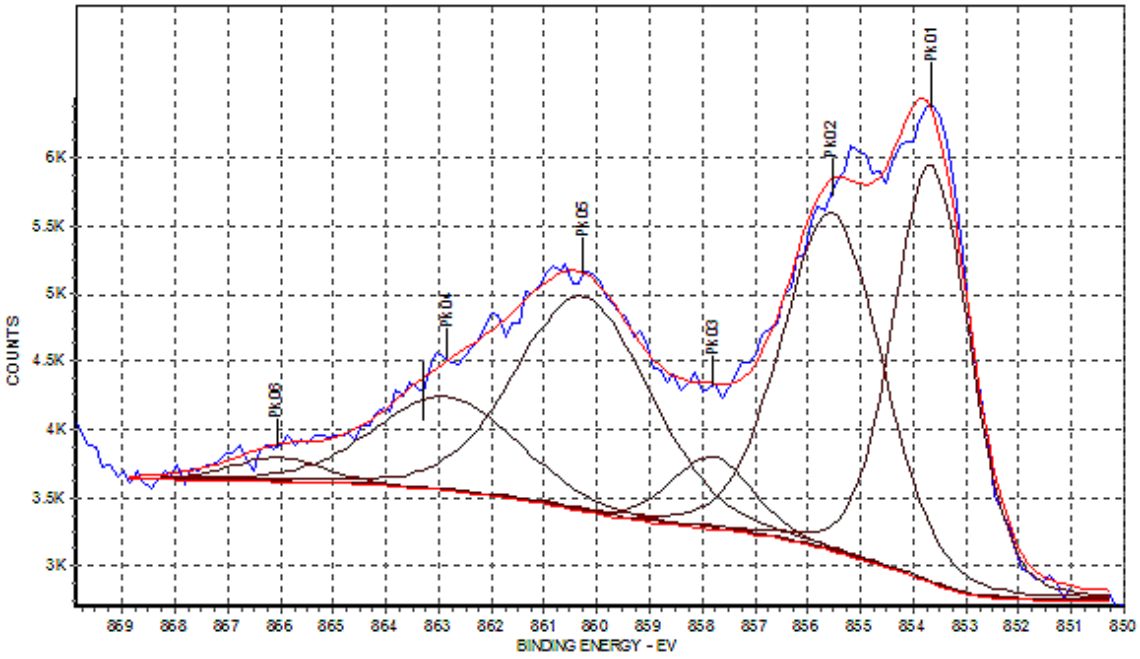

Figure 5.14: HR XPS spectrum from the Ni 2p3 region. 6 peaks are observed. NiO, $Ni(OH)_2$ and Ni_2O_3 are all observed on the surface.

The raw HR data is fit 6 Gaussian peaks which provide a reasonable curve fit to the data. The blue curve in Figure 5.14 is the raw data, while the red curve displays the curve fit. Although there are six peaks on the spectrum, only three are relevant. The peaks near 860.2, 863, and 866 eV are plasmon peaks and provide no useful information about the stoichiometry of the film. In order to identify the peaks, we consulted earlier work on RF Sputtering of NiO. Figure 5.15 presents XPS HR data from published work by Hotovy *et al*. [252] In Figure 5.15 four peaks are represent in the spectrum: metallic Ni (852.7 eV), NiO (854.3 eV), $Ni(OH)_2$ (855.6 eV), and Ni_2O_3 at (857.3 eV). [190, 252] Comparing the results of [252] to the spectra shown in Figure 5.15, we can identify NiO, $Ni(OH)_2$, and Ni_2O_3 on the surface of the sputtered NiO. The intensities (and areas) of the NiO and $Ni(OH)_2$ peaks are nearly the same, while the intensity of the Ni_2O_3 peaks is significantly less. Thus it appears that the surface of the NiO is mostly comprised of a combination of NiO and $Ni(OH)_2$ with a small amount of Ni_2O_3.

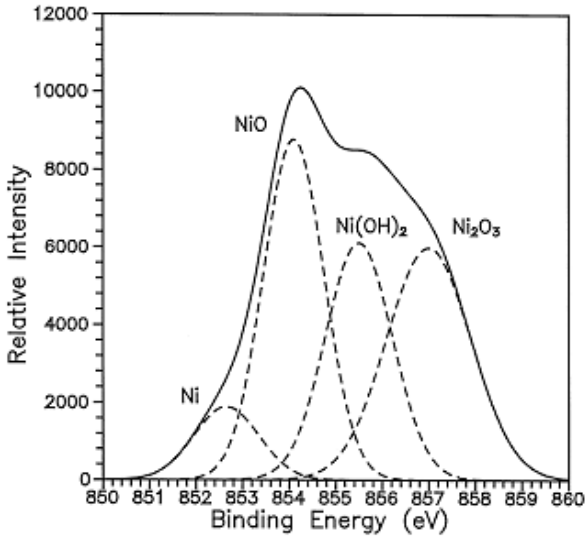

Figure 5.15: HR XPS Spectrum of the Ni 2p3 region from sputtered NiO. Reproduced from [252]. The relevant peak assignments are noted on the figure.

Figure 5.16 presents the HR XPS data from the O 1s spectrum. Three peaks are observed in the spectrum.

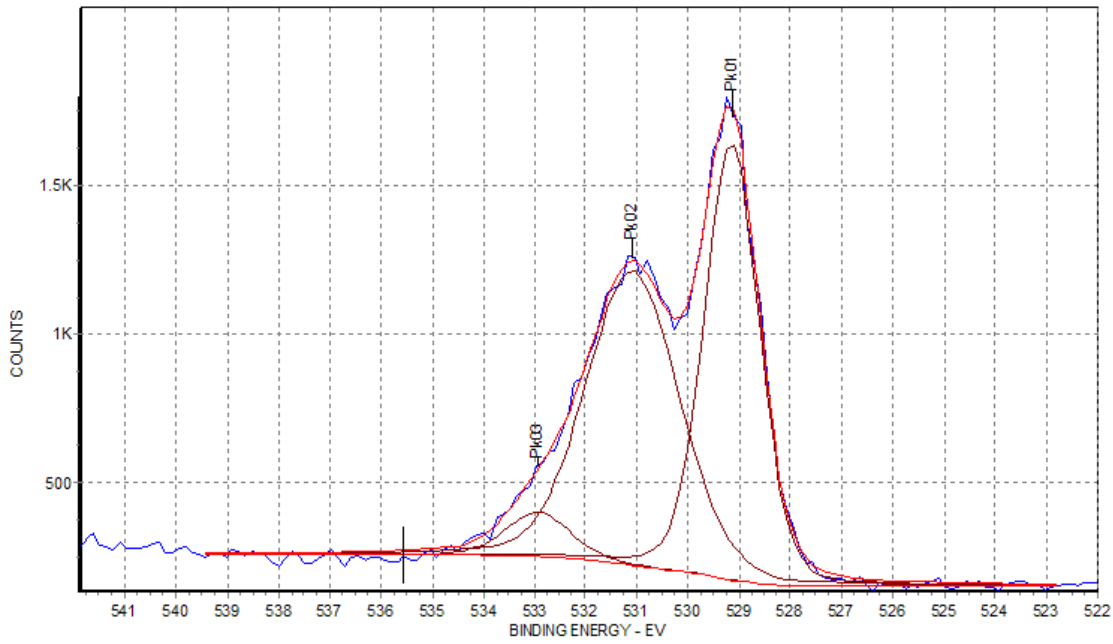

Figure 5.16: O 1s HR Spectrum from the sputtered NiO thin film.

According to Chan-Park *et al.* [190], the peaks are identified as follows. The peak near 529.2 eV is related to Ni-O, while the peak centered around 531.2 eV is more difficult to identify. It could either be related to $Ni(OH)_2$, Ni_2O_3, or C-O or a combination of the three peaks. The peak near 533 eV is believed to be related to absorbed H_2O. From the HR data of the Ni 2p3 and O 1s regions we can approximate the stoichiometry of NiO by using the expression:

$$\frac{Ni}{O} = \frac{I_{A,\,Ni}}{\sigma_{Ni}} * \frac{\sigma_O}{I_{A,\,O}}$$

where $I_{A,Ni}$ and $I_{A,O}$ are the areas under the NiO related peaks in the Ni 2p3 (854.3 eV) and O 1s spectra (529.2 eV). The other two terms are the sensitivity factors of both Ni

(σ_{Ni} = 14.61) and O (σ_O = 2.93) which can be found in any standard XPS reference guide. Plugging in the data we calculate the Ni/O ratio to be ≈ 0.568. In the ideal case, we could like this ratio to be 1, indicating that we were depositing NiO. But it is clear from the HR data as well as this simple stoichiometric calculation that we have a mixture of oxidized Ni species on the surface of the sputtered NiO.

Since the samples were exposed to air before undergoing XPS investigation there is a significant amount of C contamination on the surface of the sputtered film. Figure 5.17 presents the HR data from the C 1s spectrum. C contamination is not unexpected when samples are exposed to air. The spectrum shown in Figure 5.17 is typical of carbon contamination and is observed in the sputtered TiO_2 and ALD deposited ZnO. There are three peaks in the spectrum. The largest peak centered at 284.5 eV is related to C-C. [190] The smaller two peaks are believed to be associated with C-O (or O-C-O) and C=O bonding. [190]

It is important to note that the XPS survey scans are only provide a picture of the surface of the RF sputtered NiO under the standard depositions. In order to understand the make-up of the bulk we need to consult alternative techniques such as AES (which was shown above) or RBS which will be discussed below.

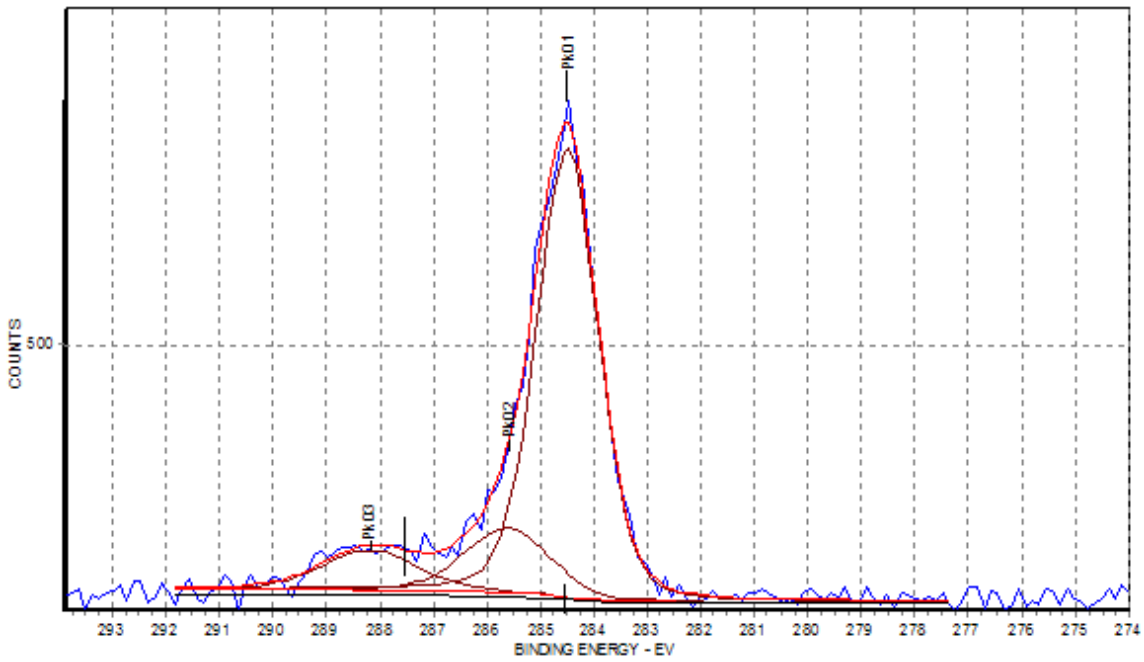

Figure 5.17: C 1s HR Spectrum from the sputtered NiO thin film.

5.3.1.3 RBS of RF Sputtered NiO

Figure 5.18 provides an RBS spectrum from a RF Sputtered NiO thin film fabricated under the same conditions as the AES and XPS shown above, with one exception, the substrate temperature was lowered to 250°C. The samples were obtained using a 2 MeV He^{2+} beam. Following the data collection, the results were analyzed using Hydra software. Table 5.1 summarizes the RBS data from three different RF sputtered NiO samples. The 2/25 NiO samples was sputtered with the same conditions as the AES and XPS samples which were discussed in section 5.3.1.1 and 5.3.1.2.

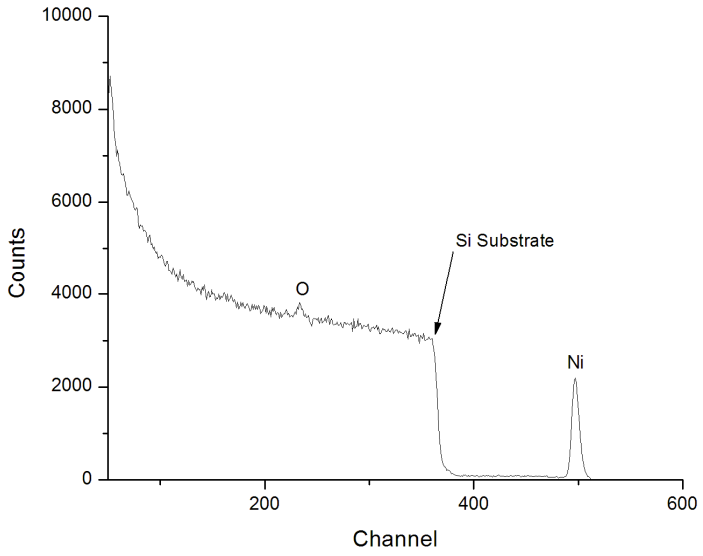

Figure 5.18: RBS Spectrum from 5/27 Sputtered NiO thin film sample. Deposition conditions are listed in Table 1.

Similar to the results observed from the AES and XPS the RBS also shows that the NiO sample is Nickel deficient when using those deposition conditions (see Table 5.1). When the substrate temperature is decreased to 250°C, the stoichiometry of the sputtered thin film approaches NiO. It appears that when the deposition conditions mirror that of the 5/22 NiO sample (Table 5.1) a stoichiometric NiO film is produced. As a result, all of the recent thin films deposited for use in the inorganic-NC based LED have used the deposition parameters from the NiO 5/22 sample (See Table 5.1).

Sample #	Process Information	Thickness (Å)	Stoichiometry
5/27 NiO	Ar-18, O_2-6, 200W, 250C, 3mT for 1.5 hrs	1170	O - 54, Ni - 46
5/22 NiO	Ar-18, O_2-2, 200W, 250C, 3mT for 2.5 hrs	150	NiO
2/25 NiO	Ar-18, O_2-2, 200W, 350C, 3mT for 1.5 hrs	470	Ni - 44, O - 56

Table 5.1 – Deposition conditions for the RF sputtered NiO thin films studied by RBS.

5.3.1.4 Auger Electron Spectroscopy and Depth Profiling of TiO_2 Films

Figure 5.19 provides an AES survey from RF sputtered TiO_2 thin films. The TiO_2 films were deposited under standard conditions where the flow of Ar and O_2 were fixed at 4 and 24 sccm respectively, the applied RF power was set to 150W, and the pressure in the system was maintained at 1 mTorr. The substrate was heated to 200°C. Total deposition time was approximately 3 hours.

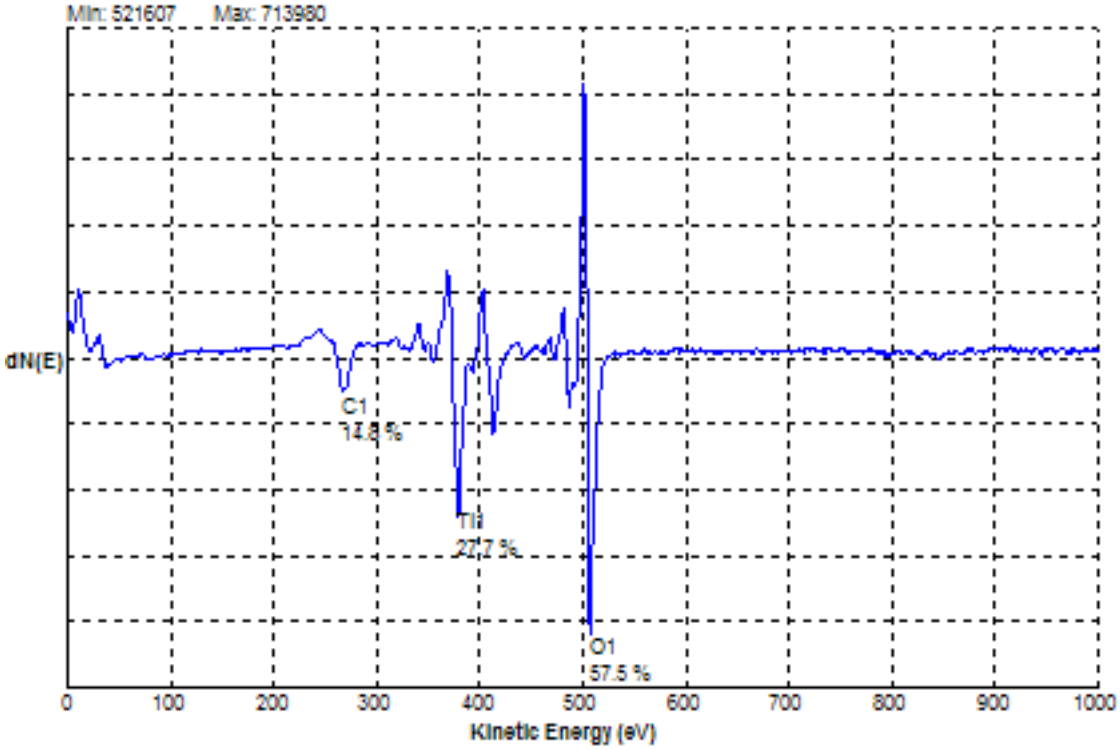

Figure 5.19: AES Survey Scan from an RF Sputtered TiO_2 thin film. Peaks related to Ti, O, and C are observed.

Examining the results from Figure 5.19, we observe that the film appears to be TiO_2. A simple ratio between the Ti and O peaks yields $Ti/O \approx 0.48$. The surface also has quite a bit of contamination and as stated before this is not surprising since the samples were exposed to air before undergoing analysis. Recall that the AES survey scan only

provides a snapshot of the surface. In order to study the bulk of the TiO_2 film, a depth profile on the same sample was performed. The depth profile is shown in Figure 5.20.

After the first sputtering cycle, the C is removed leaving a film which is composed of Ti and O whose Ti/O ratio appears to be approximately 0.5. After 7 cycles, the O begins to drop off dramatically, while the Ti drops only slightly. This indicates that a Ti-Si (titanium-silicide) layer is being formed at the interface between the silicon substrate and the TiO_2 layer. After 8 cycles it appears that we have sputtered into the substrate due to the large increase in the Si signal and the rapid decrease in both the Ti and O signal.

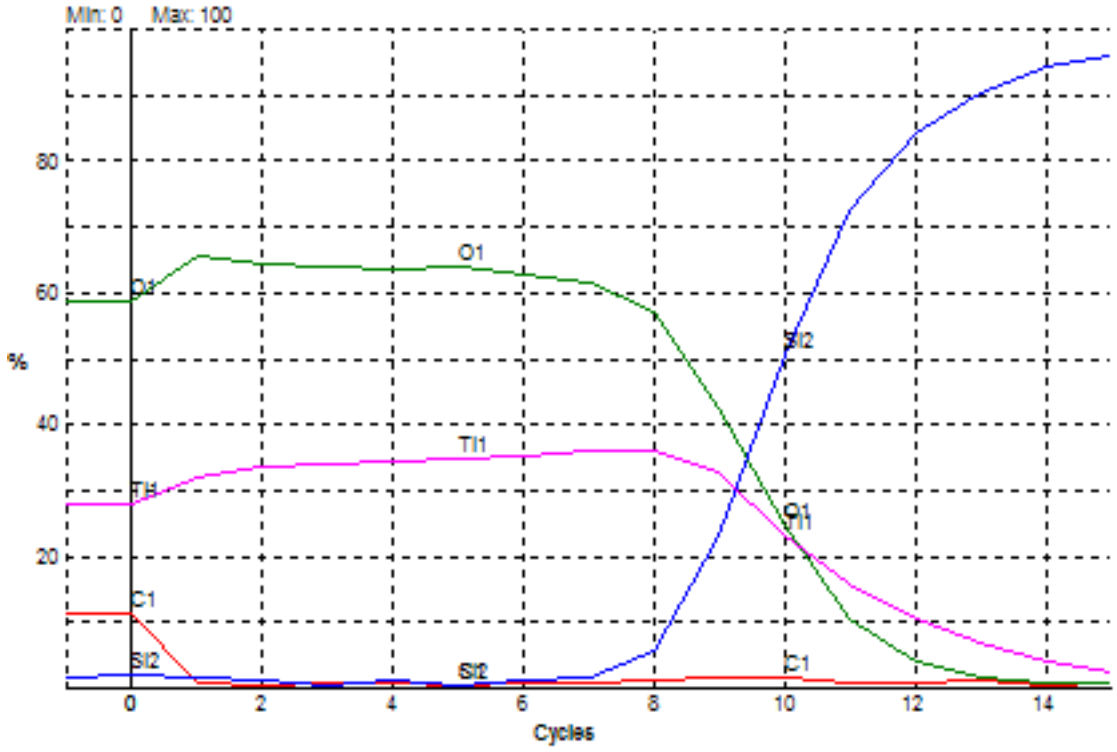

Figure 5.20: AES depth profile from an RF Sputtered TiO_2 thin film.

There is another method used to approximate the stoichiometry or oxidation state of the TiO_2 layer. According to I. Vaquilla *et al.* [253] the oxidation state of TiO_2 can be

approximated by examining the ratio of the O_{KLL} over the Ti_{LMV} peaks (Note the Ti L_{MM} peak appears near (382 eV) and Ti_{LMV} (417 eV) on the AES Survey Scan). From the AES data in Figure 5.20, the O_{KLL}/Ti_{LMV} ratios were calculated to be around three. This value is similar to data published by Vaquilla [253] and therefore we believe that the RF sputtered TiO_2 thin film is in fact TiO_2.

5.3.1.5 XPS of RF Sputtered TiO_2

Figure 5.21 presents an XPS survey spectrum taken from RF Sputtered TiO_2 using the following conditions. The flow rates of Ar and O_2 were set at 4 and 24 sccm respectively. The power coupled into the plasma was set at 175W, while the pressure in the sputtering system was held at 2 mTorr. The substrates were heated at 200°C. The films were sputtered for 5 hours.

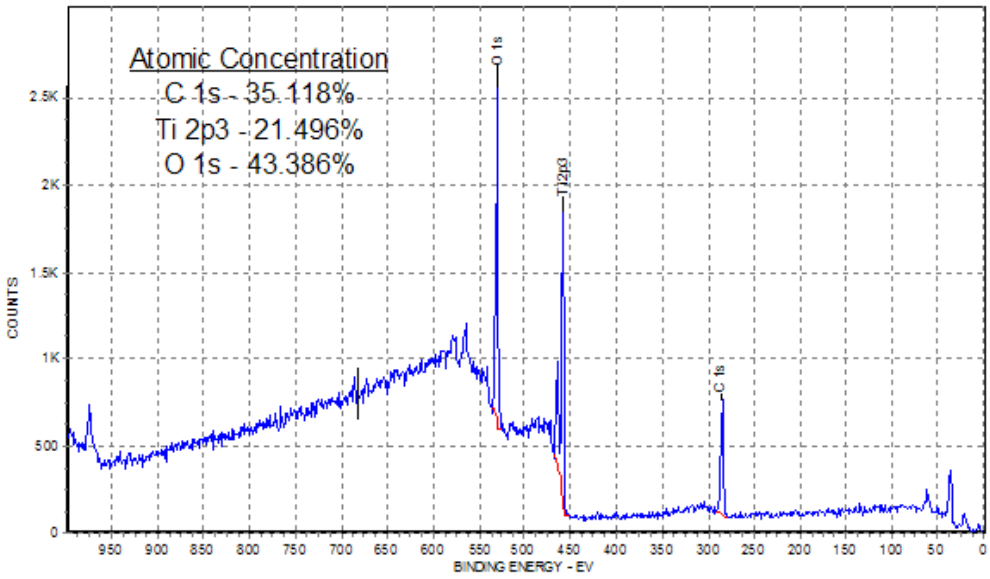

Figure 5.21: XPS Survey Spectrum from RF Sputtered TiO_2 thin film. Peaks related to Ti, O, and C are observed.

The survey spectrum displayed in Figure 5.21 shows evidence of C, Ti, and O on the surface of sputtered film. The large C contamination is due to air exposure. Calculating the Ti/O ratio from the results in Figure 5.21, one obtains a Ti/O ratio of 0.495. Ignoring the C contamination, it appears that we have TiO_2.

Figure 5.22 provides the C 1s HR XPS spectrum from the RF sputtered TiO_2 film. The C 1s HR spectrum is similar to what was observed with the NiO film (Figure 5.17). Three peaks are observed in this spectrum, all related to contamination at the surface. As discussed earlier, the peak near 285 eV is related to C-C bonds while the other two peaks (near 286.5 and 288.5 eV) are related to C-O bonds. From the AES depth profile in Figure 5.20, we know that the C only lies at the surface, thus the C 1s HR XPS spectrum provides essentially no useful information into the surface structure of the sputtered TiO_2 film. For that information we need to examine the Ti 2p3 and the O 1s HR XPS spectra.

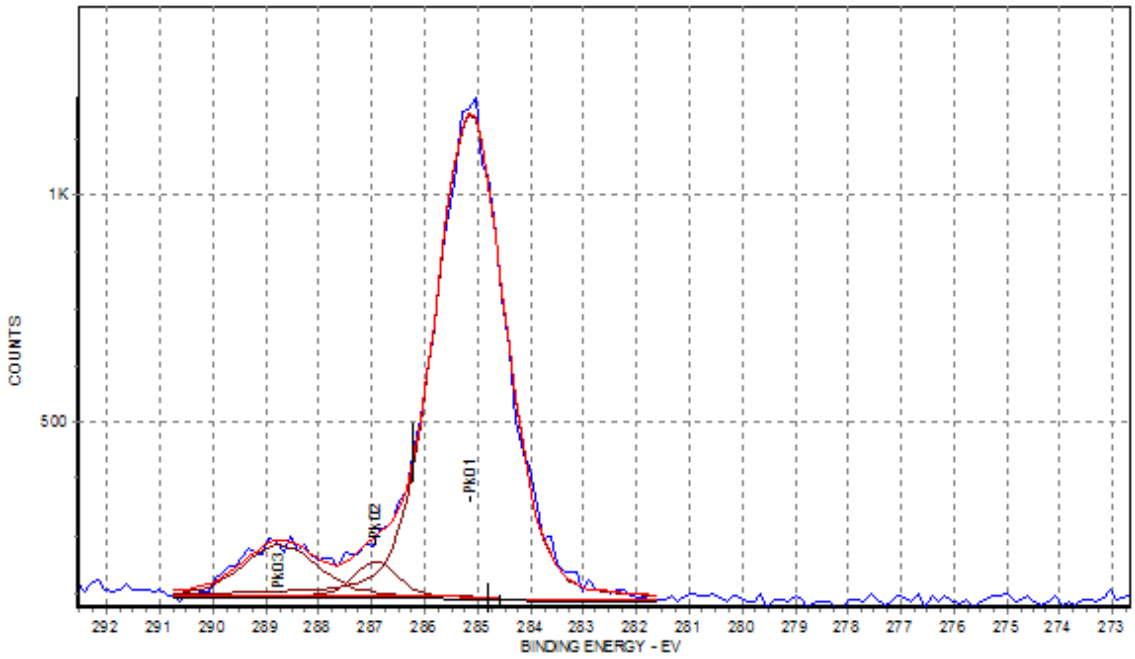

Figure 5.22: HR XPS of the C 1s Spectrum from RF Sputtered TiO_2 thin film.

Figure 5.23 presents the O 1s HR XPS spectrum. There are 3 peaks in the O 1s spectrum. The peak near 530 eV is related to TiO_2. [187, 254] The other two peaks in the spectrum are more difficult to identify. The peak near 532 eV is believed to be related to OH species. [187] The other peak near 533 eV could be related to C-O groups, but more study on both peaks is needed for a definitive identification.

Figure 5.24 presents the Ti 2p HR spectrum. First of all, the curve fit of the Ti 2p spectrum is not completely accurate. It is difficult to near impossible to generate an accurate representation of the structure of the Ti 2p HR spectrum. In Figure 5.24 two peaks are observed. The peak near 459 eV is related to the Ti 2p3/2 while the peak near 464 eV is related to the Ti 2p1/2. To help resolve what species may exist at the on this HR scan, we need to consult literature. In Figure 5.25, we show the XPS spectrum from TiO_2 layers which were grown by native oxidation. [187]

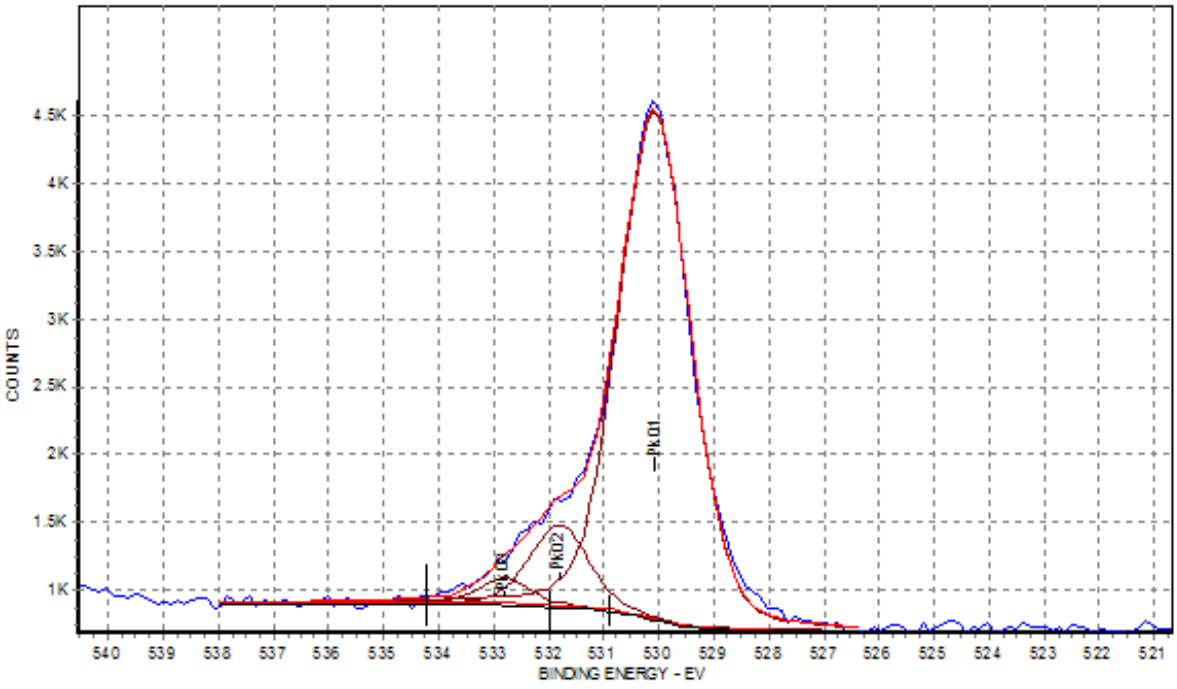

Figure 5.23: O 1s HR XPS Spectrum from the RF sputtered TiO_2 thin film.

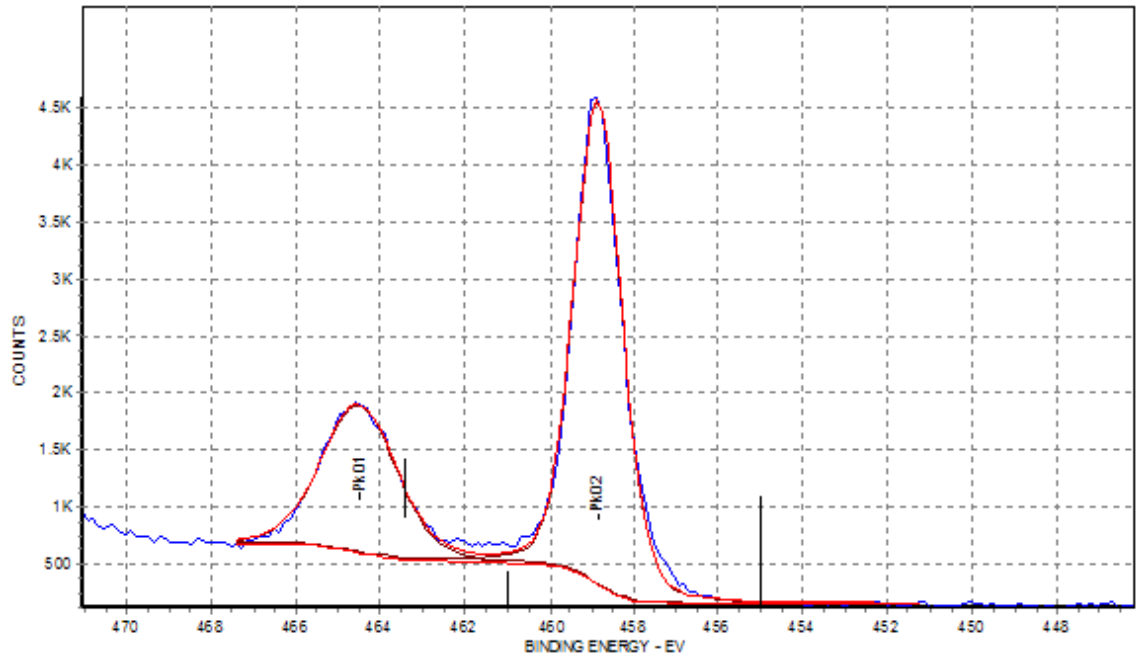

Figure 5.24: Ti 2p3 HR XPS Spectrum. 2 peaks are observed. The peak near 459 eV may be related to TiO_2.

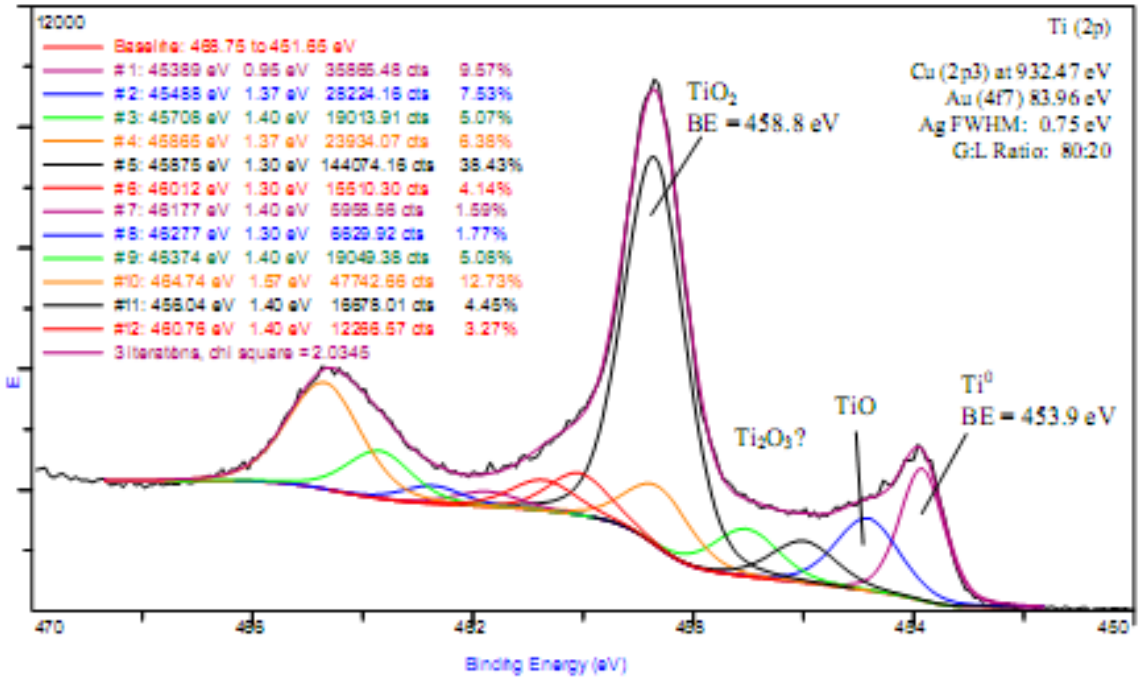

Figure 5.25: Ti 2p3 HR XPS Spectrum including the proper curve fit. Reproduced from [187].

From Figure 5.25, the TiO_2 peak appears at 458.8 eV. Comparing this value to the peaks seen in Figure 5.24 (near 459 eV); it appears that the peak is similar. Since the curve fit of the data in Figure in 5.24 is not complete, it is difficult to claim from this data that the surface is TiO_2. It is clear from Figures 5.24 and 5.25 that we do not have TiO or Ti metal incorporated into the sputtered film. The peak positions from these species are below 455 eV. Examining Figure 5.24 it is clear that there are no peaks which fall into this region. It is possible that there may be a peak related to Ti_2O_3 present in our RF sputtered films. From Figure 5.25 the Ti_2O_3 peak is defined at a binding energy of 457 eV. Carefully examining the curve fit on Figure 5.24, one notices that curve fit on the right hand side of the Ti 2p3 peak (459 eV) is not accurate. It is possible that there may be peak related to Ti_2O_3 near 457 eV. We are not concerned with the peaks around the Ti2p1/2 state at 465 eV, and therefore we will not try to identify them. A rough stoichiometric calculation can be made by using the following equation:

$$\frac{Ti}{O} = \frac{I_{A,Ti}}{\sigma_{Ti}} * \frac{\sigma_O}{I_{A,O}}$$

By taking the area under the TiO_2 peaks in both the Ti and O XPS spectra and plugging that data into the equation above along with the elemental sensitivity factors (σ_{Ti} = 5.22, σ_O = 2.93) we obtain a Ti/O ratio of ≈ 0.568. This value indicates that the sputtered film is titanium deficient. Because the curve fit is not entirely accurate, the calculated area under the TiO_2 related peak is probably not correct. Therefore, it is possible that we are overestimating how much TiO_2 exists on the surface of the sputtered film. In order to resolve this problem, a more accurate curve fit is needed. However, at present we do not have sufficiently sophisticated software to perform a curve fit similar to that shown in

Figure 5.25. We are currently investigating alternative software packages to help solve this problem.

5.3.1.6 RBS of RF Sputtered TiO_2

The RBS spectrum from a RF sputtered (similar conditions to those described in the XPS and AES measurements) TiO_2 film is shown in Figure 5.26. From the data shown in Figure 5.27, we were able to determine the Ti/O ratio at ≈ 0.5. However, we did notice a strange feature in the RBS spectrum. A peak appeared at a channel with was higher than that of Ti. This means that the peak has a higher atomic number. Using PIXE (which is an elemental identification technique, which is generated at the same time the RBS spectrum was taken; we determined that the element falls around silver. Examining the periodic table, one notices that Ruthenium, Rhodium, Palladium, Cadmium, and Indium fall near silver. The only possible material that could contaminate the TiO_2 film would be silver. Since silver is routinely sputtered in the same system in which the TiO_2 is sputtered, it is possible that some Ag atoms were knocked off the side of the chamber walls and integrated into the film. AES analysis was also performed on this film to determine if the contamination peak was simply an artifact from the RBS. However, the AES also identified a non-TiO_2 related peak. After performing the analysis on the AES survey, we determined that this peak was silver-related.

Despite the contamination issues, the depositions used in this characterization shown above produce TiO_2 films. As a result, this process has been used to deposit TiO_2 thin films for the integrated inorganic-NC based EL devices. Because of the possibility

of contamination (like the Ag contamination from the RBS spectrum) from a multiuser system like the AJA, ALD deposition of TiO_2 is currently being studied, but it is not ready for device integration.

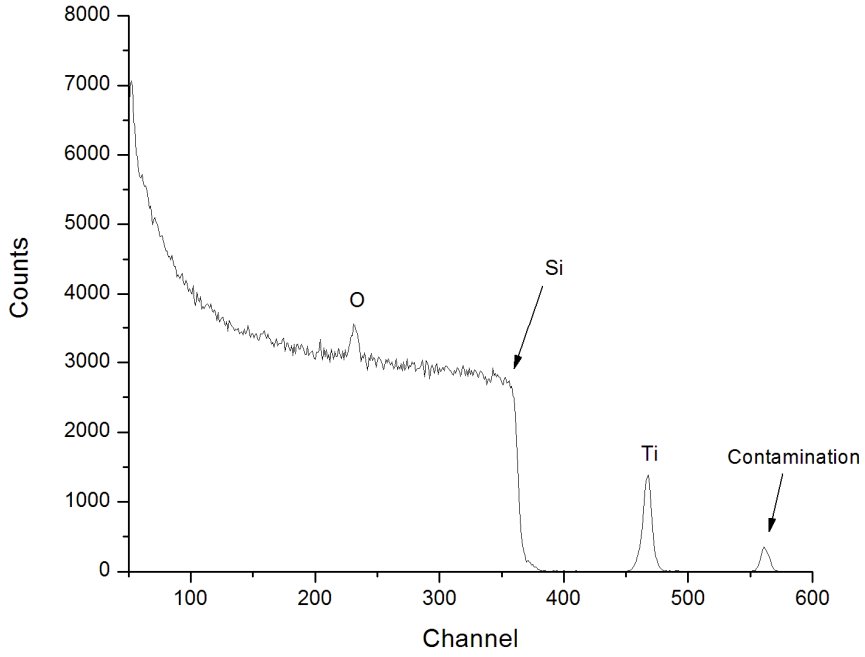

Figure 5.26: RBS Spectrum from RF Sputtered TiO_2. Some contamination is observed on the spectrum.

5.3.1.7 Auger and Depth Profiling of ZnO

Figure 5.27 provides an AES survey spectrum from a ZnO thin film deposited under the conditions described in section 5.2.4.3.

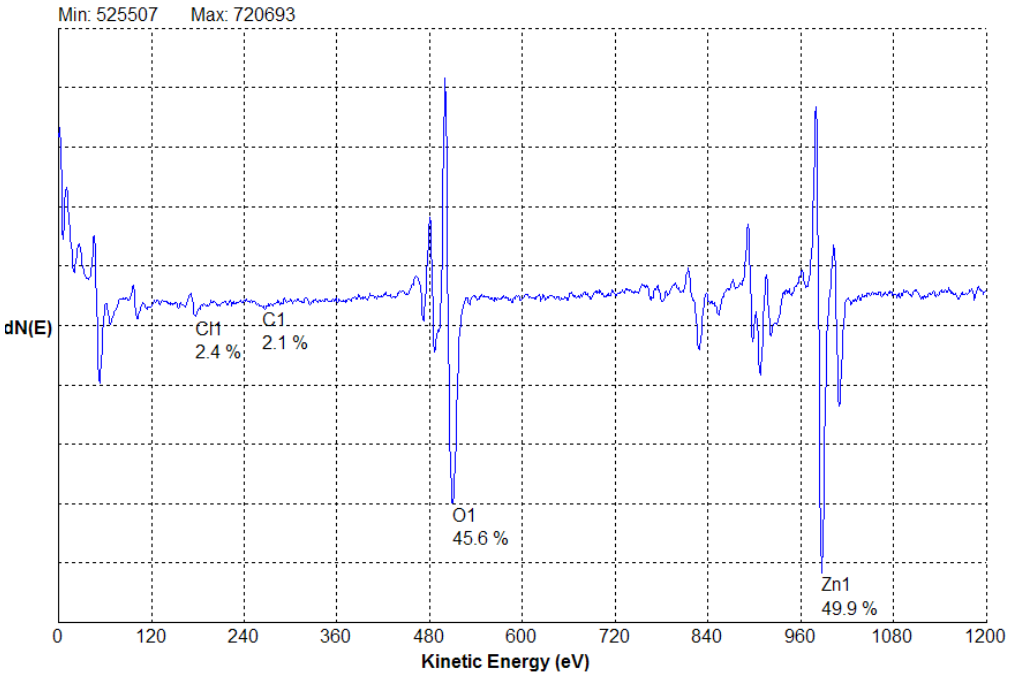

Figure 5.27: AES Survey Scan from an ALD deposited ZnO thin film. Peaks related to Zn, O, Cl, and C are observed.

The elemental analysis of ZnO thin film shows peaks related to C, O, Cl, and Zn. One problem of ALD (as discussed in section 5.2.1) is the incorporation of impurities (or contamination) into the deposited film from unwanted or incomplete reactions which occur during the ALD process. If the ALD process for ZnO was not working correctly, we would expect a larger C signal because DEZ has CH_2 and CH_3 bonds incorporated into its structure. The small C signal indicates that the reaction is occurring as expected. Furthermore, the amount of both Zn and O on the surface of the ALD deposited film is nearly identical, indicating that we have ZnO (Zn/O ≈ 1.09). Once again there is a Cl peak observed in the spectrum. The two ALD precursors for ZnO (DEZ and H_2O) do not contain any Cl. Furthermore, there is no process on the Savannah ALD system which uses Cl. Since this Cl peak was also observed in an AES spectra of NiO, the peak must

originate from somewhere in the Auger system itself. Figure 5.27 only provides a mapping of the surface of the ZnO film. In order to obtain information about the bulk, a depth profile must be performed. Figure 5.28 presents the depth profile taken from the ALD ZnO sample whose AES survey spectrum is shown in Figure 5.27.

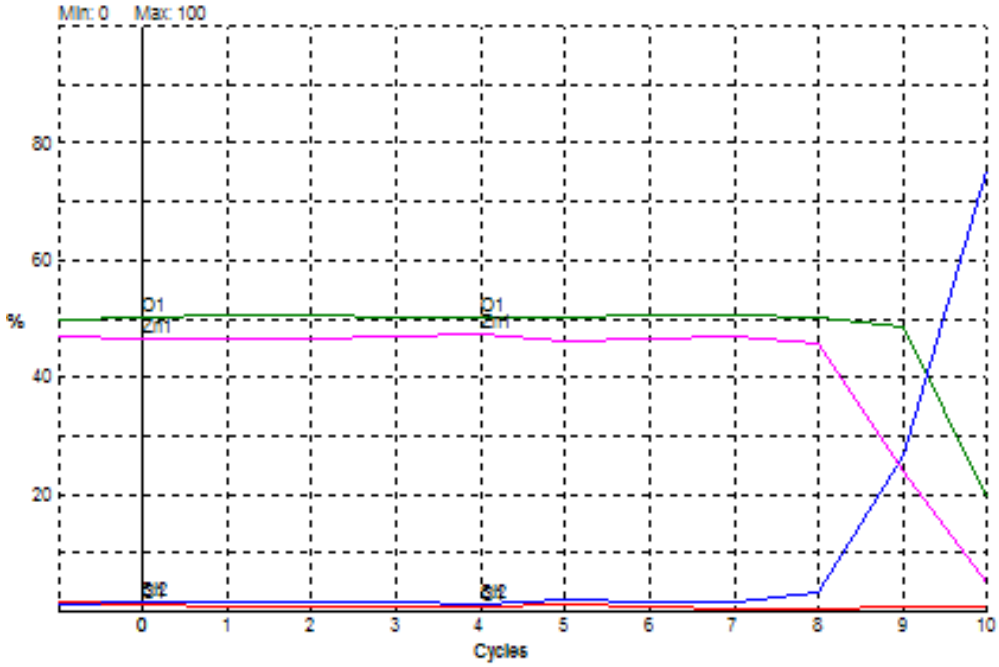

Figure 5.28: AES depth profile from an ALD deposited ZnO thin film.

Studying the depth profile in Figure 5.28 one notices that the structure of the ZnO ALD deposited film does not change when we sputter into the bulk of the ZnO film. The film appears to be nearly stoichiometric throughout. After 8 cycles, we begin to observe a change in the depth profile. The Si trace begins to increase as the Zn trace begins to decrease. At this point the sputtering process has reached an oxide (probably SiO_x) on the surface of the Si substrate. After 9 cycles we have completely sputtered into the bulk. From Figures 5.27 and 5.28 it is clear that the ZnO ALD process described in section

5.2.1 creates stoichiometric ZnO. Further proof of this can be found in the XPS spectrum.

5.3.1.8 XPS of ALD Deposited ZnO

Figure 5.29 provides an XPS survey scan from the ALD deposited ZnO thin films. There are several peaks visible in this spectrum. Most of the peaks are Zn XPS or Auger peaks. The most important peaks are noted on the spectrum.

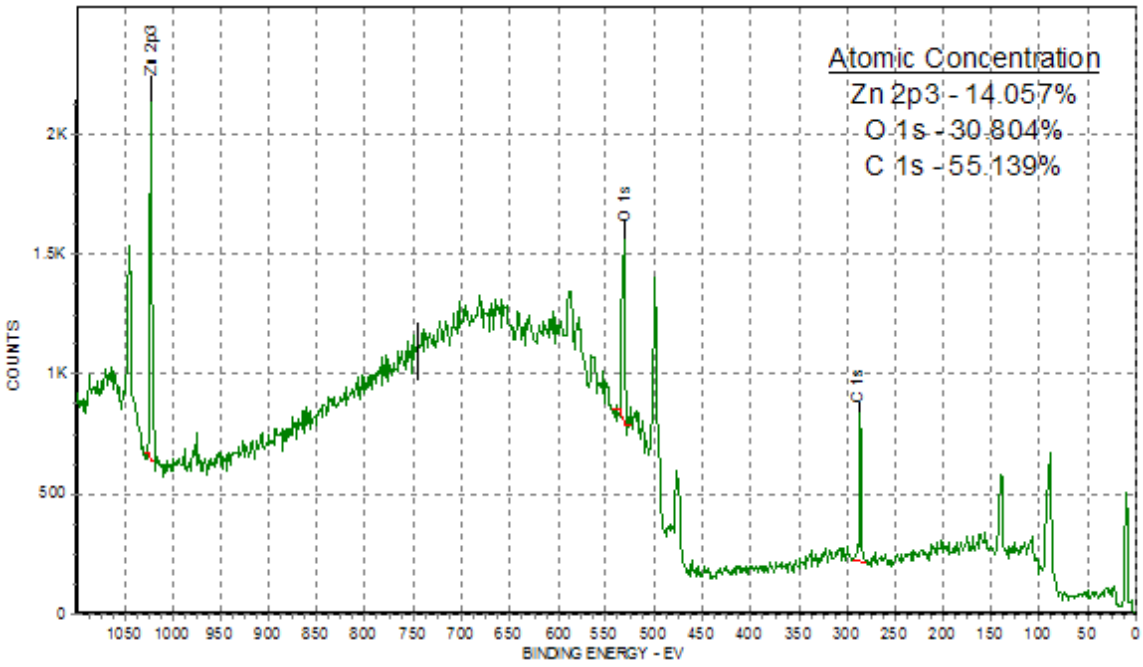

Figure 5.29: XPS Survey Scan from an ALD Deposited ZnO thin film. Peaks related to Zn, O, and C are observed.

Comparing the XPS survey spectrum to the AES survey, one notices a major difference, that being the amount of C. Since sputter profile AES is a destructive technique, the same sample could not be used for XPS. As a result, a different sample (run with similar conditions) was used to obtain the XPS data. It is possible that several days passed

before the sample was actually measured in the XPS. From the AES data which was performed within a day after synthesis, we know that the film is nearly stoichiometric with some C (≈ 2%) and Cl (≈ 2%) contamination. The XPS data seems to suggest that the surface of the sample is mostly C, and if the sample spent several days in air, this is possible. As a result, we can not simply use the concentrations from the survey scan to approximate the structure of the ZnO. Rather, we need to approximate this from the HR XPS.

Figure 5.30 shows the C 1s HR XPS data from the ALD deposited ZnO films. This spectrum appears to be similar to the C 1s spectrum observed for both NiO and TiO_2.

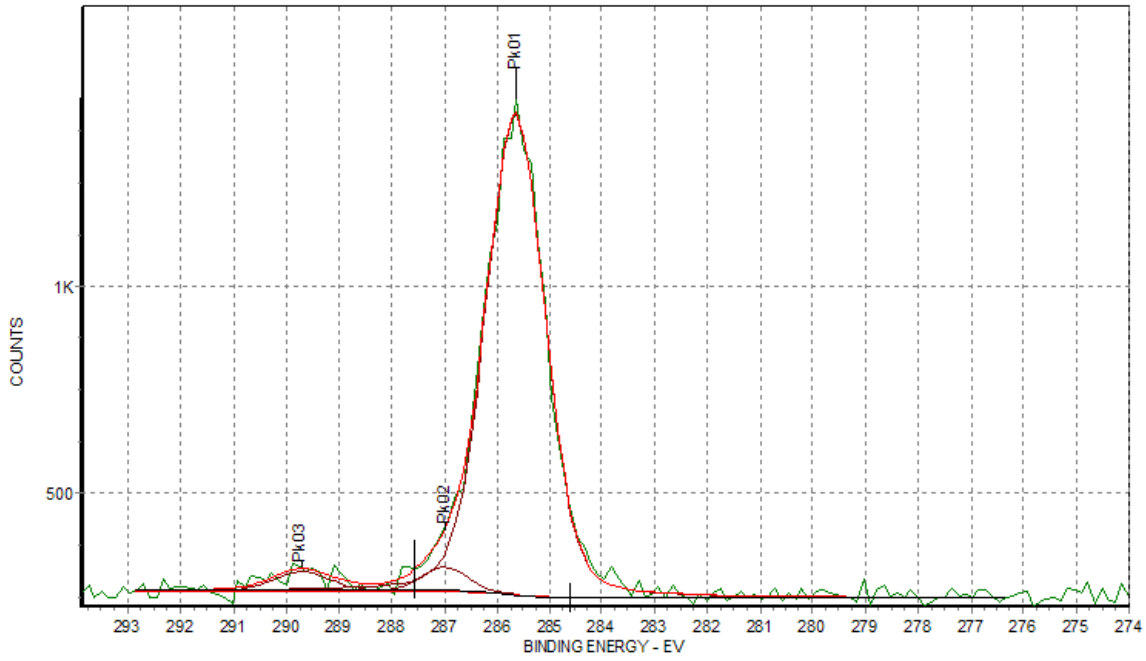

Figure 5.30: HR XPS spectrum from the C 1s region from a ZnO thin film deposited by ALD.

The large peak near 285 eV is related to C-C bonds, while the other 2 peaks are C-O related. [187] The C HR spectrum does not provide any information about the structure of the ALD ZnO thin film. We need to examine both the Zn 2p and the O 1s HR spectra. Figures 5.31 and 5.32 provide the HR XPS spectra from both Zn 2p3 and O 1s regions. The Zn 2p HR scan (Figure 5.31) shows only one peak near 1022 eV. After examining the literature [187], it appears that this peak is related to ZnO. The oxygen spectrum has two peaks one centered near 531 eV, the other near 533 eV. According to Christ [187], the peak at 531 in the O 1s spectrum is related to ZnO. The peak near 532.5 eV is related to O-H bonding. [248]

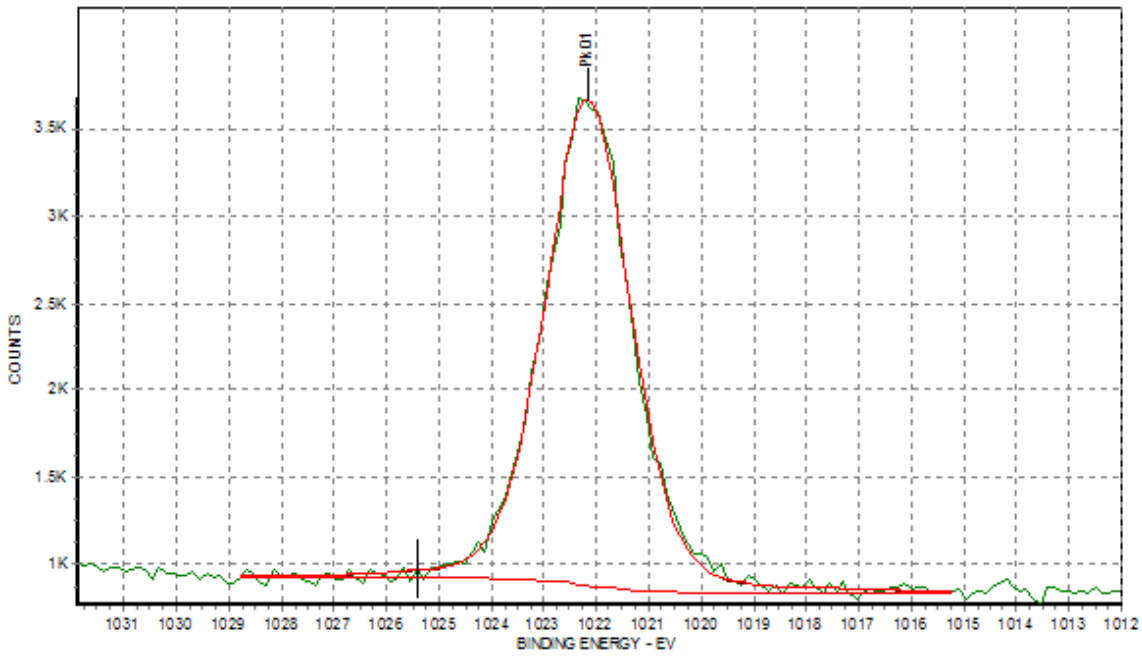

Figure 5.31: HR XPS spectrum from the Zn 2p region from a ZnO thin film deposited by ALD.

The stoichiometry of the ZnO was estimated using the same method that was used for NiO and TiO_2. From the following relationship:

$$\frac{Zn}{O} = \frac{I_{A,\,Zn}}{\sigma_{Zni}} * \frac{\sigma_O}{I_{A,\,O}}$$

we can approximate the structure of the ZnO by taking the area under the ZnO related peaks in both the ZnO ($I_{A,Zn}$) and O ($I_{A,O}$) XPS spectra and plugging that data into the equation above along with the elemental sensitivity factors (σ_{Zn} = 18.92, σ_O = 2.93) we obtain a Zn/O ratio of ≈ 0.464. The calculated Zn/O from the HR XPS data is drastically different to that observed from the AES survey and depth profile. From the AES data, we observed a Zn/O ratio of approximately 1. It is possible that the absorbed C on the surface of the ZnO is thick enough that we are not observing an accurate picture of the surface.

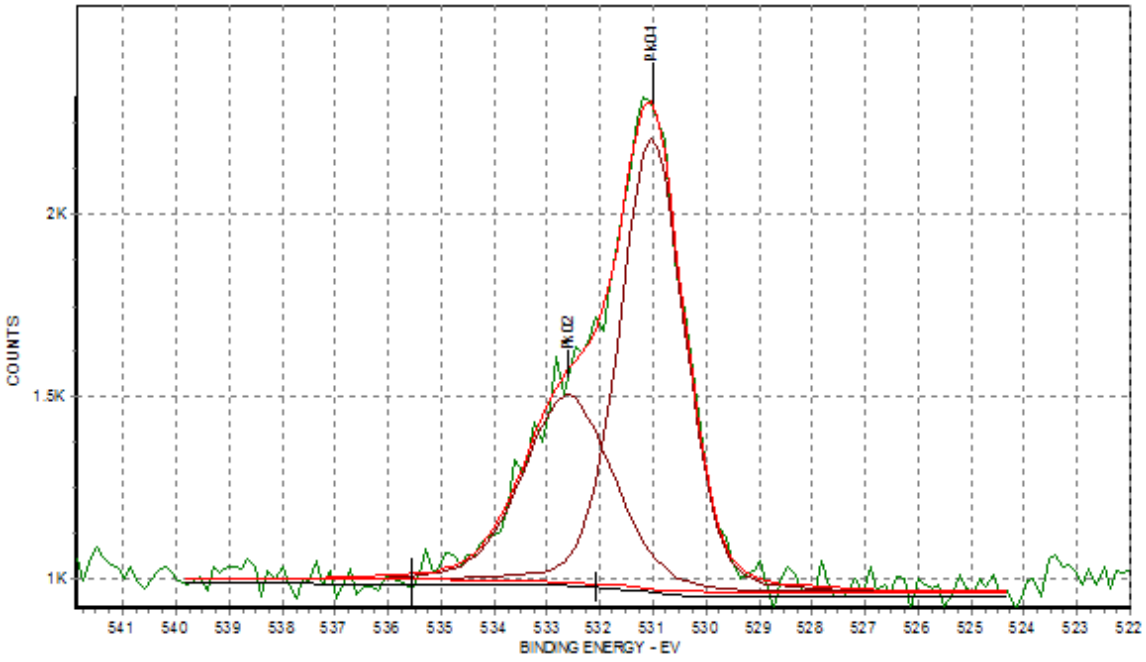

Figure 5.32: HR XPS spectrum from the O 1s region from a ZnO thin film deposited by ALD.

The XPS only provides detail on the surface of the ALD deposited ZnO. From the AES depth profile, the structure of the sputtered film is ZnO. Despite the difference observed between the AES and XPS data (at the ZnO surface), it is clear that bulk of the ALD deposited film is ZnO.

5.3.1.9 RBS of ALD Deposited ZnO

RBS was used to study the stoichiometry of the ALD deposited ZnO. Figure 5.33 provides an RBS spectrum from ALD deposited ZnO which was fabricated under the same conditions as the samples which were used for the AES and XPS analysis. Analysis of the RBS spectrum shown in Figure 5.33 yielded Zn/O ≈ 1. This result corroborates the data taken from AES and further indicates that we do infact create stoichiometric ZnO from the ALD.

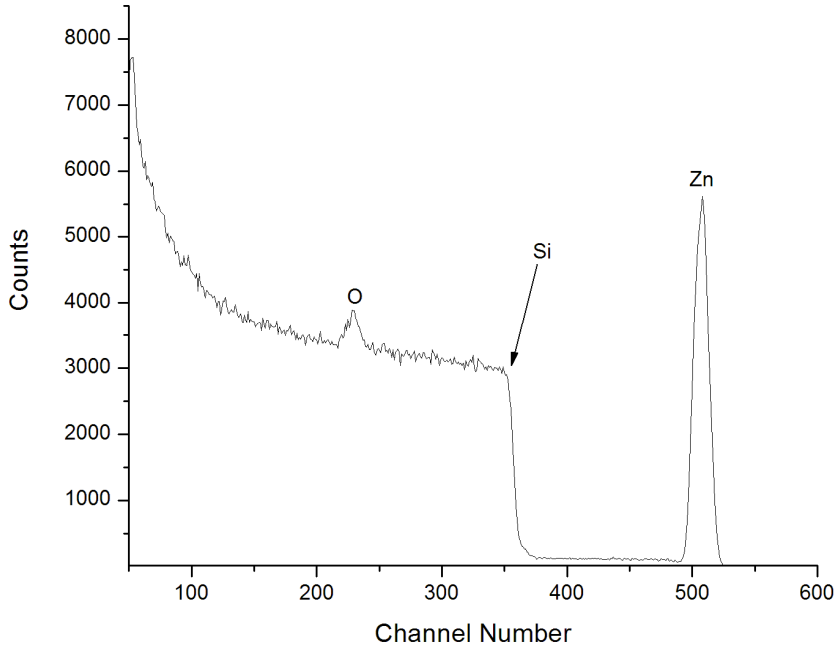

Figure 5.33: RBS Spectrum from ALD deposited ZnO.

The past section has presented surface characterization results demonstrating that the fabrication processes used to create these films will result in the proper film stoichiometry.

5.3.2 Optical Characterization

Since the metal-oxide thin films will be used as transport layers in EL devices, they need to be as optically transparent (in the visible) as possible. The more transmissive the material, the greater the possibility that a generated photon can pass through. Figure 5.34(a-b) presents transmission data from 2 different NiO and TiO_2 films sputtered onto a quartz microscope slide.

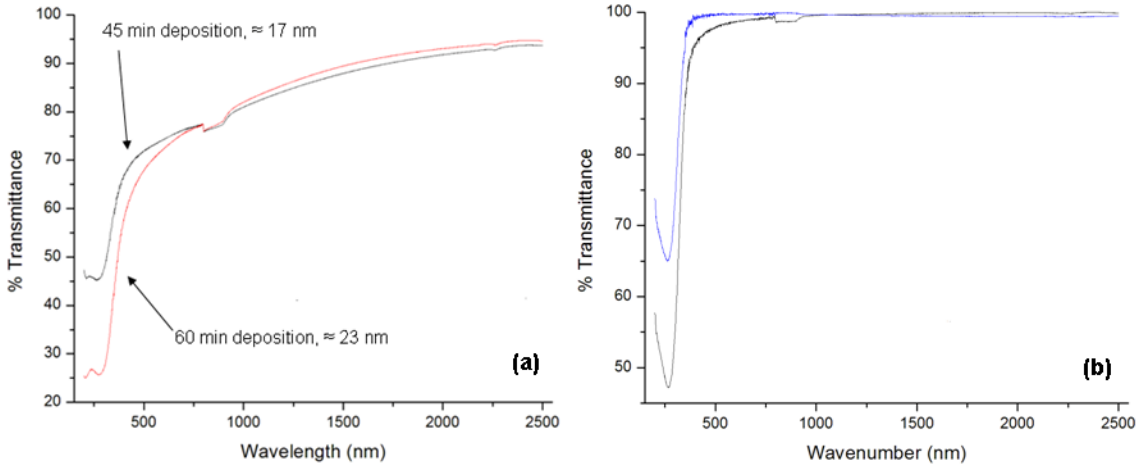

Figure 5.34: Optical transmission data from RF Sputtered (a) NiO and (b) TiO_2 thin films deposited on quartz.

Each of the films shown in Figure 5.34 appears to be fairly transmissive across the visible. The "knotch" observed at around 900 nm is a measurement artifact due to a change in the detector range. To within our ability to measure the TiO_2 thin films appear

to be ~90% transparent. However, this probably due to the fact that the TiO_2 films used in this measurement are extremely thin (< 20 nm). As a comparison, Figure 5.35(a-b) presents literature transmission results from RF sputtered TiO_2 and NiO films. [212, 255].

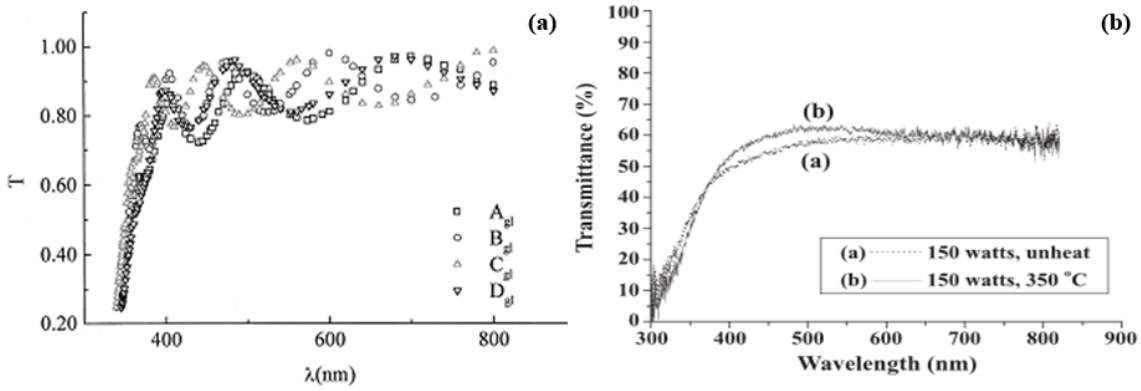

Figure 5.35: Optical transmission data for (a)TiO_2 [255] and (b) NiO [212] RF Sputtered Thin Films. TiO_2 film thickness from Figure 5.35(a) was ≈ 300 nm for samples A-C and ≈ 250 nm for sample D. The NiO film thickness (Figure 5.35(b)) was ≈ 180 nm. Presented as a comparison for the data shown in Figure 5.34.

The data in Figure 5.35 presents transmission data from 4 TiO_2 and 2 NiO sputtered thin films. Similar to the data in Figure 5.34(a-b) these films are highly transmissive across the visible indicating that RF sputtered films are good candidates for EL transport layers. We have yet to been able to measure the transmission from the ALD deposited ZnO films due to equipment problems. Figure 5.36 presents literature transmission data from photo-ALD deposited ZnO films deposited by DEZ and H_2O.

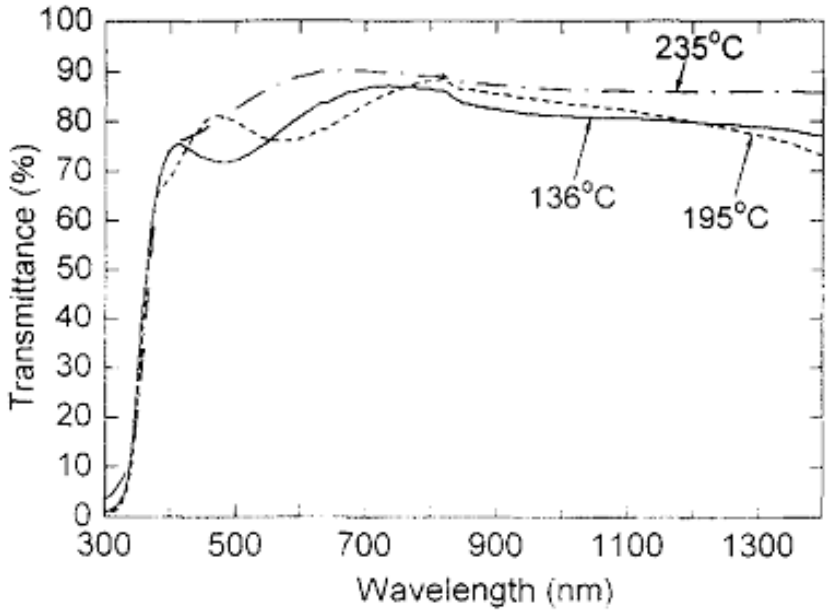

Figure 5.36: Optical transmission data from photo-ALD ZnO thin films. Reproduced from [256].

From Figure 5.36 it appears that the deposited ZnO film is fairly transparent across the visible spectrum, similar to what was observed with both TiO_2 and NiO thin films. Further investigation is needed to ensure that the ALD deposited thin films created in the Savannah reactor are as transparent as the films depicted in Figure 5.36.

5.3.3 AFM

A major requirement of these metal-oxide films is that they must be smooth. Rough surfaces lead to scattering which can cause degradation in the optical properties from an EL device. Also, rough surfaces can lead to nonuniform current distributions. In the case of the RF sputtered NiO films, the substrate was heated to minimize the amount

of surface roughness. Figure 5.37 illustrates the effect of substrate heating on the roughness of RF sputtered NiO films.

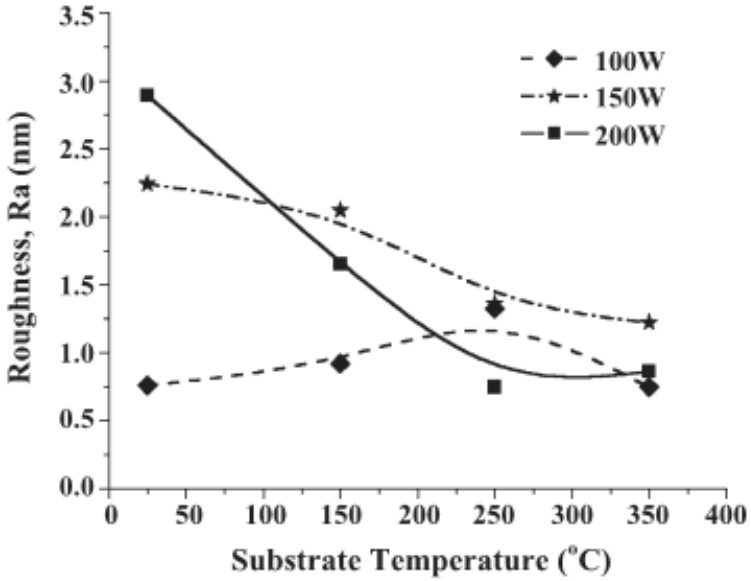

Figure 5.37: Surface roughness as a function of substrate temperature for NiO sputtered NiO thin films. Reproduced from [212].

At 200W (same RF power that is used to generate the NiO films in this study), the roughness decreases as the power decreases. As a result, during the sputtering of the NiO thin films, the substrate temperature was set between 250°C and 350°C to minimize roughness.

Figure 5.38 (a-b) presents AFM images of RF sputtered NiO thin films taken by a Digital Instruments MultiMode Nanoscope III system. The left image (Figure 5.38(a)) presents a tapping mode AFM image (1 μm x 1 μm) from NiO thin film which was synthesized before we determined ideal deposition conditions. For the most part, the film appears to be uniform and smooth. There are larger particles on the surface of the film, but the maximum height of these particles is only 7.62 nm according to the Nanoscope III

software. Despite the presence of the particles on the surface, the RMS roughness is only 0.358 nm.

Figure 5.38(b) presents a contact mode AFM image (1.5 μm x 1.5 μm) from a sputtered NiO film synthesized under the conditions described in section 5.2.3.1.

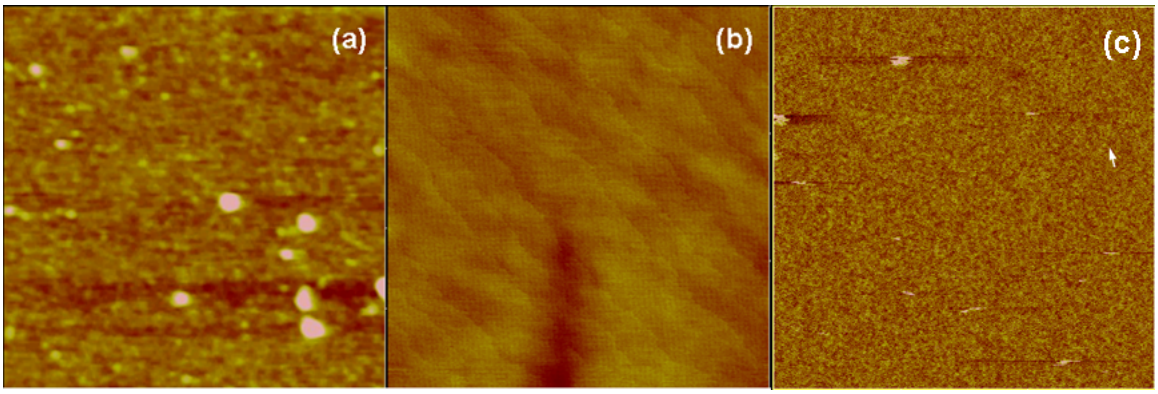

Figure 5.38: AFM images from (a) RF sputtered NiO thin films (produced under non-standard conditions, (b) RF sputtered NiO thin films produced with the standard conditions, and (c) RF sputtered TiO_2 produced under the ideal conditions.

The sputtered film depicted in Figure 5.38(b) is substantially smoother and more uniform that the film in Figure 5.38(a). This observation is validated when the RMS roughness of the films are compared. The RMS roughness from the NiO film in Figure 5.38(b) is 0.083 nm, making the film about 4X smoother than that of the film in Figure 5.38(a). From the AFM data shown above it is clear that the RF sputtering process of NiO is capable of producing uniform and smooth films which are suitable for device integration. The surface of an RF sputtered TiO_2 film (standard conditions, 1 hr deposition) is depicted in Figure 5.38(c). The AFM image is 3 μm x 3 μm, with a maximum height 16.489 nm and a RMS roughness of 0.697 nm. The TiO_2 film is considerably rougher than that of the NiO film in Figure 5.38(c), but the RMS roughness is less than 1 nm

which is more than acceptable for device integration. There are some rougher features on the surface of TiO_2 film, but it hard to tell whether or not these features are due to sputter-induced damage from O radicals or from surface contamination. Although we did not measure the surface roughness of the ZnO, we expect the film to be smooth based on results from other students using the same ALD ZnO recipe. It would be prudent to verify the actual surface topology of the ALD deposited thin films before incorporating them into a novel device architecture.

5.3.4 XRD

XRD measurements (using a Siemens D5005 diffractometer) were performed on the metal-oxide thin films to investigate their crystallinity. We wanted the films to be smooth (as shown in Figure 5.38) and compositionally amorphous to prevent electrical shorts and the formation of preferred current pathways through the device. Figure 5.39 shows XRD data from an RF sputtered NiO thin films synthesized under the conditions discussed in section 5.2.3.1.

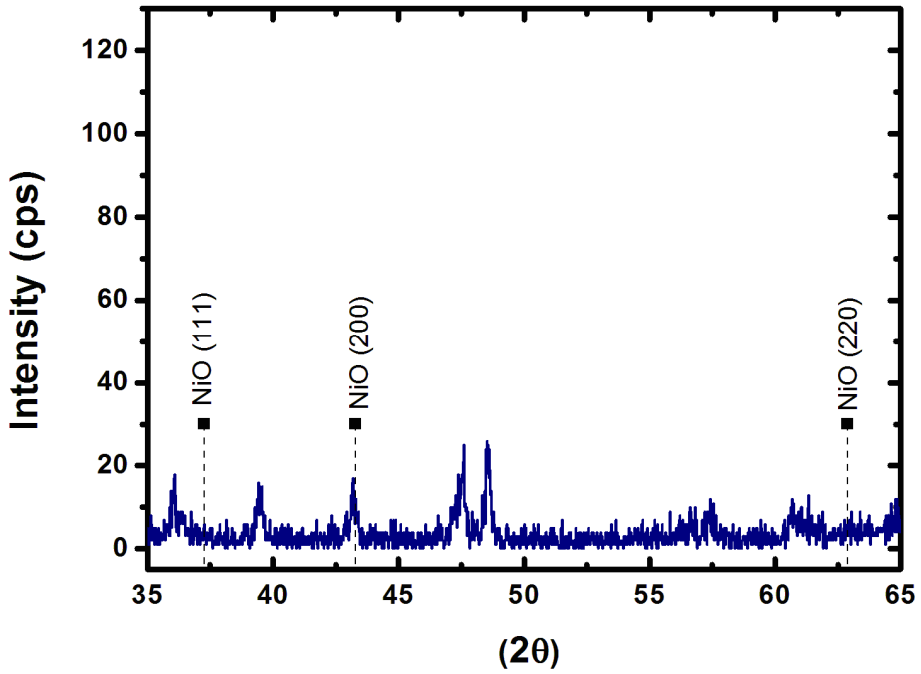

Figure 5.39: XRD scan results from a RF sputtered NiO thin film. Relevant peaks are noted in the figure. The film is ≈ 40 nm thick.

During the XRD scan 2θ was scanned between 10° and 70°. According to Richardson *et al.* [257] three NiO peaks appear in this region. NiO (111) at 37.26°, NiO (200) at 43.29°, and NiO (220) at 62.88°, are the three NiO peaks of interest in this XRD scan. Examining the XRD, it is clear that there is no peak related to NiO (111) or NiO (220). There appears to be a weak peak related to Ni (200) on the scan. The other peaks are related to the substrate material. Although a weak Ni (200) peak appears, we believe that the surface is most likely amorphous since we do not observe the other NiO related peaks and the signal from the (200) is barely above the noise level. XRD characterization was also performed on TiO_2 sputtered thin films. Unlike the NiO thin film in Figure 5.39, the XRD scan in Figure 5.40 shows no crystalline peaks related to any of the TiO_2 phases (rutile or anatase), [258] suggesting that the film is either amorphous or has only very

small grains embedded in an amorphous matrix. The only peak observed on the spectrum is related to the Si substrate. The inset of Figure 5.40 compresses the y-axis to determine whether or not there are small crystalline peaks which may have been dwarfed by the large silicon substrate signal. Examining the inset of Figure 5.40, it is clear that no crystalline peaks are observed.

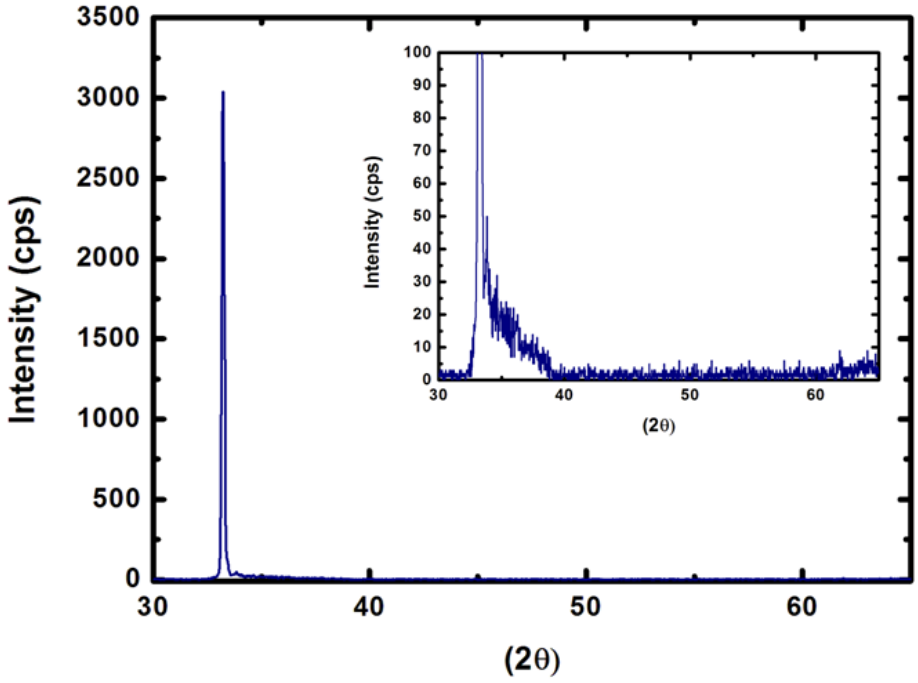

Figure 5.40: XRD scan results from a RF sputtered TiO_2 thin film. The film is ≈ 20 nm thick.

XRD characterization was also performed on the ALD deposited ZnO samples which were fabricated using the standard ZnO process. From studying publications on ALD deposited ZnO, there are three XRD peaks which may appear on a scan. Peaks related to the (100), (002), and (101) orientations are located at 2θ angles of 31.7°, 34.4°, and 36.2°. [240, 243, 248] Peaks related to the (102) and (110) orientations of ZnO has also been observed in low temperature oxidation of metallic zinc. [259] These XRD

peaks appear at 2θ angles of 47.5° and 56.7°. [259] Figure 5.41 presents the XRD spectrum from the ALD deposited ZnO.

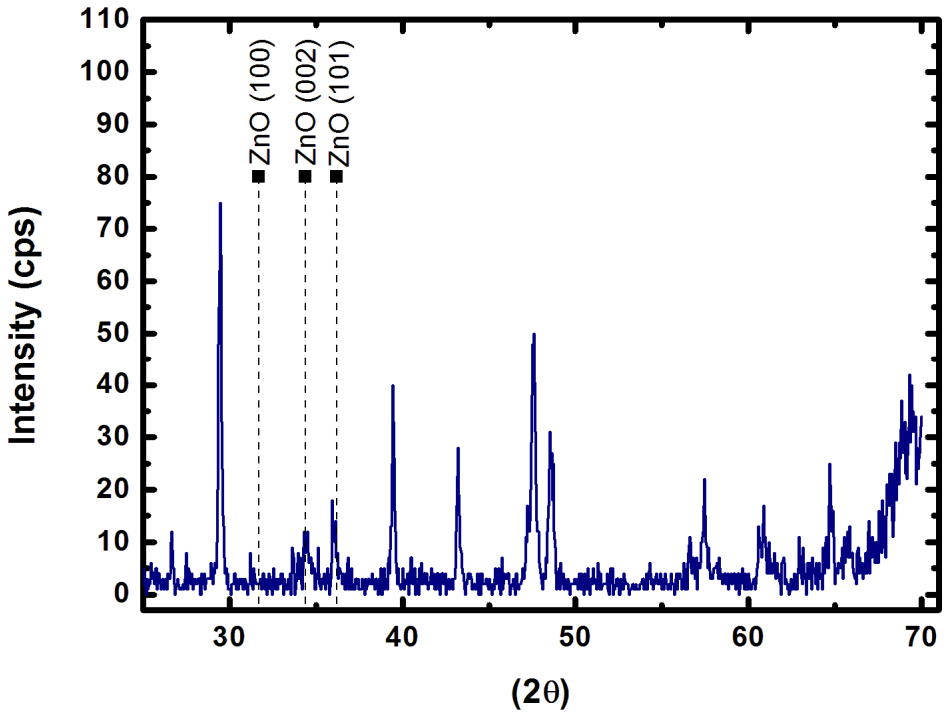

Figure 5.41: XRD scan results from an ALD deposited ZnO thin film. Relevant peaks are noted in the figure. The film is ≈ 60 nm thick.

The large peak near 2θ ≈ 29° is related to the (111) orientation of the silicon substrate. This peak was also observed in the XRD scans of both the NiO and the TiO_2 samples. The 2θ peak at ≈ 69° is also a silicon related peak (Si (400)). The three ZnO peaks of interested are highlighted in Figure 5.41. From the Figure it appears that weak peaks associated with ZnO (002) and (101) are present. However, these peaks are dwarfed compared to those related to the Si substrate. There appears to be no ZnO (100) peak. Several other peaks appear on the scan, some related to the Si substrate (Si (220) and (311) at ≈ 48° and ≈ 57° respectively). [260] The other peaks in the spectrum could be

related to other ZnO or Zn orientations. [259] In any case, the ZnO peaks observed in the XRD are extremely weak, and therefore it is likely that the ZnO sample is mostly amorphous.

5.4 Integration

5.4.1 – SiNC Based EL Devices

Silicon dominates the microelectronic industry, but due to its indirect bandgap (1.1 eV) it is a poor light emitter. As a result, II-VI and III-V compound semiconductors have dominated the LED market. An efficient Si light emitter would be cheap, stable, and could be integrated in existing microelectronic architectures such as optical interconnects. Bulk silicon has a bandgap at 1.1 eV. Even if efficient light was generated by this material, its emission would be in the infrared and not the visible. The solution to this problem is to take advantage of the quantum confinement effect in SiNCs. High PL QYs [41] and PL tunability have been demonstrated with SiNCs. [111, 112, 153]

SiNC EL devices have been investigated thoroughly since the demonstration of visible light from Si. For the most part, the EL devices are based upon SiNC embedded in an inorganic matrix, typically silicon oxide or nitride [51, 261-271] although other novel structures were explored. [74, 261, 272-274] To date, the highest EQE from a SiNC EL is 1.6%. [51] This device reported by Cho *et al*. [51], is presented in Figure 5.42:

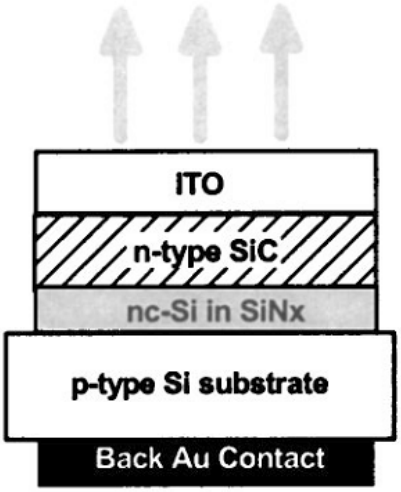

Figure 5.42: Most efficient SiNC based EL device structure (Efficiency ≈ 1.6%) Reproduced from [51].

The device presented in Figure 5.42 is simple. It incorporates an NC silicon emissive layer embedded in a silicon nitride matrix, with 2 inorganic transport layers. The transparent ITO contact allows for the generated light to escape from the device. Although efficient EL was observed, the device still incorporates NC in an insulating matrix (charge injection problems) which limits further device improvements. Therefore, in order to increase the efficiency from SiNC based EL devices, we need to investigate alternative device structures. One option may be to adapt metal-oxide transport layers utilized in II-VI NC and polymer-based EL devices. A second option would be to use a conductive polymer as a host matrix. EL was observed from oxidized SiNC dispersed in PVK. However, the device efficiency was extremely low, and because oxidized NCs were used the device emission was limited to the red-NIR range. Since we plan to integrate CF_4 or SF_6 etched NCs (to allow full-color emission) as an emissive layer,

polymer host will not work (see chapter 4). Therefore, we decided to investigate option 1, were metal-oxides will be used as charge transport layers.

5.4.2 – Emergence of Metal-Oxides as Transport Layers

Over the past several years, metal-oxide thin films have received much attention in the LED community as potential transport layers or transparent electrodes for II-VI NC or organic based electroluminescent (EL) devices. [78, 79, 275-284] Although efficient NC-organic devices have been demonstrated utilizing organic transport layers (QE ≈ 2%) [23, 75], researchers are concerned about the lifetime of these devices. Metal contacts on the organic transport layers can be unstable and furthermore, the organic materials degrade when exposed to oxygen (or air). [76, 77] Inorganic transport layers are of significant interest because of their improved electrical and chemical stability over their counterparts and their ability to tolerate higher current densities compared to their organic counterparts. To this date, only one research paper has reported a successful synthesis of an all-inorganic NC LED. Figure 5.43(a-b) illustrates this novel device design. The inorganic transport layers are sandwiched between a ZnCdSe emissive layer. Figure 5.43(b) displays the band diagram of the device in figure 5.43(a). According to Caruge [79], three common guidelines were used to fabricate this device:

(I) Smooth, amorphous films were deposited to prevent electrical shorts or preferential current pathways.

(II) Metal-oxide films with low carrier concentrations were chosen to minimize EL quenching due to plasmons. [78, 285-288]

(III) HTL and ETL were selected to have similar band offsets to ensure that charge remained balanced in the device. An excess of one charge carrier type can lead to NC charging, which may result in Auger recombination (a non-radiative process). [79, 289]

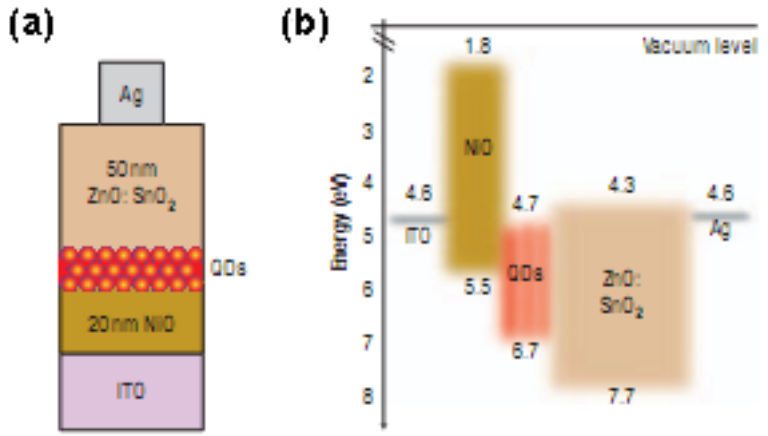

Figure 5.43: First all-inorganic (metal-oxide) NC based LED utilizing II-VI NCs as an emissive layer. The (a) device structure and the (b) band diagram are shown in the figure. Reproduced from [79].

The transport layers also serve as a blocking layer preventing free charge carriers from escaping the active region and traveling to the electrodes where recombination would occur. The maximum EQE of this device was reported to be 0.09%. One potential problem with this device is the use of NCs which are composed of toxic materials which may limit their potential integration into commercial technologies. A second issue deals with the fabrication. The II-VI NCs are synthesized in a solution-based process which may not be adaptable with common microelectronic processes.

The research presented in chapters 2-4 were focused on developing efficient silicon light emitters. Compared with the compound NC systems (specifically II-VI),

silicon is non-toxic and compatible with existing technologies. Full-color emission from SiNCs have been demonstrated from both CF_4 and SF_6 [111, 112, 153] etched NC with efficiencies as high as 55% (as a comparison the ZnCdSe NCs used in [79] had reported QY of 50-60%) which makes them an attractive alternative for an emissive layer in a hybrid inorganic-NC based LED.

5.4.3 – Early Integration Approaches

We decided to approach the fabrication of inorganic-etched NC LEDs in a systematic fashion, starting with a simple device design and building in more complexity over time. The first device that was studied is shown in Figure 5.44.

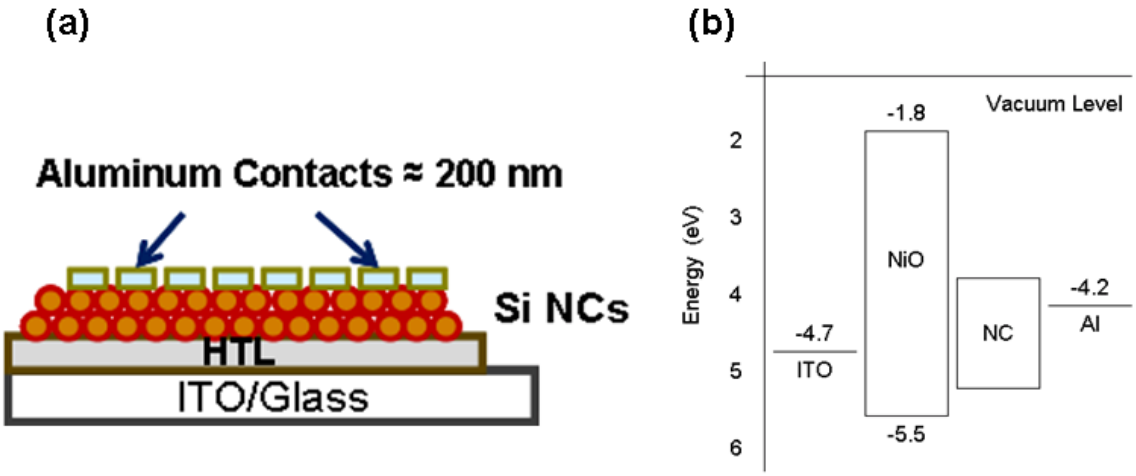

Figure 5.44: Initial all-inorganic (metal-oxide) NC based EL device. The (a) device structure and the (b) band diagram are shown in the figure. Etched SiNC are used as the emissive layer.

Figure 5.44(a) shows the device architecture. RF sputtered NiO fabricated under the conditions discussed in section 5.2.3.2 was deposited on ITO/Glass (purchased from Delta Technologies Inc.). Following the NiO deposition, the substrates were fixed to a

SS Mesh by carbon tape and placed at the exhaust of the etching plasma (Figure 4.5(a)). The NC were deposited under standard conditions (Synthesis - 55 Ar, 7 SiH_4/He @ 100W; Etching – 4 SF_6 @ 20W) and collected for 2 minutes. After NC deposition, the NCs were left in air for a day to ensure that all dangling bonds were passivated. Before the e-beam evaporation of Al, the NCs were exposed to UV light to ensure that PL was observed. 200 nm of Al were deposited on the NCs through a stencil mask. Following Al deposition the devices were characterized via I-V measurements using the HP4145A semiconductor analyzer. The EL from the NC devices was studied through use of a Newport 2835C Multi-Function Optical Meter and 818-SL photodetector.

Figure 5.44(b) presents the band diagram from the device shown in Figure 5.44(a). Ideally, the holes injected via the ITO will travel to the NiO and then to the NC layer where a recombination event could occur with an electron injected from the Al contact. Studying the band diagram, one notices several issues. First of all, the electrons are directly injected into the NC layer, while the holes have to traverse the NiO layer. This could lead to a large charge imbalance in the device which may reduce the device efficiency. Secondly, there is no hole blocking layer. Therefore, the holes could simply pass through the NC layer and be annihilated at the Al contact. The position of the NC E_V and E_C are taken from literature values and so should be considered as approximate values for the device. We attempted to perform UPS measurements on the etched NC to obtain the position of E_V, but we were unable to do so. Therefore it is possible that we may have charge imbalance issues to due to approximated position of the NC bands.

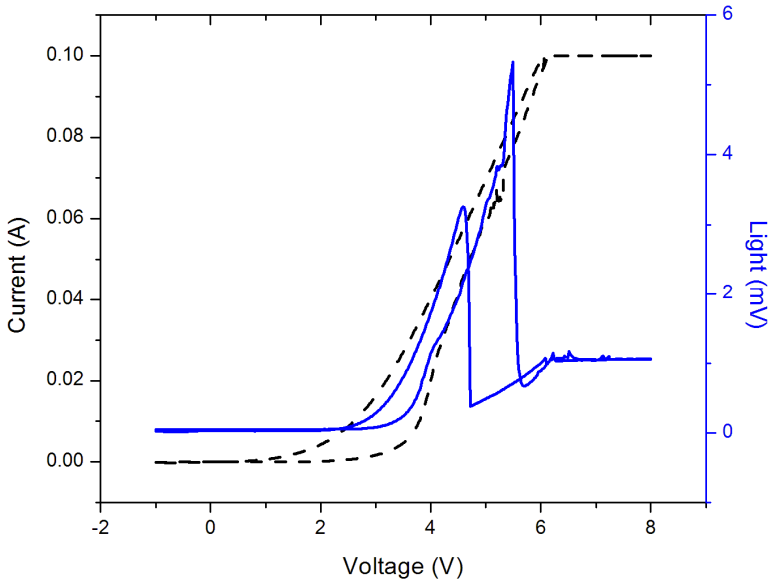

Figure 5.45: I-V data and photodetector response from the device illustrated in Figure 5.44. The I-V Trace is presented as a dashed line while the photodetector response is presented as a solid line.

Figure 5.45 presents I-V data and the photodetector response from the inorganic-NC device shown in Figure 5.44. Despite the potential issues described above, the device emits light beginning around 4V. The emission continues to increase as the current increases until the HP4145A saturates at 100 mA. Near 6V, the light output measured by the photodetector appears to drop. This drop in light output is not related to any device degradation; rather it is due to a scaling change in the photodetector. Thus the light measured by the photodetector after 6V needs to multiplied by a factor of 10 to obtain an accurate measurement by the photodetector. The corrected light output is shown in figure 5.46. The I-V data is interesting as well. The current increases until it reaches the saturation limit of the HP4145A. In an ideal material, the repeat trace should be identical to the initial trace. Thus the scan from -1 to 8V should be the same as the scan from 8 to

-1V. However, this is not observed. This indicates that there some trapping phenomenon occurs in this device. This is not unexpected because there could be dangling bonds on the NC surface or interface issues which may lead to charge trapping.

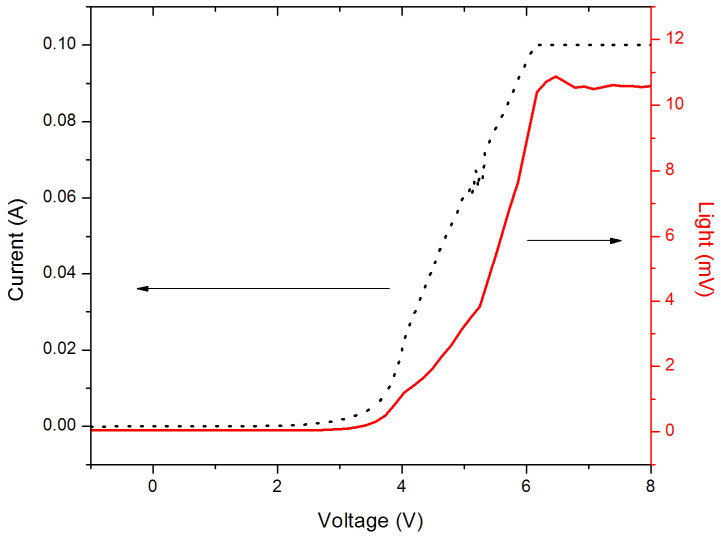

Figure 5.46: Corrected light output from the device shown in Figure 5.45. The I-V data from Figure 5.45 is reproduced in this data.

The light emitted from this device appeared to be a faint orange-red, but it was too weak for the USB2000 spectrometer to detect. Nevertheless, this simple architecture provides a starting point for more advanced inorganic-NC based EL devices.

The device discussed above only implements a NiO hole transport layer and a thick Al top contact. In order to improve device efficiency, we decided to incorporate an inorganic ETL into the device. Figure 5.47 illustrates the improved device architecture. RF sputtered TiO_2 and ALD deposited ZnO were utilized as ETLs. The fabrication for these devices is similar to that described for the device in Figure 5.44. For the "standard" device shown in Figure 5.47(b), the NiO was sputtered onto the ITO/Glass followed by the etched NC deposition. After the NC deposition, the ETL was deposited on top of the

NC layer by either ALD (ZnO) or sputtering (TiO_2). Following the ETL deposition, the top contacts Au (ZnO) and Al (TiO_2) were e-beam evaporated on top of the ETL through a stencil mask.

Figure 5.47: Improved inorganic (metal-oxide) – NC device structures. The "upside-down" architecture is shown in (a), while the standard design is shown in (b)

Figure 5.47(a) presents the "upside-down" device. Since ITO can be used as either a hole or electron injector, we decided to investigate what kind of an effect if any this change would have on the operation of the inorganic-NC based LED. Figure 5.48(a-b) shows the band diagram for the device in Figure 5.47(b) utilizing TiO_2 or ZnO.

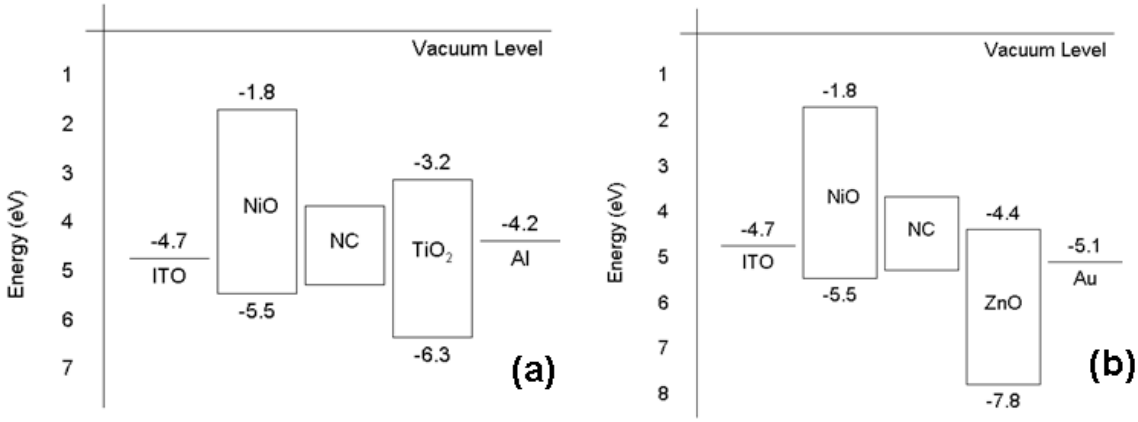

Figure 5.48: Band diagrams for the improved inorganic (metal-oxide) – NC device structures. The band diagram for a device with a TiO_2 ETL is shown in (a) while that incorporating ZnO is shown in (b).

Figure 5.48 provides the band diagrams for the improved "standard" device utilizing ETLs. In both cases, the ETL and associated contact are chosen so the band offset approximately matches that of the NiO and ITO. Once again the problem with the band structure shown in Figure 5.48 is the approximate value used for the position of the E_V and E_C in the SiNCs which is adapted from [31]. If the actual position differs from the approximation, then serious device problems could occur.

Several variations of the devices depicted in Figure 5.48 were investigated. For the most part, little or no light was observed from these devices. We attempted to change the top contact, use multilayered contacts (such as Ti/Au or Cr/Au for the ZnO), and varied the thickness of the transport and NC layers. However, no real improvement in device operation was observed. One batch of devices utilizing the "upside-down" architecture shown in Figure 5.47(a) showed promise. For this particular batch, 80 nm of ZnO was deposited onto ITO/Glass via ALD. Following the NC deposition (using the same conditions as the device shown in Figure 5.46 – time 2.5 min) the NiO HTL was sputtered on top of the NCs. After this step, an Al top contact (200 nm) was e-beam evaporated through a stencil mask. The I-V and light output of the "best" device from this batch is shown in Figure 5.49(a). The corrected light output from this device is replotted in Figure 5.49(b).

The improved device has a light output which is almost 4X greater than that of the device which did not incorporate an ETL. The "turn-on" of the light occurs near 7V. This increase in the turn-on voltage is expected because of the added voltage drop incurred by the addition of the ETL. Despite this four fold increase in the photodetector

response, the EL remained weak (emission in the orange-red region). Unfortunately, this device burned out before we were able to take an EL spectrum with the USB2000 spectrometer. There are some odd spikes observed in the I-V data. It is possible that these are related to contact problems but more study is needed. Several attempts to reproduce these results did not yield a functional device. We are currently investigating what problems exist with these inorganic-NC devices. We suspect the contacts because large craters (or holes) are observed on the contact after a small voltage is applied.

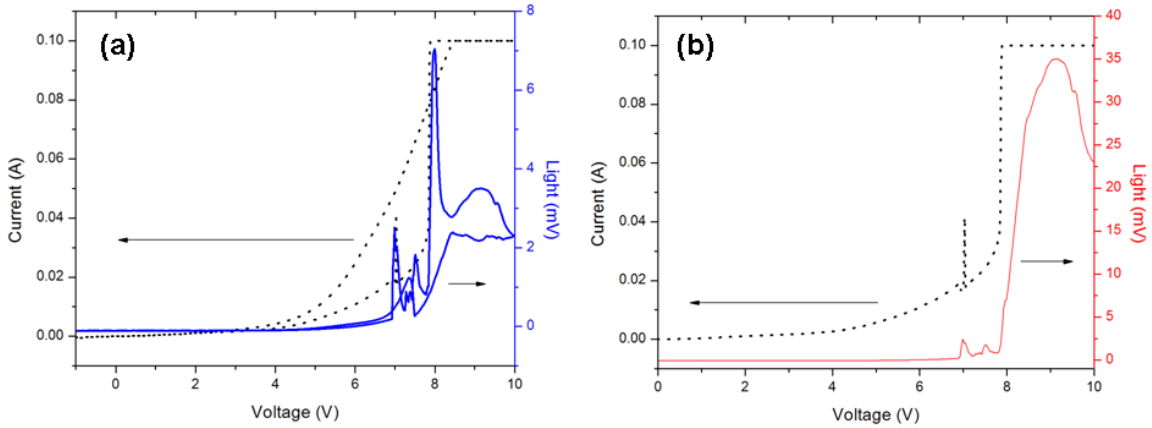

Figure 5.49(a-b): (a) IV Data and PD Response from the "Best" Improved inorganic (metal-oxide) - NC based EL Device. The corrected light output is shown in (b).

Another problem which needs to be address is the structure of the as-deposited etched NCs. Figure 5.50(a-b) presents SEM images from as-produced etched NCs collected under standard conditions for 15 minutes deposited on Au/Cr/Si substrates. The low magnification images displayed in Figure 5.50(a) shows an etched SiNC film which appears to be uniform across the substrate. However, examining the higher magnification image shown in Figure 5.50(b) one realizes that the film is porous and non-uniform. This presents a challenge to device integration. If the particles have sufficiently close spacing,

charges may be hopping along the particle chains, restricting them to small effective areas. Also, if the transport layer deposited on top of the SiNCs penetrates the NC layer, carriers may simply be bypassing the SiNCs altogether. This may be the reason why we observe little or no light output from these devices. One way to solve the second problem would be to embed the NCs in an insulating matrix with a large bandgap such as SiO_2 or Al_2O_3 such that the gaps in the NC film are filled in by the insulating material. Thus the only path of charge transport in the device could only be through percolation.

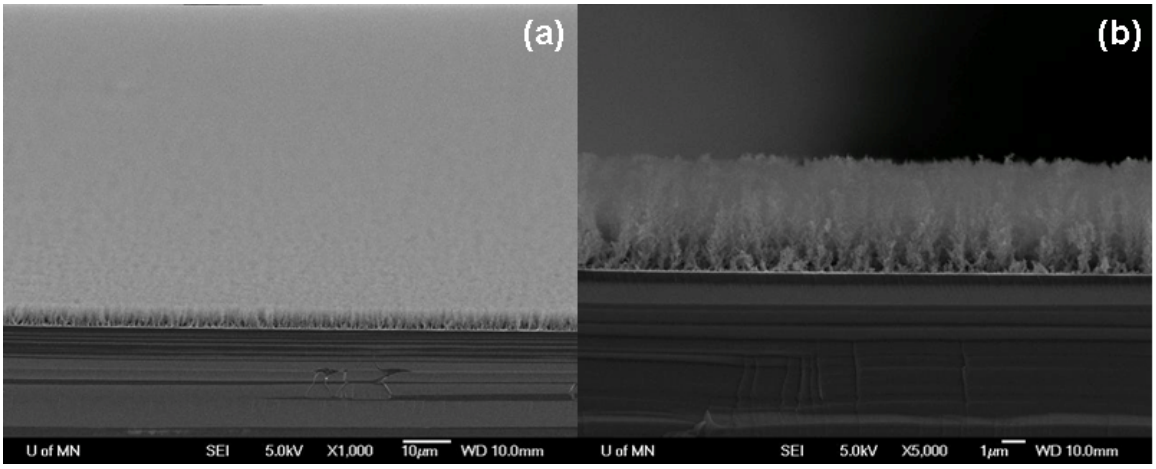

Figure 5.50: SEM images from SF_6-etched SiNC deposited on Au/Cr/Si. (a) Titled top view, (b) cross-sectional view.

5.4.4 Etched SiNCs embedded in an SiO_x matrix

The first approach to improving transport in the NC emissive layer was to use SiO_x which could be deposited by ALD. The ALD SiO_x should conform to the surface of the NCs due to the nature of the ALD process. To ensure that we would induce interface issues at the SiO_x-ETL interface, the SiO_x was chemical-mechanically polished (CMP). The CMP process smoothed out the surface and thinned (removed ≈ 10Å in 10 cycles)

the ALD SiO_x. Before integrating this material into the inorganic-NC device, we decided to investigate the morphology of the ALD SiO_x.

The SiO_x process available on the Savannah ALD system works as follows. A pulse of trimethylaluminum $(CH_3)_3Al$ is followed by a pulse of tris(tert-butoxy)silanol $((CH_3)_3CO)_3SiOH$. [290] This constitutes one cycle and results in a deposition of approximately 10 nm. Figure 5.51(a-c) provides the growth rate of SiO_x as a function of the (a) tris(tert-butoxy)silanol dose, (b) trimethylaluminum $(CH_3)_3Al$ dose, and (c) the deposition temperature.

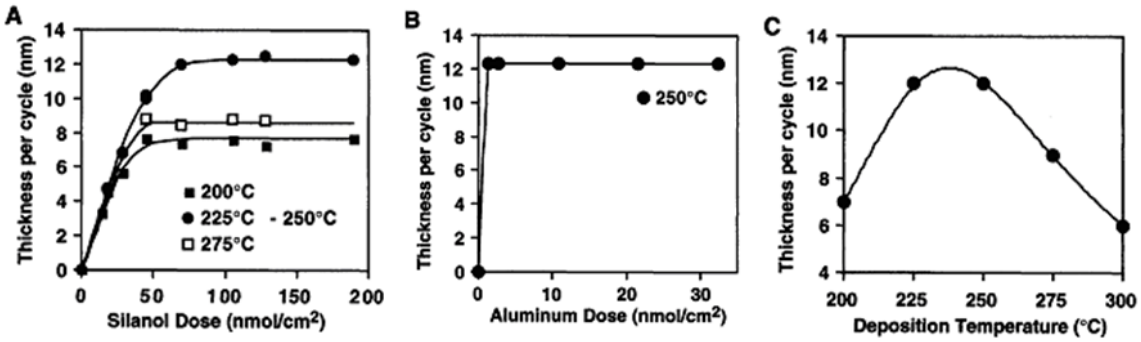

Figure 5.51: SiO_x thickness as a function of the (a) silanol dose, (b) TMA dose, and (c) deposition temperature. Reproduced from [290].

First of all, we examined the ALD deposited SiO_x by XPS. As expected, the sample was oxidized. C was also observed on the surface. The XPS was performed a day after the synthesis. The surface is nearly 19% C. It is possible that this large amount of C is related to contamination and unreacted precursor material. No Al is observed in the spectrum. Figure 5.52 presents the XPS survey spectrum from the ALD deposited SiO_x.

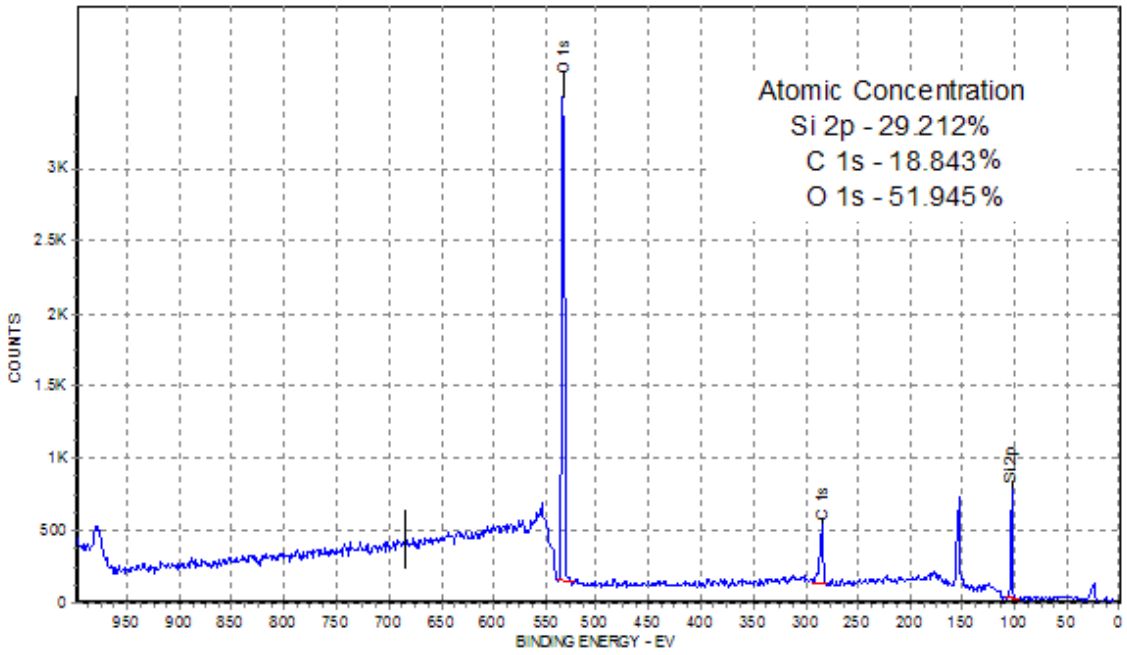

Figure 5.52: XPS Survey Spectrum from ALD deposited SiOx. Peaks related to Si, C, and O are observed on the spectra.

Figures 5.53(a-c) present the HR XPS data from the ALD deposited SiO_x films. In Figure 5.53(a) the Si 2p region is displayed. Although the curve fit is not perfect, it is clear that there is only one peak in this region. The peak is near 103 eV and is related to Si-O. [187] Figure 5.53(b) displays the O 1s HR XPS spectrum from the ALD deposited SiO_x. Similar to the Si 2p spectra, there is only one peak present on the spectrum centered near 532.3 eV. This peak is also related to Si-O. [187] The C 1s HR spectrum is shown in Figure 5.53(c). Three peaks are observed in the spectrum and are related to carbon contamination on the sample. [187]

The Si/O ratio can be calculated using the following relationship:

$$\frac{Si}{O} = \frac{I_{A,Si}}{\sigma_S} * \frac{\sigma_O}{I_{A,O}}$$

where $I_{A,Ni}$ and $I_{A,O}$ are the areas under the SiO_x related peaks in the Si 2p (103 eV) and O 1s spectra (532.3 eV). The other two terms are the sensitivity factors of both Si (σ_{Si} = 0.817) and O (σ_O = 2.93) which can be found in any standard XPS reference guide. Using this relationship, the Si/O ratio was calculated to be ≈ 0.5603.

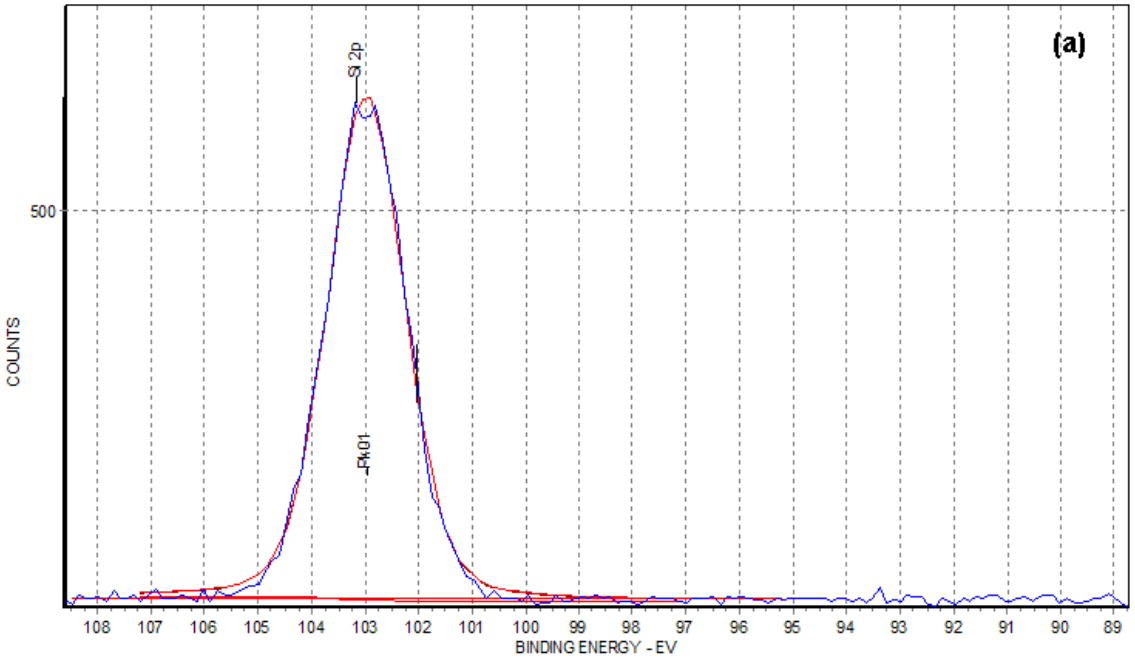

Figure 5.53(a): Si 2p HR XPS spectrum from ALD deposited SiO_x thin films.

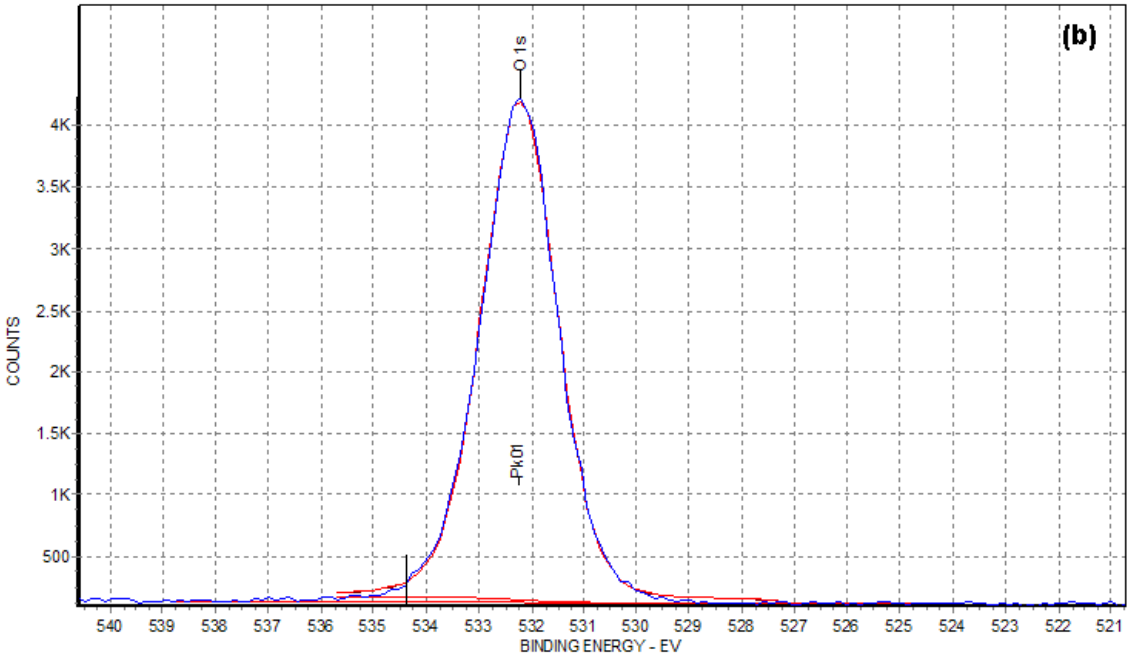

Figure 5.53(b): O 1s HR XPS spectrum from ALD deposited SiO_x thin films.

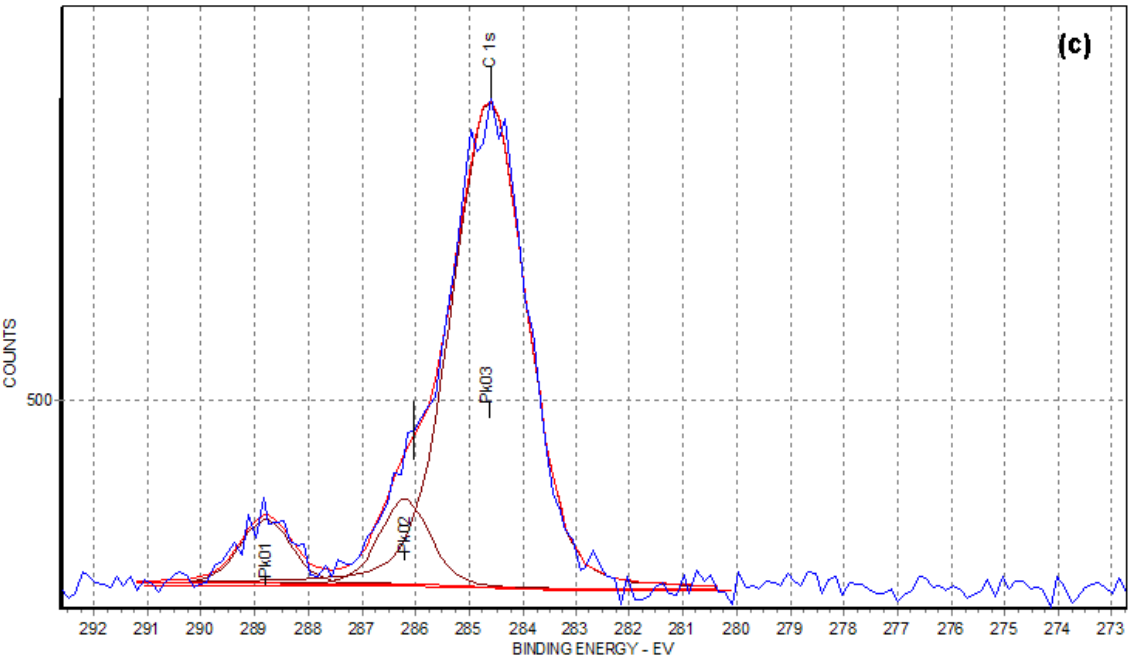

Figure 5.53(c): C 1s HR XPS spectrum from ALD deposited SiO_x films

Since the ALD process appeared to deposit SiO_x, the next step was studying the morphology of the SiO_x. Figure 5.54 presents a contact mode AFM image (5 μm x 5 μm) from ALD deposited SiO_x.

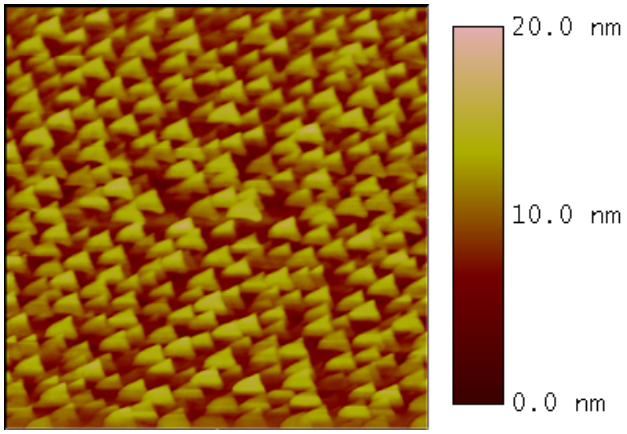

Figure 5.54: Contact mode AFM image of ALD deposited SiOx on Au/Cr/Si.

It is clear from the height image in Figure 5.54 that the ALD SiO_x process does not lead to smooth, uniform films. The surface is extremely rough and non-uniform. The RMS roughness of this film was measured to be 2.523 nm which is approximately 30X rougher than that of the sputtered NiO film. If this film were integrated into the device structure (even with CMP) it would most likely lead to the formation of a poor interface, which would lead to a reduction in device efficiency. SEM images (shown in Figure 5.55) validate the AFM image shown in Figure 5.54.

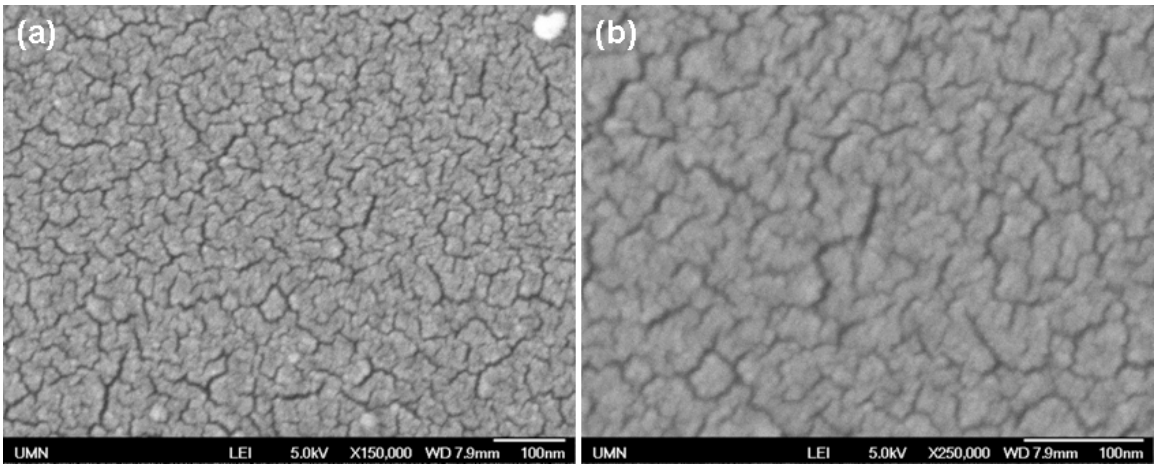

Figure 5.55: (a-b) SEM images of ALD SiO_x on Au/Cr/Si.

Both of the images (Figures 5.55(a-b)) show a surface topology which appears to be rough and non-uniform. Cracks in the film are also observed. The situation worsens when SiNCs are incorporated into the device. Figure 5.56(a-d) shows SEM images from ALD SiO_x/SiNC/Au/Cr/Si. Examining the SEM images, it is clear that the SiOx process does not follow the surface topology. Rather, it seems that the SiO_x layer may have simply coated the etched NC layer. The surface morphology appears even rougher than that observed for just SiO_x on the conductive substrates. It will be extremely difficult to fabricate an efficient EL device utilizing this layer. The interface problems at the SiO_x-ETL surface will most likely lead to numerous states which will lead to poor device performance.

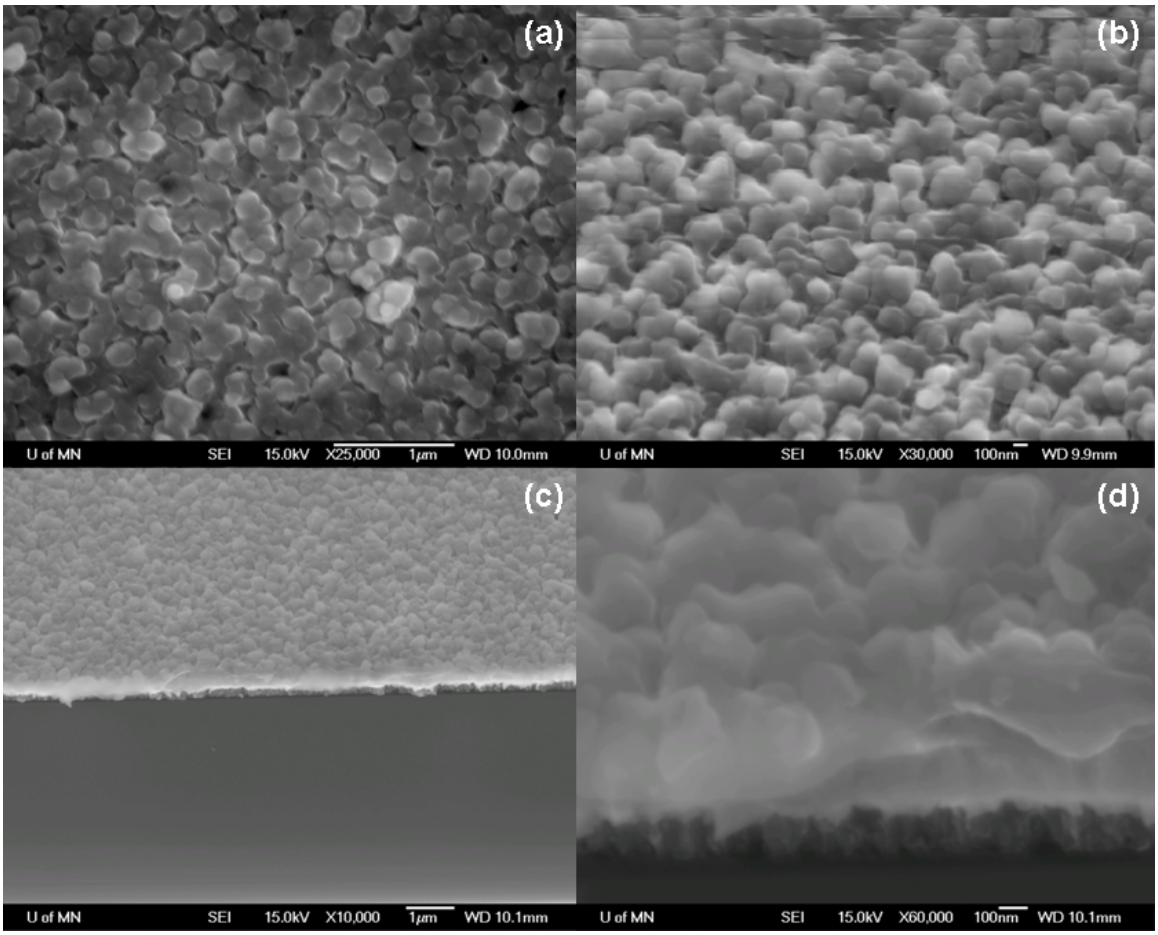

Figure 5.56. SEM images from ALD deposited SiO_x on etched SiNC/Au/Cr/Si. (a) Top view, (b) titled view, (c-d) cross-sectional views.

5.4.5 Etched NCs Embedded In Al_2O_3

After studying the ALD SiO_x process, it is clear that this layer will not work as intended. As a result, we have started investigating other alternative matrix materials. One possibility is the use of Al_2O_3. Al_2O_3 has a bandgap which is similar to SiO_2 and has a well known and characterized ALD process. [291, 292] This is currently under investigation. The proposed device structure is shown below in Figure 5.57.

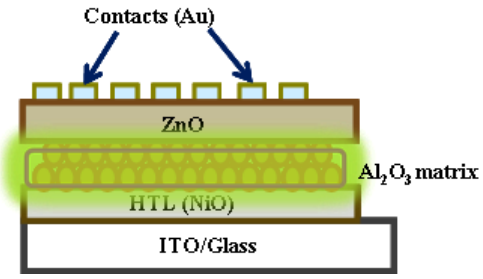

Figure 5.57: Improved inorganic (metal-oxide) – NC EL device utilizing Al_2O_3 as an insulating matrix.

Complete device fabrication is ongoing, but we have been able to investigate the structure and surface chemistry of the ALD deposited Al_2O_3 and etched SiNCs capped with ALD deposited Al_2O_3. Figure 5.58 presents an XPS survey scan from an ALD deposited Al_2O_3 thin film on Au/Cr/Si. 200 loops of the ALD process were run, yielding a thickness of ≈ 30 nm measured by ellipsometry (Note: The ALD process for Al_2O_3 is similar to the ZnO process except that the DEZ has been replaced by trimethylaluminum).

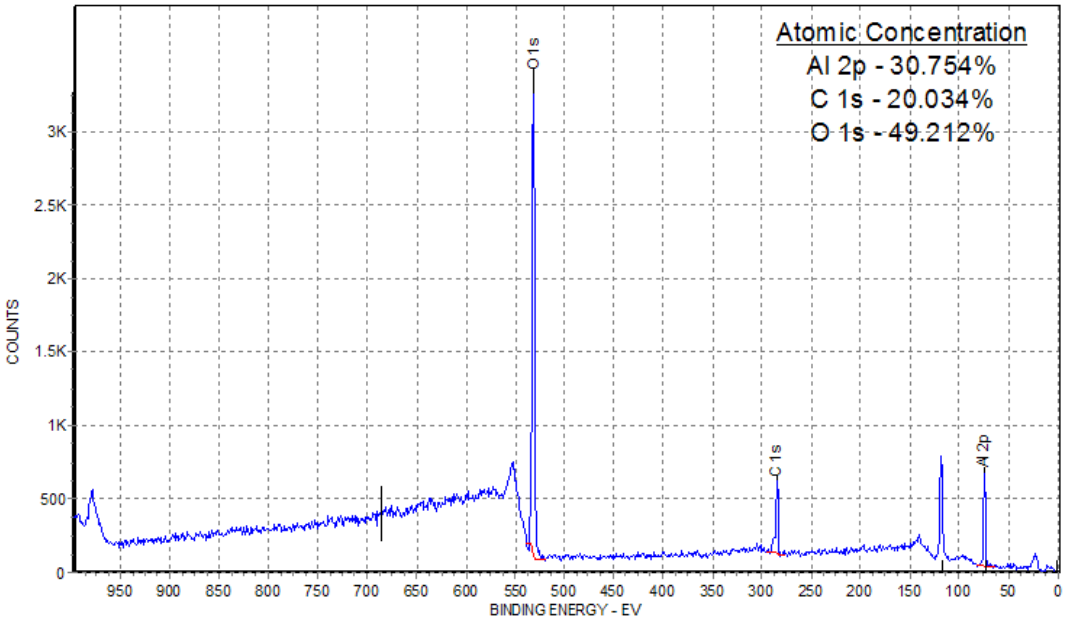

Figure 5.58: XPS survey spectrum from ALD deposited Al_2O_3 on Au/Cr/Si. Peaks related to Al, O, and C are present.

From the XPS survey Al, C, and O are observed on the surface. The surface is mostly Al and O (as expected), but as with any sample which has seen some air exposure, there is some C present at the surface since the samples were measured approximately 4 days after synthesis. The HR XPS scans (shown in Figure 5.59 (a-c)) back up the results of the survey spectrum. The calculated Al/O ratio from the HR XPS yields Al = 1.46O or $Al_2O_{2.92}$. This is stoichiometric within the accuracy of the measurement. The HR XPS data from the Al 2p spectrum is shown in Figure 5.59(a).

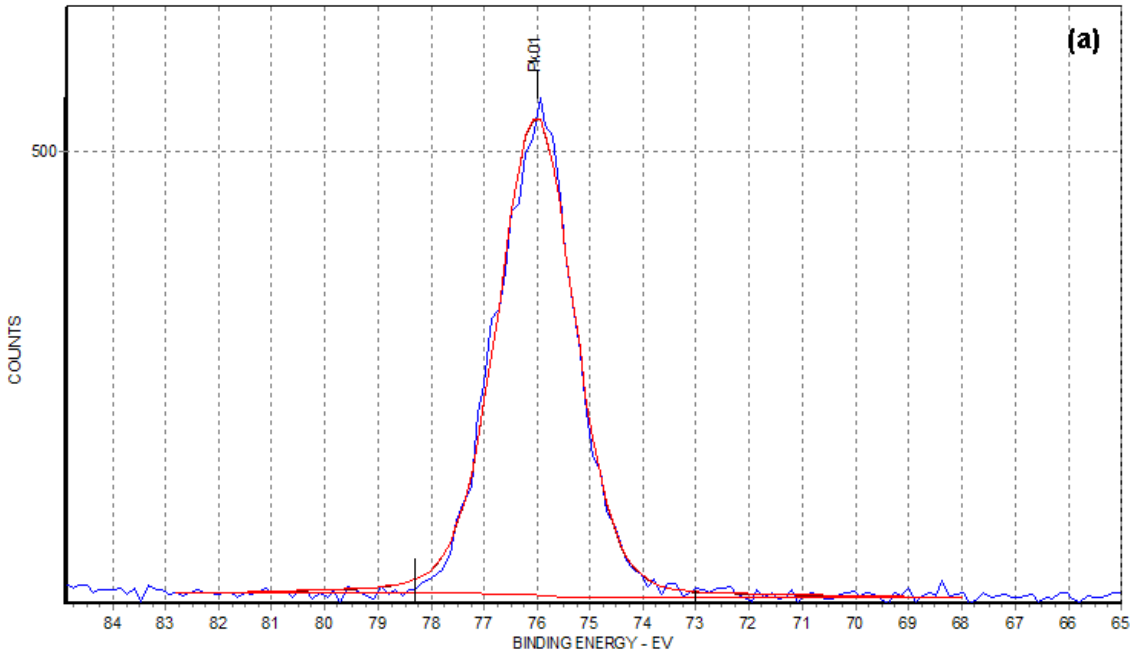

Figure 5.59(a): HR XPS of the Al 2p region from ALD deposited Al_2O_3 films.

One peak is observed on this spectrum centered near 76 eV. According to Christ [187], the Al_2O_3 peak appears near 75.6 eV. Therefore, the peak observed in the Al 2p region is most likely due to Al_2O_3. The O 1s HR spectrum is shown in Figure 5.59(b). The Al_2O_3 peak is centered near 532.3 eV. [187] This is observed on the spectrum in Figure 5.59(b).

The other peak in the O 1s spectrum is due to C-O related bonds. [187] The C 1s spectrum is presented in Figure 5.59(c).

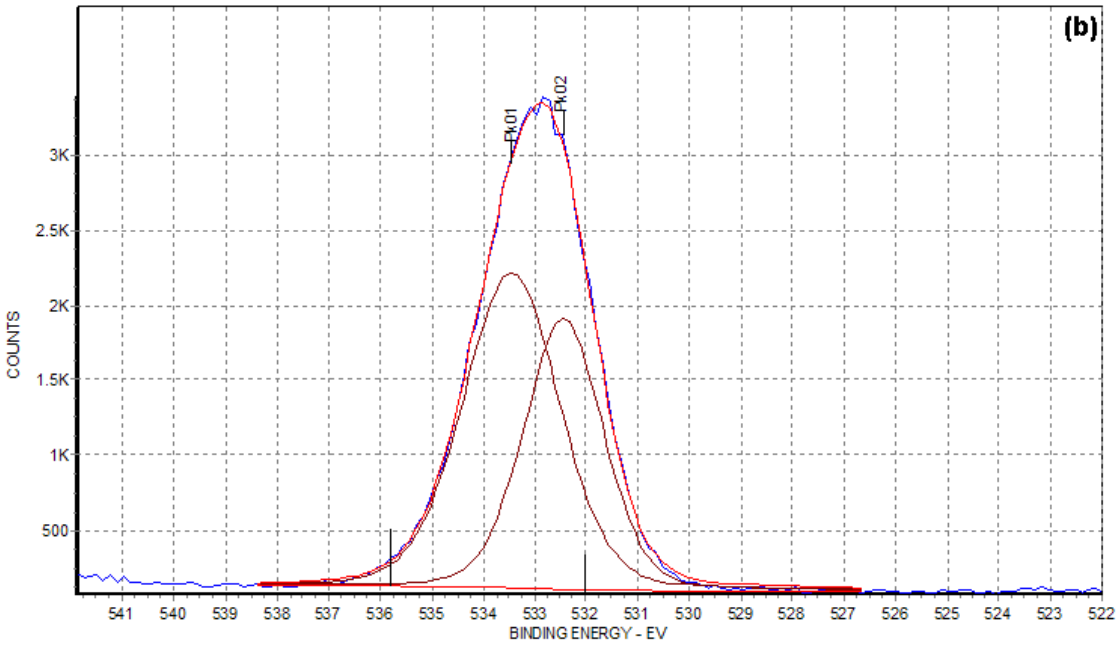

Figure 5.59(b): O 1s HR XPS Region from ALD deposited Al_2O_3 films.

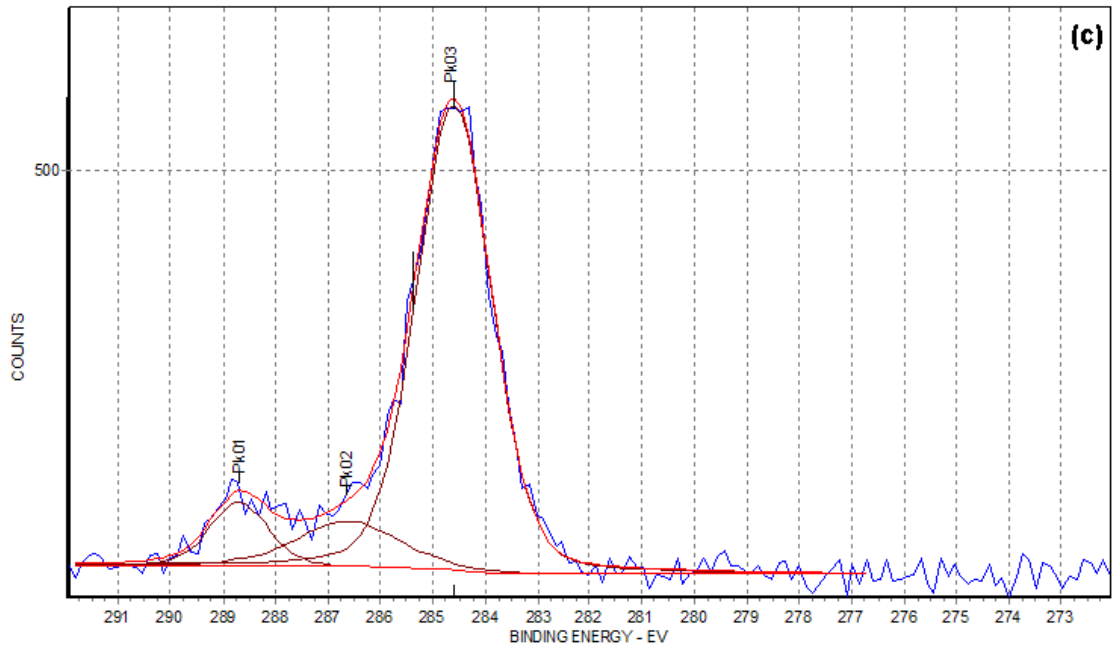

Figure 5.59(c): C 1s HR XPS Region from ALD deposited Al_2O_3 films.

Three peaks appear on the C 1s HR region. These peaks have appeared in previous HR XPS scans of NiO, TiO_2, and ZnO. They are C related peaks due to contamination. [187]

Although the surface chemistry of the ALD deposited Al_2O_3 is correct, the surface structure of the ALD capped etched SiNC is not encouraging. The etched NCs were synthesized under standard conditions were deposited on Au/Cr/Si. Following deposition 50 nm of Al_2O_3 was deposited on top of the NCs. Figure 5.60(a-e) presents several SEM images from this device.

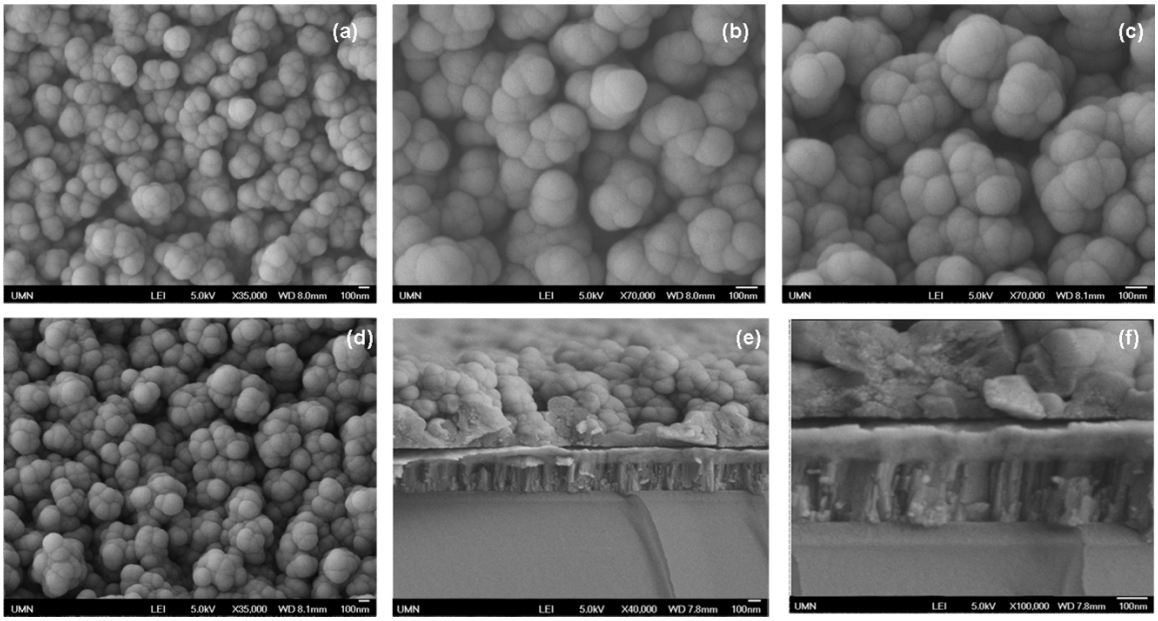

Figure 5.60: SEM Images from ALD Capped SiNC on Au/Cr/Si. (a-b) Top View, (c-d) Tilted Top View, (e-f) X-Section. Scale Bar 100 nm in each figure.

From the SEM images it appears that the structure of Al_2O_3-capped NC is similar to that of the ALD deposited SiO_x on SiNCs. The etched NCs seemed to have formed large agglomerates and there is clearly film non-uniformity. Large gaps appear in the film as well. Examining the X-section images (Figure 5.60 (e-f)) it looks as if the film is rough as well. It appears that this matrix will suffer from the same problems as the ALD

deposited SiO_2. More work is needed, especially with respect to improving the as-deposited NC film in order to fabricate high quality EL devices.

Since the EL devices have not yet been completed it is difficult to comment on the structure shown in Figure 5.60. However, the SEM images suggest that there will interface issues at the Al_2O_3/ETL interface as well as gaps in the insulating matrix were no NC exist and charge is free to move. I-V and optical measurements are needed to gauge the devices' potential as an EL device.

5.5 Other Methods Employed for Device Improvements

Beside the insulating matrix, one other step is currently used to help improve the efficiency of the inorganic-NC based devices. The ITO/Glass samples which are purchased commercially are rough (RMS roughness ≈ 3.4 nm). This roughness can lead to interface traps at the ITO-HTL interface. Therefore, the ITO substrate has been CMP polished before device construction. After 20 turns, the RMS roughness was measured at 0.091 nm (removes ≈ 0.16 nm/turn). After the CMP, the ITO films are smooth and uniform and ready for device integration.

One other step that was commonly employed was a cleaning of the ITO surface before integration to remove any surface contamination. The cleaning procedure for the ITO is outlined below:

I. Wash ITO substrate in DI H_2O for 5 minutes under sonication. Use detergent if needed.

II. Rinse substrates in H_2O

III. Dry substrates with N_2 gas

IV. Sonicate substrates in Acetone for 5 minutes. Repeat without drying.

V. Dry in N_2

VI. Sonicate in Methanol for 5 minutes. Repeat without drying.

VII. Dry in N_2

VIII. Boil substrates in 2-Propanol for 10 minutes (≈ 90 C)

IX. Dry in N_2

X. UV Exposure (in UV Ozone Cleaner) for 10 minutes.

The process outlined above was utilized in all fabricated devices. Besides the insulating matrix discussed in section 5.4.4, we are also investigating other means of improving device operation and efficiency. Clearly, there are two areas which need attention. First of all, the exact band alignment of the etched (or unetched NC) needs to be determined. To properly design transport layers (and devices) it is crucial that we understand where E_C and E_V lie for the NCs. Secondly, a thorough investigation into the growth mechanisms of the NC films is needed in order to determine how the process may be improved to construct layers which will be both smooth and compact.

5.6 Conclusions

In this section we have introduced two fabrication techniques which are suitable for the deposition of metal-oxide transport layers. Specifically, we have discussed the RF sputtering of NiO and TiO_2, and the ALD of ZnO. Thorough characterization was performed on each thin film to ensure that the ideal film properties were present before integrating them into the device. Early SiNC devices were discussed. These devices, although efficient (1.6%), used a NC embedded in an insulating matrix which could lead to charge injection issues. As a result devices utilizing metal-oxide transport layers were investigated. Early metal-oxide-NC devices which use a HTL but no ETL, emit light, however their emission is so weak that it can not be measured by a USB2000 spectrometer. The addition of an ETL increases the light output by a factor of 4. Despite the increase in the light output, the emission is still weak. To improve efficiency to insulating matrix layers were investigated. In both cases, the film deposited on the top of the NC is rough, porous, discontinuous, and potentially full of traps – certainly not the ideal film for a device. Therefore, more work is needed, specifically of the NC layer to improve the structure of the as-deposited NC film.

Chapter 6

Conclusions and Recommendations for Future Work

6.1 – Conclusions

The work discussed in this thesis builds upon previous work on the non-thermal plasma synthesis and passivation of silicon nanocrystals (SiNCs). Several in-flight gas-phase passivation approaches were introduced. Thermal and LPCVD nitride passivation schemes were discussed. FTIR and XPS characterization show differences in the surface structure of the as-produced and nitride capped SiNCs. Although the characterization indicates the growth of a nitride layer ("shell" observed from the TEM) on the NCs surface, PL is observed from the NCs within 7 days indicating O incorporation into the nitride shell.

Tunable, full-visible wavelength emission from CF_4-etched SiNCs is possible by the use of a novel two stage plasma reactor. By controlling different parameters of the experimental setup a particular NC size can be fabricated. The NCs which are etched by this process are passivated with a fluorocarbon film which results from the generation of CF_2 radicals in the etching plasma. Although this layer provides an adequate passivation, it is difficult to remove and prevents further processing of the NCs. Optical measurements indicate that the emission from red to green emitting NCs follow the quantum confinement model, but the blue emission from CF_4-etched NCs does not. The blue emission is believed to result from oxide related surface states and is observed even

in large NCs. A transition point occurs (at ≈ 540 nm, or core NC size of approximately 2.3 nm) at which the emission from the blue band begins to dominate that from quantum confinement since the widening of the NC bandgap has caused more surface states to become radiative recombination pathways. Nevertheless, air-stable QY as high as 20% have been observed for CF_4-etched NCs.

SF_6 etching of SiNCs is a viable alternative to CF_4 etching. Unlike the CF_4 based process, there is no mechanism which inhibits etching. Therefore an increase in the RF power or the SF_6 flow rate yields smaller NCs. The measured QY of SF_6-etched NCs are at least 2X that of CF_4-etched NCs at comparable wavelengths. A maximum QY of 55% (at 710 nm) was measured for SF_6-etched NCs after 15 days of exposure air. This high QY has only been observed in alkyl passivated SiNCs. The origin of the improved optical properties is under investigation, but F may play a crucial role. The native oxidation of both unetched and SF_6-etched NCs follows the Cabrera-Mott mechanism where the oxide thickness saturates near 2.3 nm regardless of surface chemistry.

We have introduced two fabrication techniques which are suitable for the deposition of metal-oxide transport layers. Specifically, we have discussed the RF sputtering of the NiO and TiO_2, and the ALD of ZnO. Thorough characterization was performed on each thin film to ensure that the ideal film properties were present before integrating them into the device. Early inorganic (metal-oxide) -NC devices which use only a hole transport layer (HTL), emit light, however their emission is so weak that it can not be measured by a spectrometer. The addition of an ETL increases the light output by a factor of 4. Despite the increase in the light output, the emission is still weak.

To improve efficiency two insulating matrix layers were investigated, ALD deposited Al_2O_3 and SiO_x. In both cases, the film deposited on the top of the NC surface is rough, porous, discontinuous, and potentially full of traps – certainly not the ideal film for a device. Therefore, more work is needed, specifically on the NC emissive layer to improve the structure of the as-deposited NC film.

6.2 – Future Work

Further work on this project should be focused on improving the efficiency of the inorganic (metal-oxide) – NC based EL devices. First of all, we need to better understand the band alignment of both as-produced and etched SiNCs. Currently, we are approximating the position of the E_V and E_C. However, if the approximation is wrong, serious charge balance issues may exist in the device. Therefore, a significant ultraviolet photoelectron spectroscopy **(**UPS) study on NCs with varying size and surface passivation should allow for an improved device design. Furthermore, similar measurements should also be performed on the inorganic transport layers. We are simply using literature provided values for E_C and E_V for the inorganic transport layers and the UPS would allow us to double-check the position of the E_V. Accurate knowledge of the band position will lead to improved device design and efficiency.

Charge balance is critical to efficient device operation. Imbalance can lead to non-radiative recombination processes such as Auger recombination. Hall measurements need to be performed on each transport layer in order to determine the carrier

concentration. Knowing both the E_V position and carrier concentration will allow for better device designs.

An operational ALD process for TiO_2 and NiO will also improve the inorganic (metal-oxide) NC device. ALD has been shown to deposit smooth, pin-hole free uniform films. The ALD process would allow us to abandon sputtering as the means for depositing NiO and TiO_2. Although the sputtering process does produce usable films, there is always the worry of contamination as well as the fact that the films are not as smooth as those deposited by ALD. Furthermore, ALD could be integrated into the NC reactor following the etching setup to allow for an in-situ deposition for the transport layers. Other metal oxide materials could be use in the device design. MoO_3, V_2O_5, and ZrO_2 have been used with polymer based materials as transport layers. It would be advantageous to determine whether or not these materials would lead to improved device efficiency (over ZnO, TiO_2, or NiO).

There is still a big unknown with respect to the etched NCs. Although the PL QY has been measured as high as 50%, we still really have no good theory on why the SF_6-etched NCs are so efficient. It is important to understand the mechanism behind the improved optical properties because we may be able to exploit this phenomenon with other NC surface passivation. A theoretical study may be needed.

The QY of the shortwave (blue and green) emitting CF_4 or SF_6-etched NCs are low (a few percent or less). This is a problem, especially if we are trying to synthesize a full-color device based on SiNCs. We need to investigate techniques to improve the short wavelength QY, such as hydrosilylation. However, we know that an F-terminated

surface can not be hydrosilylated. Changing the etch chemistry to a Cl precursor which can undergo an exchange reaction followed by hyrdosilylation may allow for improved QY from (short wavelength) etched NCs. Another approach to improving the QY of the etched NCs would be to use H etching in place of F or Cl based etching. This should leave the surface of the NCs passivated with H and as a result hydrosilylation could work. We would also have to change the etching tube reactor from fused silica to alumina to ensure that surface of the etched NC remained O free.

The deposition yield of the shortwave emitting etched NC is also a problem. We typically need to collect 3-4 hours in order to obtain enough material for PL or characterization methods. For device applications, this needs to be increased significantly. If the etched NCs are charged, we can use electrostatics and bias the substrate in order to collect more NCs. A more radical idea would be to use multiple reactors and then funnel the NCs to one central collection area.

As shown in the thesis, the as-deposited NC films are porous and non-uniform. Charge can freely flow throughout this film without interacting with a NC. One potential solution to this problem was the addition of an insulating matrix which forces the charge to move in the NC layer through percolation only. Unfortunately, these films are rough, porous, and non-uniform. This problem needs to be resolved. One option would be to use a novel orifice setup developed by Zak Holman. Zak has been able to deposit GeNC films which appear to be dense and significantly more uniform than the as-produced SiNC films. A second option would be to create the insulating matrix inside of the NC reactor. After the etching step, a parallel-plate CCP could be added to deposit SiO_2 or

$Si3N_4$ directly on the particle film. A heater could also be installed to one of plates to allow for annealing of the NC films, helping to improve film morphology.

Bibliography

[1] H. P. Rocksby, "The Colour of Selenium Ruby Glasses," *Journal of the Society of Glass Technology*, vol. 16, pg. 171-181 (1932).

[2] D. Bimberg, M. Grundmann, and N. N. Ledentsov, "Quantum Dot Heterostructures," (John Wiley and Sons, Chichester, West Sussex, England, 1999).

[3] E. Borovitskaya and M. S. Shur, "Low-Dimensional Systems," in *Quantum Dots*, edited by E. Borovitskaya and M. S. Shur, (World Scientific Publishing Company, Singapore, 2002). pg. 1-14.

[4] Al. L. Efros and A. L. Efros, "Interband Absorption of Light in a Semiconductor Sphere," *Soviet Physics – Semiconductors*, vol. 16, pg. 772-775 (1982)

[5] R. Rossetti, S. Nakahura, and L. E. Brus, "Quantum size effects in the redox potentials, resonance Raman spectra, and electronic spectra of CdS crystallites in aqueous solution," *Journal of Chemical Physics*, vol. 79, pg. 1086-1088 (1983).

[6] A. I. Ekimov and A. A. Onushchenko, "Size quantization of the electron energy spectrum in a microscopic semiconductor crystal," *JETP Letters*, vol. 40, pg. 1136-1139 (1984).

[7] L. E. Brus, "Electron–electron and electron-hole interactions in small semiconductor crystallites: The size dependence of the lowest excited electronic state," *Journal of Chemical Physics*, vol. 80, pg. 4403-4409 (1984).

[8] A. I. Ekimov, Al. L. Efros, and A. A. Onushchenko, "Quantum Size Effect in semiconductor nanocrystals," *Solid State Communcations*, vol. 56, pg. 921-924 (1985).

[9] M. A. Reed, R. T. Bate, K. Bradshaw, W. M. Duncan, W. R. Frensley, J. W. Lee, and H. D. Shih, **"**Spatial quantization in GaAs–AlGaAs multiple quantum dots," *Journal of Vacuum Science and Technology B*, vol. 4, pg. 358-360 (1986).

[10] S. Schmitt-Rink, D. A. B. Miller, and D. S. Chemla, "Theory of the linear and nonlinear optical properties of semiconductor microcrystallites," *Physics Review B*, vol. 35, pg. 8113-8125 (1987).

[11] M. G. Bawendi, W. L. Wilson, L. Rothberg, P. J. Carroll, T. M. Jedju, M. L. Steigerwald, and L. E. Brus, "Electronic structure and photoexcited-carrier dynamics in nanometer-size CdSe clusters," *Physical Review Letters*, vol. 65, pg. 1623-1626 (1996).

[12] A. R. Kortan, R. Hull, R. L. Opila, M. G. Bawendi, M. L. Steigerwald, P. J. Carroll, and L. E. Brus, "Nucleation and growth of cadmium selendie on zinc sulfide quantum crystallite seeds, and vice versa, in inverse micelle media," *Journal of the American Chemical Society*, vol. 112, pg. 1327-1332 (1990).

[13] M. G. Bawendi, P. J. Carroll, W. L. Wilson, and L. E. Brus, "Luminescence properties of CdSe quantum crystallites: Resonance between interior and surface localized states," *Journal of Chemical Physics*, vol. 96, pg. 946-954 (1992).

[14] C. B. Murray, D. J. Norris, and M. G. Bawendi, "Synthesis and characterization of nearly monodisperse CdE (E = sulfur, selenium, tellurium) semiconductor nanocrystallites," *Journal of the American Chemical Society*, vol. 115, pg. 8706-8715 (1993).

[15] C. B. Murray, C. R. Kagan, and M. G. Bawendi, "**S**ynthesis and characterization of monodisperse nanocrystals and close-packed nanocrystal assemblies," *Annual Review of Materials Science*, vol. 30, pg. 545-610 (2000).

[16] M. A. Hines and, P. Guyot-Sionnest, "Synthesis and characterization of strongly luminescing ZnS-capped CdSe nanocrystals." *Journal of Physical Chemistry*, vol. 100, pg. 468–471 (1996).

[17] B. O. Dabbousi, J. Rodriguez-Viejo, F. V. Mikulec, J. R. Heine, H. Mattoussi, R. Ober, K. F. Jensen, and M. G. Bawendi, "(CdSe)ZnS Core−Shell Quantum Dots: Synthesis and Characterization of a Size Series of Highly Luminescent Nanocrystallites," *Journal of Physical Chemistry B*, vol. 101, pg. 9463-9475 (1997).

[18] P. Reiss, "Synthesis of semiconductor nanocrystals in organic solvents," in Semiconductor Nanocrystal Quantum Dots: Synthesis, Assembly, Spectroscopy and Applications, edited by A. L. Rogach, (SpringerWeinNewYork. Vienna, Austria, 2008). pg 35-72.

[19] A. Fu, W. Gu, C. Larabell, and A. P. Alivisatos, "Semiconductor nanocrystals for biological imaging ," *Current Opinion in Neurobiology*, vol 15, pg. 568-575 (2005).

[20] D. Gerion, F. Pinaud, S. C. Williams, W. J. Parak, D. Zanchet, S. Weiss, and A. P. Alivisatos, "Synthesis and Properties of Biocompatible Water-Soluble Silica-Coated CdSe/ZnS Semiconductor Quantum Dots," *Journal of Physical Chemistry B*, vol. 105, pg. 8861-8871 (2001).

[21] S. Coe, W. –K. Woo, M. G. Bawendi, and V. Bulovic, "Electroluminscence from single monolayers in molecular organic devices," *Nature*, vol. 420, 800-803 (2002).

[22] N. C. Greenham, X. G. Peng, and A. P. Alivisatos, "Charge separation and transport in conjugated-polymer/semiconductor-nanocrystal composites studied by photoluminescence quenching and photoconductivity," *Physical Review B*, vol. 54, pg. 17628-17637 (1996).

[23] S. Coe-Sullivan, W. –K. Woo, J. S. Steckel, M. Bawendi, and V. Bulovic, "Tuning the performance of hybrid organic/inorganic quantum dot light-emitting devices," *Organic Electronics*, vol. 4, pg. 123-130 (2003).

[24] X. Peng, M. C. Schlamp, A. V. Kadavanich, and A. P. Alivisatos, "Epitaxial Growth of Highly Luminescent CdSe/CdS Core/Shell Nanocrystals with Photostability and Electronic Accessibility," *Journal of the American Chemical Society*, vol. 119, pg. 7019-7029 (1997).

[25] L. T. Canham, "Epitaxial Growth of Highly Luminescent CdSe/CdS Core/Shell Nanocrystals with Photostability and Electronic Accessibility,"*Applied Physics Letters*, vol. 57, pg. 1046-1048 (1990).

[26] K. A. Littau, P. F. Szajowski, A. J. Muller, A. R. Kortan, and L. E. Brus, "A luminescent silicon nanocrystal colloid via a high temperature aerosol reaction," *Journal of Physical Chemistry*, vol. 97, pg. 1224-1230 (1993).

[27] W. L. Wilson, P. F. Szajowski, and L. E. Brus, "Quantum confinement in size-selected, surface-oxidized silicon nanocrystals," *Science*, vol. 262, 1242-1244 (1993).

[28] L. –W. Wang and A. Zunger, "Electronic structure pseudopotential calculation of large (~1000 atoms) Si quantum dots," *Journal of Physical Chemistry*, vol. 98, pg. 2158-2165 (1994).

[29] A. Zunger and L. –W. Wang, "Theory of silicon nanostructures," *Applied Surface Science*, vol. 102, pg. 350-359 (1996).

[30] L. E. Brus, P. F. Szajowski, W. L. Wilson, T. D. Harris, S. Schuppler, and P. H. Citrin, "Electronic spectroscopy and photophysics of Si nanocrystals: relationship to bulk c-Si and porous Si," *Journal of the American Chemical Society*. vol. 117, pg. 2915-2922 (1995)

[31] M. V. Wolkin, J. Jorne, P. M. Fauchet, G. Allan, and C. Delerue, "Electronic States and Luminescence in Porous Silicon Quantum Dots," *Physical Review Letters*, vol. 82, pg. 197-200 (1999).

[32] L. E. Ramos, J. Furthmuller, and F. Beckstedt, "Effect of backbond oxidation on silicon nanocrystallites," *Physical Review B*, vol. 70, pg. 033311 (2004).

[33] X. Li, Y. He, S. S. Talukdar, and M. T. Swihart, "Process for Preparing Macroscopic Quantities of Brightly Photoluminescent Silicon Nanoparticles with Emission Spanning the Visible Spectrum," *Langmuir*, vol. 19, pg. 8490-8496 (2003).

[34] X. Li, Y. He, and M. T. Swihart, "Surface Functionalization of Silicon Nanoparticles Produced by Laser-Driven Pyrolysis of Silane followed by $HF-HNO_3$ Etching," *Langmuir*, vol. 20, pg. 4720-4727 (2004).

[35] X. Li, Y. He, S. S. Talukdar, and M. T. Swihart, "Preparation of luminescent silicon nanoparticles by photothermal aerosol synthesis followed by acid etching," *Phase Transitions: A Multinational Journal*, vol. 77, pg. 131-137 (2004).

[36] B. Sweryda-Krawiec, R. R. Chandler-Henderson, J. L. Coffer, Y. Gyu Rho, and R. F. Pinizzotto, "A comparison of porous silicon and silicon nanocrystallite photoluminescence quenching with amines," *Journal of Physical Chemistry*, vol. 100, pg. 13776-13780 (1996).

[37] W. D. Kirkey, A. N. Cartwright, X. Li, Y. He, M. T. Swihart, Y. Sahoo, and P. N. Prasad, "Optical properties of polymer-embedded silicon nanoparticles," *Materials Research Society Symposium Proceedings*, vol. 789, pg. 357 (2004).

[38] F. Hua, M. T. Swihart, and E. Ruckenstein, "Efficient surface grafting of luminescent silicon quantum dots by photoinitiated hydrosilylation," *Langmuir*, vol. 21, pg. 6054-6062 (2005).

[39] F. Hua, F. Erogbogbo, M. T. Swihart, and E. Ruckenstein, "Organically capped silicon nanoparticles with blue photoluminescence prepared by hydrosilylation followed by oxidation," *Langmuir*, vol. 22, pg. 4363-4370 (2006).

[40] S. Sato and M. T. Swihart, "Propionic acid terminated silicon nanoparticles: Synthesis and optical characterization," *Chemistry of Materials*, vol. 18, pg. 4083-4088 (2006).

[41] D. Jurbergs, E. Rogojina, L. Mangolini, and U. Kortshagen, "Silicon nanocrystals with ensemble quantum yields exceeding 60%," *Applied Physics Letters*, vol. 88, pg. 233116 (2006).

[42] G. Ledoux, O. Guillois, D. Porterat, C. Reynaud, F. Huisken, B. Kohn, and V. Paillard, "Photoluminescence properties of silicon nanocrystals as a function of their size," *Physical Review B*, vol. 62, pg. 15942-15951 (2000).

[43] F. A. Reboredo and G. Galli, "Theory of alkyl-terminated silicon quantum dots", *Journal of Physical Chemistry B*, vol. 109, pg. 1072-1078 (2005).

[44] H. M'Saad, J. Michel, A. Reddy, and L. C. Kimerling, "Monitoring and Optimization of Silicon Surface Quality," *Journal of the Electrochemical Society*, vol. 142, pg. 2833-2835 (1995).

[45] A. A. Seraphin, S. -T. Ngiam, and K. D. Kolenbrander, "Surface control of luminescence in silicon nanoparticles," *Journal of Applied Physics*, vol. 80, pg. 6429-6433 (1996).

[46] R. K. Baldwin, K. A. Pettigrew, J. C. Garno, P. P. Power, G. –Y. Liu, and S. M. Kauzlarich, "Room Temperature Solution Synthesis of Alkyl-Capped Tetrahedral Shaped Silicon Nanocrystals," *Journal of the American Chemical Society*, vol. 124, pg. 1150-1151 (2002).

[47] M. –S. Yang, K. –S. Cho, J. –H. Jhe, S. –Y. Seo, J. H. Shin, K. J. Kim and D. W. Moon, "Effect of nitride passivation on the visible photoluminescence from Si-nanocrystals," *Applied Physics Letters*, vol. 85, pg. 3408-3410 (2004).

[48] P. Pellegrino, B. Garrido, C. Garcia, R. Ferre, J. A. Moreno, and J. R. Morante, "Enhancement of the emission yield of silicon nanocrystals in silica due to surface passivation," *Physica E*, vol. 16, pg. 424-428 (2003).

[49] M. Zacharias, J. Heitmann, R. Scholz, U. Kahler, M. Schmidt, and J. Blasing, "Size-controlled highly luminescent silicon nanocrystals: A SiO/SiO_2 superlattice approach," *Applied Physics Letters*, vol. 80, pg. 661-663 (2002).

[50] F. Iacona, G. Franzò, and C. Spinella, "Correlation between luminescence and structural properties of Si nanocrystals," *Journal of Applied Physics*, vol. 87, pg. 1295-1303 (2002).

[51] K. S. Cho, N. –M. Park, T. –Y. Kim, K. –H. Kim, G. Y. Sung, and J. H. Shin, "High efficiency visible electroluminescence from silicon nanocrystals embedded in silicon nitride using a transparent doping layer", *Applied Physics Letters*, vol. 86, pg. 071909 (2005).

[52] R. J. Walters, G. I. Bourianoff, and H. A. Atwater, "Field-effect electroluminescence in silicon nanocrystals", *Nature Materials*, vol. 4, pg. 143-146 (2005).

[53] N. –M. Park, T. –S. Kim, and S. –J. Park, "Band gap engineering of amorphous silicon quantum dots for light-emitting diodes", *Applied Physics Letters*, vol. 78, pg. 2575-2577 (2001).

[54] M. Molinari, H. Rinnert, M. Vergnat, and P. Weisbecker, "Evolution with annealing treatments of the size of silicon nanocrystallites embedded in a SiN_x matrix and correlation with optical properties," *Materials Science and Engineering B*, vol. 101, pg. 186-189 (2003).

[55] P. Photopoulos and A. Nassiopolulou, "Room- and low-temperature voltage tunable electroluminescence from a single layer of silicon quantum dots in between two thin SiO_2 layers", *Applied Physics Letters*, vol. 77, pg. 1816-1818 (2000).

[56] C. Lui, C. Li, A. Ji, L. Ma, Y. Wang, and Z. Cao, "Exploring extreme particle density and size for blue photoluminescence from as-deposited amorphous Si-in-SiN_x films", *Applied Physics Letters*, vol. 86, pg. 223111 (2005).

[57] L. Chen, W. Chen, and F. C. Hong, "Visible electroluminescence from silicon nanocrystals embedded in amorphous silicon nitride matrix", *Applied Physics Letters*, vol. 86, pg. 193506 (2005).

[58] O. Jambios, H. Rinnert, X. Devaux, and M. Vergnat, "Photoluminescence and electroluminescence of size-controlled silicon nanocrystallites embedded in SiO_2 thin films", *Journal of Applied Physics*, vol. 98, pg. 046105 (2005).

[59] J. G. Simmons, "Conduction in thin dielectric films", *Journal of Physics D: Applied Physics*, vol. 4, pg. 613-657 (1971).

[60] T. A. Burr, A. A. Seraphin, E. Werwa, and K. D. Kolenbrander, "Carrier transport in thin films of silicon nanoparticles", *Physical Review B*, vol. 56, pg. 4818-4824 (1997).

[61] L. Dinh, L. L. Chase, M. Balooch, W. J. Siekhaus, and F. Wooten, "Optical properties of passivated Si nanocrystals and SiO_x nanostructures," *Physical. Review. B*, vol. 54, pg. 5029-5037 (1996).

[62] S. Yatsuya, S. Kasukabe, and R. Uyeda, "Formation of ultrafine metal particles by gas-evaporation technique — Aluminum in helium," *Journal of Crystal Growth*, vol. 24-25, pg. 319-322 (1974).

[63] S. Hayashi, S. Tanimoto, and K. Yamamoto, "Analysis of surface oxides of gas-evaporated Si small particles with infrared spectroscopy, high-resolution electron microscopy, and x-ray photoemission spectroscopy," *Journal of Applied Physics*, vol. 68, pg. 5300-5308 (1990).

[64] J. J. Boland, **"**Scanning tunneling microscopy study of the adsorption and recombinative desorption of hydrogen from the Si(100)-2×1 surface," *Journal of Vacuum Science and Technology A*, vol. 10, pg. 2458-2464 (1992).

[65] J. W. Lyding, G. C. Abelin, T. C. Shen, C. Wang, and J. R. Tucker, "Nanometer scale patterning and oxidation of silicon surfaces with an ultrahigh vacuum scanning tunneling microscope,**"** *Journal Vacuum Science and Technology B*, vol. 12, pg. 3735-3740 (1994).

[66] Y. –C. Liao, A. M. Nienow, and J. T. Roberts, "Surface Chemistry of Aerosolized Nanoparticles: Thermal Oxidation of Silicon," *Journal of Physical Chemistry B*, vol. 110, pg. 6190-6197 (2006).

[67] A. M. Nienow, J. T. Roberts, "Chemical Vapor Deposition of Zirconium Oxide on Aerosolized Silicon Nanoparticles," *Chemistry of Materials*, vol. 18, pg. 5571-5577 (2006)

[68] Y.-C. Liao, J. T. Roberts, "Self-Assembly of Organic Monolayers on Aerosolized Silicon Nanoparticles," *Journal of the American Chemical Society*, vol. 128, pg. 9061-9065 (2006).

[69] L. Mangolini and U. Kortshagen, "Plasma-Assisted Synthesis of Silicon Nanocrystal Inks," *Advanced Materials*, vol. 19, pg. 2513-2519 (2007)

[70] L. Mangolini, E. Thimsen, and U. Kortshagen, "High-Yield Plasma Synthesis of Luminescent Silicon Nanocrystals," *Nano Letters*, vol. 5, pg. 655-659 (2005).

[71] Z. F. Li, M. T. Swihart, and E. Ruckenstein, "Luminescent Silicon Nanoparticles Capped by Conductive Polyaniline through the Self-Assembly Method," *Langmuir*, vol. 20, pg. 1963-1971 (2004).

[72] J. K. M. Chun, A. B. Bocarsly, T. R. Cottrell, J. B. Benziger and J. C. Yee, "Proton gated emission from porous silicon," *Journal of the American Chemical Society*, vol. 115, pg. 3024-3025 (1993).

[73] J. M. Rehm, G. L. McLendon and P. M. Fauchet, "Conduction and Valence Band Edges of Porous Silicon Determined by Electron Transfer," *Journal of the American Chemical Society*, vol. 118, pg. 4490-4491 (1996).

[74] R. Ligman, L. Mangolini, U. Kortshagen, and S. A. Campbell, "Electroluminescence from surface oxidized silicon nanoparticles dispersed within a polymer matrix,"*Applied Physics Letters*, vol. 90, pg. 061116 (2007).

[75] S. Coe-Sullivan, J. S. Steckel, W. –K. Woo, M. G. Bawendi, and V. Bulovic, **"**Large-Area Ordered Quantum-Dot Monolayers via Phase Separation During Spin-Casting," *Advanced Functional Materials*, vol. 15, pg. 1117-1124 (2005).

[76] A. P. Gosh, L. J. Gerenser, C. M. Jarman, and J. E. Formalik, "Thin-film encapsulation of organic light-emitting devices," *Applied Physics Letters*, vol. 86, pg. 223503 (2005)

[77] J. M. McElvain, H. Antoniadis, M. R. Hueschen, J. N. Miller, D. M. Roitman, J. R. Sheats, and R. L. Moon, "Formation and growth of black spots in organic light-emitting diodes," *Journal of Applied Physics*, vol. 80, pg. 6002-6007 (1996).

[78] J. –M. Caruge, J. E. Helpert, V. Bulovic, and M. G. Bawendi, "NiO as an Inorganic Hole-Transporting Layer in Quantum-Dot Light-Emitting Devices," *Nano Letters*, vol. 6, pg. 2991-2994 (2006).

[79] J. M. Cargue, J. E. Helpert, V. Wood, V. Bulovic, and M. G. Bawendi, "Colloidal quantum-dot light emitting diodes with metal-oxide charge transport layers," *Nature Photonics*, vol. 2, pg. 247-250 (2008).

[80] P. M. Fauchet, "Monolithic silicon light sources," in *Silicon Photonics, Topics in Applied Physics Volume 94*, eds. L. Pavesi and D. J. Lockwood (Springer-Verlag, Berlin, 2004). pg. 177-199.

[81] L. T. Canham, "Silicon quantum wire array fabrication by electrochemical and chemical dissolution of wafers," *Applied Physics Letters*, vol. 57, pg. 1046-1048 (1990).

[82] S. Schuppler, S. L Friedman, M. A. Marcus, D. L. Adler, Y. –H. Xie, F. M. Ross, T. D. Harris, W. L. Brown, Y. J. Chabal, L. E. Brus, and P. H. Citrin, "Dimensions of luminescent oxidized and porous silicon structures," *Physical Review Letters*, vol. 72, pg. 2648-2651 (1994).

[83] L. Pavesi, L. Dal Negro, C. Mazzoleni, G. Franzò and F. Priolo, "Optical gain in silicon nanocrystals," *Nature*, vol. 408, pg. 440-444 (2000).

[84] T. Shimizu-Iwayama, S. Nakao, K. Saitoh and N. Itoh**, "**Photoluminescence from nanoparticles of silicon embedded in an amorphous silicon dioxide matrix," *Journal of Physics: Condensed Matter*, vol. 6, pg. L601-L606 (1994).

[85] Z. H. Lu, D. J. Lockwood, and J. –M. Baribeau, "Quantum confinement and light emission in SiO_2/Si superlattices," *Nature*, vol. 378, pg. 258-260 (1995).

[86] C. –S. Yang, R. A. Bley, S. M. Kauzlarich, H. W. H. Lee, and G. Delgado, "Synthesis of alkyl-terminated silicon nanoclusters by a solution route," *Journal of the American Chemical Society*, vol. 121, pg. 5191-5195 (1999).

[87] J. D. Holmes, K. J. Ziegler, R. C. Doty, L. E. Pell, K. P. Johnston, and B. A. Korgel, "Highly luminescent silicon nanocrystals with discrete optical transitions," *Journal of the American Chemical Society*, vol. 123, pg. 3743-3748 (2001).

[88] J. P. Wilcoxon, G. A. Samara, and P. N Provencio, "Optical and electronic properties of Si nanoclusters synthesized in inverse micelles," *Physical Review B*, vol. 60, pg. 2704-2714 (1999).

[89] M. Tabe, "Thermal Nitridation of Si(111) Surfaces with N_2 Molecules Studied by X-Ray Photoelectron Spectroscopy," *Japenese Journal of Applied Physics*, vol. 34, pg. L1375-L1378 (1994).

[90] P. G. Pai, S. S. Chao, Y. Takagi, and G. Lucovsky, **"**Infrared spectroscopic study of SiO_x films produced by plasma enhanced chemical vapor deposition," *Journal of Vacuum Science and Technology A*, vol. 4, pg. 689-694 (1986).

[91] X. D. Pi, L. Mangolini, S. A. Campbell, and U. Kortshagen, "Room-temperature atmospheric oxidation of Si nanocrystals after HF etching," *Physical Review B*, vol. 75, pg. 085423 (2007).

[92] J. Holm and J. T. Roberts, "Thermal oxidation of 6 nm aerosolized silicon nanoparticles: Size and surface chemistry changes," *Langmuir*, vol. 23, pg. 11217-11224 (2007).

[93] B. B. Stefanov, A. B. Gurevich, M. K. Weldon, K. Raghavachari, and Y. Chabal, "Silicon epoxide: Unexpected intermediate during silicon oxide formation," *Physical Review Letters*, vol. 81, pg. 3908-3911 (1998).

[94] E. A. Petrova, L. A. Bogoslovskaya, L. A. Balagurov, and G. I. Kochoradze, "Room temperature oxidation of porous silicon in air," *Materials Science and Engineering B*, vol. 69-70, pg. 152-156 (2000).

[95] T. Miura, M. Niwano, D. Shoji, and N. Miyamoto, "Kinetics of oxidation on hydrogen-terminated Si(100) and (111) surfaces stored in air," *Journal of Applied Physics*, vol. 79, pg. 4373-4380 (1996).

[96] W. A. Lanford and M. J. Rand, "The hydrogen content of plasma-deposited silicon nitride," *Journal of Applied Physics*, vol. 49, 2473-2477 (1978).

[97] D. C. Marra, E. A. Edelberg, R. L. Naone, and E. S. Aydil, "Silicon hydride composition of plasma-deposited hydrogenated amorphous and nanocrystalline silicon films and surfaces," *Journal of Vacuum Science and Technology A*, vol. 16, pg. 3199-3210 (1998).

[98] T. Yamauchi, R. Barillon, E. Balanzat, T. Asuka, K. Izumi, T. Masutani, and K. Oda, "Yields of CO_2 formation and scissions at ether bonds along nuclear tracks in CR-39," *Radiation Measurements*, vol. 40, pg. 224-228 (2005).

[99] S. K. Ray, S. Das, C. K. Maiti, S. K. Lahiri, N. B. Chakraborti, "Effect of reactive-ion bombardment on the properties of silicon nitride and oxynitride films deposited by ion-beam sputtering," *Journal of Applied Physics*, vol. 75, pg. 8145-8152 (1994).

[100] S. K. Ghosh and T. K. Hatwar, "Preparation and characterization of reactively sputtered silicon nitride thin films," *Thin Solid Films*, vol. 166, pg. 359-366 (1988).

[101] S. P. Speakman, P. M. Read, and A. Kiermasz, "Characterization of PECVD deposited silicon oxy-nitride thin-films," *IPAT 87*, 6th International Conference on Ion and Plasma Assisted Techniques, pg. 273-282 (1987).

[102] T. Kanata, H. Takakura, and Y. Hamakawa, "Preparation of composition-controlled silicon oxynitride films by sputtering; deposition mechanism, and optical and surface properties," *Applied Physics A*, vol. 49, pg. 305-311 (1989)

[103] E. Baclez, B. Mutel, O. Dessaux, P. Goudmand, J. Grimblot, and L. Gengembre, "Elaboration and study of an elastic hard Si-based coating obtained at room temperature from a far cold remote nitrogen plasma," *Thin Solid Films*, vol. 303, pg. 156-166 (1997).

[104] D. V. Tsu, G. Lucovsky, M. J. Mantini, and S. S. Chao, **"**Deposition of silicon oxynitride thin films by remote plasma enhanced chemical vapor deposition," *Journal of Vacuum Science and Technology A*, vol. 5, pg. 1998-2002 (1987).

[105] Y. Cros, N. Jaffrezic-Renault, J. M. Chovelon, and J. J. Fombon, "Study of PECVD Silicon Oxynitride Thin Layers as ISFET Sensitive Insulator Surface for pH Detection," *Journal of the Electrochemical Society*, vol. 139, pg. 507-511 (1992).

[106] G. S. Oehrlein, R. M. Tromp, J. C. Tsang, Y. H. Lee, and E. J. Petrillo, "Near-Surface Damage and Contamination after CF_4/H_2 Reactive Ion Etching of Si," *Journal of the Electrochemical Society*, vol. 132, pg. 1441-1447 (1985).

[107] D. –C. Park, T. Yano, S. –H. Kim, W. –Y. Choi, and J. –H. Cho, "Surface characterization of the milled-silicon nitride nano powders by XPS and TEM," *Key Engineering Materials*, vol. 326-328, pg. 409-412 (2006).

[108] J. M. Olson, "Analysis of LPCVD process conditions for the deposition of low stress silicon nitride. Part I: preliminary LPCVD experiments," *Materials Science in Semiconductor Processing*, vol. 5, pg. 51-60 (2002).

[109] A. A. Bagatur`yants, K. P. Novoselov, A. A. Safonov, J. V. Cole, M. Stoker, and A. A. Korkin, "Silicon nitride chemical vapor deposition from dichlorosilane and ammonia: theoretical study of surface structures and reaction mechanism," *Surface Science*, vol. 486, pg. 213-225 (2001).

[110] X. –J. Liu, J. –J. Zhang, X. –W. Sun, Y. –B. Pan, L. –P. Huang, and C. –Y. Jin, "Growth and properties of silicon nitride films prepared by low pressure chemical vapor deposition using trichlorosilane and ammonia," *Thin Solid Films*, vol. 460, pg. 72-77 (2004).

[111] X. D. Pi, R. W. Liptak, S. A. Campbell, and U. Kortshagen, "In-flight dry etching of plasma-synthesized silicon nanocrystals," *Applied Physics Letters*, vol. 91, pg. 083112 (2007).

[112] X. D. Pi, R. W. Liptak, J. D. Nowak, N. P. Wells, C. B. Carter, S. A. Campbell, and U. Kortshagen, "Air-stable full-visible-spectrum emission from silicon nanocrystals synthesized by an all-gas-phase plasma approach," Nanotechnology, vol. 19, pg. 245603 (2008)

[113] G. S. Oehrlein and H. L. Williams, "Silicon etching mechanisms in a CF_4/H_2 glow discharge," *Journal of Applied Physics*, vol. 62, pg. 662-672 (1987).

[114] M. Inayoshi, M. Ito, M. Hori, and T. Goto, "Surface reaction of CF_2 radicals for fluorocarbon film formation in SiO_2/Si selective etching process," *Journal of Vacuum Science and Technology A*, vol. 16, pg. 233-238 (1998)

[115] G. S. Oehrlein, I. Remains, and Y. H. Lee, "Plasma-deposited fluorocarbon films on silicon studied by ellipsometry," *Thin Solid Films*, vol. 143, pg. 269-278 (1986).

[116] L. M. Ephrath and E. J. Petrillo, "Parameter and Reactor Dependence of Selective Oxide RIE in $CF_4 + H_2$," *Journal of the Electrochemical Society*, vol. 129, pg. 2282-2287 (1982).

[117] T. E. F. M. Standaert, M. Schaepkens, N. R. Rueger, P. G. M. Sebel, G. S. Oehrlein, and J. M. Cook, "High density fluorocarbon etching of silicon in an inductively coupled plasma: Mechanism of etching through a thick steady state fluorocarbon layer ," *Journal of Vacuum Science and Technology A*, vol. 16, pg. 239-249 (1998).

[118] J. H. Thomas III and J. –S. Maa, "X-ray photoelectron spectroscopy study of the surface chemistry of freon-oxygen plasma etched silicon," *Applied Physics Letters*, vol. 43, pg. 859-861 (1983).

[119] J. H. Thomas III, J. T. McGinn, and L. H. Hammer, "Analysis of ion indeed surface damage on silicon etched in a CF_4 plasma," *Applied Physics Letters*, vol. 47, pg. 746-748 (1985).

[120] S. A. Campbell, *The Science and Engineering of Microelectronic Fabrication*, 2nd Ed. (Oxford University Press, New York City, NY, 2001).

[121] C. J. Mogab, A. C. Adams, and D. L. Flamm, "Plasma etching of Si and SiO_2 – The effect of additions to CF_4 plasmas," *Journal of Applied Physics*, vol. 49, pg. 3796-3803 (1978).

[122] D. L. Flamm, "Introduction to Plasma Chemistry," in Plasma Etching: An Introduction, eds. D. L. Manos and D. L. Flamm (Academic Press, London, 1989), pg 91-178.

[123] R. Benoit, "XPS, AES, UPS, and ESCA," WWW document, (http://www.lasurface.com/accueil/index.php)

[124] C. D. Wagner, A. V. Naumkin, A. Kraut-Vass, J. W. Allison, C. J. Powell, and J. R. Rumble, Jr., "NIST X-ray Photoelectron Spectroscopy Database," WWW document, (http://srdata.nist.gov/xps/)

[125] T. R. Gengenback and H. J. Grisser, "Compositional Changes in Plasma-deposited Fluorocarbon Films during Ageing," *Surface Interface Analysis*, vol. 26, pg. 498-511 (1998)

[126] J. Hedman, Y. Baer, A. Berndtsson, M. Klasson, G. Leonhardt, R. Nilsson, C. Nordling, "Influence of doping on the electron spectrum of silicon," *Journal of Electron Spectroscopy and Related Phenomena*, vol. 1, pg. 101-104 (1972).

[127] J. A. Taylor, "Further examination of the Si KLL Auger line in silicon nitride thin films," *Applications of Surface Science*, vol. 7, pg. 168-184 (1981).

[128] J. A. Taylor, G. M. Lancaster, A. Ignatiev, and J. W. Rabalais, "Interactions of ion beams with surfaces. Reactions of nitrogen with silicon and its oxides," *Journal of Chemical Physics*, vol. 68, pg. 1776-1784 (1978).

[129] H. –H. Park, K. –H. Kwon, J. –L. Lee, K. –S. Suh, O. –J. Kwon, K. –I. Cho, and S. –C. Park, "Characterization and removal of silicon surface residue resulting from CHF_3/C_2F_6 reactive ion etching," *Journal of Applied Physics*, vol. 76, pg. 4596-4602 (1994).

[130] G. Lucovsky, J. Yang, S. S. Chao, J. E. Tyler, and W. Czubatyj, "Oxygen-bonding environments in glow-discharge-deposited amorphous silicon-hydrogen alloy films," *Physical Review B*, vol. 28, pg. 3225-3233 (1983)

[131] D. V. Tsu, G. Lucovsky, and B. N. Davidson, "Effects of the nearest neighbors and the alloy matrix on SiH stretching vibrations in the amorphous SiO_r:H ($0<r<2$) alloy system," *Physical Review B*, vol. 40, pg. 1795-1805 (1989).

[132] Y. Xin, Z. Y. Ning, C. Ye, S. H. Xu, J. Chen, and X. H. Liu, "The structural and dielectric properties of SiO_x/a-C,F/SiO_x multi-layer thin films deposited by microwave electron cyclotron resonance plasma method," *Thin Solid Films*, vol. 472, pg. 44-48 (2005).

[133] A. J. Steckl, J. Devrajan, C. Tran, and R. A. Stall, "SiC rapid thermal carbonization of the (111)Si semiconductor-on-insulator structure and subsequent metalorganic chemical vapor deposition of GaN," *Applied Physics Letters*, vol. 69, pg. 2264-2266 (2006).

[134] S. K. Jangjian and Y. L. Wang, "Bonding configuration and electrical properties of nitrogen and fluorine incorporated SiOC:H thin film prepared by plasma enhanced chemical vapor deposition," *Surface and Coatings Technology*, vol. 200, pg. 3140-3144 (2006).

[135] A. Puzder, A. J. Williamson, J. C. Grossman, and G. Galli, "Surface Chemistry of Silicon Nanoclusters," *Physical Review Letters*, vol. 88, pg. 097401 (2002).

[136] A. G. Cullis and L. T. Canham, "Visible light emission due to quantum size effects in highly porous crystalline silicon," *Nature*, vol. 353, pg. 335-338 (1991).

[137] A. Gupta, M. T. Swihart, and H. Wiggers, "Luminescent Colloidal Dispersion of Silicon Quantum Dots from Microwave Plasma Synthesis: Exploring the Photoluminescence Behavior Across the Visible Spectrum," *Advanced Functional Materials*, vol. 19, pg. 696-703 (2009).

[138] A. Hryciw, J. Laforge, C. Blois, M. Glover, and A. Meldrum, "Tunable Luminescence from a Silicon-Rich Oxide Microresonator," *Advanced Materials*, vol. 17, pg. 845-849 (2005).
[139] X. D. Pi, O. H. Y. Zalloum, T. Roscik, J. Wojick, A. P. Knights, P. Mascher, and P. J. Simpson, "Light emission from Si nanoclusters formed at low temperatures," *Applied Physics Letters*, vol. 88, pg 103111 (2006).
[140] G. Belomoin, J. Therrien, A. Smith, S. Rao, R. Twesten, S. Chaieb, M. H. Nayfeh, L. Wagner, and L. Mitas, "Observation of a magic discrete family of ultrabright Si nanoparticles," *Applied Physics Letters*, vol. 80, pg. 841-843 (2002).
[141] R. A. Morgan, "Plasma Etching in Semiconductor Fabrication," (Elsevier, Amsterdam, 1985).
[142] C. Delerue, G. Allan, and M. Lannoo, "Theoretical aspects of the luminescence of porous silicon," *Physical Review B*, vol. 48, pg. 11024-11036 (1993).
[143] R. P. H. Chang, C. C. Chang, S. Darack, "Hydrogen plasma etching of semiconductors and their oxides," *Journal of Vacuum Science and Technology*, vol. 20, pg. 45-50 (1982).
[144] H. I. Liu, D. K. Biegelsen, F. A. Ponce, N. M. Johnson, and R. F. W. Pease, "Self-limiting oxidation for fabricating sub-5 nm silicon nanowires," *Applied Physics Letters*, vol. 64, pg. 1383-1385 (1994).
[145] G. Ledoux, J. Gong, and F. Huisken, "Effect of passivation and aging on the photoluminescence of silicon nanocrystals," *Applied Physics Letters*, vol. 79, pg. 4028-4030 (2001).
[146] L. Mangolini, "Non-Thermal Plasma Synthesis and Passivation of Luminescent Silicon Nanocrystals," Ph.D. Disseration, University of Minnesota, 2007.
[147] L. Mangolini, D. Jurbergs, E. Rogojina, and U. Kortshagen, "High efficiency photoluminescence from silicon nanocrystals prepared by plasma synthesis and organic surface passivation," *Physica Status Solidi (C)*, vol. 3, pg. 3975-3978 (2006).
[148] L. Mangolini, D. Jurbergs, E. Rogojina, and U. Kortshagen, "Plasma synthesis and Liquid-phase surface passivation of brightly luminescent Si nanocrystals," *Journal of Luminescence*, vol. 121, pg. 327-334 (2006).
[149] J. Linnros, N. Lalic, A. Galeckas, and V. Grivickas, "Analysis of the stretched exponential photoluminescence decay from nanometer-sized silicon crystals in SiO_2," *Journal of Applied Physics*, vol. 86, pg. 6128-6134 (1999).
[150] C. Delerue, G. Allan, C. Reynaud, O. Guillos, G. Ledoux, and F. Huisken, "Multiexponential photoluminescence decay in indirect-gap semiconductor nanocrystals," *Physical Review B*, vol. 73, pg. 235318 (2006).
[151] D. I. Kovalev, I. D. Yaroshetzkii, T. Muschik, V. Petrova-Koch, and F. Koch, "Fast and slow visible luminescence bands of oxidized porous Si," *Applied Physics Letters*, vol. 64, pg. 214-216 (1994).
[152] M. Bertino, A. Corazza, M. Martini, A. Mervic, and G. Spinolo, "The 2.7 eV photoluminescence band in high-purity synthetic silica," *Journal of Physics: Condensed Matter*, vol. 6, pg. 6345-6352 (1994).

[153] R. W. Liptak, B. Devetter, J. H. Thomas III, U. Kortshagen, and S. A. Campbell, "SF_6 plasma etching of silicon nanocrystals," *Nanotechnology*, vol. 20, pg. 035603 (2009).
[154] R. W. Liptak, U. Kortshagen, and S. A. Campbell, "Surface chemistry dependence of native oxidation formation on silicon nanocrystals," *Journal of Applied Physics*, vol. 106, pg. 064313 (2009).
[155] T. J. Kolter and M. Elta, "Plasma-etch technology," *IEEE Circuits Device Magazine*, vol. 6, pg. 38-43 (1990).
[156] K. M. Eisele, "SF_6, a Preferable Etchant for Plasma Etching Silicon," *Journal of the Electrochemical Society*, vol. 128, pg. 123-126 (1981).
[157] K. Ninomiya, K. Suzuki, S. Nishimatsu, Y. Gotoh, and O. Okada, "An experimental system for surface reaction studies in microwave plasma etching," *Journal of Vacuum Science and Technology B*, vol. 2, pg. 645-652 (1984)
[158] J. W. Robinson, "Practical Handbook of Spectroscopy," (CRC Press, Boca Raton, FL, 1991).
[159] S. M. Han and E. S. Aydil, "Structure and chemical composition of fluorinated SiO_2 films deposited using SiF_4/O_2 plasmas**,"** *Journal of Vacuum Science and Technology A*, vol. 15, pg. 2893-2904 (1997).
[160] M. Yoshimaru, S. Koizumi, and K. Shimokawa, "Structure of fluorine-doped silicon oxide films deposited by plasma-enhanced chemical vapor deposition," *Journal of Vacuum Science and Technology A*, vol. 15, pg. 2908-2914 (1997).
[161] K. Yamamoto, M. Tsuji, K. Washio, H. Kasahara, and K. Abe, "The Annealing Behavior of Si–F Bonding Structure of Amorphous Si–F Films," *Journal of the Physical Society of Japan*, vol. 52, pg. 925-933 (1983).
[162] C. T. Kirk, "Quantitative analysis of the effect of disorder-induced mode coupling on infrared absorption in silica," *Physical Review B*, vol. 38, pg. 1255-1273 (1988).
[163] V. M. Bermudez, "Study of fluorine (XeF_2) adsorption and of oxygen/fluorine coadsorption on silicon using infrared reflection absorption spectroscopy," *Journal of Vacuum Science and Technology* A, vol. 10, pg. 3478-3485 (1992).
[164] T. Shimada, Y. Katayama, and S. Horigome, "Infrared Spectra of Amorphous Silicon-Fluorine Alloys Prepared by Sputtering in Fluorosilane-Argon Gas Mixture," *Japanese Journal of Applied Physics*, vol. 19, pg. L265-L268 (1980).
[165] A. J. Watts, W. J. Varhue, and M. L. Gibson, "SiO_2 deposition as a byproduct of SF_6 plasma in an electron cyclotron resonance reactor," *Thin Solid Films*, vol. 220, pg. 55-58 (1992).
[166] J. W. Coburn and H. J. Winters, "Ion- and electron-assisted gas-surface chemistry—An important effect in plasma etching" *Journal of Applied Physics*, vol. 50, pg. 3189-3196 (1979).
[167] J. W. Butterbaugh, D. C. Gray, and H. H. Sawin, **"**Plasma–surface interactions in fluorocarbon etching of silicon dioxide," *Journal of Vacuum Science and Technology B*, vol. 9, pg. 1461-1470 (1991).
[168] J. W. Coburn and H. J. Winters, **"**Plasma etching—A discussion of mechanisms," *Journal of Vacuum Science and Technology*, vol. 16, pg. 391-403 (1979).

[169] R. d'Agostino and D. L. Flamm, "Plasma etching of Si and SiO_2 in SF_6–O_2 mixtures," *Journal of Applied Physics*, vol. 52, pg. 162-167 (1981).
[170] D. L. Flamm, V. M. Donnelly, and J. A. Mucha, "Plasma etching of Si and SiO_2 in SF_6–O_2 mixtures," *Journal of Applied Physics*, vol. 52, pg. 3633-3639 (1981).
[171] S. I. Raider, R. Flitsch, and M. J. Palmer, "Oxide Growth on Etched Silicon in Air at Room Temperature," *Journal of the Electrochemical Society*, vol. 122, pg. 413-418 (1975).
[172] C. Ocal, S. Ferrer, and N. Garcia, "Cabrera-Mott mechanism for oxidation of metals explains diffusion of metallic atoms through thin defective oxide layers," *Surface Science*, vol. 163, pg. 335-336 (1985).
[173] G. F. Cerofolini and L. Meda, "Mechanisms and kinetics of room-temperature silicon oxidation," *Journal of Non-Crystalline Solids*, vol. 216, pg. 140-147 (1997).
[174] S. Y. Elovich and G. M. Zhabrova, "Mechanism of the catalytic hydrogenation of ethylene on nickel. I. Kinetics of the process,". *Zhurnal Fizicheskoi Khimii (Russian Journal of Physical Chemistry)*, vol. 13, pg. 1761-1764 (1939).
[175] G. F. Cerofolini, D. Mascolo, and M. O. Vlad, "A model for oxidation kinetics in air at room temperature of hydrogen-terminated (1 0 0) Si," *Journal of Applied Physics*, vol. 100, pg. 054308 (2006).
[176] M. Morita, T. Ohmi, E. Hasegawa, M. Kawakami, and M. Ohwada, "Growth of native oxide on a silicon surface," *Journal of Applied Physics*, vol. 68, pg. 1272-1281 (1990).
[177] G. Mende, J. Finster, D. Flamm and D. Schulze, "Oxidation of etched silicon in air at room temperature; Measurements with ultrasoft X-ray photoelectron spectroscopy (ESCA) and neutron activation analysis," *Surface Science*, vol. 128, pg. 169-175 (1983).
[178] N. S. McIntyre, T. C. Chan and C. Chen, "Characterization of Oxide Structures Formed on Nickel-Chromium Alloy During Low Pressure Oxidation at 500-600°C," *Oxidation of Metals*, vol. 33, pg. 457-479 (1990).
[179] A. P. Grosvenor, M. C. Biesinger, R. St. C. Smart, and N. S. McIntyre, "New interpretations of XPS spectra of nickel metal and oxides," *Surface Science*, vol. 600, pg. 1771-1779 (2006).
[180] C. Scharfschwerdt, J. Kutschera, F. Schneider, M. Neumanna and S. Tougaard, "Quantitative XPS of NiO, CoO and MnO. The effects of elastic and inelastic electron scattering," *Journal of Electron Spectroscopy and Related Phenomena*, vol. 60, pg. 321-335 (1992).
[181] D. H. Lee, S. Y. Yoon, D. H. Yoon and S. J. Suh, "Effect of a NiO Sputtering Condition on the Exchange Coupling of a NiFe/NiO Bilayer," *Journal of the Korean Physical Society*, vol. 44, pg.1079-1082 (2004).
[182] N. S. McIntyre, and M. G. Cook, "X-ray photoelectron studies on some oxides and hydroxides of cobalt, nickel, and copper," *Analytical Chemistry*, vol. 47, pg. 2208-2213 (1975).
[183] R. P. Furstenau, G. McDougall and M .A. Langell, "Initial stages of hydrogen reduction of NiO(100)," *Surface Science*, vol. 150, pg. 55-79 (1985).

[184] M. T. Simnad, R. Smoluchowski, A. Spilners, "Effect of Proton Irradiation Upon Hydrogen Reduction of NiO," *Journal of Applied Physics*, vol. 29, pg. 1630-1632 (1958).
[185] T. L. Barr, "An ESCA study of the termination of the passivation of elemental metals," *Journal of Physical Chemistry*, vol. 82, pg. 1801-1810 (1978).
[186] I. Hotovy, J. Huran, J. Janik and A. P. Kobzev, "Deposition and properties of nickel oxide films produced by DC reactive magnetron sputtering," *Vacuum*, vol. 51, pg. 157-160 (1998).
[187] B. V. Crist, "Handbooks of Monochromatic XPS Spectra, Vol. 1: XPS of Elements and Native Oxides," (XPS International, Mountain View, CA, 1999).
[188] J. F. Moulder K. D. Bomben, P. E. Sobel, and W. F. Stickle, "Handbook of X-Ray Photoelectron Spectroscopy," (Physical Electronics, Eden Prairie, MN, 1995).
[189] M. Datta, H.J. Mathieu and D. Landolt, "Characterization of transpassive films on nickel by sputter profiling and angle resolved AES/XPS," *Applications of Surface Science*, vol. 18, pg. 299-314 (1984).
[190] M. B. Chan-Park, J.X. Gao and A. L. Koo, "Surface characterization of nickel alloy plasma-treated by O_2/CF_4 mixture.," *Journal of Adhesion Science and Technology*, vol. 17, pg. 1979-2004 (2003).
[191] M. Lorenz and M. Schulze, "Reduction of oxidized nickel surfaces," *Surface Science*, vol. 454-456, pg. 234-239 (2000).
[192] S. A. Campbell, "Fabrication Engineering at the Micro- and Nanoscale," 3rd Ed. (Oxford University Press, New York City, NY, 2008).
[193] T. Suntola and J. Anston, "Method for producing compound thin films," U. S. Patent No. 4,058,430 (15 November 1977).
[194] T. Suntola, J. Anston, A. Pakkala, and S. Lindfors, "Thin Film Electroluminescent device," *Society of Information Display 80 Digest*, pg. 108 (1980).
[195] M. Ahonen, M. Pessa, and T. Suntola, "A study of ZnTe films grown on glass substrates using an atomic layer evaporation method," *Thin Solid Films*, vol. 65, 301-307 (1980).
[196] T. Suntola and J. Hyvärinen, "Atomic Layer Epitaxy," *Annual Review of Materials Science*, vol. 15, pg. 177-195 (1985).
[197] T. Suntola, "Atomic layer epitaxy," *Thin Solid Films*, vol. 216, pg. 84-89 (1992).
[198] H. Kim, "Atomic layer deposition of metal and nitride thin films: Current research efforts and applications for semiconductor device processing," *Journal of Vacuum Science and Technology B*, vol. **21**, 2231-2261 (2006).
[199] W. R. Grove, "On the Electro-Chemical Polarity of Gases," ***The Philosophical Transactions of the Royal Society (London)***, vol. **142**, pg. 87-101 (1852).
[200] I. Langmuir, "Positive ion currents in the positive column of the mercury arc," *General Electric Review*, vol. **26**, pg. 731 (1923).
[201] G. K. Wehner, "Sputtering by Ion Bombardment," in *Advances in Electronics and Electron Physics*, vol. 7, ed. L. Marton, (Academic Press, New York City, NY, 1955) pg. 253.

[202] M. A. Lieberman and A. J. Lichtenberg, "Principles of Plasma Discharges and Materials Processing," 2nd Ed. (John Wiley & Sons, New York, NY, 2005).
[203] M. Ohring, "Materials Science of Thin Films: Deposition and Structure," 2nd Ed. (Academic Press, San Diego, CA, 2002).
[204] A. Agrawal, H. R. Habibi, R. K. Agrawal, J. P. Cronin, D. M. Roberts, C. P. R' Sue and C. M. Lampert, "Effect of deposition pressure on the microstructure and electrochromic properties of electron-beam-evaporated nickel oxide films," *Thin Solid Films*, vol. 221, pg. 239-253 (1992).
[205] Y. Kakehi, S. Nakao, K. Satoh and T. Kusaka, "Room-temperature epitaxial growth of NiO(1 1 1) thin films by pulsed laser deposition," *Journal of Crystal Growth*, vol. 237-239, pg. 591-595 (2002).
[206] Y. R. Park and K. J. Kim, "Sol–gel preparation and optical characterization of NiO and $Ni_{1-x}Zn_xO$ thin films," *Journal of Crystal Growth*, vol. 258, pg. 380-384 (2003).
[207] P. Puspharajah, S. Radhakrishna and A. K. Arof, "Transparent conducting lithium-doped nickel oxide thin films by spray pyrolysis technique," *Journal of Materials Science*, vol. 32, pg. 3001-3006 (1997).
[208] K. Sugimoto, M. Seto, S. Tanaka and N. Hara, "Corrosion Resistance of Artificial Passivation Films of Fe_2O_3-Cr_2O_3-NiO Formed by Metalorganic Chemical Vapor Deposition," *Journal of the Electrochemical Society*, vol. 140, pg. 1586-1592 (1993).
[209] J –K. Kang and S. –W. Rhee, "Chemical vapor deposition of nickel oxide films from $Ni(C_5H_5)_2/O_2$," *Thin Solid Films*, vol. 391, pg. 57-61 (2001).
[210] H. Sato, T. Minami, S. Takata, and T. Yamada, "Transparent conducting p-type NiO thin films prepared by magnetron sputtering,"*Thin Solid Films*, vol. 236, pg. 27-31 (1993).
[211] Y. M. Liu, W. S. Huang, and J. S. Yang, "Effects of substrate temperature on the resistivity of non-stoichiometric sputtered NiO_x films," *Surface and Coatings Technology*, vol. 155, pg. 231-235 (2002).
[212] H. –L. Chen, Y. –M. Lu, and W. –S. Hwang, "Characterization of sputtered NiO thin films," *Surface and Coatings Technology*, vol. 198, pg. 138-142 (2002).
[213] H. –L. Chen and Y. –S. Yang, "Effect of crystallographic orientations on electrical properties of sputter-deposited nickel oxide thin films," *Thin Solid Films*, vol. 516, pg. 5590-5596 (2008).
[214] K. Okimura, N. Maeda, and A. Shibata, "Characteristics of rutile TiO_2 films prepared by r.f. magnetron sputtering at a low temperature," *Thin Solid Films*, vol. 281-282, 427-430 (1996).
[215] P. Alexandrov, J. Koprinarova, and D. Todorov, "Dielectric properties of TiO_2-films reactively sputtered from Ti in an RF magnetron," *Vacuum*, vol. 47, pg.1333-1336 (1996).
[216] P. Alexandrov, J. Koprinarova, and D. Todorov, "Influence of the deposition parameters on the chemical composition of reactively rf sputtered TiO_2 on Si," *Applied Surface Science*, vol. 115, pg. 128-134 (1997).

[217] M. Kitao, Y. Oshima, and K. Urabe, "Preparation and Electrochromism of RF-Sputtered TiO_2 Films," *Japanese Journal of Applied Physics*, vol. 36, pg. 4423-4426 (1997).

[218] D. Mardare and G. I. Rusu, "Structural and electrical properties of TiO_2 RF sputtered thin films," *Materials Science and Engineering B*, vol. 75, pg. 68-71 (2000).

[219] L. Miao, P. Jin, K. Kaneko, A. Terai, N. Nabatova-Gabain, and S. Tanemura, "Preparation and characterization of polycrystalline anatase and rutile TiO_2 thin films by rf magnetron sputtering," *Applied Surface Science*, vol. 212-213, pg. 255-263 (2003).

[220] T. Asanuma, T. Matsutani, C. Liu, T. Mihara, and M. Kiuchi, "Structural and optical properties of titanium dioxide films deposited by reactive magnetron sputtering in pure oxygen plasma," *Journal of Applied Physics*, vol. 95, pg. 6011-6016 (2004).

[221] K. –T. Lin and J. –M. Wu, "Rf-Magnetron Sputtering of Titanium Dioxide for Microelectronic Applications," *Japanese Journal of Applied Physics*, vol. 43, pg. 232-236 (2004).

[222] C. –C. Huang, J. –C. Tang, and W. –H. Tao, "Optical properties of tungsten and titanium oxide thin films prepared by plasma sputter deposition," *Solar Energy Materials and Solar Cells*, vol. 83, pg. 15-28 (2004).

[223] C. H. Heo, S. –B. Lee, and J. –H. Boo, "Deposition of TiO_2 thin films using RF magnetron sputtering method and study of their surface characteristics," *Thin Solid Films*, vol. 475, pg. 183-188 (2005).

[224] A. A. Akl, H. Kamal, and K. Abdel-Hady, "Fabrication and characterization of sputtered titanium dioxide films," *Applied Surface Science*, 252, pg. 8651-8656 (2006).

[225] Y. –M. Sung and H. –J. Kim, "Sputter deposition and surface treatment of TiO_2 films for dye-sensitized solar cells using reactive RF plasma," *Thin Solid Films*, vol. 515, pg. 4996-4999 (2007).

[226] L. Niinistö, J. Päiväsaari, J. Niinistö, M. Putkonen, and M. Nieminen, "Advanced electronic and optoelectronic materials by Atomic Layer Deposition: An overview with special emphasis on recent progress in processing of high-k dielectrics and other oxide materials," *Physica Status Solidi (A)*, vol. 201, pg. 1443-1452 (2004).

[227] H. Kumagai, M. Matsumoto, K. Toyoda, and M. Obara, "Preparation and characteristics of nickel oxide thin film by controlled growth with sequential surface chemical reactions," *Journal of Material Science Letters*, vol. 15, pg. 1081-1083 (1996).

[228] T. S. Yang, W. Cho, M. Kim, K. –S. An, T. –M. Chung, C. G. Kim and Y. Kim, "Atomic layer deposition of nickel oxide films using $Ni(dmamp)_2$ and water," *Journal of Vacuum Science and Technology A*, vol. 23, pg. 1238-1243 (2005).

[229] H. L. Liu, G. Scarel, C. Wiemer, M. Perego, S. Spiga, M. Fanciulli and G. Pavia, "Atomic Layer Deposition of NiO Films on Si(100) Using Cyclopentadienyl-Type Compounds and Ozone as Precursors," *Journal of the Electrochemical Society*, vol. 155, pg. H807-H811 (2008).

[230] E. Lindahl, M. Ottosson, and J. –O Carlsson, "Atomic Layer Deposition of NiO by the $Ni(thd)_2/H_2O$ Precursor Combination," *Chemical Vapor Deposition*, vol. 15, pg. 186-191 (2009).

[231] J. Aarik, A. Aidla, V. Sammelselg, Hele Siimon, and T. Uustare, "Control of thin film structure by reactant pressure in atomic layer deposition of TiO_2," *Journal of Crystal Growth*, vol. 169, pg. 496-502 (1996).

[232] J. Aarik, A. Aidla, H. Mändar, and T. Uustare, "Atomic layer deposition of titanium dioxide from $TiCl_4$ and H_2O: investigation of growth mechanism," *Applied Surface Science*, vol. 172, pg. 148-158 (2001).

[233] J. D. Ferguson, A. R. Yoder, A. W. Weimer, and S. M. George, "TiO_2 atomic layer deposition on ZrO_2 particles using alternating exposures of $TiCl_4$ and H_2O," *Applied Surface Science*, vol. 226, pg. 393-404 (2004).

[234] A. Sinha, D. W. Hess, and C. L. Henderson, "Area selective atomic layer deposition of titanium dioxide: Effect of precursor chemistry," *Journal of Vacuum Science and Technology B*, vol. 24, pg. 2523-2532 (2006)

[235] J. Aarik, A. Aidla, T. Uustare, M. Ritala, and M. Leskelä, "Titanium isopropoxide as a precursor for atomic layer deposition: characterization of titanium dioxide growth process," *Applied Surface Science*, vol. 161, pg. 385-395 (2000).

[236] M. Schuisky, A. Harsta, A. Aidla, K. Kukli, A.-A. Kiisler, and J. Aarik, "Atomic Layer Chemical Vapor Deposition of TiO_2 Low Temperature Epitaxy of Rutile and Anatase," *Journal of the Electrochemical Society*, vol. 147, pg. 3319-3325 (2000).

[237] J. Lee, Y. Jang, and M. Sung, "Atomic Layer Deposition of TiO_2 Thin Films on Mixed Self-Assembled Monolayers Studied as a Function of Surface Free Energy," *Advanced Functional Materials*, vol. 138, pg. 873-876 (2003).

[238] Q. Xie, Y. –L. Jiang, C. Detavernier, D. Deduytsche, R. L. Van Meirhaeghe, G. –P. Ru, B. –Z. Li, and X. –P. Qu, "Atomic layer deposition of TiO_2 from tetrakis-dimethyl-amido titanium or Ti isopropoxide precursors and H_2O," *Journal of Applied Physics*, vol. 102, pg. 083521 (2007).

[239] M. Ritala, M. Leskelä and E. Rauhala, "Atomic layer epitaxy growth of titanium dioxide thin films from titanium ethoxide," *Chemistry of.Materials*, vol. 6, pg. 556-561 (1994).

[240] B. Sang and M. Konagai, "Growth of Transparent Conductive Oxide ZnO Films by Atomic Layer Deposition, *Japanese Journal of Applied Physics*, vol. 35, pg. L602-L605 (1996).

[241] A. Yamada, B. Sang, and M. Konagai, "Atomic layer deposition of ZnO transparent conducting oxides," *Applied Surface Science*, vol. 112, pg. 216-222 (1997).

[242] B. Sang, A. Yamada, and M. Konagai, "Highly Stable ZnO Thin Films by Atomic Layer Deposition," *Japanese Journal of Applied Physics*, vol. 37, pg. L1125-L1128 (1998).

[243] S. –H. K. Park and Y. E. Lee, "Controlling preferred orientation of ZnO thin films by atomic layer deposition," *Journal of Materials Science*, vol. 39, pg. 2195-2197 (2004).

[244] S. K. Kim, C. S. Hwang, S. –H. K. Park, and S. J. Yun, "Comparison between ZnO films grown by atomic layer deposition using H_2O or O_3 as oxidant," *Thin Solid Films*, vol. 478, pg. 103-108 (2005).

[245] J. Lim and C. Lee, "Effects of substrate temperature on the microstructure and photoluminescence properties of ZnO thin films prepared by atomic layer deposition," *Thin Solid Films*, vol. 515, pg. 3335-3338 (2007).

[246] E. Guziewicz, I. A. Kowalik, M. Godlewski, K. Kopalko, V. Osinniy, A. Wojcik, S. Yansunenko, E. Lusakowska, W. Paszkowicz, and M. Guziewicz, "Extremely low temperature growth of ZnO by atomic layer deposition," *Journal of Applied Physics*, vol. 103, pg. 033515 (2008).

[247] S. –Y. Pung, K. –L. Choy, X. Hou, and C. Shan, "Preferential growth of ZnO thin films by the atomic layer deposition technique," *Nanotechnology*, vol. 19, pg. 435609 (2008).

[248] S. Jeon, S. Bang, S. Lee, S. Kwon, W. Jeong, H. Jeon, H. J. Chang, and H. –H. Park, "Structural and Electrical Properties of ZnO Thin Films Deposited by Atomic Layer Deposition at Low Temperature," *Journal of the Electrochemical Society*, vol. 155, pg. H738-H743 (2008).

[249] A. Wojcik, M. Godlewski, E. Guziewicz, R. Minikayev, and W. Paszkowicz, "Controlling the preferential growth mode of ZnO thin films grown by atomic layer deposition," *Journal of Crystal Growth*, vol. 310, 284-289 (2008).

[250] A. Pourret, P. Guyot-Sionnest, and J. W. Elam, "Atomic Layer Deposition of ZnO in Quantum Dot Thin Films," *Advanced Materials*, vol. 21, pg. 232-235 (2009).

[251] D. K. Schroder, "Semiconductor Material and Device Characterization", 3rd Ed. (John Wiley & Sons, Hoboken, NJ, 2006).

[252] I. Hotovy, J. Huran, L. Spiess, S. Hascik, and V. Rehacek, "Preparation of nickel oxide thin films for gas sensors applications," *Sensors and Actuators B*, vol. 57, pg. 147-152 (1999).

[253] I. Vaquilla, M. C. G. Passeggi Jr., and J. Ferron, "Oxide stoichiometry in the early stages of titanium oxidation," *Surface Science Letters*, vol. 292, L795-L800 (1993).

[254] S. Bourgeois, P. Le Seigneur, M. Perdereau, "Study by XPS of ultra-thin nickel deposits on TiO_2(100) supports with different stoichiometries," *Surface Science*, vol. 328, pg. 105-110 (1995).

[255] D. Mardare, M. Tasca, M. Delibasm, and G. I. Rusu, "On the structural properties and optical transmittance of TiO_2 r.f. sputtered thin films," *Applied Surface Science*, vol. 156, pg. 200-206 (2006).

[256] K. Saito, Y. Watanabe, K. Takahashi, T. Matsuzawa, B. Sang, and M. Konagai, "Photo atomic layer deposition of transparent conductive ZnO films," *Solar Energy Materials and Solar Cells*, vol. 49, pg. 187-193 (1997).

[257] J. T. Richardson, R. Scates, and M. V. Twigg, "X-ray diffraction study of nickel oxide reduction by hydrogen," *Applied Catalysis A*, vol. 246, pg. 137-150 (2003).

[258] J. V. Grahn, M. Linder, and E. Fredriksson, "In situ growth of evaporated TiO_2 thin films using oxygen radicals: Effect of deposition temperature," *Journal of Vacuum Science and Technology A*, vol. 16, pg. 2495-2500 (1998).

[259] J. Zhao, L. Hu, Z. Wang, Y. Zhao, X. Liang, and M. Wang, "High-quality ZnO thin films prepared by low temperature oxidation of metallic Zn," *Applied Surface Science*, vol. 229, pg. 311-315 (2004).
[260] N. Ikram and M. Akhter, "X-ray diffraction analysis of silicon prepared from rice husk ash," *Journal of Materials Science*, vol. 23, 2379-2381 (1988).
[261] B. Gelloz and N. Koshida, "Nanocrystalline Silicon EL Devices," in *Device Applications of Silicon Nanocrystals and Nanostructures*, edited by N. Koshida, (Springer, New York, 2008). pg. 25-70.
[262] J. Valenta, N. Lalic and J. Linnros, "Electroluminescence of single silicon nanocrystals," *Applied Physics Letters*, vol. 84, pg. 1459-1461 (2004).
[263] H. Z. Song, X. M. Bao, N. S. Li and J. Y. Zhang, "Relation between electroluminescence and photoluminescence of Si^+-implanted SiO_2," *Journal of Applied Physics*, vol. 82, pg. 4028-4032 (1997).
[264] K. Luterova, I. Pelant, J. Valenta, J. L. Rehspringer, D. Muller, J. J. Grob, J. Dian and B. Honerlage, "Red electroluminescence in Si^+-implanted sol–gel-derived SiO_2 films," *Applied Physics Letters*, vol. 77, pg. 2952-2954 (2000).
[265] N. Lalic and J. Linnros, "Light emitting diode structure based on Si nanocrystals formed by implantation into thermal oxide," *Journal of Luminescence*, vol. 80, pg. 263-267 (1998).
[266] J. De La Torre, A. Souifi, A. Poncet, C. Busseret, M. Lemiti, G. Bremond, G. Guillot, O. Gonzalez, B. Garrido, J. R. Morante, and C. Bonafos, "Optical properties of silicon nanocrystal LEDs," *Physica E*, vol. 16, pg. 326-330 (2003).
[267] J. De La Torre, A. Souifi, M. Lemiti, A. Poncet, C. Busseret, G. Guillot, G. Bremond, O. Gonzalez, B. Garrido, and J. R. Morante, "Optical and electrical transport mechanisms in Si-nanocrystal-based LEDs," *Physica E*, vol. 17, pg. 604-606 (2003).
[268] G. R. Lin, C. J. Lin, C. K. Lin, L. J. Chou and Y. L. Chueh, "Oxygen defect and Si nanocrystal dependent white-light and near-infrared electroluminescence of Si-implanted and plasma-enhanced chemical-vapor deposition-grown Si-rich SiO_2," *Journal of Applied Physics*, vol. 97, pg. 093406 (2005).
[269] G. G. Qin, A. P. Li, B. R. Zhang and B. C. Li, "Visible electroluminescence from semitransparent Au film/extra thin Si-rich silicon oxide film/*p*-Si structure," *Journal of Applied Physics*, vol. 78, pg. 2006-2009 (1995).
[270] S. Yanagisawa, K. Sato, and K. Hirakuri, "Electrical and optical properties of electroluminescent device using nanocrystalline silicon," *Thin Solid Films*, vol. 515, pg. 7990-7993 (2007).
[271] L. Y. Chen, W. H. Chen and F. C. N. Hong, "Visible electroluminescence from silicon nanocrystals embedded in amorphous silicon nitride matrix," *Applied Physics Letters*, vol. 86, pg. 193506 (2005).
[272] G. Franzo, A. Irrera, E. C. Moreira, M. Miritello, F. Iacona, D. Sanfilippo, G. Di Stefano, P. G. Fallica, and F. Priolo, "Electroluminescence of silicon nanocrystals in MOS structures," *Applied Physics A*, vol. 74, pg. 1-5 (2002).

[273] A. Fojtik, J. Valenta, T. H. Stuchlikova, J. Stuchlik, I. Pelant, and J. Kocka, "Electroluminescence of silicon nanocrystals in p–i–n diode structures," *Thin Solid Films*, vol. 515, pg. 775-777 (2006).

[274] R. J. Walters, J. Carreras, T. Feng, L. D. Bell, and H. A. Atwater, "Silicon Nanocrystal Field-Effect Light-Emitting Devices," *IEEE Journal of Selected Topics in Quantum Electronics*, vol. 12, pg. 1647-1656 (2006).

[275] G. Wakefield, P. J. Dobson, Y. Y. Foo, A. Loni, A. Simons, and J. L. Hutchison, **"**The fabrication and characterization of nickel oxide films and their application as contacts to polymer/porous silicon electroluminescent devices," *Semiconductor Science and Technology*, vol. 12, pg. 1304-1309 (1997).

[276] G. L. Frey, K. J. Reynolds, and R. H. Friend, "Novel Electrodes from Solution-Processed Layer-Structure Materials**,**" *Advanced Materials*, vol. 14, 265-268 (2002).

[277] S. –W. Park, J. –M. Choi, E. Kim, and S. Im, "Inverted top-emitting organic light-emitting diodes using transparent conductive NiO electrode," *Applied Surface Science*, vol. 244, pg. 439-443 (2005).

[278] H. You, Y. Dai, Z. Zhang, and D. Ma, "Improved performances of organic light-emitting diodes with metal oxide as anode buffer," *Journal of Applied Physics*, vol. 101, pg. 026105 (2007).

[279] J. Meyer, S. Hamwi, T. Bulow, H. –H. Johannes, T. Riedl, and W. Kowalsky, "Highly efficient simplified organic light emitting diodes," *Applied Physics Letters*, vol. 91, pg. 113506 (2007).

[280] B. Wei, S. Yamamoto, M. Ichikawa, C. Li, T. Fukuda, and Y. Taniguchi, "High-efficiency transparent organic light-emitting diode with one thin layer of nickel oxide on a transparent anode for see-through-display application," *Semiconductor Science and Technology*, vol. 22, pg. 788-792 (2007).

[281] S. A. Hague, S. Koops, N. Tokmoldin, J. R. Durant, J. Huang, D. D. C. Bradley, and E. Palomares, "A Multilayered Polymer Light-Emitting Diode Using a Nanocrystalline Metal-Oxide Film as a Charge-Injection Electrode," *Advanced Materials*, vol. 19, pg. 683-687 (2007).

[282] H. C. Im, D. C. Choo, T. W. Kim, J. H. Kim, J. H. Seo, and Y. K. Kim, "Highly efficient organic light-emitting diodes fabricated utilizing nickel-oxide buffer layers between the anodes and the hole transport layers," *Thin Solid Films*, vol. 515, pg. 5099-5102 (2007).

[283] H. J. Bolink, E. Coronado, D. Repetto, M. Sessolo, E. M. Barea, J. Bisquert, G. Garcia-Belmonte, J. Prochazka, and L. Kavan, **"**Inverted Solution Processable OLEDs Using a Metal Oxide as an Electron Injection Contact," *Advanced Functional Materials*, vol. 18, pg. 145-150 (2008).

[284] K. –S. Cho, E. K. Lee, W. –J. Joo, E. Jang, T. –H. Kim, S. J. Lee, S. –J. Kwon, J. Y. Han, B. –K. Kim, B. L. Choi, and J. M. Kim, "High-performance crosslinked colloidal quantum-dot light-emitting diodes," *Nature Photonics*, vol. 3, pg. 341-345 (2009).

[285] C. –H. Liao, M. –T. Lee, C. –H. Tsai, and C. H. Chen, "Highly efficient blue organic light-emitting devices incorporating a composite hole transport layer," *Applied Physics Letters*, vol. 86, pg. 203507 (2005).

[286] S. A. VanSlyke, C. H. Chen, and C. W. Tang, *Applied Physics Letters*, vol. 69, pg. 2160-2162 (1996).

[287] H. Aziz, Z. D. Popovic, N. –X. Hu, A. –M. Hor, and G. Xu, "Degradation Mechanism of Small Molecule-Based Organic Light-Emitting Devices," *Science*, vol. 283, pg. 1900-1902 (1999).

[288] H. Aziz, and Z. D. Popovic, "Study of organic light emitting devices with a 5,6,11,12-tetraphenylnaphthacene (rubrene)-doped hole transport layer," *Applied Physics Letters*, vol. 80, pg. 2180-2182 (2002).

[289] K. T. Shimatsu, W. K. Woo, B. R. Fischer, H. I. Eisler, and M. G. Bawendi, "Surface-Enhanced Emission from Single Semiconductor Nanocrystals," *Physical Review Letters*, vol. 89, pg. 117401 (2002).

[290] D. Hausmann, J. Becker, S. Wang, and R. G. Gordon, "Rapid Vapor Deposition of Highly Conformal Silica Nanolaminates," *Science*, vol. 298, 402-406 (2002).

[291] L. G. Gosset, J. –F. Damlencourt, O. Renualt, D. Rouchon, P. Holliger, A. Ermolieff, I. Trimaille, J. –J. Ganem, F. Martin, and M. N. Semeria, "Interface and material characterization of thin Al_2O_3 layers deposited by ALD using TMA/H_2O," *Journal of Non-Crystalline Solids*, vol. 303, pg. 17-23 (2002).

[292] M. D. Groner, F. H. Fabreguette, J. W. Elam, and S. M. George, "Low-Temperature Al_2O_3 Atomic Layer Deposition," *Chemistry of Materials*, vol. 16, pg. 639-645 (2004).